DEVELOPMENT OF SMOOTHED METHODS FOR FLUID STRUCTURE INTERACTIONS

WANG SHENG

NATIONAL UNIVERSITY OF SINGAPORE
2012

DEVELOPMENT OF SMOOTHED METHODS FOR FLUID STRUCTURE INTERACTIONS

WANG SHENG

(B.Eng., University of Science and Technology Beijing
M.Eng., University of Science and Technology Beijing)

A THESIS SUBMITTED
FOR THE DEGREE OF DOCTOR OF PHILOSOPHY
DEPARTMENT OF MECHANICAL ENGINEERING
NATIONAL UNIVERSITY OF SINGAPORE
2012

Declaration

I hereby declare that the thesis is my original work and it has been written by me in its entirety. I have duly acknowledged all the sources of information which have been used in the thesis.

This thesis has also not been submitted for any degree in any university previously.

Wangsheng

Wang Sheng

20 November 2012

Preface

This dissertation is submitted for the degree of Doctor of Philosophy in the Department of Mechanical Engineering, National University of Singapore (NUS) under the supervision of Prof. Khoo Boo Cheong. To the best of my knowledge, all of the results presented in this dissertation are original, and references are provided on the works by other researchers. A major portion of this dissertation have been published or submitted to international journals or presented at various international conferences as listed below:

1. Papers published or under review

1. **S. Wang**, G.R. Liu, K.C. Hoang. Identifiable range of osseointegration of dental implants through resonance frequency analysis. Medical Engineering & Physics 32 (2010) 1094-1106.
2. **S. Wang**, G.R. Liu, G.Y. Zhang, L. Chen. Accurate bending strength analysis of the asymmetric gear using the novel ES-PIM with triangular mesh. International Journal of Automotive & Mechanical Engineering 3 (2011) 373-397.
3. **S. Wang**, G.R. Liu, Z.Q. Zhang, L. Chen. Nonlinear 3D numerical computations for the square membrane versus experimental data. Engineering Structures 33 (2011) 1828-1837.
4. **S. Wang**, G.R. Liu, G.Y. Zhang, L. Chen. Design of asymmetric gear and accurate bending stress analysis using the ES-PIM with triangular mesh. International Journal of Computational Methods 8 (2011) 759-772.
5. **S. Wang**, B.C. Khoo, G.R. Liu, G.X. Xu. An arbitrary Lagrangian-Eulerian gradient smoothing method (GSM/ALE) for interaction of fluid and a moving rigid body. Computers and Fluids, doi: 10.1016/j.compfluid.2012.10.028.
6. **S. Wang**, B.C. Khoo, G.R. Liu, G.X. Xu. A matrix-free implicit gradient smoothing method (GSM) for compressible flows. International Journal of Aerospace and Lightweight Structures. International Journal of Aerospace and Lightweight Structures, 2 (2012) 245-280.

7. **S. Wang**, B.C. Khoo, G.R. Liu, G.X. Xu. Coupling of the GSM/ALE with ES-FEM-T3 for fluid-structure interactions. Computer Methods in Applied Mechanics and Engineering, under revision.

8. G.R. Liu, Z. Wang, G.Y. Zhang, Z. Zong, **S. Wang**. An edge-based smoothed point interpolation method for material discontinuity. Mechanics of Advanced Materials and Structures, 19 (2012) 3-17.

9. G.R. Liu, **S. Wang**, G.Y. Zhang. A novel Petrov-Galerkin finite element method based on triangular mesh (FEM-T3/T6). International Journal for Computational methods, under revision.

10. S. Jian, Y. Guo, **S. Wang**, K.B.C. Tan, G.R. Liu, F.Q. Zhang. Three dimensional finite element analysis of post-core systems and cements in endodontically treated central maxillary incisors with a full coverage crown. European Journal of Oral Sciences, under revision.

2. Papers for conference presentation

1. **S. Wang**, G.R. Liu, Z.Q. Zhang, L. Chen. Design of Asymmetric Gear and Accurate Bending Stress Analysis Using the ES-PIM with Triangular Mesh. The 9th World Congress on Computational Mechanics and 4th Asian Pacific Congress on Computational Mechanics (WCCM/APCOM2010), Sydney, Australia July 19-23, 2010.

2. G.R. Liu, K.C. Hoang, B.C. Khoo, N.C. Nguyen, A.T. Paterra, **S. Wang**. Inverse identification of material properties of the interface tissue in dental implant systems using reduced basis method. The 14th Asia Pacific Vibration Conference, Hong Kong Polytechnic University, December 5-8, 2011.

Acknowledgements

I would like to express my deepest gratitude and appreciation to my supervisors, Prof. Khoo Boo Cheong and Prof. Liu Guirong for their dedicated support and invaluable guidance. Their extensive knowledge, serious research attitude, constructive suggestions and encouragement are extremely valuable to me. Their influence on me is far beyond this thesis and will benefit me in my future research. I am particularly grateful to Prof. Khoo Boo Cheong, for his inspirational help not only in my research but also in many aspects of my life especially after Prof. Liu Guirong has resigned from NUS.

I would also like to extend a great thank to Dr. Zhang Zhiqian, Dr. Xu Xiangguo, George, Dr. Zhang Guiyong and Dr. Chen Lei for their helpful discussions, suggestions, recommendations and valuable perspectives. To my friends and colleagues, Dr. Li Zirui, Dr. Hoang Khac Chi, Dr. Sayedeh Nasibeh Nourbakhsh Nia, Dr. Li Quanbing Eric, Mr. Liu Jun, Mr. Jiang Yong, Dr. Xu Xu, Dr. Wang Zhen, Dr. Yang Aili, Dr. Yao Jianyao, Dr. Nguyen Thoi Trung, Dr. Khin Zaw, Dr. Wu Shengchuan, Dr. Cui Xiangyang, Dr. Cheng Jing, Dr. He zhicheng, Dr. Tang Qian, Dr. Zhang Lingxin, Dr. Wang Chao and many others, I would like to thank them for their friendship and help.

I appreciate the National University of Singapore for granting me the research scholarship to pursue my graduate study. Many thanks are conveyed to Center for Advanced Computations in Engineering Science (ACES) and Department of Mechanical Engineering, for their material support to every aspect of this work.

In particular, I would like to give my special thanks to my family members, especially to my wife, Bi Hanbing. Without their endless and considerable love, I would not be able to complete this work.

Table of Contents

Summary

Fluid-structure interaction (FSI) problems with moving boundaries and largely deformable solids are great challenging problems, which exist in vast areas from the traditional automobile and airplane industries to the newly developed biomechanics. Numerous advanced numerical methods and algorithms including the conventional finite element method (FEM) and finite volume method (FVM) have been developed for the purpose of accurately tracking the transient deformation of the solid and the resultant fluid flow field. Recently, a family of smoothed methods based on the smoothed theory in $\mathbb{G}$ space has been proposed for solving the pure solid and fluid flow problems. Interesting properties such as super convergence, high convergence rate and accuracy are observed for these smoothed methods in comparison with the conventional ones. Some of these properties have been mathematically proven, however, some others are just concluded from various numerical tests. The theoretical aspects on why they work so well and how much well they can still be are still not clear.

This thesis gives a further exploration of two typical smoothed methods, i.e. the edge-based smoothed finite element method with linear triangular mesh (ES-FEM-T3) and gradient smoothing method (GSM), in solving the pure solid and fluid flow problems, and for the first time to couple these two together for solving challenging FSI problems. Hence, the primary objectives of the present work can be summarized into the following three parts:

1) Formulate the implicit/explicit ES-FEM-T3 schemes and the first time to explore their performances in solving practical engineering problems in solid mechanics;
2) Develop the novel GSM/ALE method to solve the fluid flows over moving mesh;
3) Propose the novel FSI scheme and couple the GSM/ALE with ES-FEM-T3 for solving FSI problems.

For the first part of this work, both implicit and explicit ES-FEM-T3 schemes are formulated to solve two practical engineering problems, i.e. the implicit ES-FEM-T3 for the two-dimensional (2D) linear elastic bending stress analysis found in the gear tooth during gear transmission and the explicit ES-FEM-T3 for the nonlinear deflection of the membrane structure in three-dimensional (3D) space. Numerical results show that the ES-FEM-T3 performs much better than the standard FEM-T3 in solving both problems, which demonstrates the potential of the ES-FEM-T3 in the practical areas. Particularly, i) the implicit ES-FEM-T3 is further implemented into the optimization of the novelly designed gear tooth profiles. The optimized asymmetric gear tooth profile with pressure angle of $\alpha_d / \alpha_c = 35^\circ / 20^\circ$ is finally determined. ii) The nonlinear strain term is particularly added into the explicit ES-FEM-T3 membrane model after an in-depth discussion of the necessity and difficulty of introducing the nonlinear strain term into the analytical expression of the membrane deflections. Two factors, i.e. the pressure fluctuations in the experiment and boundary constraints in numerical models, are found to illustrate the slight differences observed between the numerical and experimental results.

In the second part of this work, the novel GSM/ALE is proposed to solve the incompressible fluid flows over moving mesh, in which the ALE form of Navier-Stokes equations is discretized with GSM in the spatial domain and a moving mesh source term derived directly from the geometric conservation law (GCL) is incorporated into the discrete equations to ensure the recovery of uniform flow by the GSM/ALE while the fluid mesh is moving. The gradient smoothing operation is utilized based on the carefully designed node/mid-point based gradient smoothing domains for approximating the 1st and 2nd order spatial derivatives of the field variables at the nodes. The second order Roe flux differencing splitting unwinding scheme is adopted to deal with the convective flux to ensure the spatial stability. The artificial compressibility formulation is utilized with a dual time stepping approach for the accurate time integration. Convergence, accuracy and robustness of the proposed GSM/ALE are examined through a series of benchmark tests. Numerical results show that the proposed method can preserve the 2nd order accuracy in both spatial and temporal domains and can produce reliable results even on extremely distorted mesh. Good agreement of calculated results with other numerical and experimental results in several examples further demonstrates the robustness of the proposed GSM/ALE for solving the problems of fluid flows over moving mesh.

In consideration of the superior performances of the ES-FEM-T3 and GSM/ALE in, respectively, solving the pure solid and fluid flow problems, they are the first time coupled together for solving the challenging fluid-deformable solid interaction problems. The GSM/ALE is implemented in the fluid domain and the ES-FEM-T3 is implemented in the solid domain. The solutions from these two domains are “linked” through the carefully formulated FSI coupling conditions on the FSI interface. An explicit ES-FEM-T3 scheme is established for solving the transient deformation of the solid portion. A flowchart is presented on how to implement the GSM/ALE with ES-FEM-T3 for solving FSI problems. Through benchmark tests it can be seen that the formulated FSI coupling conditions are accurately formulated and correctly

implemented in the FSI code. The proposed coupling smoothed method can give accurate and convergent solutions for both transient and steady state FSI problems.

The success of coupling GSM/ALE with ES-FEM-T3 for solving FSI problems should be a good start for implementing the family of smoothed methods in solving more complex cross-area problems. Numerical innovations created in the solid, fluid and FSI formulations could provide further understanding of the characteristics of the smoothed methods and fundamentals of the smoothed theory.

Nomenclature

N_{ele}	Number of elements in the domain
N_{node}	Number of nodes in the domain
Ω_i^{sd}	Smoothing domain, the superscript “sd” denotes “smoothing domain”
Γ_i^{sd}	Boundary of the smoothing domain Ω_i^{sd}
A_i^{sd}	Area of the smoothing domain Ω_i^{sd}
N_{sd}	Number of smoothing domains
N_{seg}	Number of segments of the boundary Γ_i^{sd}
N_{gau}	Number of Gauss points used in each segment of the boundary Γ_i^{sd}
N_{sup}	Number of nodes supporting a domain
$\mathbf{N}_I$	Shape function corresponding to node I in an element
nGSD	Node-based gradient smoothing domains
mGSD	Midpoint (edge)-based gradient smoothing domains
A_i^{nGSD}	Area of the nGSD
A_M^{mGSD}	Area of the mGSD
n	Normal vector of an edge, $\mathbf{n}=n_x\mathbf{i}+n_y\mathbf{j}$ in 2D space
t	Physical time
τ	Pseudo time
$(\cdot)^{\mathrm{s}}$	Any physical parameter belonging to the solid domain, subscript “s” denote solid
$(\cdot)^{\mathrm{f}}$	Any physical parameter belonging to the fluid domain, subscript “f” denotes fluid
${}^{n}(\cdot)$	Any physical parameter evaluated at time step n, i.e. at time t^n
u	Displacement vector, $\mathbf{u}=u_x\mathbf{i}+ u_y\mathbf{j}$ in 2D space

$\dot{\mathbf{u}}$	First order time derivation of the displacement, i.e. velocity
$\ddot{\mathbf{u}}$	Second order time derivation of the displacement, i.e. acceleration
ρ	Density of the media
$\mathbf{v}$	Velocity vector, $\mathbf{v}=v_x\mathbf{i}+v_y\mathbf{j}$ in 2D space
$\mathbf{v}_g$	Velocity of the mesh point, $\mathbf{v}_g=v_{gx}\mathbf{i}+v_{gy}\mathbf{j}$ in 2D space
V_s	Contravariant velocity of the fluid, $V_s=\mathbf{v}\cdot\mathbf{n}=v_xn_x+v_yn_y$ in 2D space
V_g	Contravariant velocity of the mesh, $V_g=\mathbf{v}_g\cdot\mathbf{n}=v_{gx}n_x+v_{gy}n_y$ in 2D space
p	Pressure
$\boldsymbol{\sigma}$	Cauchy stress tensor
$\mathbf{F}_c$	Tensor of the convective flux
$\bar{\mathbf{F}}_c$	Smoothed convective flux
$\mathbf{F}_v$	Tensor of the viscous flux
$\bar{\mathbf{F}}_v$	Smoothed viscous flux
β_p	Artificial compressibility
E	Young’s modulus
v	Poisson’s ratio
μ	Dynamic viscosity coefficient
Re	Reynolds number
C_D	Drag coefficient
C_L	Lift coefficient
S_t	Strouhal shedding frequency

List of Tables

List of Figures

Chapter 1

Introduction

Fluid-structure interactions (FSIs) are frequently encountered in practical areas, e.g. from the traditional automobile and airplane industries [1, 2] to the relatively newer field of biomechanics [3-6]. In most cases the interactions just occur at the FSI interface rather than the whole FSI domain. Thus the fluid and solid can be seen as two independent subsystems except for the interaction region at the FSI interface. The dynamic response of the structure is stimulated by the periodic or random FSI force from the FSI interface partially induced by the vortex shedding of the fluid flow. It is this force that gives rise to the solid rotation, deformation, translation or a combined mode of these motions. It is also this force that may lead to solid catastrophic failure, e.g. fatigue and fracture. Therefore, accurately determining the FSI force and thus the dynamic response of the solid immersed in a fluid can be quite essential especially for the safety of the solid part.

Numerical analysis is a powerful tool for solving FSI problems. In the past decades, significant advances have been achieved in the development of stable and efficient computational methods and coupling algorithms for solving fluid flows with structure interactions [7]. Generally, there are two most used coupling algorithms, i.e. the weak (or partitioned) [8-10] and strong (or simultaneous) [11-13] coupling algorithms. The weak coupling algorithm is much more convenient than the strong coupling in several circumstances because it allows for the implementations of different numerical methods into the solid and fluid subsystems, respectively, without any major changing to the routines of the respective methods. The solutions of these two subsystems are “linked” by the FSI coupling conditions on the FSI interface. With this weak coupling algorithm the partial differential equations (PDEs) governing the fluid and solid parts can be solved alternately while the FSI coupling conditions are applied on the FSI interface during the alternate intervals in the time marching process [1].

Various numerical methods have been proposed to solve the pure fluid and solid problems. The most used methods to solve the fluid flows are the finite difference method (FDM) and finite volume method (FVM), while the finite element method (FEM) is most preferred by solid mechanics researchers. Meshfree methods are developed to solve either solid or fluid flow problems. Recently, a family of smoothed methods [14, 15] has also been developed over a so-called $\mathbb{G}$ space [16, 17] to solve the pure solid and fluid flow problems. A series of attractive properties such as super convergence, high convergence rate, accuracy and stability have been observed for these smoothed methods in comparison with the conventional FDM, FVM, FEM and meshfree method. Some of these properties have already been mathematically proven, however, some others are just concluded from numerous numerical tests. The theoretical aspects on why they work so well and how much well they can still be are not so clear. Thus further explorations of the performances of these smoothed methods on solving the pure solid and fluid flow problems are still needed. Furthermore, a coupling of those valid smoothed methods for solving the challenging FSI problems could also be significant, which would give a more broad application to the family of smoothed methods.

In this thesis, it is the intent to explore two typical smoothed methods, i.e. the edge-based smoothed finite element method with linear triangular mesh (ES-FEM-T3) and gradient smoothing method (GSM), in solving the pure solid and fluid flow problems, respectively, and the first time to couple these two valid smoothed methods for solving challenging FSI problems. Numerical innovations created in the solid, fluid and FSI formulations should provide further understanding of the characteristics of the smoothed methods possible lead to consummating the fundamentals of the smoothed theory.

An overview of the family of smoothed methods is presented in this chapter. Since there is a close link between the smoothed and conventional methods, these conventional ones are reviewed firstly in Section 1.1. An overview of the smoothed methods is then presented in Section 1.2, in which the ES-FEM-T3 and GSM are emphasized. Different types of coupling methods are compared in Section 1.3 and the arbitrary Lagrangian-Eulerian (ALE) method is finally chosen for the FSI formulation. The overall objectives, significances and organization of the present thesis are summarized at the end of this chapter.

1.1 Conventional numerical methods

1.1.1 An overview

Classical mathematic models have already been well established in the form of partial differential equations (PDEs) for the pure solid and fluid flows problems [14]. However, analytical solutions of these PDEs are usually unavailable except for some special cases of regular geometrical domains. In order to track the solutions of the PDEs for general cases, the numerical tool should be a better choice. Many types of numerical methods, including the conventional FDM, FVM, FEM and the meshfree method, have been proposed to resolve the PDEs with a proper set of boundary and initial conditions. Different numerical methods are proposed according to different principles and hence possess particular advantages and disadvantages in the simulation process.

The FDM being the oldest numerical method among these four conventional ones can be possibly traced back to the 18th century by Euler [18, 19]. In the FDM, the differential (strong) form of the PDEs are discretized directly based on the Taylor series expansion, using single or multiple block structure mesh. A system of algebraic equations with a banded matrix of coefficients is then built based on the discretized governing equations. Efficient direct or indirect numerical techniques can be used to quickly get the solutions of such a system of algebraic equations [20]. Some special technologies such as the upwind scheme are introduced into the numerical approximations to ensure the spatial stability of the numerical formulation. As only the structure mesh is valid for the FDM, it especially works well for problems of simple geometries.

The FVM is a widely used method for solving fluid flow problems. Early well-documented use of FVM was made by Evans and Harlow [21] and Gentry *et al.* [22]. In late 70's and early 80's, it was further applied to structure mesh [23, 24]. By early 90's, unstructured FVM had been comprehensively developed [25-27]. The FVM is now widely adopted for solving both compressible and incompressible fluid flow problems and implemented in well-known commercial CFD packages [28]. In the FVM, the integral form of PDEs is discretized on the predefined background volumes (meshes). Conservation laws of mass, momentum and energy are enforced on each of these finite volumes, which lead to a system of algebraic equations [28]. These algebraic equations usually involve fluxes of the conserved variable, and thus the vital FVM procedure is how to accurately calculate the fluxes [29]. The resultant solutions for the algebraic equations can be stored at the cell centers or nodes. The values of field variables at non-storage locations are obtained using interpolation [30]. Comparatively, the FVM is conservative even on coarse mesh [18].

The FEM is a robust method and has been developed for static and dynamic, linear and nonlinear stress analysis of solids, structures, as well as fluid flows [31-33]. It was first used by Courant [34] in 1943 for solving torsion problems, and lately named by Clough [35] in 1960 working on the plane stress analysis. Since then, the FEM has made remarkable progress. By now it has become perhaps the most powerful method for solving practical engineering problems with arbitrary geometries and complex boundary conditions due to its flexibility, effectiveness and accuracy [14]. In the standard FEM, the Galerkin weak form of PDEs is firstly constructed based on the potential energy principle (or the virtual work principle), through which the consistency requirement on the field variables is reduced from the 2nd order to the 1st order that gives a consistent relaxation of these variables. The Galerkin weak form is then discretized over the background mesh to get a set of algebraic equations with the unknowns stored at the nodes. After properly applying the Dirichlet/Neumann boundary conditions, the algebraic equations can be finally solved with usual numerical techniques such as the Gauss elimination method and Gauss-Seidel iterative method. Accordingly, the standard procedures of solving a problem with the FEM can be summarized as i) domain discretization, ii) field variables construction via shape functions, and iii) weak formulation to derive the discretized algebraic equations system that can be solved using standard routines [14, 15, 31].

A common ground of these three conventional methods reviewed above is that they all rely on the predefined background mesh during the numerical formulation process. On the contrary, the meshfree method is free of mesh, or uses easily generable mesh in a much more flexible manner [14, 36]. The field functions are approximated locally using a set of nodes scattered within the problem domain as well as on the boundaries [14]. Typical meshfree methods are such as the smooth particle hydrodynamics (SPH) [37-40], the local point collocation method [41], the finite point method [42], the element-free Galerkin (EFG) method [43, 44], the meshless local Petrov-Galerkin (MLPG) method [45], the reproducing kernel particle method (RKPIM) [46], the point interpolation method (PIM) [16, 17, 47-59], and so forth. A survey paper written by Babuška *et al.* [60] provides the mathematical foundation of various meshfree methods. An overview of the theoretical, computational and implementation issues related to various meshfree methods can be found in the monographs by Liu [19]. By removing the restrictions of using the background mesh, the meshfree method is much more flexible and suitable for adaptive analyses. The meshfree method has already been successfully applied to solve problems such as the cracks, underwater shock, explosion and free surface problems [36, 61, 62], all of which the element based methods are not easy to deal with. As the methodology of meshfree method is still in a rapid development stage, new meshfree methods and techniques are constantly proposed [14].

These four conventional numerical methods reviewed above can be roughly classified into two categories, i.e. the strong form method and weak form method, according to different principles of handling the PDEs [14]. The strong form method solves the differential form of the PDEs directly. The assumed functions of field variables are required to have the 2nd order consistency which is the same order of the differentiation in PDEs. The FDM is a typical strong form method. The meshfree methods, e.g. the smooth particle hydrodynamics (SPH) [37-40], the local point collocation methods [41], and the finite point method [42], may also fall under this category. The weak form method, in contrast to the strong form, establishes an alternative weak form (usually in integral form) of the PDEs before discretizing the system equations. The assumed functions of field variables only need to satisfy the PDEs in an integral (average) sense [14], in which the consistent requirement of the assumed functions of filed variables is weakened from the 2nd order to the 1st order. The FEM can be classified into this category, where the integral Galerkin weak formulation are constructed and a so-called test function is introduced into the integral weak form to “absorb” one derivative of the field variables. The FVM that discretizes the integral form of the PDEs over the predefined background control volumes may also belong to this category. Similarly, the meshfree methods such as the EFG method [43, 44], the meshless local Petrov-Galerkin (MLPG) method [45], reproducing kernel particle method (RKPIM)[46], the point interpolation method (PIM) [16, 17, 47-59], can also be classified into this category.

Beyond the traditional categories, a family of weakened-weak (W^2) form methods and weak-form like methods have been recently proposed by Liu *et al*. [16, 17, 51, 63, 64] for solving both the solid and fluid flows problems via applying the smoothing technique back into the conventional settings, by which the consistency requirement of the field variables is *further* reduced by 1 order comparing with the corresponding conventional methods.

1.1.2 What is the smoothing technique?

The smoothing technique [65] can be seen as a strain/gradient field local reconstruction technique [14, 15]. Fundamental of the smoothing technique is that a field variable (or its any order derivations) at a point can be replaced by a weighted integral fashion of this field variable (or its any order derivations) over a local smoothing domain that contains this point [14, 15, 66].

1.1.3 Why to introduce the smoothing technique?

Different conventional numerical methods have their own advantages for solving particular problems. However, they also have unavoidable disadvantages during particular simulations.

For example, the FDM is especially convenient for fluid flows with simple geometries. If complex geometries are involved, the FDM may encounter some difficulties of generating structure mesh. Although FDM could also be used to solve problems with slightly complicated geometry, issues relating to the mapping from the physical domain to the computational domain complicate the process of the numerical implementations [67, 68]. Similarly, the FVM also has some disadvantages. False diffusion usually occurs in the numerical predictions, especially when simple numeric is engaged. It is also difficult to develop schemes with higher than 2nd order accuracy for multi-dimensional problems [26, 29, 30].

The standard FEM are quite powerful for many practical problems, however, there are still several limitations that are becoming increasingly evident [14, 15]: i) the well known “overly stiff” phenomenon, which can have possible consequences of a) the so-called “locking” behavior for many problems, b) inaccuracy in stress solutions, and c) poor solutions when using a triangular mesh; ii) significant accuracy loss when the element mesh is heavily distorted, which is due to the badly conditioned Jacobian matrix during the mapping technique used in isoparametric elements; and iii) difficulty of generating quality mesh. In 2D space, it is well known that the standard FEM model can give more accurate solution with quadrilateral element. However, this kind of element is usually not so easily generated for complicated domains. On the contrary, the triangular element can be generated efficiently and automatically without manual over-ride. Moreover, only the triangular element can be re-meshed fairly automatically. However, the FEM model does not like such element because it always gives solutions of very poor accuracy especially in the stress field [15]. Thus how to improve the accuracy of the standard FEM with the more convenient triangular element is an important issue.

The meshfree strong form method is very simple and straightforward compared with the weak form method. However, instability and poor accuracy issues usually occur to the meshfree strong form method due to the factors such as the node irregularity, the application of the boundary condition and the selection of the nodes for the function approximations [61, 66]. Special techniques are needed to stabilize the solutions [41, 61, 69]. Furthermore, the discretized system equations are also asymmetric for irregularly distributed meshes, even for problems with symmetric operators in the PDEs [66], which complicates the solution process. The meshfree weak form method usually gives stable, robust and accurate solutions for solving many types of problems [61, 66]. However, a main drawback of this kind of method is its high computational cost and complicated formulation procedure due to the use of weak form that requires integrations locally or globally [41].

In consideration of the disadvantages of the conventional numerical methods, the smoothing technique [65] has been employed into these conventional ones considered in the hope to resolve or partially resolve the drawbacks of these conventional methods. Accordingly, a family of smoothed numerical methods has been proposed by Liu *et al*. [16, 17, 51, 63, 64] with the weakened-weak (W^2) or weak-form-like formulations of the PDEs for solving both the solid and fluid flows problems:

i) For the solid mechanics, the W^2 formulation is built upon the Galerkin weak form of PDEs with the application of the smoothing technique [65] over the smoothing domains constructed on top of the background mesh. In the W^2 formulation, the consistency requirement of the field variables is further reduced by 1 order upon the already reduced weak formulation: it enables the assumed displacements in $\mathbb{G}_h^1$ space [16, 17, 70] and hence discontinuous. The smoothed finite element methods (S-FEMs) [15] are the typical smoothed methods, which will be further reviewed in Section 1.2.1.

ii) For the fluid flows, the weak-form like formulation is constructed by applying the smoothing technique [65] to approximate the derivatives of the velocities and pressures in the strong from of PDEs over a series of local smoothing domains. The smoothing operation reduces by 1 order the requirement of consistency on the approximated field functions. The gradient smoothing method (GSM) is a case of the weak-form like methods. A review of the GSM will be presented in Section 1.2.2.

1.2 Smoothed methods with strain/gradient smoothing operations

1.2.1 ES-FEM-T3 with strain smoothing operation in solid mechanics

1.2.1.1 Strain smoothing, generalized smoothing and strain construction operations

By applying the smoothing technique back into the FEM setting, a family of S-FEMs is constructed. Correspondingly, the compatible strain in the standard FEM, which is a function of the derivatives of the shape functions, is now replaced by the smoothed strain in the S-FEMs, which is only a function of the shape functions themselves. Accordingly, the surface integration for the compatible strains over the whole element is transferred to the line integration for the smoothed strains along the boundary of the smoothing domain via the Divergence's theorem. Simultaneously, the constrained conditions on the shape of integrated domain are removed. In doing so, on one hand the computing procedures of the stiffness matrix in the implicit S-FEMs are much easier than those in the standard FEM, on the other hand no coordinate transformations and mappings are needed in the strain construction process in the S-FEMs, which enables the use of highly distorted mesh during the calculation. Most importantly, superior properties such as the bound property, high convergence rate and computational efficiency are achieved by the S-FEMs without increasing any effort in both the modeling and computation processes.

In the S-FEM models, a mesh of elements is still required. It can be created exactly in the same manner as in the standard FEM. The smoothing domains are constructed on top of these elements in the cell-based, node-based or edge-based fashions. Theoretically, any polygonal elements, e.g. the three node triangular (T3), four node quadrilateral element (Q4), *n*-sided polygonal elements in 2D space and tetrahedral element (T4), hexahedral elements in 3D space, or hybrid of these elements, can be used as the background mesh. If the smoothing technique is implemented on the smoothing domains constructed over the T3 or T4 background mesh, the assumed displacement field is continuous in the smoothing domains and thus it falls into the $\mathbb{H}^1$ space [14], which leads to the so-called strain smoothing operation and the corresponding Smoothed-Galerkin formulation of the PDEs [16, 17, 51]. While if the smoothing technique is implemented on the smoothing domains constructed over the higher order Q4 [51, 71-74], *n*-sided polygonal [74] or hexahedral background element [47, 48, 50, 52, 75, 76], the assumed displacement field will be discontinuous in the smoothing domains and thus it falls into the $\mathbb{G}$ space [14], which leads to the so-called generalized smoothing operation and the corresponding Generalized-Smoothed Galerkin formulation of the PDEs [16, 17, 51].

As a continuous field function in a $\mathbb{H}_h^1$ space is included in the $\mathbb{G}_h^1$ space, we could say that the strain smoothing operation is a special case of the generalized smoothing operation [14].

Moreover, both the strain and generalized smoothing operations belong to a more broad category, i.e. the strain construction category, in which more flexible strain construction techniques are allowed to reconstruct the strain field as long as the newly constructed strain field satisfies the admissible conditions such as the orthogonal condition, norm equivalence condition, strain convergence condition and zero-sum condition [14], so as to ensure the stability and convergence of the newly developed method. A relative relationship of different smoothing techniques is illustrated in Fig. 1.1.

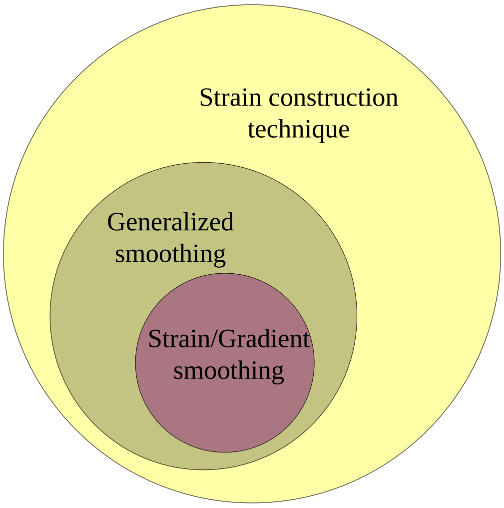

Fig. 1.1 Containment relationships of different smoothing techniques

In practice, the strain smoothing operation is most preferred because of: i) the easy generation of the T3 or T4 elements even for complicated domains; ii) the low computational efforts due to the small band width of the stiffness matrix; iii) the high computational efficiency; and iv) the easy generation of the T3 or T4 elements in the adaptive analysis. So the S-FEMs based on the strain smoothing operation over T3 or

T4 background meshes are of main concerned in the present thesis. Details of the smoothed methods based on generalized smoothing operation or other strain construction techniques can be found in [14].

1.2.1.2 S-FEMs with strain smoothing operation

In 2D space, according to different ways of constructing the smoothing domains over the T3 background mesh, there are in total three main types of S-FEM methods, i.e. the cell-based smoothed finite element method (CS-FEM-T3), the node-based smoothed finite element method (NS-FEM-T3), and the edge-based smoothed finite element method (ES-FEM-T3).

In the CS-FEM-T3 [74], the smoothing domains are the three sub triangular elements that nested in the original triangular element, and the smoothed strains are calculated based on the three sub triangular elements. Because each of these three sub triangular elements has only three supporting nodes, piecewise linear shape functions for each of these three triangular smoothing domains are in fact the same. Therefore, the smoothed strains in each of the triangular smoothing domains are all the same as compatible strain field in the original triangular element. As such, the CS-FEM-T3 and the FEM-T3 are in fact identical in this circumstance. In the following discussions of the performance of the S-FEMs, we thus indentify the CS-FEM-T3 as FEM-T3. However, can we still use T3 element to formulate a cell-based smoothed model that is different from the FEM-T3 model? The answer is “yes” and very accurate model can be formulated, but it requires the use of the general PIM. Interested readers may refer to recent work on the cell-based smoothed PIM [77].

The NS-FEM-T3 model is another typical model of S-FEMs. The smoothing strains in NS-FEM-T3 are calculated based on the node-based smoothing domains that are constructed by simply connecting the centroids of relevant triangles with midpoints of influenced cell-edges. These smoothed strains are then substituted into the Galerkin weak form of the PDEs to get a system of smoothed algebraic equations. By solving these algebraic equations with the same routines as in the standard FEM, we can then get the results. The NS-FEM-T3 can give upper-bounded solutions in both the energy and displacement norms to the exact solutions [48, 78]. Furthermore, it has also natural immunization from volumetric locking, ultra-accuracy, and super-convergence of the stress solution. The NS-FEM-T3 is stable in the spatial domain. A drawback of this method is its temporal instability (spurious non-zero-energy modes in free vibration analyses and numerical instability in forced vibration analyses) encountered in solving dynamic problems, similar to some meshfree methods [79-81]. The temporal instability may due to the “overly soft” behavior resulting from the overcorrection to the “overly stiff” behavior of the standard FEM [78]. Special attention should be paid during solving the dynamic problems via NS-FEM-T3.

The ES-FEM-T3 [82] is the third S-FEM model, where the smoothed strains are calculated based on the edge-based smoothing domain that i) connects the two vortexes of an inner edge and the two centers of the cells corresponding to this edge; or ii) connects the two vortexes of an boundary edge and the centroid of the boundary element. The smoothed strains are substituted into the Galerkin weak form of the PDEs to get a system of smoothed algebraic equations. The ES-FEM-T3 possesses the good properties of both spatially and temporally stability, and ultra- accuracy (even more accurate than the FEM-Q4).

A summary of the properties of different S-FEM models is presented in Table 1.1.

Table 1.1 Versions of S-FEMs and their properties in 2D space

Name	Methods for creation	Main features/properties
CS-FEM-T3	i) Smoothed Galerkin ii) Smoothed strain based on element or cells created by further dividing the elements	i) Identical with the FEM-T3
NS-FEM-T3	i) Smoothed Galerkin ii) Smoothed strain based on each of the nodes of the mesh by connecting portions of the surrounding elements sharing the node	i) Linear conforming ii) Volumetric locking free iii) Upper bound iv) Strong super convergence in energy norm v) Spatially stable, temporally instable
ES-FEM-T3	i) Smoothed Galerkin ii) Smoothed strain based on each edges of the mesh by connecting portions of the surrounding elements sharing the edge	i) Linear conforming ii) Ultra-accuracy iii) Very efficient iv) Strong super convergence in displacement/energy norm v) Spatially and temporally stable

1.2.1.3 Superior of ES-FEM-T3 among S-FEMs

If we consider the computational efficiency (the CPU time needed for solution of the same accuracy) of these three methods, it can be found that the ES-FEM-T3 can achieve the highest computational efficiency among all these three methods. A quantitative comparison of these three methods presented in [83, 84] shows the computational efficiency of ES-FEM-T3 is around 20 times than that of NS-FEM-T3 and around 10 times than that of FEM-T3 according to the displacement norm errors. Therefore, the ES-FEM-T3 seems to offer a more excellent platform for solid analysis than the other two methods. That is one consideration of choosing the ES-FEM-T3 for solving the solid mechanics as well as FSI problems in the present thesis.

1.2.2 GSM with gradient smoothing operation in fluid mechanics

Enlightened by the strain smoothing operation in the Galerkin weak form in solid mechanics, the smoothing technique is also tentatively implemented to directly solve the strong form (differential form) of the PDEs. In this case, all the unknowns of field variables are stored at the vertexes of the background triangular mesh, and the 1st and 2nd order spatial derivatives of the field variables are directly approximated with the smoothing technique in a weighted integral fashion over relevant smoothing domains surrounding the point of interest. As the smoothing technique is used to deal with the gradient of the velocities and pressures in fluid mechanics, we will denote the smoothing technique as “gradient smoothing” here to distinguish from the “strain smoothing” operation on the strains in the solid mechanics.

By using the gradient smoothing operation, the consistency requirement on the approximated field functions is properly reduced by 1 order. Therefore, it is much like a weak-form like method as that in the standard FEM. The main difference of the “weakening” between the gradient smoothing operation for fluid and the strain smoothing operation for solid lies in their implementation procedures. The weakening for fluid is implemented in the stage of function approximation while that for solid is in the stage of creating the system equations. Such a “weakening” formulation can be termed as a weak-form like formulation [14]. It is because in using the gradient smoothing operation, the proposed scheme performs quite stably. The error of the function approximation can also be smeared, which ensures that the error can be properly bounded by the interpolation error caused by the function approximation using the nodal values for a discretized model [14].

By implementing the gradient smoothing operation to discretize the Navier-Stokes equations, the so-called gradient smoothing method (GSM) is proposed [63, 64]. The GSM has already been implemented to solve both compressible and incompressible fluid flows as well as adaptive analysis [30]. Numerical results show that the GSM is conservative, conformal, efficient, robust and accurate to the 2nd order in the spatial domain. It is also stable for arbitrarily distributed nodes and for problems with finite domains. Besides that, the GSM has some relations to the FDM and FVM [30].

- **GSM vs. FDM**

1) The spatial derivatives are approximated using Taylor-series expansion in the FDM. In the GSM, the gradient smoothing operation is used, which is in fact a boundary flux approximation. After the derivatives are approximated, the follow on treatment for GSM and FEM are essentially the same.
2) The standard FDM works well usually for structured meshes. The GSM, however, works well also for unstructured mesh with irregular triangular cells and hence applicable to domains of arbitrarily complicated geometry.
3) The FDM can be applied for less regular domains via domain transformation. However, there exist problems and limitations with such a transformation, and it is far from being efficient for complicated problem domains. On the contrary, in the GSM, the governing equations are always discretized directly on the physical space. No transformation is needed, and naturally no related complications.
4) Most FDM schemes are usually not conservative, while all the proposed GSM schemes are locally conservative and can be made global conservative with proper treatment of the boundary conditions.
5) When regular mesh is used, and a proper set of GSDs are used, the GSM becomes an FDM. Therefore, an FDM can be viewed as a special case of GSM in this regard.

- **GSM vs. FVM**

The GSM has many similarities to the FVM and thus many techniques implemented in the FVM can be utilized for the GSM procedure. However, they are distinct from each other in the following ways.

1) The FVM was derived from physical conservation laws with respect to physical quantities such as mass, momentum and energy using control volumes. FVM works without knowing the strong form PDEs. The GSM was originated from the gradient smoothing operation to approximate the directives of any function regardless of its physical background. It is a purely mathematical treatment applied directly to the strong form PDEs. GSM works only when the strong form equations are available. The procedure of GSM is in fact more like the FDM in this regard.
2) The FVM is a typical weak form method based on physical laws, while the GSM is more like a strong form method with a weak formulation flavor and is called weak-form like method.
3) The traditional FVM uses directly the original elements/cells as control volumes to which the governing equations are discretized. In the GSM, the original cells formed by triangulation are used as background cells. All sorts of different smoothing domains (nGSD, mGSD and cGSD) are then formed based on these background cells, and the strong form PDEs are discretized using these GSDs in various ways.
4) In the GSM formulation, we are not confined to use the Heaviside (piecewise constant) smoothing function. When different smoothing functions are used, we could have many alternatives. For example, the piecewise linear smoothing function has already been explored in the LWGSM [30]. Of course, when the smoothing function becomes more sophisticated, the numerical treatments can be more complicated which may require special techniques.

5) When GSM with Heaviside type smoothing function and proper selected smoothing domains are used, the GSM becomes the FVM. In this regards, the FVM may be viewed as a special case of GSM.

Hence, the GSM is an innovative and unique numerical method with its distinctive features, and which possesses great potentials for solving fluid flow problems. Due to its attractive properties, it is thus further employed for solving the fluid-rigid/deformable solid interaction problems in the present thesis.

1.2.3 Coupling GSM with ES-FEM-T3 for FSI analysis

From the review above it can be seen that the ES-FEM-T3 and GSM possess interesting characteristics and can perform better than the other smoothed and conventional methods in solving the pure solid and fluid flow problems, respectively. However, no work has been done by now by combining these two attractive smoothed methods. Thus the following simple question is raised:

How will it be if the smoothed methods are combined for FSI analysis, and what special characteristics will the combined method exhibit?

If the combined smoothed method work well for FSI problems, it will certainly extend the family of smoothed methods into a much broader area, and the numerical innovations developed in the FSI numerical implementations will certainly complement and contribute to the fundamentals of the smoothed theory. A coupling of the GSM with ES-FEM-T3 is proposed for FSI analysis in the present thesis. The methods used to realize the FSI coupling process will be reviewed in the following section.

1.3 Fluid-structure interactions

The fluid-structure interaction analysis originates from the traditional industrial applications, including the water-dam [85, 86] and water-tank [87-89] interactions during the earthquakes, the ship oscillation in the open sea [90, 91] and the pipe line vibration containing flowing fluid [92, 93]. In recent years, the fluid-structure interaction analysis becomes important in other scientific and engineering fields. Typical applications are such as the fluid induced vibration of the structure in aeronautical and naval engineering [1, 2], the wind-induced vibration in high-rise building or large bridge girder [94, 95], the cyclic response of offshore structure exposed to sea current [96] and the deformation of heart valve affected by the blood flows during the valve’ s opening and closing processes [3-6].

One common feature of the FSI interactions is that these interactions just occur at the FSI interface rather than the whole FSI domain, where the fluid and solid can be seen as two independent subsystems except for the unique interaction occurring at the FSI interface. Any efficient and mature methods can be implemented for the fluid and solid domains, respectively, and the solutions of these two domains are successively exchanged according to the FSI coupling conditions of displacement/velocity compatibility and traction equilibrium on the FSI interface [8, 97, 98].

In a numerical modeling process, the fluid part is most conveniently described with an Eulerian description, while a Lagrangian formulation is more appropriate for the solid part [9]. However, these two formulations are incompatible which will raise difficulties to the successive information exchanges on the FSI interface. Literature survey reveals that there are mainly two distinct classes of methods proposed to tackle this incompatibility [99]: i) the moving mesh method and ii) the fixed mesh method.

1.3.1 Moving mesh method

The moving mesh method allows the movement of the FSI interface and thus the movement of mesh inside the fluid domain. The arbitrary Lagrangian-Eulerian (ALE) method is a typical moving mesh method. In using ALE to solve FSI problems, the fluid flow is described over the moving fluid mesh with ALE description while the solid is described with the Lagrangian description. The compatibility of these two descriptions is ensured on the FSI interface in a consistent and accurate manner that the nodal displacements/velocities of the fluid mesh on the FSI interface should be equal to those of solid particles at the same point. Accordingly, the rest of the mesh inside the fluid domain should be updated timely according to the velocity/displacement interpolation algorithm [99, 100] or the “pseudo-structure” algorithm [101-105]. Because of the freedom of moving the fluid mesh, greater distortions of the continuum can be avoid in ALE than would be allowed by a purely Lagrangian method and greater resolution than that afforded by purely Eulerian approach [106].

One of the earliest scheme similar with the ALE nature may be found in the report by Nor [107] and Trulio [108] for solving compressible flow problems. Hirt *et al*. [109] firstly proposed the ALE technique with FDM (ICED-ALE) for solving FSI problems at different flow speeds. Pracht [110] successfully extended the idea of Hirt *et al*. [109] to 3D case. Besides, the ALE technique was also implemented with FVM [111-113], where the ALE form of PDEs governing the fluid flows are discretized with the standard FVM and the geometric conservation law (GCL) needs to be satisfied by introducing an extra term including the velocities of the mesh in the discretized PDEs. Early implementations of the ALE technique with FEM are developed by Donea *et al*. [114] in 1977, Belytschko *et al*. [115] in 1978, Bathe *et al*. [116] in 1979, and Hughes *et al*. [117] in 1981 for solving fluid-structure interactions, free surface problems, pressurized bubbles and fluid sloshing and swirling problems. The subsequent implementations of the ALE technique in the finite element context can be found in [100, 118-120]. Recently, Bathe *et al*. [7, 8] developed a finite element procedure for solving FSI problems for general fluids and provided a series of benchmarks for testing newly developed schemes for FSI analysis. In order to overcome the spurious spatial oscillations with FEM for solving fluid flows with high Peclet numbers, techniques such as the characteristic-Galerkin formulation [121], the streamline-upwind/Petrov-Galerkin formulation (SUPG) [122] and the Galerkin/least-square formulation [123-126] should be further employed.

Different with the ALE formulation where the governing equations of fluid are constructed over mesh on the deformed configuration, another type of moving mesh method constructs the governing equations of fluid over the mesh on the undeformed configuration [127]. The moved mesh is mapped back to the originally (fixed) mesh in each FSI time step. This leads to a time dependent transformation between the physical and the computational coordinates [99]. Because of the mesh mapping, the structure mesh with certain governing equations can only be utilized. Recently developments of this type of moving mesh method can be found in [128, 129]. This kind of ALE formulation will not be concerned in the present thesis.

1.3.2 Fixed mesh method

In the fixed mesh method, the fluid flow is described with the Eulerian description while the solid is described with the Lagrangian description. The moving FSI interface is tracked on this set of Eulerian mesh [130]. Different methods, e.g. the immersed boundary (IB) method [131], the fictitious domain method [132], the hybrid Cartesian/immersed boundary (HCIB) methods [133-136], the extended immerse boundary method (EIBM) [137] and the immersed finite element method [130, 138, 139], have been proposed to tackle the incompatibility of these two descriptions.

Among these, the IB method, which is firstly developed by Peskin [131] to solve the interactions between the blood flow and the human heart and heart valves, is the foundation for the other fixed mesh methods. In the IB method, the solid is treated as a set of discrete Lagrangian markers embedded in the Eulerian fluid domain. These markers can be treated as force generators in the fluid field and move along with the fluid. The interaction between the Lagrangian markers and the fluid variables defined on the fixed Eulerian grid is linked by a well-chosen discretized delta function [102, 140, 141]. It is these forces imposing the kinematic constraints that the velocity at each of these solid points is coupled (interpolated) to the fluid velocity at that point. By using the IB method, the FSI interface could be tracked automatically without the time consuming mesh updating process as in ALE. However, as point out by Zhang *et al*. in [130, 138], a major obstacle of the IB method is its assumption of the fiber-like immersed elastic structure, which impedes realistic analysis and modeling of the physical deformation of the immersed structure with complicated nonlinear constitutive laws and an accurate representation of the finite volume they occupy within the fluid domain. Thus Zhang *et al*. [130, 138] proposed the so-called immersed finite element method (IFEM) for solving large deformations of incompressible hyper-elastic solid immersed in an incompressible or slightly compressible fluid. In the IFEM, the delta functions are used as the shape functions in meshfree methods, which may not only provide higher order smoothness on the FSI interface but also improve the ability to handle non-uniform fluid grids. Based on the idea of IFEM, the immersed smoothed finite element method (IS-FEM) is most recently proposed by Zhang *et al*. [142], which analyzes the physical motion and deformation of the solids fully immersed inside the fluid domain like IFEM but adopts efficient direct forcing technique from IB/HCIB. Furthermore, the artificial fluids assumption in IFEM is not required in the proposed immersed S-FEM method.

1.3.3 Why to choose ALE for FSI analysis?

The attractiveness of fixed mesh method is their easy handling of FSI problems with very complex geometries as well as multiple solid bodies moving in complex motions in the fluid domain. The main challenge encountered by the fixed method is to maintain the accurate solutions near the FSI interface region [7, 141]. In order to accurately resolve the fluid flow near the FSI interface, the solid mesh is suggested to be refined as much as possible near the FSI interface region. This operation on the one hand helps to improve the accuracy of the fluid flow, on the other hand introduces more degree of freedoms leading to more computation time thereby decreasing the computational efficiency. Additionally, as pointed out by Su *et al*. in [141], the existing IB techniques are also restricted for FSI problems with small CFL number due to the formulation of feedback force and the determinations of the forcing locations. How to accurately track the solutions near the FSI interface is still a main task for the IB methods.

In different with the fixed mesh method, accurate solutions can be achieved near the FSI interface region by the ALE method due to its avoidance of the interpolations of velocities and traction on the FSI interface. The main drawback of the ALE method is the time consuming mesh updating process in the fluid domain. Furthermore, if the solid undergoes large deformations, the fluid mesh near the FSI interface may be extremely distorted, which will lead to poor or even divergent results for the FSI system. In that case, the adaptive re-meshing process is suggested in this extremely distorted region. This, however, introduces extra interpolation errors during transferring the flow solutions from the old mesh onto the newly generated mesh. Thus the adaptive re-meshing procedure need only be invoked when the other algorithms of the ALE formulation do not succeed in updating the fluid mesh [7]. Beyond that, the so called geometric conservation law (GCL) is also suggested to be obeyed [143], which gives further constrains in the ALE formulation.

In the light of the above discussions, it can be argued that for problems with moderately complex interface and medium deformations/movements in the solid domain, the ALE method may be a much cheaper and more accurate choice because: i) the body-fitted mesh conformed to the FSI interface can be generated, which eliminates the force/velocity interpolations across the FSI interface as in the IB methods and thus leads to accurate solutions of the tractions and velocities near the FSI interface [7]; ii) the adaptive re-meshing process is not needed, which avoids the time-consuming mesh regenerations and inaccurate mapping of the flow solutions from the existing mesh onto the newly generated mesh. Thus the ALE formulation is employed in this thesis by combining with GSM for solving fluid flow problems over moving mesh.

1.4 Objectives and significances of the thesis

One objective of this thesis is to explore two typical smoothed methods, i.e. the ES-FEM-T3 and GSM, in solving the pure solid and fluid flow problems and then couple these two valid methods for solving challenging FSI problems. Thus the broad outlines of the thesis can be summarized as the following three parts:

1) Formulate the implicit/explicit ES-FEM-T3 schemes and explore their performances in solving practical engineering problems in solid mechanics;
2) Develop the novel GSM/ALE method to solve the fluid flows over moving mesh;
3) Propose the novel FSI scheme and couple the GSM/ALE with ES-FEM-T3 for solving FSI problems.

The significances of the present study are as follows:

- Formulate the implicit ES-FEM-T3 for the bending stress analysis of the gear tooth during the gear transmission. The transferred concentration load is converted to a distributed load near the loading point in the formulation process of the implicit ES-FEM-T3 model to avoid the stress singularity at that point. Novel asymmetric gear tooth profiles are designed and the implicit ES-FEM-T3 is used to optimize the gear tooth profiles in consideration of both the stress distributions and the transmission ability of the gear pair. Finally the optimized asymmetric gear tooth profile with pressure angle $\alpha_d / \alpha_c = 35^\circ / 20^\circ$ is determined.
- Demonstrate the necessity of introducing the nonlinear strain term in analytically estimating the membrane deflections, and thus construct the novel explicit ES-FEM-T3 model including the crucial nonlinear strain term for membrane deflection analysis. The local co-rotational coordinate system is constructed for correctly estimating the smoothed strains. Explicit time integration scheme is used to compute the transient response of the 3D spatial membrane structure. And the dynamic relaxation method is employed to obtain steady-state solutions. Factors such as pressure fluctuations and boundary constraints are found to illustrate the observed differences between the numerical and experimental results.

- Propose the novel GSM/ALE method for solving the fluid flows over moving mesh. The ALE form of Navier-Stokes equations is derived according to the Reynolds transport theorem. The GSM is used to spatially discretize the governing equations. A moving mesh source term derived directly from the GCL is incorporated into the discrete equations to ensure the recovery of uniform flow while the mesh is moving. The second order Roe flux differencing splitting unwinding scheme is used in the convective flux to ensure spatial stability. The artificial compressibility formulation is utilized with a dual time stepping approach for the accurate time integration. The coefficient of irregularity of the fluid mesh is introduced to demonstrate the robustness of the proposed GSM/ALE on extremely distorted mesh.
- Couple GSM/ALE with ES-FEM-T3 for solving FSI problems, and it is also the first time to extend the family of smoothed methods into the cross-disciplinary problems. The coupling conditions of displacement/velocity compatibility and traction equilibrium are carefully formulated and the weak coupling algorithm is successfully established to link the GSM/ALE and ES-FEM-T3 in the fluid and solid subsystems, respectively. The constant physical time step is used in the simulation process. The same mesh densities of the fluid and solid mesh are set at the FSI interface to make it easy to implement the FSI boundary conditions. The sensitivity of either the fluid or solid mesh to the FSI results is discussed. Results from several benchmark tests show the validity of the novel coupled smoothed methods in solving FSI problems.

The crucial properties of the newly proposed methods, e.g. the accuracy, convergence, reliability of efficiency and robustness, are quantitatively checked through numerous of benchmark examples for the pure solid or fluid or FSI problems, so as to demonstrate the superior performances of the proposed methods.

1.5 Organization of the thesis

The organization of the present thesis is organized as follows.

Chapter 1 includes background information and research objectives of this study. A general review of the conventional as well as novel smoothed numerical methods is presented. Comments on the conventional methods indicate the necessity of introducing the smoothing technique. Two broad categories of methods, i.e. the fixed and moving mesh methods, are reviewed for FSI analysis. After careful considerations the ALE method is finally chosen as the candidate for FSI analysis in this work.

Chapter 2 gives the fundamental of the smoothing technique and its implementation in the PDEs governing both the solid and fluid mechanics. General procedures of the S-FEMs and GSM are summarized. Distinguished features of these smoothed methods are presented.

Chapter 3 constructs both implicit and explicit ES-FEM-T3 for solving two practical engineering problems, i.e. the implicit ES-FEM-T3 for a 2D linear elastic bending stress problem found in gear tooth during gear transmissions and the explicit ES-FEM-T3 for the nonlinear deflections of the membrane structure in 3D space. Properties of the proposed methods are carefully checked during solving these two practical problems.

Chapter 4 proposes a novel GSM/ALE method for solving fluid-moving rigid body interaction problems. Convergence, accuracy and robustness of the proposed method, i.e. GSM/ALE, are examined through a series of benchmark tests.

Chapter 5 couples the GSM/ALE and ES-FEM-T3 for the FSI analysis. The FSI coupling conditions as well the coupling procedures are presented in details. Both transient and steady state benchmarks are tested to verify the validity of the coupled smoothed method.

Chapter 6 concludes the contributions of this thesis and suggests some further potential research topics.

One appendix about the governing equations of the novel asymmetric gear tooth profile is attached in the end of this thesis.

References for Chapter 1

1. Farhat, C., van der Zee, K.G. and Geuzaine, P., *Provably second-order time-accurate loosely-coupled solution algorithms for transient nonlinear computational aeroelasticity.* Computer Methods in Applied Mechanics and Engineering, 2006. **195**(17): p. 1973-2001.
2. Cavagna, L., Quaranta, G. and Mantegazza, P., *Application of Navier–Stokes simulations for aeroelastic stability assessment in transonic regime.* Computers & Structures, 2007. **85**(11): p. 818-832.
3. Causin, P., Gerbeau, J.F. and Nobile, F., *Added-mass effect in the design of partitioned algorithms for fluid–structure problems.* Computer Methods in Applied Mechanics and Engineering, 2005. **194**(42): p. 4506-4527.
4. Vierendeels, J., Lanoye, L., Degroote, J. and Verdonck, P., *Implicit coupling of partitioned fluid–structure interaction problems with reduced order models.* Computers & Structures, 2007. **85**(11): p. 970-976.
5. Van Loon, R., Anderson, P.D. and Van De Vosse, F.N., *A fluid-structure interaction method with solid-rigid contact for heart valve dynamics.* Journal of Computational Physics, 2006. **217**(2): p. 806-823.
6. Dumont, K., Vierendeels, J., Kaminsky, R., Van Nooten, G., Verdonck, P. and Bluestein, D., *Comparison of the hemodynamic and thrombogenic performance of two bileaflet mechanical heart valves using a CFD/FSI model.* Journal of Biomechanical Engineering, 2007. **129**: p. 558.
7. Bathe, K.J. and Ledezma, G.A., *Benchmark problems for incompressible fluid flows with structural interactions.* Computers & Structures, 2007. **85**(11-14): p. 628-644.
8. Bathe, K.J. and Zhang, H., *Finite element developments for general fluid flows with structural interactions.* International Journal for Numerical Methods in Engineering, 2004. **60**(1): p. 213-232.
9. Tai, C.H., Liew, K.M. and Zhao, Y., *Numerical simulation of 3D fluid–structure interaction flow using an immersed object method with overlapping grids.* Computers & Structures, 2007. **85**(11): p. 749-762.
10. Heil, M., *An efficient solver for the fully coupled solution of large-displacement fluid–structure interaction problems.* Computer Methods in Applied Mechanics and Engineering, 2004. **193**(1): p. 1-23.
11. Walhorn, E. *Ein simultanes berechnungsverfahren für fluid-struktur-wechselwirkungen mit finiten raum-zeit-elementen*. 2002, Ph.D. thesis, Universitätsbibliothek Greifswald: Mecklenburg-Vorpommern, Deutschland.
12. Hübner, B. *Simultane analyse von bauwerk-wind-wechselwirkungen*. 2003, Ph.D. thesis, Universitätsbibliothek Greifswald: Mecklenburg-Vorpommern, Deutschland.
13. Rugonyi, S. and Bathe, K.J., *On finite element analysis of fluid flows fully coupled with structural interactions.* Computer Modeling in Engineering and Sciences, 2001. **2**(2): p. 195-212.
14. Liu, G.R., *Meshfree methods: moving beyond the finite element method, 2nd Edition*. 2009: CRC.
15. Liu, G.R. and Nguyen, T.T., *Smoothed finite element methods*. 2010: CRC Pr I Llc.

16. Liu, G.R., *A G space theory and a weakened weak (W2) form for a unified formulation of compatible and incompatible methods: Part I theory.* International Journal for Numerical Methods in Engineering, 2010. **81**(9): p. 1093-1126.
17. Liu, G.R., *A G space theory and a weakened weak (W2) form for a unified formulation of compatible and incompatible methods: Part II applications to solid mechanics problems*. International Journal for Numerical Methods in Engineering, 2010. **81**(9): p. 1127-1156.
18. Ferziger, J.H. and Peri , M., *Computational methods for fluid dynamics*. Vol. 2. 1999: Springer Berlin.
19. Richardson, L.F., *The approximate arithmetical solution by finite differences of physical problems involving differential equations, with an application to the stresses in a masonry dam.* Philosophical Transactions of the Royal Society of London. Series A, Containing Papers of a Mathematical or Physical Character, 1911. **210**: p. 307-357.
20. Tannehill, J.C., Anderson, D.A. and Pletcher, R.H., *Computational fluid mechanics and heat transfer*. 1997: Taylor & Francis Group.
21. Evans, M.W. and Harlow, F.H., *The particle-in-cell method for hydrodynamic calculations*. 1957, Los Alamos Scientific Lab., N. Mex.
22. Gentry, R.A., Martin, R.E. and Daly, B.J., *An Eulerian differencing method for unsteady compressible flow problems.* Journal of Computational Physics, 1966. **1**(1): p. 87-118.
23. Jameson, A., Schmidt, W. and Turkel, E., *Numerical solutions of the Euler equations by finite volume methods using Runge-Kutta time-stepping schemes.* AIAA Paper, 1981. **81**(-125): p. 9.
24. Jameson, A. and Yoon, S., *Multigrid solution of the Euler equations using implicit schemes.* AIAA Paper, 1986. **24**(11): p. 1737-1743.
25. Barth, T.J., *Aspects of unstructured grids and finite-volume solvers for the Euler and Navier-Stokes equations*, in *Special Course on Unstructured Grid Methods for Advection Dominated Flows*. 1992.
26. Barth, T.J., *Numerical methods for conservation laws on structured and unstructured meshes.* VKI March, 2003.
27. Barth, T.J. and Jespersen, D.C. *The design and application of upwind schemes on unstructured meshes*. *27th Aerospace Sciences Meeting*. 1989. Reno, Nevada, UNITED STATES.
28. Versteeg, H.K. and Malalasekera, W., *An introduction to computational fluid dynamics: the finite volume method*. 2007: Prentice Hall.
29. Blazek, J., *Computational fluid dynamics: principles and applications*. 2005: Elsevier Science.
30. George, X.X. *Development of Gradient Smoothing method (GSM) for Fluid Flow Problems*. Department of Mechanical Engineering, 2009, Ph.D. thesis, National University of Singapore: Singapore.
31. Zienkiewicz, O., Taylor, R. and Zhu, J., *The finite element method: its basis and fundamentals*. Vol. 1. 2005: Butterworth-Heinemann, Amsterdam, London.
32. Zienkiewicz, O.C. and Taylor, R.L., *The finite element method for solid and structural mechanics*. Vol. 2. 2005: Butterworth-Heinemann, Amsterdam, London.
33. Zienkiewicz, O., Taylor, R.L. and Nithiarasu, P., *The finite element method: fluid dynamics*. Vol. 3. 2005: Butterworth-Heinemann, Amsterdam, London.

34. Courant, R., *Variational methods for the solution of problems of equilibrium and vibrations.* Bulletin of the American Mathematical Society, 1943. **49**: p. 1-23.
35. Clough, R.W. *The finite element method in plane stress analysis. In Proceedings of 2nd ASCE Conference on Electronic Computation, Pittsburgh* 1960.
36. Idelsohn, S.R. and Onate, E., *To mesh or not to mesh. That is the question.* Computer Methods in Applied Mechanics and Engineering, 2006. **195**(37-40): p. 4681-4696.
37. Lucy, L.B., *A numerical approach to the testing of the fission hypothesis.* The Astronomical Journal, 1977. **82**: p. 1013-1024.
38. Gingold, R.A. and Monaghan, J.J., *Smoothed particle hydrodynamics-theory and application to non-spherical stars.* Monthly Notices of the Royal Astronomical Society, 1977. **181**: p. 375-389.
39. Liu, G.R. and Liu, M., *Smoothed Particle Hydrodynamics: A Meshfree Particle Method.* 2003: World Scientific Pub Co Inc.
40. Liu, M.B., Liu, G.R. and Zong, Z., *An overview on smoothed particle hydrodynamics.* International Journal of Computational Methods, 2008. **5**(1): p. 135-188.
41. Liu, G.R., Kee, B.B.T. and Chun, L., *A stabilized least-squares radial point collocation method (LS-RPCM) for adaptive analysis.* Computer Methods in Applied Mechanics and Engineering, 2006. **195**(37-40): p. 4843-4861.
42. Onate, E., Perazzo, F. and Miquel, J., *A finite point method for elasticity problems.* Computers & Structures, 2001. **79**(22): p. 2151-2163.
43. Belytschko, T., Lu, Y.Y. and Gu, L., *Element-free Galerkin methods.* International Journal for Numerical Methods in Engineering, 1994. **37**(2): p. 229-256.
44. Belytschko, T., Krongauz, Y., Organ, D., Fleming, M. and Krysl, P., *Meshless methods: an overview and recent developments.* Computer Methods in Applied Mechanics and Engineering, 1996. **139**(1-4): p. 3-47.
45. Atluri, S. and Zhu, T., *A new meshless local Petrov-Galerkin (MLPG) approach in computational mechanics.* Computational mechanics, 1998. **22**(2): p. 117-127.
46. Liu, W.K., Adee, J. and Jun, S., *Reproducing kernel and wavelet particle methods for elastic and plastic problems.* Advanced Computational Methods for Material Modeling, 1993: p. 175-190.
47. Liu, G.R., Zhang, G.Y., Dai, K.Y., Wang, Y.Y., Zhong, Z.H., Li, G.Y. and Han, X., *A linearly conforming point interpolation method (LC-PIM) for 2D solid mechanics problems.* International Journal of Computational Methods, 2005. **2**(4): p. 645-666.
48. Liu, G.R. and Zhang, G.Y., *Upper bound solution to elasticity problems: A unique property of the linearly conforming point interpolation method (LC-PIM).* International Journal for Numerical Methods in Engineering, 2008. **74**(7): p. 1128-1161.
49. Li, Y., Liu, G.R., Dai, K.Y., Luan, M.T., Zhong, Z.H., Li, G.Y. and Han, X., *Contact analysis for solids based on linearly conforming radial point interpolation method.* Computational Mechanics, 2007. **39**(4): p. 537-554.
50. Zhang, G.Y., Liu, G.R., Nguyen, T.T., Song, C.X., Han, X., Zhong, Z.H. and Li, G.Y., *The upper bound property for solid mechanics of the linearly conforming radial point interpolation method (LC-RPIM).* International Journal of Computational Methods, 2007. **4**(3): p. 521.

51. Liu, G.R., *A generalized gradient smoothing technique and the smoothed bilinear form for Galerkin formulation of a wide class of computational methods.* International Journal of Computational Methods, 2008. **5**(2): p. 199-236.
52. Liu, G.R. and Zhang, G.Y., *Edge-based smoothed point interpolation methods.* International Journal of Computational Methods, 2008. **5**(4): p. 621-646.
53. Liu, G.R., Xu, X., Zhang, G.Y. and Gu, Y.T., *An extended Galerkin weak form and a point interpolation method with continuous strain field and superconvergence using triangular mesh.* Computational Mechanics, 2009. **43**(5): p. 651-673.
54. Liu, G.R., Xu, X., Zhang, G.Y. and Nguyen Thoi, T., *A superconvergent point interpolation method (SC - PIM) with piecewise linear strain field using triangular mesh.* International Journal for Numerical Methods in Engineering, 2009. **77**(10): p. 1439-1467.
55. Xu, X., Liu, G.R. and Zhang, G.Y., *A point interpolation method with least square strain field (PIM-LSS) for solution bounds and ultra-accurate solutions using triangular mesh.* Computer Methods in Applied Mechanics and Engineering, 2009. **198**(17-20): p. 1486-1499.
56. Liu, G.R. and Zhang, G.Y., *A novel scheme of strain-constructed point interpolation method for static and dynamic mechanics problems.* International Journal of Applied Mechanics, 2009. **1**(1): p. 233-258.
57. Liu, G.R. and Gu, Y.T., *A point interpolation method for two-dimensional solids.* International Journal for Numerical Methods in Engineering, 2001. **50**(4): p. 937-951.
58. Liu, G.R. and Gu, Y.T., *A matrix triangularization algorithm for the polynomial point interpolation method.* Computer Methods in Applied Mechanics and Engineering, 2003. **192**(19): p. 2269-2295.
59. Liu, G.R., *A point assembly method for stress analysis for two-dimensional solids.* International Journal of Solids and Structures, 2002. **39**(1): p. 261-276.
60. Babuška, I., Banerjee, U. and Osborn, J.E., *Survey of meshless and generalized finite element methods: a unified approach.* Acta Numerica, 2003. **12**(1): p. 1-125.
61. Liu, G.R. and Gu, Y.T., *An introduction to meshfree methods and their programming*. 2005: Springer Verlag.
62. Onate, E., Idelsohn, S., Zienkiewicz, O.C. and Taylor, R.L., *A finite point method in computational mechanics. Applications to convective transport and fluid flow.* International Journal for Numerical Methods in Engineering, 1996. **39**(22): p. 3839-3866.
63. Liu, G.R. and George, X.X., *A gradient smoothing method (GSM) for fluid dynamics problems.* International Journal for Numerical Methods in Fluids, 2008. **58**(10): p. 1101-1133.
64. Xu., G.X., Liu, G.R. and Tani, A., *An adaptive gradient smoothing method (GSM) for fluid dynamics problems.* International Journal for Numerical Methods in Fluids, 2010. **62**(5): p. 499-529.
65. Chen, J.S., Wu, C.T., Yoon, S. and You, Y., *A stabilized conforming nodal integration for Galerkin mesh-free methods.* International Journal for Numerical Methods in Engineering, 2001. **50**(2): p. 435–466.
66. Liu, G.R., *Mesh free methods: moving beyond the finite element method, 1st Edition*. 2003: CRC.

67. Hoffmann, K.A., *Computational fluid dynamics for engineers*. 1989, Austin, TX, United States.: Engineering Education System
68. Fletcher, C.A.J., *Computational techniques for fluid dynamics: Fundamental and general techniques*. 2000: Springer.
69. Kee, B.B.T., Liu, G. and Lu, C., *A regularized least-squares radial point collocation method (RLS-RPCM) for adaptive analysis.* Computational Mechanics, 2007. **40**(5): p. 837-853.
70. Liu, G.R., *On a G space theory.* International Journal of Computational Methods, 2009. **6**(2): p. 257-289.
71. Dai, K. and Liu, G., *Free and forced vibration analysis using the smoothed finite element method (SFEM).* Journal of Sound and Vibration, 2007. **301**(3): p. 803-820.
72. Dai, K., Liu, G. and Nguyen, T., *An n-sided polygonal smoothed finite element method (nSFEM) for solid mechanics.* Finite Elements in Analysis and Design, 2007. **43**(11-12): p. 847-860.
73. Liu, G.R., Nguyen, T.T., Dai, K.Y. and Lam, K.Y., *Theoretical aspects of the smoothed finite element method (SFEM).* International Journal for Numerical Methods in Engineering, 2007. **71**(8): p. 902-930.
74. Liu, G.R., Dai, K.Y. and Nguyen, T.T., *A smoothed finite element method for mechanics problems.* Computational Mechanics, 2007. **39**(6): p. 859-877.
75. Zhang, G.Y., Liu, G.R., Wang, Y.Y., Huang, H.T., Zhong, Z.H., Li, G.Y. and Han, X., *A linearly conforming point interpolation method (LC PIM) for three dimensional elasticity problems.* International Journal for Numerical Methods in Engineering, 2007. **72**(13): p. 1524-1543.
76. Liu, G.R., Zhang, G.Y., Wang, Y.Y., Zhong, Z.H., Li, G.Y. and Han, X., *A nodal integration technique for meshfree radial point interpolation method (NI-RPIM).* International Journal of Solids and Structures, 2007. **44**(11-12): p. 3840-3860.
77. Liu, G.R. and Zhang, G.Y., *A normed G space and weakened weak (W2) formulation of a cell-based smoothed point interpolation method.* International Journal of Computational Methods, 2009. **6**(1): p. 147-179.
78. Liu, G.R., Nguyen-Thoi, T., Nguyen-Xuan, H. and Lam, K.Y., *A node-based smoothed finite element method (NS-FEM) for upper bound solutions to solid mechanics problems.* Computers & Structures, 2009. **87**(1-2): p. 14-26.
79. Nagashima, T., *Node-by-node meshless approach and its applications to structural analyses.* International Journal for Numerical Methods in Engineering, 1999. **46**(3): p. 341-385.
80. Puso, M.A., Chen, J.S., Zywicz, E. and Elmer, W., *Meshfree and finite element nodal integration methods.* International Journal for Numerical Methods in Engineering, 2008. **74**(3): p. 416-446.
81. Puso, M.A. and Solberg, J., *A stabilized nodally integrated tetrahedral.* International Journal for Numerical Methods in Engineering, 2006. **67**(6): p. 841-867.
82. Liu, G.R., Nguyen-Thoi, T. and Lam, K.Y., *An edge-based smoothed finite element method (ES-FEM) for static, free and forced vibration analyses of solids.* Journal of Sound and Vibration, 2009. **320**(4-5): p. 1100-1130.
83. Chen, L. *Development of smoothed numerical methods for fracture analyses and interfacial toughness characterization in thin film systems*. Department of

Mechanical Engineering, 2011, Ph.D. thesis, National University of Singapore: Singapore.

84. Chen, L., Nguyen-Xuan, H., Nguyen-Thoi, T., Zeng, K. and Wu, S., *Assessment of smoothed point interpolation methods for elastic mechanics.* International Journal for Numerical Methods in Biomedical Engineering, 2010. **26**(12): p. 1635-1655.
85. Westergaard, H.M., *Water pressures on dams during earthquakes.* Transactions of the American Society of Civil Engineers, 1933. **98**(2): p. 418-433.
86. Chopra, A.K., *Earthquake response of concrete gravity dams.* Journal of the Engineering Mechanics Division, 1970. **96**(4): p. 443-454.
87. Housner, G.W., *Dynamic pressures on accelerated fluid containers.* Bulletin of the Seismological Society of America, 1957. **47**(1): p. 15-35.
88. Moiseev, N.N., *Introduction to the theory of oscillations of liquid-containing bodies.* Advances in Applied Mechanics, 1964. **8**: p. 233-289.
89. Moiseev, N.N. and Petrov, A.A., *The Calculation of Free Oscillations of a Liquid in a Motionless.* Advances in Applied Mechanics, 1966. **9**: p. 91-154.
90. St Dinis, M. and Pierson Jr, W.J., *On the motions of ships in confused seas*. 1953, DTIC Document.
91. Korvin-Kroukovsky, B., *Investigation of ship motions in regular waves*. 1955: SNAME.
92. Housner, G., *Bending vibrations of a pipe line containing flowing fluid.* Journal of Applied Mechanics, 1952. **19**(2): p. 205-208.
93. Paidoussis, M.P., *Flow-induced instabilities of cylindrical structures.* Applied Mechanics Reviews, 1987. **40**: p. 163.
94. Glück, M., Breuer, M., Durst, F., Halfmann, A. and Rank, E., *Computation of fluid–structure interaction on lightweight structures.* Journal of Wind Engineering and Industrial Aerodynamics, 2001. **89**(14): p. 1351-1368.
95. Frandsen, J. *Computational fluid-structure interaction applied to long-span bridge design*. 1999, Ph.D. thesis, University of Cambridge: Cambridge, United Kingdom.
96. Sarpkaya, T., Isaacson, M. and Isaacson, M.S.Q., *Mechanics of wave forces on offshore structures*. 1981: Van Nostrand Reinhold New York.
97. Bathe, K., Zhang, H. and Wang, M., *Finite element analysis of incompressible and compressible fluid flows with free surfaces and structural interactions.* Computers & Structures, 1995. **56**(2): p. 193-213.
98. Bathe, K.J., Zhang, H. and Ji, S., *Finite element analysis of fluid flows fully coupled with structural interactions.* Computers & Structures, 1999. **72**(1): p. 1-16.
99. Anwer, S.F., Hasan, N., Sanghi, S. and Mukherjee, S., *Computation of unsteady flows with moving boundaries using body fitted curvilinear moving grids.* Computers & Structures, 2009. **87**(11-12): p. 691-700.
100. Takashi, N. and Hughes, T.J.R., *An arbitrary Lagrangian-Eulerian finite element method for interaction of fluid and a rigid body.* Computer Methods in Applied Mechanics and Engineering, 1992. **95**(1): p. 115-138.
101. Farhat, C., Degand, C., Koobus, B. and Lesoinne, M., *Torsional springs for two-dimensional dynamic unstructured fluid meshes.* Computer Methods in Applied Mechanics and Engineering, 1998. **163**(1): p. 231-245.

102. Van Loon, R., Anderson, P.D., Van de Vosse, F.N. and Sherwin, S.J., *Comparison of various fluid-structure interaction methods for deformable bodies.* Computers & Structures, 2007. **85**(11): p. 833-843.
103. Blom, F.J., *Considerations on the spring analogy.* International Journal for Numerical Methods in Fluids, 2000. **32**(6): p. 647-668.
104. Bottasso, C.L., Detomi, D. and Serra, R., *The ball-vertex method: a new simple spring analogy method for unstructured dynamic meshes.* Computer Methods in Applied Mechanics and Engineering, 2005. **194**(39): p. 4244-4264.
105. Degand, C. and Farhat, C., *A three-dimensional torsional spring analogy method for unstructured dynamic meshes.* Computers & Structures, 2002. **80**(3): p. 305-316.
106. Stein, E., de Borst, R. and Hughes, T.J.R., *Encyclopedia of computational mechanics*. 2004: Wiley.
107. Noh, W.F., *A time-dependent, two-space-dimensional, coupled Eulerian-Lagrange code*. 1963, Lawrence Radiation Lab., Univ. of California, Livermore.
108. Trulio, J.G., *Air force weapons laboratoy, Kirtland air force base report number AFWL-TR-66-19*. 1966.
109. Hirt, C., Amsden, A.A. and Cook, J., *An arbitrary Lagrangian-Eulerian computing method for all flow speeds.* Journal of Computational Physics, 1974. **14**(3): p. 227-253.
110. Pracht, W.E., *Calculating three-dimensional fluid flows at all speeds with an Eulerian-Lagrangian computing mesh.* Journal of Computational Physics, 1975. **17**(2): p. 132-159.
111. Ahn, H.T. and Kallinderis, Y., *Strongly coupled flow/structure interactions with a geometrically conservative ALE scheme on general hybrid meshes.* Journal of Computational Physics, 2006. **219**(2): p. 671-696.
112. Kallinderis, Y. and Ahn, H.T., *Incompressible Navier-Stokes method with general hybrid meshes.* Journal of Computational Physics, 2005. **210**(1): p. 75-108.
113. Zhang, Z., Gil, A.J., Hassan, O. and Morgan, K., *The simulation of 3D unsteady incompressible flows with moving boundaries on unstructured meshes.* Computers & Fluids, 2008. **37**(5): p. 620-631.
114. Donea, J., Fasoli-Stella, P. and Giuliani, S., *Lagrangian and Eulerian finite element techniques for transient fluid-structure interaction problems.* Trans. SMiRT-4, San Francisco, August, 1977.
115. Belytschko, T. and Kennedy, J.M., *Computer models for subassembly simulation.* Nuclear Engineering and Design, 1978. **49**(1-2): p. 17-38.
116. Bathe, K. and Hahn, W., *On transient analysis of fluid-structure systems.* Computers & Structures, 1979. **10**(1-2): p. 383-391.
117. Hughes, T.J.R., Liu, W.K. and Zimmermann, T.K., *Lagrangian-Eulerian finite element formulation for incompressible viscous flows.* Computer Methods in Applied Mechanics and Engineering, 1981. **29**(3): p. 329-349.
118. Donea, J., Giuliani, S. and Halleux, J., *An arbitrary Lagrangian-Eulerian finite element method for transient dynamic fluid-structure interactions.* Computer Methods in Applied Mechanics and Engineering, 1982. **33**(1): p. 689-723.
119. Belytschko, T., Flanagan, D. and Kennedy, J., *Finite element methods with user-controlled meshes for fluid-structure interaction.* Computer Methods in Applied Mechanics and Engineering, 1982. **33**(1): p. 669-688.

120. Nomura, T., *ALE finite element computations of fluid-structure interaction problems*. Computer Methods in Applied Mechanics and Engineering, 1994. **112**(1-4): p. 291-308.
121. Glowinski, R. and Pironneau, O., *Finite element methods for Navier-Stokes equations.* Annual Review of Fluid Mechanics, 1992. **24**(1): p. 167-204.
122. Brooks, A.N. and Hughes, T.J.R., *Streamline upwind/Petrov-Galerkin formulations for convection dominated flows with particular emphasis on the incompressible Navier-Stokes equations.* Computer Methods in Applied Mechanics and Engineering, 1982. **32**(1): p. 199-259.
123. Hughes, T.J.R., Franca, L.P. and Hulbert, G.M., *A new finite element formulation for computational fluid dynamics: VIII. The Galerkin/least-squares method for advective-diffusive equations.* Computer Methods in Applied Mechanics and Engineering, 1989. **73**(2): p. 173-189.
124. Shakib, F. *Finite element analysis of the compressible Euler and Navier-Stokes equations*. 1989, Ph.D. thesis, Stanford University: Stanford, California.
125. Johnson, C. and Saranen, J., *Streamline diffusion methods for the incompressible Euler and Navier-Stokes equations.* Mathematics of Computation, 1986. **47**(175): p. 1-18.
126. Souli, M. and Zolesio, J.P., *Arbitrary Lagrangian–Eulerian and free surface methods in fluid mechanics.* Computer Methods in Applied Mechanics and Engineering, 2001. **191**(3): p. 451-466.
127. Shanks, S.P. and Thompson, J.H. *Solution of Navier-Stokes flow over a hydrofoil beneath a water surface in curvilinear co-ordinate system. 2nd international conference on numerical hydrodynamics, Berkeley* 1977.
128. Liu, H. and Kawachi, K., *A numerical study of insect flight.* Journal of Computational Physics, 1998. **146**(1): p. 124-156.
129. Liu, H., Ellington, C. and Kawachi, K., *A computational fluid dynamic study of hawkmoth hovering.* Journal of Experimental Biology, 1998. **201**(4): p. 461-477.
130. Zhang, L., Gerstenberger, A., Wang, X. and Liu, W.K., *Immersed finite element method.* Computer Methods in Applied Mechanics and Engineering, 2004. **193**(21-22): p. 2051-2067.
131. Peskin, C.S., *Numerical analysis of blood flow in the heart.* Journal of Computational Physics, 1977. **25**(3): p. 220-252.
132. Glowinski, R., Pan, T.W. and Periaux, J., *A fictitious domain method for external incompressible viscous flow modeled by Navier-Stokes equations.* Computer Methods in Applied Mechanics and Engineering, 1994. **112**(1-4): p. 133-148.
133. Mohd-Yusof, J., *Combined immersed-boundary/B-spline methods for simulations of flow in complex geometries.* CTR Annual Research Briefs, 1997: p. 317-327.
134. Fadlun, E., Verzicco, R., Orlandi, P. and Mohd-Yusof, J., *Combined immersed-boundary finite-difference methods for three-dimensional complex flow simulations*. Journal of Computational Physics, 2000. **161**(1): p. 35-60.
135. Gilmanov, A. and Sotiropoulos, F., *A hybrid Cartesian/immersed boundary method for simulating flows with 3D, geometrically complex, moving bodies.* Journal of Computational Physics, 2005. **207**(2): p. 457-492.
136. Uhlmann, M., *An immersed boundary method with direct forcing for the simulation of particulate flows.* Journal of Computational Physics, 2005. **209**(2): p. 448-476.

137. Wang, X. and Liu, W.K., *Extended immersed boundary method using FEM and RKPM.* Computer Methods in Applied Mechanics and Engineering, 2004. **193**(12): p. 1305-1321.
138. Zhang, L.T. and Gay, M., *Immersed finite element method for fluid-structure interactions.* Journal of Fluids and Structures, 2007. **23**(6): p. 839-857.
139. Liu, W.K., Liu, Y., Farrell, D., Zhang, L., Wang, X.S., Fukui, Y., Patankar, N., Zhang, Y., Bajaj, C. and Lee, J., *Immersed finite element method and its applications to biological systems.* Computer Methods in Applied Mechanics and Engineering, 2006. **195**(13): p. 1722-1749.
140. Liao, C.C., Chang, Y.W., Lin, C.A. and McDonough, J.M., *Simulating flows with moving rigid boundary using immersed-boundary method.* Computers & Fluids, 2010. **39**(1): p. 152-167.
141. Su, S.W., Lai, M.C. and Lin, C.A., *An immersed boundary technique for simulating complex flows with rigid boundary.* Computers & Fluids, 2007. **36**(2): p. 313-324.
142. Zhang, Z.Q. and Liu, G.R., *An immersed smoothed finite element method for fluid-structure interaction problems.* International Journal of Computational Methods, 2011. **8**(4): p. 747-757.
143. Thomas, P.D. and Lombard, C.K., *Geometric conservation law and its application to flow computations on moving grids.* AIAA Paper, 1979. **17**(10): p. 1030-1037.

Chapter 2

Theories of the strain/gradient smoothing technique

The strain/gradient smoothing technique has been reviewed in the previous chapter. By applying the strain/gradient smoothing operation into the FEM and FVM settings, a family of smoothed methods, i.e. the S-FEMs for solid mechanics and the GSM for fluid mechanics, was proposed. Particularly, the ES-FEM-T3 performs the best in accordance with the criterion of computational efficiency (the CPU time needed for solution of the same accuracy) among all the S-FEM models. It is thus chosen and further explored in solving the solid mechanics in Chapter 3 as well as the solid portion in the FSI analysis in Chapter 5 in the present thesis.

In this chapter, fundamental theories of the smoothing technique implemented in both the solid and fluid mechanics are introduced. Theoretical details about the smoothing technique are firstly presented in Section 2.1. The implementation of the strain smoothing technique into the solid mechanics that leads to the family of S-FEMs is presented in Section 2.2, together with the discussion of some main properties of the S-FEM models. The gradient smoothing technique applied for solving the incompressible fluid flows is presented in Section 2.3, together with some theoretical aspects during the implementation of GSM. The discussions and formulations are given in 2D space. The extension to 3D domain can be more complicated in implementation, but it should be trivial technically.

2.1 Smoothing technique

Smoothing technique has already been used in numerical simulations for various purposes [1-4]. A common ground of the smoothing technique is that the field variable (or its any order derivations) at an arbitrary point can be replaced by a weighted integral fashion of this field variable (or its any order derivations) over a local smoothing domain containing this point [5, 6]. Accordingly, the surface integration of the derivatives of the field variables over the smoothing domain is transformed to the line integration of the field variables themselves along the boundary of this smoothing domain according to the Gauss Divergence's theorem, by which the consistency requirement on the field variables is reduced by 1 order [6, 7].

Consider an arbitrary field variable $u(\mathbf{x})$ at point $\mathbf{x}_i$ surrounded by a smoothing domain Ω_i^{sd} bounded by Γ_i^{sd}. The gradient (1st order derivative) of $u(\mathbf{x})$ can be approximated in the form of [8, 9]

$$\nabla u_i \equiv \nabla u(\mathbf{x}_i) \approx \int_{\Omega_i^{\mathrm{sd}}} \nabla u(\mathbf{x})\,\hat{w}(\mathbf{x};\mathbf{x}-\mathbf{x}_i)\,\mathrm{d}\Omega$$

$$\text{or} \qquad (2.1)$$

$$\frac{\partial u}{\partial x_h}(\mathbf{x}_i) = \int_{\Omega_i^{\mathrm{sd}}} \frac{\partial u}{\partial x_h}(\mathbf{x})\,\hat{w}(\mathbf{x};\mathbf{x}-\mathbf{x}_i)\,\mathrm{d}\Omega,\ h = x, y$$

where ∇ is the gradient operator; $\hat{w}(\mathbf{x};\mathbf{x}-\mathbf{x}_i)$ is the weighted function that can be chosen in any form as long as it satisfies the essential requirements of [3, 9]

$$\hat{w}(\mathbf{x};\mathbf{x}-\mathbf{x}_i) \geq 0 \text{ and } \int_{\Omega_i^{\mathrm{sd}}} \hat{w}(\mathbf{x};\mathbf{x}-\mathbf{x}_i)\,\mathrm{d}\Omega = 1. \qquad (2.2)$$

The subscript "*i*" and superscript "sd" marked in Ω_i^{sd} denote, respectively, the "*i*th" discrete smoothing domain ("sd") in the whole domain Ω bounded by Γ, as shown in Fig. 2.1. $\mathbf{n} = \left[n_x, n_y\right]^{\mathrm{T}}$ is the unit normal vector of the boundary Γ_i^{sd}.

If we integrate Eq. (2.1) by parts, we can get

$$\nabla u(\mathbf{x}_i) \approx \int_{\Gamma_i^{\mathrm{sd}}} u(\mathbf{x})\mathbf{n}\hat{w}(\mathbf{x};\mathbf{x}-\mathbf{x}_i)\,\mathrm{d}\Gamma - \int_{\Omega_i^{\mathrm{sd}}} u(\mathbf{x})\nabla\hat{w}(\mathbf{x};\mathbf{x}-\mathbf{x}_i)\,\mathrm{d}\Omega. \qquad (2.3)$$

As proposed by Liu in [5, 6], a piecewise constant smoothing function is usually adopted as the weight function for the purpose of simplicity, i.e.

$$\hat{w}\left(\mathbf{x};\mathbf{x}-\mathbf{x}_i\right)=\begin{cases}1/A_i^{\mathrm{sd}}, & \mathbf{x}\in\Omega_i^{\mathrm{sd}}\\ 0, & \mathbf{x}\notin\Omega_i^{\mathrm{sd}}\end{cases} \tag{2.4}$$

where A_i^{sd} is the area of the smoothing domain Ω_i^{sd}.

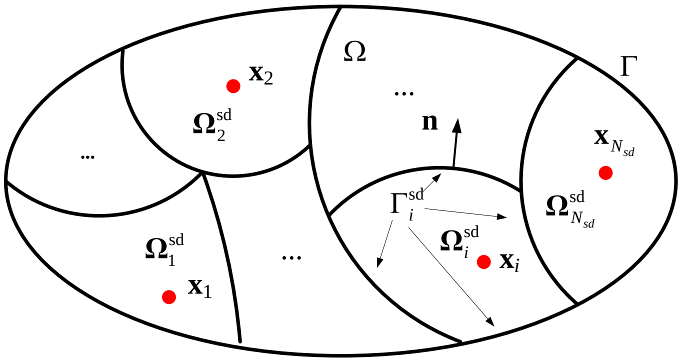

Fig. 2.1 Division of problem domain Ω into N_{sd} non-overlapping smoothing domains Ω_i^{sd}. The smoothing domain is also used as the basis for integration.

Substitute Eq. (2.4) back into Eq. (2.3), the second term of Eq. (2.3) will vanish because A_i^{sd} is now constant and not a function of **x**. That is,

$$\nabla u\left(\mathbf{x}_i\right)\approx\frac{1}{A_i^{\mathrm{sd}}}\int_{\Gamma_i^{\mathrm{sd}}}u\left(\mathbf{x}\right)\mathbf{n}\mathrm{d}\Gamma$$

or (2.5)

$$\frac{\partial u}{\partial x_h}\left(\mathbf{x}_i\right)=\frac{1}{A_i^{\mathrm{sd}}}\int_{\Gamma_i^{\mathrm{sd}}}n_h u\left(\mathbf{x}\right)\mathrm{d}\Gamma,\ h=x,y.$$

Comparing Eq. (2.1) and Eq. (2.5) it can be seen that the integration of the $\nabla u\left(\mathbf{x}_i\right)$ over the smoothing domain Ω_i^{sd} is now transformed to the line integration of the product of $u\left(\mathbf{x}\right)$ and **n** along the boundary Γ_i^{sd}. This transformation can also be regarded as a direct implementation of the Gauss divergence theorem on Eq. (2.1) [6, 10].

It should be noted that when this transformation is implemented into Eq. (2.3), the field variable $u(\mathbf{x})$ should be continuous over the smoothing domain Ω_i^{sd}. Otherwise, it will be mathematically invalid. However, as proved by Liu in [7], Eq. (2.5) can still work well even for discontinuous $u(\mathbf{x})$ as long as it satisfies the admissible orthogonal, norm equivalence, strain convergence and zero-sum conditions during its construction process [6, 7]. This leads to the $\mathbb{G}$ space theory and the so-called weakened weak (W^2) foundation [6, 7].

By using Eq. (2.5) instead of Eq. (2.1), the evaluation of the gradient of $u(\mathbf{x})$ is avoided and only $u(\mathbf{x})$ itself is needed. This change on the one hand reduces the consistency requirement of $u(\mathbf{x})$ by 1 order which expands the range of choosing $u(\mathbf{x})$ especially for discontinuous problems, on the other hand avoids the time consuming evaluations of the derivatives of $u(\mathbf{x})$ and thus improve the computational efficiency.

Analogously, by applying the smoothing operation for approximating the 2nd order derivatives of the field variable $u(\mathbf{x})$, the Laplace operator at point $\mathbf{x}_i$ can be readily obtained as [4]

$$\nabla\cdot\left[\nabla u\left(\mathbf{x}_i\right)\right]\approx\frac{1}{A_i^{\mathrm{sd}}}\int_{\Gamma_i^{\mathrm{sd}}}\mathbf{n}\cdot\nabla u\left(\mathbf{x}\right)\mathrm{d}\Gamma$$

or (2.6)

$$\frac{\partial^2 u}{\partial x_I\partial x_J}\left(\mathbf{x}_i\right)\approx\frac{1}{A_i^{\mathrm{sd}}}\int_{\Gamma_i^{\mathrm{sd}}}\left(\frac{\partial u}{\partial x_I}n_J+\frac{\partial u}{\partial x_J}n_I\right)\mathrm{d}\Gamma,\quad I,J=x,y\,.$$

It could be determined as long as one knows the values of the 1st order derivatives of $u(\mathbf{x})$ at the corresponding nodes.

In order to determine the line integrations of Eqs. (2.5) and (2.6) numerically, the Gauss integration rule is usually employed with a minimal number of sample points along the boundary segments, as follows

$$\nabla u\left(\mathbf{x}_i\right)\approx\frac{1}{A_i^{\mathrm{sd}}}\sum_{m=1}^{N_{seg}}\left[\sum_{n=1}^{N_{gau}}w_{mn}\mathbf{n}\left(\mathbf{x}_{mn}\right)u\left(\mathbf{x}_{mn}\right)\right]$$

or (2.7)

$$\frac{\partial u}{\partial x_h}\left(\mathbf{x}_k\right)\approx\frac{1}{A_i^{\mathrm{sd}}}\sum_{m=1}^{N_{seg}}\left[\sum_{n=1}^{N_{gau}}w_{mn}n_h\left(\mathbf{x}_{mn}\right)u\left(\mathbf{x}_{mn}\right)\right],\ h=x,y$$

$$\nabla\cdot\left[\nabla u\left(\mathbf{x}_i\right)\right]\approx\frac{1}{A_i^{\mathrm{sd}}}\sum_{m=1}^{N_{seg}}\left[\sum_{n=1}^{N_{gau}}w_{mn}\mathbf{n}\left(\mathbf{x}_{mn}\right)\cdot\nabla u\left(\mathbf{x}_{mn}\right)\right]$$

or

$$\frac{\partial^2 u}{\partial x_I\partial x_J}\left(\mathbf{x}_i\right)\approx\frac{1}{A_i^{\mathrm{sd}}}\sum_{m=1}^{N_{seg}}\left[\sum_{n=1}^{N_{gau}}w_{mn}\left(\frac{\partial u}{\partial x_I}\left(\mathbf{x}_{mn}\right)n_J\left(\mathbf{x}_{mn}\right)+\frac{\partial u}{\partial x_J}\left(\mathbf{x}_{mn}\right)n_I\left(\mathbf{x}_{mn}\right)\right)\right],\ I,J=x,y \tag{2.8}$$

where N_{seg} is the number of segments of the boundary Γ_i^{sd}; N_{gau} is the number of Gauss points used in each segment; $\mathbf{x}_{mn}$ is the coordinates of the n^{th} Gaussian point on the m^{th} segment; w_{mn} is the corresponding weight at the Gauss point $\mathbf{x}_{mn}$; and $\mathbf{n}(\mathbf{x}_{mn})$ is the outward unit normal at this Gauss point.

Hence, spatial derivatives at any point of interest can be numerically approximated with the smoothing operation of Eqs. (2.7) and (2.8) over properly defined smoothing domains. These spatial derivatives possessing particular physical meanings in either solid or fluid mechanics will be implemented to indirectly/directly discretize the PDEs for solving solid and fluid flow problems.

2.2 Strain smoothing for solid mechanics

In solid mechanics, the compatible strain is expressed as a function of the 1st order derivatives of displacement. Smoothing operation described in Eq. (2.7) can be directly applied into the compatible strain, getting the smoothed strain. Substituting the smoothed strain into the Galerkin weak form of the PDEs, the smoothed Galerkin weak form of the PDEs is obtained and a set of algebraic equations is induced. Using routinely available linear equation solver, the unique solutions of the displacements can be obtained. This family of methods with smoothed strain is exactly the S-FEMs.

Different S-FEM models are distinguished according to the implementation of strain smoothing operation over different types of smoothing domains. These smoothing domains can be cell-based, node-based or edge-based constructed on top of the background triangular mesh, corresponding to the CS-FEM-T3 [11-15], NS-FEM-T3 [16-19] and ES-FEM-T3 [20], respectively.

Formulations of these S-FEMs are detailed in this section, and the ES-FEM-T3 would be highlighted. Similar with the standard FEM, the S-FEMs can be used to solve any kind of problems, e.g. from the small deformation [20, 21] to large deformation problems [22], from the elastic [20, 21] to visco-elastoplastic problems [23]. An illustration of the formulation details will be given based on the simplest small deformation elastic problem. Strain smoothing operation on other kinds of problems can follow exactly the same way.

2.2.1 Strain smoothing operation

For an elastic model with the small-displacement assumption, the strain $\boldsymbol{\varepsilon}$ is defined as

$$\boldsymbol{\varepsilon} = \mathbf{L}_d \mathbf{u} \tag{2.9}$$

where $\mathbf{u} = \left[u_x, u_y\right]^{\mathrm{T}}$ is the displacement vector, respectively, in x- and y-directions at any point in the domain Ω; and $\mathbf{L}_d$ is a matrix of differential operator in the form of

$$\mathbf{L}_d\left(\frac{\partial}{\partial x}, \frac{\partial}{\partial y}\right) = \begin{bmatrix} \frac{\partial}{\partial x} & 0 \\ 0 & \frac{\partial}{\partial y} \\ \frac{\partial}{\partial y} & \frac{\partial}{\partial x} \end{bmatrix}. \tag{2.10}$$

In the standard FEM, this strain $\boldsymbol{\varepsilon}$ can be approximated numerically over the element with the compatible strain of

$$\tilde{\boldsymbol{\varepsilon}}_i = \sum_{I=1}^{N_{sup}} \mathbf{L}_d \mathbf{N}_I \mathbf{u}_I \tag{2.11}$$

where the subscript “*i*” denotes the i^{th} element in the domain Ω, i=1,2,3,…, N_{ele} where N_{ele} is the total number of element in the domain Ω; N_{sup} is the total number of nodes supporting the i^{th} element; $\mathbf{N}_I$ is the shape function corresponding to node I in this element; and $\mathbf{u}_I$ is the nodal displacement vector at node I.

By applying the smoothing operation of Eq. (2.7) into Eq. (2.11), the smoothed strain $\bar{\boldsymbol{\varepsilon}}_k$ can thus be obtained over a smoothing domain instead of the element as

$$\bar{\boldsymbol{\varepsilon}}_k = \frac{1}{A_k^{\mathrm{sd}}}\int_{\Gamma_k^{\mathrm{sd}}} \mathbf{L}_n \mathbf{N}_I \mathbf{u}_I \,\mathrm{d}\Gamma = \left\{\bar{\boldsymbol{\varepsilon}}_{11}, \bar{\boldsymbol{\varepsilon}}_{22}, 2\bar{\boldsymbol{\varepsilon}}_{12}\right\}^{\mathrm{T}} = \sum_{I\in S_k^{\mathrm{sd}}} \bar{\mathbf{B}}_I \mathbf{u}_I \tag{2.12}$$

where the “bar-hat” here indicates a parameter after being applied the smoothed operation; A_k^{sd} is the area of k^{th} smoothing domain Ω_k^{sd} bounded by Γ_k^{sd}, k=1,2,3,…, N_{sd} where N_{sd} is the total number of smoothing domains; $\mathbf{L}_n$ is the matrix of unit outward normal of the boundary Γ_k^{sd} that can be expressed as

$$\mathbf{L}_n\left(n_x, n_y\right) = \begin{bmatrix} n_x & 0 \\ 0 & n_y \\ n_y & n_x \end{bmatrix}; \tag{2.13}$$

S_k^{sd} is the set of nodes that “supporting” the smoothing domain Ω_k^{sd}. For ES-FEM-T3, the edge-based smoothing domains are constructed, as shown in Fig. 2.2. The set of supporting nodes is $S_k^{\mathrm{sd}} = \{A, B, C, D\}$ for the smoothing domain associating with inner edge e_i and $S_k^{\mathrm{sd}} = \{O, P, Q\}$ for the boundary edge e_b. $\bar{\mathbf{B}}_I$ is the smoothed strain-displacement matrix evaluated as

$$\bar{\mathbf{B}}_I = \frac{1}{A_k^{\mathrm{sd}}}\int_{\Gamma_k^{\mathrm{sd}}} \mathbf{L}_n \mathbf{N}_I \,\mathrm{d}\Gamma = \begin{bmatrix} \bar{b}_{Ix} & 0 \\ 0 & \bar{b}_{Iy} \\ \bar{b}_{Iy} & \bar{b}_{Ix} \end{bmatrix} \tag{2.14}$$

with

$$\begin{aligned}\bar{b}_{Ih} &= \frac{1}{A_k^{\mathrm{sd}}}\int_{\Gamma_k^{\mathrm{sd}}} n_{kh} N_I \,\mathrm{d}\Gamma \\ &= \frac{1}{A_k^{\mathrm{sd}}}\sum_{m=1}^{N_{seg}}\left[\sum_{n=1}^{N_{gau}} w_{mn} n_h\left(\mathbf{x}_{mn}\right) N_I\left(\mathbf{x}_{mn}\right)\right],\ h = x, y\end{aligned} \tag{2.15}$$

For the ES-FEM-T3 model, N_{seg} is the number of segments of the boundary of the edge-based smoothing domain. As shown in Fig. 2.2, $N_{seg} = 4$ (e.g. *AE*, *EC*, *CF*, *FA*) for the inner edge e_i and $N_{seg} = 3$ (*OP*, *PI*, *IO*) for the boundary edge e_b. N_{gau} is the total number of Gauss point used in the mth segment, and N_{gau}=1 is enough for ES-FEM-T3 for the Gauss integration.

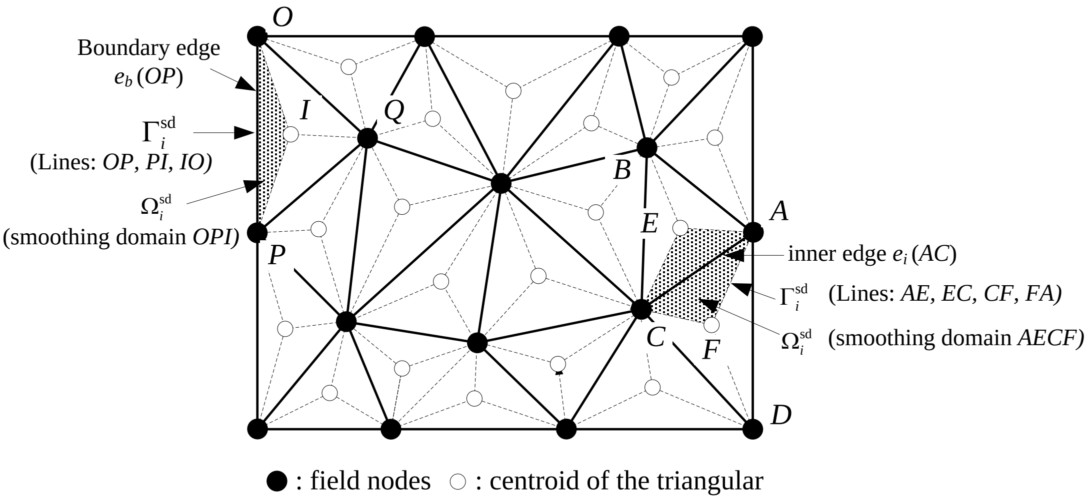

Fig. 2.2 Illustration of smoothing domains (shaded area) in ES-FEM-T3

Remark 2.1: *The procedures of constructing the smoothing domains can be summarized as*

i) the problem domain Ω *is firstly divided into* N_{ele} *non-overlapping and seamless (NOSL) triangular elements such that* $\Omega = \sum_{i=1}^{N_{ele}} \Omega_i^e$ *and* $\Omega_i^e \cap \Omega_j^e = \phi,\ \forall i \neq j$, $A_i^e > 0$, *i=1,2,…,*N_{ele}, $h_i > 0$, *i=1,2,…,*N_{ele} . *Such an NOSL element division results in a set of* N_n *nodes and* N_{eg} *edges* $L_i^e > 0$, *i=1,2,…,*N_{eg} *in the entire problem domain* Ω.

ii) On top of the triangular element mesh, a total of N_{sd} NOSL smoothing domains are constructed such that $\Omega = \sum_{i=1}^{N_{sd}} \Omega_i^{\mathrm{sd}}$ *and* $\Omega_i^{\mathrm{sd}} \bigcap \Omega_j^{\mathrm{sd}} = \phi, \ \forall i \neq j$. *For the edge-based smoothing domains as shown in Fig. 2.2, they are created by connecting the two vortexes of the edge* L_i^e *and the center(s) of the cell(s) that relate(s) to this edge, where* $N_{sd}=N_{eg}$ *and* $A_i^{\mathrm{sd}} > 0$, *i=1,2,…,*N_{sd}.

2.2.2 Formulation of the discretized system of equations

After getting the smoothed strain $\bar{\boldsymbol{\varepsilon}}_k$ of Eq. (2.12), the remaining work is to replace the compatible strain $\tilde{\boldsymbol{\varepsilon}}_i$ with the smoothed strain $\bar{\boldsymbol{\varepsilon}}_k$ in the Galerkin weak form of the PDEs, to get the smoothed Galerkin weak form of the PDEs. Then follow the same procedures as in the standard FEM for solving the system equations.

The smoothed Galerkin weak form of the dynamic equilibrium equations can be derived as

$$\begin{gathered}\int_\Omega \delta\bar{\boldsymbol{\varepsilon}}^{\mathrm{T}}(\mathbf{u})\mathbf{D}\bar{\boldsymbol{\varepsilon}}(\mathbf{u})\mathrm{d}\Omega - \int_\Omega \delta\mathbf{u}^{\mathrm{T}}\left[\mathbf{b} - \rho\ddot{\mathbf{u}} - c\dot{\mathbf{u}}\right]\mathrm{d}\Omega - \int_\Gamma \delta\mathbf{u}^{\mathrm{T}}\mathbf{t}_\Gamma \mathrm{d}\Gamma = \mathbf{0} \\ \text{or} \\ \sum_{k=1}^{N_{sd}} A_k^{\mathrm{sd}} \delta\bar{\boldsymbol{\varepsilon}}_k^{\mathrm{T}}\mathbf{D}_k\bar{\boldsymbol{\varepsilon}}_k - \int_\Omega \delta\mathbf{u}^{\mathrm{T}}\left[\mathbf{b} - \rho\ddot{\mathbf{u}} - c\dot{\mathbf{u}}\right]\mathrm{d}\Omega - \int_\Gamma \delta\mathbf{u}^{\mathrm{T}}\mathbf{t}_\Gamma \mathrm{d}\Gamma = \mathbf{0}\end{gathered} \tag{2.16}$$

where $\bar{\boldsymbol{\varepsilon}}(\mathbf{u})$ is the smoothed strain vector with the entries of $\bar{\boldsymbol{\varepsilon}}_k$ on each smoothing domain; **D** is the matrix of material constant; $\delta\mathbf{u}$ is the internal displacement vector; **b** is the body force vector; ρ is the density of the solid; $\dot{\mathbf{u}}$ and $\ddot{\mathbf{u}}$ are the 1st and 2nd order temporal derivatives of the displacement; and $\mathbf{t}_\Gamma$ is the traction applied on the boundary Γ of the domain Ω.

From Eq. (2.16) we can observe that in the smoothed Galerkin weak form only the assumed displacement but not the derivative of the assumed displacement field is required, which coincides the statement we argued previously that the consistency requirement on the assumed displacement function is further weakened from the Galerkin weak formulation.

The resultant discrete form of Eq. (2.16) can be written as

$$\tilde{\mathbf{M}}\ddot{\mathbf{u}} + \tilde{\mathbf{C}}\dot{\mathbf{u}} + \bar{\mathbf{K}}\mathbf{u} = \tilde{\mathbf{f}} \tag{2.17}$$

where $\mathbf{u} \in \mathbb{R}_0^{dN_n}$ is the nodal displacement vector in the whole domain; $\tilde{\mathbf{M}}$ is the mass matrix with

$$\tilde{\mathbf{M}} = \int_\Omega \mathbf{N}^\mathrm{T} \rho \mathbf{N} \mathrm{d}\Omega\,; \tag{2.18}$$

$\tilde{\mathbf{C}}$ is the damping matrix with

$$\tilde{\mathbf{C}} = \int_\Omega \mathbf{N}^\mathrm{T} c \mathbf{N} \mathrm{d}\Omega \tag{2.19}$$

where c is the damping coefficient; $\tilde{\mathbf{f}}$ is the external nodal force vector with

$$\tilde{\mathbf{f}} = -\int_\Omega \mathbf{N}^\mathrm{T} \mathbf{b} \mathrm{d}\Omega + \int_{\Gamma_t} \mathbf{N}^\mathrm{T} \mathbf{t}_\Gamma \mathrm{d}\Gamma\,; \tag{2.20}$$

and $\bar{\mathbf{K}}$ is the smoothed stiffness matrix with the entries of

$$\bar{\mathbf{K}}_{IJ} = \int_\Omega \bar{\mathbf{B}}_I^\mathrm{T} \mathbf{D} \bar{\mathbf{B}}_J^\mathrm{T} \mathrm{d}\Omega = \sum_{k=1}^{N_\mathrm{sd}} \int_{\Omega_k^\mathrm{sd}} \bar{\mathbf{B}}_I^\mathrm{T} \mathbf{D} \bar{\mathbf{B}}_J^\mathrm{T} \mathrm{d}\Omega = \sum_{k=1}^{N_\mathrm{sd}} \bar{\mathbf{B}}_I^\mathrm{T} \mathbf{D} \bar{\mathbf{B}}_J^\mathrm{T} A_k^\mathrm{sd}\,. \tag{2.21}$$

The smoothed stiffness matrix $\bar{\mathbf{K}}$ is symmetric positive definite (SPD) and sparse because its entry, $\bar{\mathbf{K}}_{IJ}$, only needs to be computed when nodes I and J share the same smoothing domain. Otherwise, it is zero. Hence, Eq. (2.17) can be solved by using standard routines with ease because $\bar{\mathbf{K}}$ is SPD and sparse. After getting the nodal displacement, we can then retrieve the smoothed strain field using Eq. (2.12), the stress field using the constitutive equation, and finally the solution of the strain energy of solid with the integration of the smoothed strain and stress over the entire problem domain.

The main difference between S-FEMs and FEM can be found from Eq. (2.17) that only the stiffness matrix $\bar{\mathbf{K}}$ is operated with a smoothing operation. The matrixes of $\tilde{\mathbf{M}}$, $\tilde{\mathbf{C}}$ and $\tilde{\mathbf{f}}$ are constructed exactly the same as in the standard FEM. In other words, *the S-FEM models change only the stiffness matrix*. A comparison of the numerical procedures in FEM and S-FEMs is schematically given in Fig. 2.3.

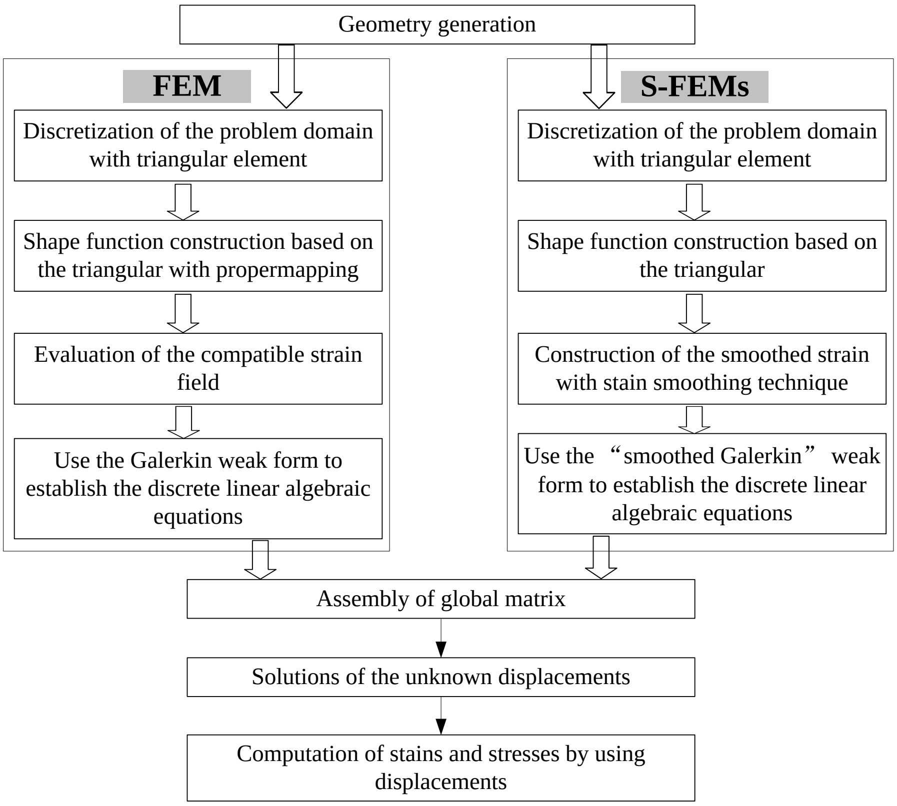

Fig. 2.3 Comparison of the formulation procedures in FEM and S-FEMs

2.2.2.1 Static and dynamic problems

Different problems can be generated from Eq. (2.17) as long as omitting some terms in it [24].

1) Static problem

For static problems, the equation can be obtained by removing the dynamic terms in Eq. (2.17) which becomes

$$\bar{\mathbf{K}}\mathbf{u} = \tilde{\mathbf{f}} . \tag{2.22}$$

2) Free vibration problem

For free vibration analysis, we do not consider the damping and the force terms, and hence Eq. (2.17) reduce to

$$\tilde{\mathbf{M}}\ddot{\mathbf{u}} + \bar{\mathbf{K}}\mathbf{u} = \mathbf{0}\,. \tag{2.23}$$

A general solution of such an equation can be written as

$$\mathbf{u} = \mathbf{u}_A \exp\left(i\omega t\right) \tag{2.24}$$

where t is the physical time; $\mathbf{u}_A$ is the amplitude of the nodal displacement and ω is the natural frequency that is found from

$$-\omega^2\tilde{\mathbf{M}} + \bar{\mathbf{K}} = \mathbf{0}\,. \tag{2.25}$$

3) Force vibration problem

For forced vibration analysis, Eq. (2.17) can be solved with any existing standard schemes such as the Newmark method and the Crank-Nicholson method [25]. The Rayleigh damping is usually used by linear combining of $\tilde{\mathbf{M}}$ and $\bar{\mathbf{K}}$ for the sake of simplicity, as

$$\tilde{\mathbf{C}} = \alpha\tilde{\mathbf{M}} + \beta\bar{\mathbf{K}} \tag{2.26}$$

where α and β are the Rayleigh damping coefficients.

2.2.2.2 Stability and convergence

The cell-based, node-based or edge-based smoothing domains utilized for approximating the smoothed strains are constructed according to the principles of: i) non-overlapping and seamless for the smoothing domains, and ii) at least a minimum number of smoothing domains (i.e. $N_{sd}^{\min} = n_{total}/2$ where n_{total} is the total (unconstrained) nodal unknowns [10]) used in creating the smoothed models, through which all the columns of the smoothed strain matrix are linearly independent [26, 27]. Therefore, the first term in Eq. (2.16) will be strictly larger than zero for $\mathbf{u} \in \mathbb{H}_{h,0}^{1}$, and the corresponding smoothed stiffness matrix $\bar{\mathbf{K}}$ is SPD. Therefore the S-FEM models will be stable as long as the material is stable [26, 27].

When the mesh is refined, the dimension of the elements approaches zero ($\Omega_i^e \rightarrow 0$) and thus the dimension of smoothing domains also approaches zero ($\Omega_k^{\mathrm{sd}} \rightarrow 0$). Accordingly, the weighed function in Eq. (2.4) approaches the Delta function ($\hat{w}\left(\mathbf{x};\mathbf{x}-\mathbf{x}_i\right) \rightarrow \delta\left(\mathbf{x};\mathbf{x}-\mathbf{x}_i\right)$). At such a limit, the smoothed strain $\bar{\boldsymbol{\varepsilon}}$ in Eq. (2.12) approaches the compatible strain $\tilde{\boldsymbol{\varepsilon}}$ in Eq. (11), i.e. $\bar{\boldsymbol{\varepsilon}} \rightarrow \tilde{\boldsymbol{\varepsilon}}$ thus $\bar{\mathbf{B}} \rightarrow \tilde{\mathbf{B}}$ and $\bar{\mathbf{K}} \rightarrow \tilde{\mathbf{K}}$. This means that the smoothed Galerkin model approaches the standard Galerkin model with the refinement of the mesh. Because the solution of a standard Galerkin model has already been proven to converge to the exact solution for a well-posed problem, the solution of the smoothed Galerkin model will thus also converge to the exact solution of the same problem. Consequently, the solution of Eqs. (2.16) and (2.17) is stable and converges to the exact solution when $\Omega_k^{\mathrm{sd}} \rightarrow 0$ [6]. Thus the S-FEMs are convergent. Details about the mathematical proof of the stability and convergence of the S-FEM models can be found in [12].

2.2.3 Properties of S-FEM models

Various S-FEM models have distinguished properties, advantages and disadvantages. Three important properties of the smoothed models, i.e. convergence rate, bound property, computational efficiency, are discussed in this section. A further verification of these properties will be done in Chapter 3.

2.2.3.1 Convergence rate

Theoretically, for a fully compatible model (e.g. FEM-T3) the convergence rate in energy norm should be 1.0, and for a fully equilibrium model the convergence rate in energy norm should be 2.0 [28]. However, the convergence rates of different S-FEM models are different but fall in the range $[1.0,\ 2.0]$, which is perhaps due to their hybrid features of compatibility and equilibrium [10] in the S-FEM models. Detailed illustrations of the compatibility of the smoothed strain field and the state of the stress equilibrium within smoothing domains are presented in [10].

2.2.3.2 Bound property

It is well known that the displacement-based fully compatible FEM provides a *stiffening* effect and gives the lower bound of the exact solution in strain energy in elasticity problems. Meanwhile, the S-FEM models possess the *softening* effect to the FEM model and thus give higher solutions in strain energy than the FEM model. When the *softening* effect is used in the ES-FEM-T3, the solution is even closer to the exact solution. While when the *softening* effect is used in the NS-FEM-T3, the solution possesses the upper bound of the exact solution in the energy norm. The detailed mathematical proofs of the bound property of the S-FEM models can be found in [18]. Because of the upper and lower bound properties of the S-FEMs, it gives a systematical way to numerically obtain both upper and lower bounds of the exact solution to elasticity problems.

2.2.3.3 Computational efficiency

The computational efficiency is a much fairer indicator on quantitative examination of a numerical method. It is a most important factor for the applicability of a numerical method for solving practical engineering problems. A Detailed discussion about the computational efficiency of different S-FEM models is given in [29, 30]. ES-FEM-T3 can achieve the highest computational efficiency among all the methods: it can achieve around 20 times accuracy than the NS-FEM-T3 and around 10 times accuracy than the FEM-T3. Therefore, the ES-FEM-T3 offers an excellent platform for analyzing the practical engineering problems. That is one reason we chose the ES-FEM-T3 in the present thesis.

2.3 Gradient smoothing for fluid mechanics

The Navier-Stokes equations are the basic equations governing compressible and incompressible flows, in which both the 1st and 2nd order spatial derivatives of the field variables (e.g. the velocity, pressure, momentum and energy contain both) are found. Numerical methods such as FDM and FVM are usually used to track the solutions of the Navier-Stokes equations on a set of structured or unstructured background mesh. The GSM, on the other hand, is an innovative numerical method belonging to the gradient smoothing family [6], which works well for both compressible and incompressible flows [31, 32]. It directly deals with the differential (strong) form of the Navier-Stokes equations as the FDM. However, the spatial derivatives of the field variables are not approximated with the Taylor series expansion but with the gradient smoothing technique integrating over a set of smoothing domains, which is similar with the “integral” FVM. Although the background mesh is still needed in GSM, its ability to resist extremely distorted meshes is much better than either FDM or FVM [31].

The fundamental formulation of GSM on fixed mesh is presented in this section. Based on this formulation, a novel method of discretizing the ALE form of the Navier-Stokes equations with GSM, i.e. GSM/ALE, will be developed in Chapter 4 for solving fluid-rigid solid interaction problems and in Chapter 5 for solving fluid-deformable solid interaction problems. As the incompressible fluid flow is main focus of interest in this thesis, the development and discussion of GSM are directed on this kind of flow.

2.3.1 Governing equations

For an isothermal incompressible Newtonian flow problem, the conservative Navier-Stokes equations can be written in the following differential form [33]

$$\begin{gathered}\frac{\partial v_x}{\partial x}+\frac{\partial v_y}{\partial y}=0\\ \frac{\partial \rho v_x}{\partial t}+\frac{\partial\left(\rho v_x{}^2+p\right)}{\partial x}+\frac{\partial \rho v_x v_y}{\partial y}=\frac{\partial \tau_{xx}}{\partial x}+\frac{\partial \tau_{xy}}{\partial y}\\ \frac{\partial \rho v_y}{\partial t}+\frac{\partial \rho v_x v_y}{\partial x}+\frac{\partial\left(\rho v_y{}^2+p\right)}{\partial y}=\frac{\partial \tau_{yx}}{\partial x}+\frac{\partial \tau_{yy}}{\partial y}\end{gathered} \tag{2.27}$$

where variables ρ, p, v_x and v_y denote, respectively, the density, static pressure and velocity component in x- and y-directions, $\mathbf{v}= v_x\mathbf{i}+v_y\mathbf{j}$; $\tau_{ij}=\mu\left(v_{i,j}+v_{j,i}\right)$ ($i,j=x,y$) denotes the viscous stresses in which μ is the kinematics viscosity; and t is the physical time.

Accordingly, the generic vector form of Eq. (2.27) can be written as

$$\frac{\partial \mathbf{U}}{\partial t}+\nabla\cdot\left(\mathbf{F}_c-\mathbf{F}_v\right)=\mathbf{0} \tag{2.28}$$

where the relevant vectors are in the form of

$$\mathbf{U}=\begin{bmatrix}\rho\\ \rho v_x\\ \rho v_y\end{bmatrix},\ \mathbf{F}_c=\begin{bmatrix}\rho v_x & \rho v_x v_y\\ \rho v_x{}^2+p & \rho v_x v_y\\ \rho v_x v_y & \rho v_y{}^2+p\end{bmatrix},\ \mathbf{F}_v=\begin{bmatrix}0 & 0\\ \tau_{xx} & \tau_{xy}\\ \tau_{yx} & \tau_{yy}\end{bmatrix}. \tag{2.29}$$

Here $\mathbf{F}_c$ and $\mathbf{F}_v$ are the tensors of the convective and viscous fluxes, respectively.

One main challenge of numerically solving the incompressible flows comes from the weak coupling of the velocity and pressure fields, which has to be accomplished in such a way to ensure the divergence of the velocity field [34]. The pressure-based method such as the fractional step method [35-39] and the density-based method such as the artificial compressibility method [33, 40, 41] are the two typical methods for handling the velocity-pressure coupling in incompressible flows. Particularly, in the artificial compressibility method, an artificial compressible term is introduced in the continuity equation and the unsteady terms in the momentum equations are retained, which lead the system of equations to take on the hyperbolic behavior [34]. Thus, the time marching techniques developed for solving hyperbolic system of compressible flows can be directly used for solving the incompressible flow problems.

By adding an artificial compressible term into Eq. (2.27), a total of two temporal terms, i.e. the physical temporal term with t and the pseudo temporal term with τ, are included in the governing equations, i.e.

$$\begin{gathered}
\frac{1}{\beta_p}\frac{\partial p}{\partial \tau}+\frac{\partial \rho v_x}{\partial x}+\frac{\partial \rho v_y}{\partial y}=0 \\
\frac{\partial \rho v_x}{\partial \tau}+\frac{\partial \rho v_x}{\partial t}+\frac{\partial\left(\rho v_x{}^2+p\right)}{\partial x}+\frac{\partial \rho v_x v_y}{\partial y}=\frac{\partial \tau_{xx}}{\partial x}+\frac{\partial \tau_{xy}}{\partial y} \\
\frac{\partial \rho v_y}{\partial \tau}+\frac{\partial \rho v_y}{\partial t}+\frac{\partial \rho v_x v_y}{\partial x}+\frac{\partial\left(\rho v_y{}^2+p\right)}{\partial y}=\frac{\partial \tau_{yx}}{\partial x}+\frac{\partial \tau_{yy}}{\partial y}
\end{gathered} \tag{2.30}$$

where coefficient β_p is the artificial compressibility, the square root of which can be interpreted as the speed of artificial pressure wave with the unit of m/s. During the numerical simulation, the value of β_p should be predefined with special care so as to ensure the good convergence of the overall iterative solution procedures. Usually it is case-dependent in the range of $\left[0.1,\ 10\right]$ [42]. A higher β_p will give a higher convergence speed, however, this higher β_p can lead the system to be too stiff and unstable in the time marching process [31].

The generic vector form of Eq. (2.30) can be written as

$$\mathbf{P}\frac{\partial \mathbf{Q}}{\partial \tau}+\frac{\partial \mathbf{U}}{\partial t}+\nabla\cdot\left(\mathbf{F}_c-\mathbf{F}_v\right)=\mathbf{0} \tag{2.31}$$

where the vector **Q** and matrix **P** are in the form of

$$\mathbf{Q}=\begin{bmatrix} p \\ \rho u \\ \rho v \end{bmatrix},\ \mathbf{P}=\begin{bmatrix} 1/\beta_p & 0 & 0 \\ 0 & 1 & 0 \\ 0 & 0 & 1 \end{bmatrix}. \tag{2.32}$$

By now, the augmented equations, with respect to pressure (p) and momentum components (ρv_x and ρv_y), have exhibited hyperbolic properties according to pseudo time. With this augmented sets of governing equations, the time-dependent solutions can be obtained efficiently with the help of dual time stepping techniques. When the steady-state solutions are considered, those physical temporal terms occurring in the respective systems of equations are neglected but the pseudo temporal terms are retained only.

2.3.2 Gradient smoothing operation

Both the 1st and 2nd order spatial derivatives of the field variables (the velocities and pressure) are found in the Navier-Stokes equations of Eq. (2.31). In GSM, the gradient smoothing operations proposed in Eqs. (2.5) and (2.6) can be directly used to determine the 1st and 2nd order spatial derivatives of the nodal field variables over the node-based gradient smoothing domains (nGSDs). Furthermore, the 1st order spatial derivatives of the midpoint field variables should be extra evaluated with Eq. (2.5) over the midpoint(edge)-based gradient smoothing domains (mGSDs), so as to complete the estimation of the corresponding 2nd order derivatives of the nodal field variables. After that, these derivatives are substitute into Eq. (2.31) for the approximations of the divergences of $\mathbf{F}_c$ and $\mathbf{F}_v$. Before implementing the gradient smoothing operations in GSM, the constructions of nGSDs and mGSDs should be predefined.

2.3.2.1 Types of smoothing domains

In order to construct these smoothing domains, the whole computational domain Ω needs to be firstly divided into N_{ele} (regular or irregular) triangular volumes (elements) such that $\Omega = \sum_{i=1}^{N_{ele}} \Omega_i^e$ and $\Omega_i^e \bigcap \Omega_j^e = \phi, \ \forall i \neq j$, the same as in the solid mechanics. The nGSDs and mGSDs are then constructed on top of these triangular volumes, as illustrated in Fig. 2.4.

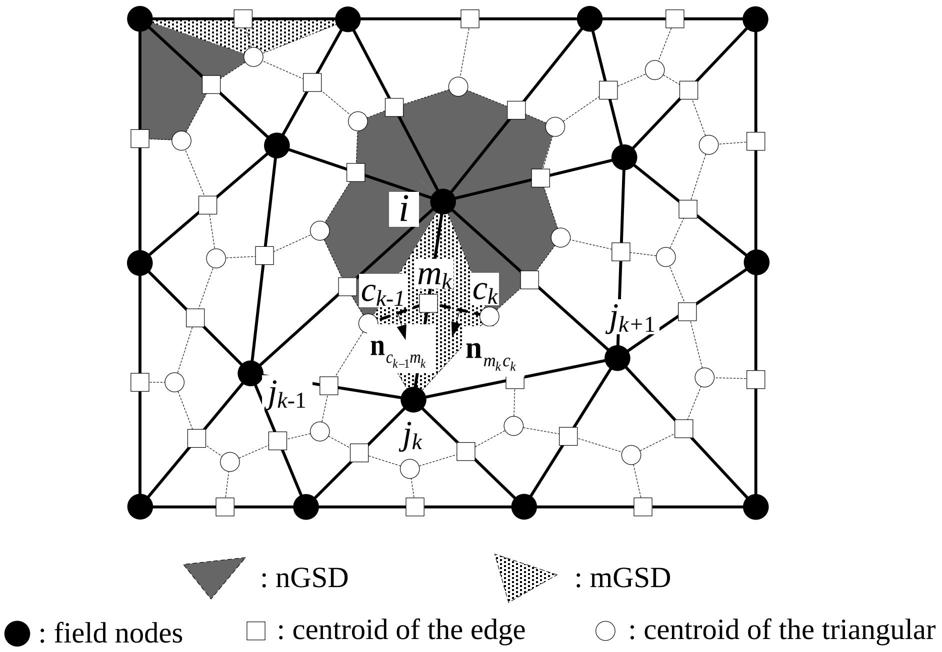

Fig. 2.4 Types of smoothing domains and domain-edge vectors adopted in GSM

The nGSDs are constructed for the approximation of 1st order derivatives of the field variables at a node of interest. It is formed by connecting the centroids of relevant triangles with midpoints of influenced cell-edges. And the mGSD is used for the calculation of the gradients at the midpoint of a cell-edge of interest and thus further for the 2nd order derivatives of the field variables at a node of interest. For the element inside the fluid domain, the mGSD is the connection of two vortexes of the edge ij_k and the two centers of the cells; for the boundary element, the mGSD are just a connection of the two vertexes of the edge ij_k and the centroid of the boundary element. By virtue of Eqs. (2.5) and (2.6), spatial derivatives at any point of interest can be approximated based on the corresponding smoothing domain described above.

2.3.2.2 Spatial approximations for the field variables

A total of eight discretization schemes have been proposed in [31] for numerically approximating the line integrations in Eqs. (2.5) and (2.6) according to different quadrature (rectangular or trapezoidal) rules. Accuracy, efficiency and stability of these schemes have been examined with a benchmark heat conduction problem. Finally, the most favorable scheme, i.e. scheme VII with the rectangular quadrature rule, was chosen for numerically approximating the line integrations. The name of “GSM” used in this thesis is a special representative of this scheme. Details of the others schemes can be found in [31] and not repeated here. Below the formulation procedures of this scheme VII are presented, which will be the basis of the subsequent ALE formulation for fluid-rigid/deformable body interaction analyses in Chapters 4 and 5.

Consider a general parameter U_N that can represent the velocity v_x or v_y or pressure p. The 1st and 2nd order spatial derivatives of U_N in Eq. (2.30) can be approximated with the gradient smoothing operation as follows.

1) 1st order spatial derivative of U_N at the vortexes

With the gradient smoothing operation of Eq. (2.5) and (2.7) over nGSD, the 1st order spatial derivatives of U_N at a node i can be approximated as

$$\frac{\partial}{\partial x}\left(U_N\right)_i \approx \frac{1}{A_i^{\mathrm{nGSD}}}\sum_{k=1}^{N_{sup}}\left(\Delta S_N^x\right)_{ij_k}\left(U_M\right)_{ij_k} \tag{2.33}$$

$$\frac{\partial}{\partial y}\left(U_N\right)_i \approx \frac{1}{A_i^{\mathrm{nGSD}}}\sum_{k=1}^{N_{sup}}\left(\Delta S_N^y\right)_{ij_k}\left(U_M\right)_{ij_k} \tag{2.34}$$

where

$$\begin{aligned}\left(\Delta S_N^x\right)_{ij_k} &= \Delta S_{M_{ij_k}C_{ij_kj_{k+1}}}\left(n_x\right)_{M_{ij_k}C_{ij_kj_{k+1}}} + \Delta S_{M_{ij_k}C_{ij_{k-1}j_k}}\left(n_x\right)_{M_{ij_k}C_{ij_{k-1}j_k}} \\ \left(\Delta S_N^y\right)_{ij_k} &= \Delta S_{M_{ij_k}C_{ij_kj_{k+1}}}\left(n_y\right)_{M_{ij_k}C_{ij_kj_{k+1}}} + \Delta S_{M_{ij_k}C_{ij_{k-1}j_k}}\left(n_y\right)_{M_{ij_k}C_{ij_{k-1}j_k}} .\end{aligned}$$

Here, j_k denotes the k^{th} node surrounding the node i; M_{ij_k} denotes the mid-point of the cell-edge ij_k; $C_{ij_kj_{k+1}}$ and $C_{ij_{k-1}j_k}$ represent the centroids of two triangular cells connected to the cell-edge ij_k; the total number of supporting nodes within the stencil of the node i is denoted by N_{sup}; U_N and U_M denote the values of the field variables at vortexes and mid-points of cell-edges, respectively, where U_M is computed by simple interpolation of function values at two end-nodes of the edge ij_k, $\left(U_M\right)_{ij_k} = \left[\left(U_N\right)_i + \left(U_N\right)_{j_k}\right] / 2$; ΔS_N^x and ΔS_N^y correspond to the two components of the paired domain-edges; n_x and n_y represent the two components of the unit normal vector of the domain edge under the Cartesian coordinate system, $\mathbf{n}=n_x\mathbf{i}+n_y\mathbf{j}$; and A_i^{nGSD} is the area of the i^{th} nGSD surrounding the node i.

2) 2nd order spatial derivatives of U_N at the vortexes

With the gradient smoothing operation of Eqs. (2.6) and (2.8) over nGSD, the 2nd order derivatives in Laplace operator are approximated in the following fashion

$$\nabla\cdot\left(\nabla U_N\right)_i \approx \frac{1}{A_i^{\text{nGSD}}}\sum_{k=1}^{N_{sup}}\left[\frac{\partial}{\partial x}\left(U_M\right)_{ij_k}\left(\Delta S_N^x\right)_{ij_k} + \frac{\partial}{\partial y}\left(U_M\right)_{ij_k}\left(\Delta S_N^y\right)_{ij_k}\right]. \tag{2.35}$$

It is apparent that the 1st order gradients at the mid-point of edge ij_k, i.e. $\partial\left(U_M\right)_{ij_k} / \partial x$ and $\partial\left(U_M\right)_{ij_k} / \partial y$, should be evaluated to complete the approximation of 2nd order derivatives. These two gradients can be approximated with Eqs. (2.33) and (2.34) based on the related mGSD associated with the edge ij_k. Similarly, the geometrical parameters in these two equations, including the areas, domain-edge vectors and normal vectors of domain edges related to mGSDs, should be predetermined and stored for use in the iterative process of solving the algebraic equations. Here,

$$\begin{aligned}\frac{\partial}{\partial x}\left(U_M\right)_{ij_k} \approx \Bigg\{ & \frac{1}{2}\left(\Delta S_M^x\right)_{iC_{ij_k j_{k+1}}}\left[\left(U_N\right)_i+\left(U_C\right)_{ij_k j_{k+1}}\right] \\ & +\frac{1}{2}\left(\Delta S_M^x\right)_{j_k C_{ij_k j_{k+1}}}\left[\left(U_N\right)_{j_k}+\left(U_C\right)_{ij_k j_{k+1}}\right] \\ & +\frac{1}{2}\left(\Delta S_M^x\right)_{iC_{ij_{k-1} j_k}}\left[\left(U_N\right)_i+\left(U_C\right)_{ij_k j_{k+1}}\right] \\ & +\frac{1}{2}\left(\Delta S_M^x\right)_{j_k C_{ij_{k-1} j_k}}\left[\left(U_N\right)_{j_{k-1}}+\left(U_C\right)_{ij_k j_{k+1}}\right]\Bigg\}\frac{1}{\left(A_M^{\text{mGSD}}\right)_{ij_k}}\end{aligned} , \qquad (2.36)$$

$$\begin{aligned}\frac{\partial}{\partial y}\left(U_M\right)_{ij_k} \approx \Bigg\{ & \frac{1}{2}\left(\Delta S_M^y\right)_{iC_{ij_k j_{k+1}}}\left[\left(U_N\right)_i+\left(U_C\right)_{ij_k j_{k+1}}\right] \\ & +\frac{1}{2}\left(\Delta S_M^y\right)_{j_k C_{ij_k j_{k+1}}}\left[\left(U_N\right)_{j_k}+\left(U_C\right)_{ij_k j_{k+1}}\right] \\ & +\frac{1}{2}\left(\Delta S_M^y\right)_{iC_{ij_{k-1} j_k}}\left[\left(U_N\right)_i+\left(U_C\right)_{ij_k j_{k+1}}\right] \\ & +\frac{1}{2}\left(\Delta S_M^y\right)_{j_k C_{ij_{k-1} j_k}}\left[\left(U_N\right)_{j_{k-1}}+\left(U_C\right)_{ij_k j_{k+1}}\right]\Bigg\}\frac{1}{\left(A_M^{\text{mGSD}}\right)_{ij_k}}\end{aligned} \qquad (2.37)$$

where A_M^{mGSD} represents the area of the mGSD. The relevant domain edge vectors, ΔS_M^x and ΔS_M^y, for the mGSD of interest are calculated as

$$\begin{aligned}&\left(\Delta S_M^x\right)_{iC_{ij_k j_{k+1}}}=\Delta S_{iC_{ij_k j_{k+1}}}\left(n_x\right)_{iC_{ij_k j_{k+1}}} \\ &\left(\Delta S_M^y\right)_{iC_{ij_k j_{k+1}}}=\Delta S_{iC_{ij_k j_{k+1}}}\left(n_y\right)_{iC_{ij_k j_{k+1}}} \\ &\left(\Delta S_M^x\right)_{j_k C_{ij_k j_{k+1}}}=\Delta S_{j_k C_{ij_k j_{k+1}}}\left(n_x\right)_{j_k C_{ij_k j_{k+1}}} \\ &\left(\Delta S_M^y\right)_{j_k C_{ij_k j_{k+1}}}=\Delta S_{j_k C_{ij_k j_{k+1}}}\left(n_y\right)_{j_k C_{ij_k j_{k+1}}}\end{aligned} , \quad \begin{aligned}&\left(\Delta S_M^x\right)_{iC_{ij_{k-1} j_k}}=\Delta S_{iC_{ij_{k-1} j_k}}\left(n_x\right)_{iC_{ij_{k-1} j_k}} \\ &\left(\Delta S_M^y\right)_{iC_{ij_{k-1} j_k}}=\Delta S_{iC_{ij_{k-1} j_k}}\left(n_y\right)_{iC_{ij_{k-1} j_k}} \\ &\left(\Delta S_M^x\right)_{iC_{ij_{k-1} j_k}}=\Delta S_{iC_{ij_{k-1} j_k}}\left(n_x\right)_{iC_{ij_{k-1} j_k}} \\ &\left(\Delta S_M^y\right)_{iC_{ij_{k-1} j_k}}=\Delta S_{iC_{ij_{k-1} j_k}}\left(n_y\right)_{iC_{ij_{k-1} j_k}}\end{aligned} .$$

The field variable U_C at the centroid of the cell is computed by simple interpolation of the function values at the related vortexes, in the fashion of

$$\left(U_C\right)_{ij_k j_{k+1}}=\begin{cases}\dfrac{\left(U_N\right)_i+\left(U_N\right)_{j_k}+\left(U_N\right)_{j_{k+1}}}{3}, & 1\le k<N_i\\ \dfrac{\left(U_N\right)_i+\left(U_N\right)_{j_{N_i}}+\left(U_N\right)_{j_1}}{3}, & k=N_i\end{cases},$$

$$\left(U_C\right)_{ij_{k-1} j_k}=\begin{cases}\dfrac{\left(U_N\right)_i+\left(U_N\right)_{j_k}+\left(U_N\right)_{j_{k-1}}}{3}, & 1\le k<N_i\\ \dfrac{\left(U_N\right)_i+\left(U_N\right)_{j_1}+\left(U_N\right)_{j_{N_i}}}{3}, & k=N_i\end{cases}.$$

As shown in Eqs. (2.33)-(2.35), only the values for the field variables and its gradients at the mid-points of cell edges are needed in the approximations. As such, vectors for a pair of domain edges connected with the cell edge can be lumped together, which in turn reduces the storage space for geometrical parameters. Furthermore, an edge-based data structure together with the scatter-gather approach is adopted, which has proven to be quite efficient during the GSM calculation [31].

2.3.3 Formulation of the discretized system of equations

There are both spatial and temporal terms in the Navier-Stokes equations in Eq. (2.31). Separate discretizations in the spatial and temporal domains can be implemented to achieve different accuracies in these two domains [43]. The gradient smoothing operation is implemented into Eq. (2.31) for the spatial discretization, and a dual time stepping temporal scheme is implemented into Eq. (2.31) for the temporal discretization.

2.3.3.1 Spatial discretization with gradient smoothing operation

Substitute Eqs. (2.33)-(2.35) into Eq. (2.31), the divergences of $\mathbf{F}_c$ and $\mathbf{F}_v$ can be written as

$$\begin{aligned}
\nabla\cdot\mathbf{F}_{ci} &\approx \frac{1}{A_i^{\mathrm{nGSD}}}\overline{\mathbf{F}}_{ci} = \frac{1}{A_i^{\mathrm{nGSD}}}\sum_{k=1}^{N_{sup}}\left[\left(\overline{\mathbf{F}}_c\right)_{ij_k}\Delta S_k\right] = \frac{1}{A_i^{\mathrm{nGSD}}}\sum_{k=1}^{N_{sup}}\left\{\begin{bmatrix}\left(\beta\rho V_s\right)\\ \rho v_x V + n_x p\\ \rho v_y V + n_y p\end{bmatrix}_{ij_k}\Delta S_k\right\},\\
\nabla\cdot\mathbf{F}_{vi} &\approx \frac{1}{A_i^{\mathrm{nGSD}}}\overline{\mathbf{F}}_{vi} = \frac{1}{A_i^{\mathrm{nGSD}}}\sum_{k=1}^{N_{sup}}\left[\left(\overline{\mathbf{F}}_v\right)_{ij_k}\Delta S_k\right] = \frac{1}{A_i^{\mathrm{nGSD}}}\sum_{k=1}^{N_{sup}}\left\{\begin{bmatrix}0\\ n_x\tau_{xx} + n_y\tau_{xy}\\ n_x\tau_{yx} + n_y\tau_{yy}\end{bmatrix}_{ij_k}\Delta S_k\right\}
\end{aligned}\tag{2.38}$$

where ΔS_k is the length of the k^{th} edge of the i^{th} nGSD; $V_s = \mathbf{v}\cdot\mathbf{n} = v_x n_x + v_y n_y$ is the contravariant velocity of fluid; and $(n_x)_k$ and $(n_y)_k$ are the x- and y-components of the normal vector $\mathbf{n}$ of the k^{th} edge, respectively.

Correspondingly, the generic vector form of Eq. (2.31) becomes

$$\frac{\partial\mathbf{Q}_i}{\partial\tau} + \frac{\partial\mathbf{U}_i}{\partial t} + \frac{1}{A_i}\left(\overline{\mathbf{F}}_{ci} - \overline{\mathbf{F}}_{vi}\right) = \mathbf{0} \tag{2.39}$$

with

$$\mathbf{Q}_i = \begin{bmatrix} p_i\\ \left(\rho v_x\right)_i\\ \left(\rho v_y\right)_i\end{bmatrix},\ \mathbf{U}_i = \begin{bmatrix}\rho_i\\ \left(\rho v_x\right)_i\\ \left(\rho v_y\right)_i\end{bmatrix}. \tag{2.40}$$

In order to ensure the stability of the discrete equations, some special techniques should be implied to the fluxes.

- **Smoothed convective flux $\left(\overline{\mathbf{F}}_c\right)_{ij_k}$**

One main work of solving the incompressible equations is to deal with the convective flux term. It is intrinsic to use the arithmetic average values of the conservative variables at the two constitutive nodes, *i* and j_k, for the convective flux at the midpoint of the edge. Such a treatment is similar to a central difference operation. However, it is only valid for low Reynolds number flows. As Reynolds number becomes larger, it breaks down because of the presence of high frequency spurious oscillation associated with the increasingly nonlinear nature of the governing equations. Various methods, e.g. the Roe method [44], the Jameson method [45] and the HLLC method [46], were developed to circumvent such a drawback. In the present study, the second order Roe flux differencing splitting unwinding scheme (Roe2) is employed, and a Riemann problem is solved at the cell interface to evaluate the numerical fluxes, which leads to the approximation of the convective flux $\overline{\mathbf{F}}_c$ at the midpoint of edge ij_k as

$$\left(\overline{\mathbf{F}}_c\right)_{ij_k} = \frac{1}{2}\left[\overline{\mathbf{F}}_c\left(\mathbf{Q}^L_{ij_k}\right)+\overline{\mathbf{F}}_c\left(\mathbf{Q}^R_{ij_k}\right)+\left|\overline{\mathbf{A}}_{Roe}\right|\left(\mathbf{Q}^L_{ij_k}-\mathbf{Q}^R_{ij_k}\right)\right] \tag{2.41}$$

where L and R denote the left and right sides of the nGSD boundary assuming that the edge is directed outward with respect to node-dual i, as shown in Fig. 2.5; $\mathbf{Q}^L_{ij_k}$ and $\mathbf{Q}^R_{ij_k}$ are the conservative variables at the left and right sides of a dual face ij_k; $\left|\overline{\mathbf{A}}_{Roe}\right|$ corresponds to the absolute eigenvalues of the Roe matrix $\overline{\mathbf{A}}_{Roe}$, $\left|\overline{\mathbf{A}}_{Roe}\right| = \mathbf{R}\left|\overline{\mathbf{\Lambda}}_{Roe}\right|\mathbf{R}^{-1}$ in which $\mathbf{R}$ and $\mathbf{R}^{-1}$ are the right and left eigenvector matrix of $\overline{\mathbf{A}}_{Roe}$, respectively, and $\left|\overline{\mathbf{\Lambda}}_{Roe}\right|$ is a diagonal matrix whose components are the absolute values of the eigenvalues. Solutions of the non-singular eigensystems of the Roe's matrix $\overline{\mathbf{A}}_{Roe}$ can be found in [32, 47] for 2D case.

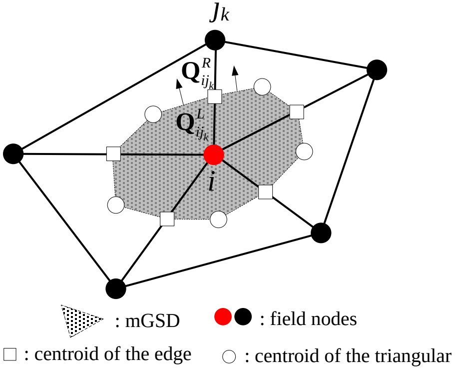

Fig. 2.5 Connection of node i and j_k illustrating for the Roe2 scheme

The order of the Roe scheme depends on the construction of $\mathbf{Q}_{ij_k}^L$ and $\mathbf{Q}_{ij_k}^R$. For Roe2, the $\mathbf{Q}_{ij_k}^L$ and $\mathbf{Q}_{ij_k}^R$ are linearly constructed by using the Taylor series expansion [48] as

$$\begin{cases} \mathbf{Q}_{ij_k}^L = \mathbf{Q}_i + \dfrac{1}{2}\nabla\mathbf{Q}_i \cdot \mathbf{r}_{ij_k} \\ \mathbf{Q}_{ij_k}^R = \mathbf{Q}_{j_k} - \dfrac{1}{2}\nabla\mathbf{Q}_{j_k} \cdot \mathbf{r}_{ij_k} \end{cases} \tag{2.42}$$

where $\mathbf{r}_{ij_k}$ is the vector from the node *i* to *j_k*, $\mathbf{r}_{ij_k} = \mathbf{x}_{j_k} - \mathbf{x}_i = \left(x_{j_k} - x_i\right)\mathbf{i} + \left(y_{j_k} - y_i\right)\mathbf{j}$; $\nabla\mathbf{Q}_i$ and $\nabla\mathbf{Q}_{j_k}$ are the variable gradients at node *i* and j_k, respectively, which can be evaluated according to the gradient smoothing operation of Eqs. (2.33) and (2.34) on the nGSD.

The approximation of the convective flux $\overline{\mathbf{F}}_{ci}$ at node *i* can thus be finally expressed as

$$\overline{\mathbf{F}}_{ci}\left(\mathbf{Q},\mathbf{x}\right) = \sum_{k=1}^{N_{sup}} \left[\left(\overline{\mathbf{F}}_c\right)_{ij_k} \Delta S_k \right]. \tag{2.43}$$

❖ **Smoothed viscous flux $\left(\overline{\mathbf{F}}_v\right)_{ij_k}$**

To estimate the viscous fluxes at a node, the 2nd order derivatives of velocities in the Laplace operator should be approximated, in which the velocity gradients at the midpoint of each edge should be further evaluated with the graduate smoothing operation over the mGSD. Comparing with the simple linear interpolation of gradients at the two constitutive nodes, the gradient smoothing operation can result in a favorable compact stencil with positive coefficients at nodes of influence, and can also circumvent the checkerboard problem [32].

The viscous flux $\overline{\mathbf{F}}_v$ at node *i* can be evaluated in the form of

$$\overline{\mathbf{F}}_{vi}\left(\mathbf{Q},\mathbf{x}\right)=\sum_{k=1}^{N_{sup}}\left[\left(\overline{\mathbf{F}}_{v}\right)_{ij_k}\Delta S_k\right] \tag{2.44}$$

where $\left(\overline{\mathbf{F}}_{v}\right)_{ij_k}$ is associated with the velocity gradients (∇u and ∇v) at the mid-point of edge ij_k that are calculated according to Eqs. (2.33) and (2.34).

Finally, by substituting the discretized forms of Eqs. (2.43) and (2.44) into Eq. (2.39), the semi-discrete form of the Navier-Stokes equations is finally obtained as

$$\mathbf{R}_i^*\left(\mathbf{Q},\mathbf{x}\right)=A_i^{\mathrm{nGSD}}\frac{\partial \mathbf{U}_i}{\partial t}+\overline{\mathbf{F}}_{ci}\left(\mathbf{Q},\mathbf{x}\right)-\overline{\mathbf{F}}_{vi}\left(\mathbf{Q},\mathbf{x}\right)=\mathbf{0}. \tag{2.45}$$

2.3.3.2 Dual time-stepping temporal discretization

The dual time stepping approach is adopted for the accurate time integration, in which the computation is performed by marching along the physical time with a user specified physical time step (Δt). At each physical time level, steady-state solution with respect to pseudo time ($\Delta\tau$) is pursued by using the iterative time marching method. That is,

$$\mathbf{P}\frac{\mathrm{d}}{\mathrm{d}\tau}\left(\mathbf{Q}_i A_i^{\mathrm{nGSD}}\right)+\mathbf{R}_i^*\left(\mathbf{Q},\mathbf{x}\right)=\mathbf{0} \tag{2.46}$$

where $\mathbf{R}_i^*\left(\mathbf{Q},\mathbf{x}\right)$ is the semi-discrete equations of Eq. (2.45), named here as the unsteady residual at node *i*.

The BFD2 is used to discretize the physical time term in the unsteady residual $\mathbf{R}_i^*\left(\mathbf{Q},\mathbf{x}(t),\dot{\mathbf{x}}(t)\right)$ as

$$\mathbf{R}_i^*\left(\mathbf{Q},\mathbf{x}\right)=A_i^{\mathrm{nGSD}}\left(\frac{3\mathbf{U}_i-4\,{}^{n}\mathbf{U}_i+{}^{n-1}\mathbf{U}_i}{2\Delta t}\right)+\overline{\mathbf{F}}_{ci}\left(\mathbf{Q},\mathbf{x}\right)-\overline{\mathbf{F}}_{vi}\left(\mathbf{Q},\mathbf{x}\right)=\mathbf{0} \tag{2.47}$$

where $\mathbf{U}_i$ is the value at the “*k*-1” level of 5-stage Runge-Kutta (RK5) method in the pseudo time step as illustrated below; and *n* denotes the *n*th physical time level.

The performance of the dual time stepping method evidently relies on the time marching method used in the pseudo time level. In the present study, the RK5 method with residual smoothing is used in the pseudo time level [32, 43] for its high efficiency of the steady-state solver. The general form for RK5 method with residual smoothing applied to Eq. (2.48) is given as

$$ {}^{k}\mathbf{Q}_i = {}^{0}\mathbf{Q}_i - \frac{\alpha_k \lambda}{1+\alpha_k \lambda}\left[{}^{0}\mathbf{Q}_i + \frac{2}{3}\frac{\Delta t}{A_i^{\text{nGSD}}}\left({}^{k-1}\mathbf{R}_i^{*} \right) - {}^{k-1}\mathbf{Q}_i \right], \quad k=1,...,5 \tag{2.48} $$

where $\lambda = \text{CFL} \times \Delta\tau / (2\Delta t)$; and α_k (α_1=0.0695, α_2=0.1602, α_3=0.2898, α_4=0.5060, α_5=1.0) is the optimized coefficients for convergence acceleration to steady state. It should be noted that the residual smoothing technique used in the RK5 method can significantly stabilize the iterative process during the time marching [32]. As a result, relatively larger local pseudo-time steps ($\Delta\tau$) are allowed, resulting in greater acceleration in convergence. This scheme is also stable for high CFL values.

The dual time stepping scheme is driven by the time integration scheme for the pseudo steady-state problem. Once the steady-state in pseudo time is reached, the pseudo time derivative vanishes and the solution advances to the next time step, which means that the procedure for steady-state solutions is a simplified subset of the dual time stepping approach. An illustration of the dual time stepping scheme from physical time step t^n to t^{n+1} can be summarized as

```
${}^{m=1}\mathbf{Q}={}^{n}\mathbf{U}$
Loop $m$=1, $m_{\max}$
    ${}^{0}\mathbf{Q}={}^{n+1,m}\mathbf{U}$
    Loop $k$=1,$k_{max}$
        ${}^{k+1}\mathbf{R}' = \frac{\alpha_k \lambda}{(1+\alpha_k \lambda)}\left[ {}^{0}\mathbf{Q} - \frac{2\Delta t}{3A_i^{\text{nGSD}}}\mathbf{R}^{*}\left( {}^{n+1,m,k-1}\mathbf{Q}, {}^{n}\mathbf{U}, {}^{n-1}\mathbf{U} \right) - {}^{n+1,m,k-1}\mathbf{Q} \right]$
        ${}^{n+1,m,k}\mathbf{Q} = {}^{0}\mathbf{Q} - {}^{k+1}\mathbf{R}'$
    End Loop
    If $error<tol$
        Break
```

```
        Else
            $^{n+1,m+1}\mathbf{Q}={}^{n+1,m,p}\mathbf{Q}$
        EndIf
End Loop
$^{n+1}\mathbf{U}={}^{n+1,m+1}\mathbf{Q}$
```

where m denotes the m^{th} pseudo time step, and the work is to march to a steady solution at the time step "n+1, m+1"; k_{max} denotes the total stages of RK method, k_{max} =5 presently; *tol* denotes the tolerant error in the calculation; *error* denotes the numerical error in each pseudo time step defined as

$$error=\left[\sum_{i=1}^{N_{node}}\left({}^{n+1,m+1}\mathbf{U}_i-{}^{n+1,m}\mathbf{U}_i\right)\Big/\sum_{i=1}^{N_{node}}\left({}^{n+1,1}\mathbf{U}_i-{}^{n}\mathbf{U}_i\right)\right]^{1/2} \tag{2.49}$$

where ${}^{n}\mathbf{U}_i$ denotes the predicted value of the field variable at the node i at the n^{th} iteration, and N_{node} is the total number of nodes in the domain. The value of *error* is monitored during iterations and used to terminate the iterative process. In most simulations, in order to exclude the effect owing to the temporal discretization, computations are not stopped until this *error* becomes an extremely small value.

2.3.4 Theoretical aspects of GSM

2.3.4.1 Truncation error

The truncation errors of the gradient smoothing operation for approximating the 1st and 2nd order spatial derivatives are theoretically derived based on two sets of structured meshes [31, 32], i.e. the square mesh and equilateral triangle mesh, as listed in Table 2.1. From this table it can be seen that the 2nd order accuracy can be achieved by the GSM for approximating both the 1st and 2nd derivations in the spatial domain. The orders of these truncation errors will be numerically verified over the unstructured meshes in Chapter 4.

Table 2.1 Truncation errors in the approximations of the 1st order derivatives and Laplace operator

Operator	Shape of mesh	Truncation error
1st order spatial derivative	Square	$\begin{cases} O_x\left(h^2\right) = -\dfrac{h^2}{6}\dfrac{\partial^3 U_{ij}}{\partial x^3} + O\left(h^3\right) \\ O_y\left(h^2\right) = -\dfrac{h^2}{6}\dfrac{\partial^3 U_{ij}}{\partial y^3} + O\left(h^3\right) \end{cases}$
	Equilateral triangle	$\begin{cases} O_x\left(h^2\right) = -h^2\left(\dfrac{1}{24}\dfrac{\partial^3 U_{ij}}{\partial x^3} + \dfrac{1}{8}\dfrac{\partial^3 U_{ij}}{\partial x \partial y^2}\right) + O\left(h^3\right) \\ O_y\left(h^2\right) = -h^2\left(\dfrac{1}{24}\dfrac{\partial^3 U_{ij}}{\partial y^3} + \dfrac{1}{8}\dfrac{\partial^3 U_{ij}}{\partial x^2 \partial y}\right) + O\left(h^3\right) \end{cases}$
Laplace operator	Square	$O\left(h^2\right) = -\dfrac{h^2}{12}\left(\dfrac{\partial^4 U_{ij}}{\partial x^4} + \dfrac{\partial^4 U_{ij}}{\partial y^4}\right) + O\left(h^3\right)$
	Equilateral triangle	$O\left(h^2\right) = -\dfrac{h^2}{16}\left(\dfrac{\partial^4 U_{ij}}{\partial x^4} + 2\dfrac{\partial^4 U_{ij}}{\partial x^2 \partial y^2} + \dfrac{\partial^4 U_{ij}}{\partial y^4}\right) + O\left(h^3\right)$

2.3.4.2 Boundary conditions

There are four main classes of boundary conditions encountered in solving the fluid flow problems, i.e. solid wall, farfield, inlet/outlet and symmetric boundary conditions. In treating these boundary conditions, particular care should be taken as any improper implementation may either result in inaccurate simulation of the real system or influence the stability and convergence speed of the solution scheme [43].

1) Solid wall

In viscous flows, the non-slip wall conditions are usually used. Since $v_{wx} = v_{wy} = 0$, the momentum equations on the wall are not needed to be solved. And the convective fluxes on the wall take the same formulation as those in the inviscid flow. In the current study, the wall is assumed to be adiabatic. Hence, it is not necessary to compute any convective or viscous fluxes at the wall. The residuals of the momentum equations should be set to zero, in order to prevent the generation of nonzero velocity components at the wall nodes.

As indicated by Luo *et al.* [49], for high accuracy, the pressure on the wall used in the calculation of convective fluxes is predicted in the form of

$$p_w = \frac{1}{6}(5p_i + p_{j_k}) \tag{2.50}$$

instead of the arithmetic average. This is also true for predicting the gradients on boundaries (except at symmetry or periodic boundaries). The contribution from the domain faces at boundaries of an nGSD is calculated as $\mathbf{n}_{ij_k}\frac{\Delta S_{ij_k}}{2}\cdot\left[\frac{1}{6}(5\mathbf{U}_i + \mathbf{U}_{j_k})\right]$.

2) Farfield

The farfield boundary conditions are imposed on the external bounds of the computational domains. As addressed in [43], the numerical implementation of the farfield conditions has to fulfill two basic requirements: i) the truncation of the domain should have no notable effects on the flow solution as compared to the infinite domain; ii) any outgoing perturbations must not be reflected back into the flow field. In order to simplify the computation of the gradient of the field variables along the farfield as well as the inlet/outlet boundaries, a set of dummy nodes are added outside the physical domain [43], as shown in Fig. 2.6. After applying the boundary conditions to these dummy nodes through an interpolation of the field variables at both infinity and boundary nodes, the governing equations at the boundaries can then be solved in the same way as that for the inner computational domain. In this case, the geometrical quantities corresponding to these dummy nodes, e.g. normal vectors, are taken from the corresponding control volume at the boundary [43].

The characteristic farfield conditions used here are derived based on the inviscid governing equations and vary with the first eigenvalue (λ_1) which is equal to the contravariant velocity, V_s.

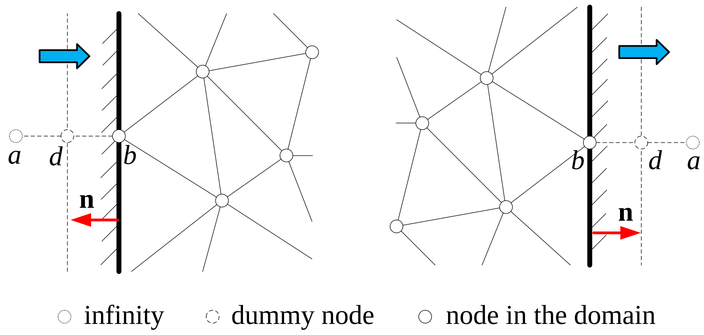

a) subsonic inflow boundary b) subsonic outflow boundary

Fig. 2.6 Definition of farfield boundaries in fluid mechanics

In the case of V_s <0, the fluid will flow into the fluid domain of interest, as shown in Fig. 2.6a, and the following inflow conditions are used at the boundary

$$\begin{aligned} p_d &= \frac{p_a + p_b}{2} - \frac{1}{2c_0}\left[\beta\left(\Theta_a - \Theta_b\right) - \Theta_0\left(p_a - p_b\right)\right] \\ v_{dx} &= u_a - \frac{p_a - p_d}{\beta_p c_0}\left[v_{0x}\left(\Theta_0 - c_0\right) + \beta_p n_x\right] \qquad . \\ v_{dy} &= v_a - \frac{p_a - p_d}{\beta_p c_0}\left[v_{0y}\left(\Theta_0 - c_0\right) + \beta_p n_y\right] \end{aligned} \tag{2.51}$$

When V_s >0, the fluid will flow out of the domain of interest, as shown in Fig. 2.6b, and the following outflow conditions are imposed at the boundary

$$\begin{aligned} p_d &= p_a \\ v_{dx} &= u_b - \frac{p_b - p_d}{\beta_p c_0}\left[v_{0x}\left(\Theta_0 - c_0\right) + \beta_p n_x\right] \\ v_{dy} &= v_b - \frac{p_b - p_d}{\beta_p c_0}\left[v_{0y}\left(\Theta_0 - c_0\right) + \beta_p n_y\right] \end{aligned} \tag{2.52}$$

where the subscripts *a*, *d* and *b*, respectively, denote the flow conditions at infinity, dummy and boundary nodes in Fig. 2.6. Reference values for v_{0x}, v_{0y}, c_0 and are evaluated at the boundary nodes. Details about the derivation of characteristic variable boundary conditions can be found in [50]. The farfield boundary conditions as shown in Eqs. (2.51) and (2.52) should be updated in each Runge-Kutta iterative loop.

3) Inlet/outlet

For inlet/outlet boundaries, special attention is required. As the artificial compressibility method is used for solving incompressible flow in the present study, the flow field thus possesses the features of compressible flow until the solution is completely converged. Hence, the application of the inlet/outlet boundary conditions should follow that of the compressible flow. For subsonic compressible flows, there is one out-going characteristic wave and three incoming waves at the inlet, and three out-going and one in-coming characteristic waves at the outlet [51, 52]. Typically, at the inlet pressure is extrapolated to account for the unique out-going wave, and all velocity components are specified with free stream values for the three in-coming characteristic waves. At the outlet, all velocity components are extrapolated for the three out-going waves and only the pressure is specified as the free stream quantity due to the one in-coming wave [52].

In our GSM implementation, the boundary condition at the inlet is set as

$$\begin{cases} v_{dx} = v_{ax} \\ v_{dy} = v_{ay} \\ p_d = p_b \end{cases} . \tag{2.53}$$

And at the outlet it is set as

$$p_d = p_a . \tag{2.54}$$

4) Symmetry

On the symmetric plane, all quantities should be extrapolated except the velocity component normal to the plane, which is set to zero [52]. Accordingly, the following conditions should be satisfied [32]

$$\begin{aligned} &\mathbf{n}\cdot\nabla U = 0 \\ &\mathbf{n}\cdot\nabla(\mathbf{t}\cdot\mathbf{v}) = 0 \\ &\mathbf{n}\cdot\nabla(\mathbf{n}\cdot\mathbf{v}) = 0 \end{aligned} \tag{2.55}$$

where U denotes a scalar quantity, e.g. pressure or components of the velocity vector; **n** and **t** denote the unit normal and tangential vectors of the symmetric plane, respectively; and **v** denotes the velocity vector at this plane.

In applying these four boundary conditions in solving the incompressible flow in the present thesis, a corner point, where two or more boundaries meet with each other, is split into two points for each boundary condition separately.

2.3.4.3 Local time

Since the explicit RK5 method is used for the time integration in the pseudo domain, the so-called Courant-Friedrichs-Lewy (CFL) condition should be fulfilled in order to stabilize this explicit time integration process [43, 53]. The CFL condition for an explicit time integration scheme the local time step should be equal to or smaller than the critical time required to transport information across the stencil of the spatial discretization scheme [43]. In our calculation of the 2D incompressible fluid flows, the local time step $\Delta\tau_i$ at a node, i, of interest over the unstructured mesh can be approximated as [32, 43]

$$\Delta\tau_i = \sigma \frac{V_{si}}{\left(\Lambda_x + \Lambda_y + D\right)_i} \tag{2.56}$$

where $\left(\Lambda_x\right)_i = \left[\left(\left|v_x\right| + c_x\right) S_x\right]_i$, $\left(\Lambda_y\right)_i = \left[\left(\left|v_x\right| + c_y\right) S_y\right]_i$ and $D_i = \frac{2}{\mathrm{Re}} \frac{V_{si}}{\left(S_x + S_y\right)_i}$. The artificial speeds of sound are evaluated as $\left(c_x\right)_i = \left(v_{xi}^2 + \beta_p\right)^{1/2}$ and $\left(c_y\right)_i = \left(v_{yi}^2 + \beta_p\right)^{1/2}$. The projected areas of the smoothing domain are denoted by $\left(S_x\right)_i$ and $\left(S_y\right)_i$, which are defined as $\left(S_x\right)_i = \frac{1}{2}\sum_{k=1}^{n_i}\left|\Delta S_{ij_k}^x\right|$ and $\left(S_y\right)_i = \frac{1}{2}\sum_{k=1}^{n_i}\left|\Delta S_{ij_k}^y\right|$, respectively.

References for Chapter 2

1. Chen, J.S., Wu, C.T. and Belytschko, T., *Regularization of material instabilities by meshfree approximations with intrinsic length scales.* International Journal for Numerical Methods in Engineering, 2000. **47**(7): p. 1303-1322.
2. Eringen, A.C., *Nonlocal polar elastic continua.* International Journal of Engineering Science, 1972. **10**(1): p. 1-16.
3. Chen, J.S., Wu, C.T., Yoon, S. and You, Y., *A stabilized conforming nodal integration for Galerkin mesh-free methods.* International Journal for Numerical Methods in Engineering, 2001. **50**(2): p. 435–466.
4. Yoo, J.W., Moran, B. and Chen, J.S., *Stabilized conforming nodal integration in the natural element method.* International Journal for Numerical Methods in Engineering, 2004. **60**(5): p. 861-890.
5. Liu, G.R., *Mesh free methods: moving beyond the finite element method, 1st Edition*. 2003: CRC.
6. Liu, G.R., *Meshfree methods: moving beyond the finite element method, 2nd Edition*. 2009: CRC.
7. Liu, G.R., *A generalized gradient smoothing technique and the smoothed bilinear form for Galerkin formulation of a wide class of computational methods.* International Journal of Computational Methods, 2008. **5**(2): p. 199-236.
8. Lucy, L.B., *A numerical approach to the testing of the fission hypothesis.* The Astronomical Journal, 1977. **82**: p. 1013-1024.
9. Liu, G.R. and Liu, M., *Smoothed Particle Hydrodynamics: A Meshfree Particle Method*. 2003: World Scientific Pub Co Inc.
10. Liu, G.R. and Nguyen, T.T., *Smoothed finite element methods*. 2010: CRC Pr I Llc.
11. Liu, G.R., Dai, K.Y. and Nguyen, T.T., *A smoothed finite element method for mechanics problems.* Computational Mechanics, 2007. **39**(6): p. 859-877.
12. Liu, G.R., Nguyen, T.T., Dai, K.Y. and Lam, K.Y., *Theoretical aspects of the smoothed finite element method (SFEM).* International Journal for Numerical Methods in Engineering, 2007. **71**(8): p. 902-930.
13. Liu, G.R., Nguyen Thoi, T., Nguyen Xuan, H., Dai, K.Y. and Lam, K.Y., *On the essence and the evaluation of the shape functions for the smoothed finite element method (SFEM).* International Journal for Numerical Methods in Engineering, 2009. **77**(13): p. 1863-1869.
14. Dai, K., Liu, G. and Nguyen, T., *An n-sided polygonal smoothed finite element method (nSFEM) for solid mechanics.* Finite Elements in Analysis and Design, 2007. **43**(11-12): p. 847-860.
15. Nguyen, T.T., Liu, G.R., Dai, K.Y. and Lam, K.Y., *Selective smoothed finite element method.* Tsinghua Science & Technology, 2007. **12**(5): p. 497-508.
16. Liu, G.R., Nguyen-Thoi, T., Nguyen-Xuan, H. and Lam, K.Y., *A node-based smoothed finite element method (NS-FEM) for upper bound solutions to solid mechanics problems.* Computers & Structures, 2009. **87**(1-2): p. 14-26.
17. Nguyen-Thoi, T., Liu, G. and Nguyen-Xuan, H., *Additional properties of the node-based smoothed finite element method (NS-FEM) for solid mechanics problems.* International Journal of Computational Methods, 2009. **6**(4): p. 633-666.

18. Liu, G.R. and Zhang, G.Y., *Upper bound solution to elasticity problems: A unique property of the linearly conforming point interpolation method (LC-PIM).* International Journal for Numerical Methods in Engineering, 2008. **74**(7): p. 1128-1161.
19. Liu, G.R., Zhang, G.Y., Dai, K.Y., Wang, Y.Y., Zhong, Z.H., Li, G.Y. and Han, X., *A linearly conforming point interpolation method (LC-PIM) for 2D solid mechanics problems.* International Journal of Computational Methods, 2005. **2**(4): p. 645-666.
20. Liu, G.R., Nguyen-Thoi, T. and Lam, K.Y., *An edge-based smoothed finite element method (ES-FEM) for static, free and forced vibration analyses of solids.* Journal of Sound and Vibration, 2009. **320**(4-5): p. 1100-1130.
21. Wang, S., Liu, G.R., Zhang, G.Y. and Chen, L., *Design of Asymmetric Gear and Accurate Bending Stress Analysis Using the ES-PIM with Triangular Mesh.* International Journal of Computational Methods, 2011. **8**(4): p. 759-772.
22. Wang, S., Liu, G.R., Zhang, Z.Q. and Chen, L., *Nonlinear 3D numerical computations for the square membrane versus experimental data.* Engineering Structures, 2011. **33**(5): p. 1828-1837.
23. Nguyen-Thoi, T., Liu, G.R., Vu-Do, H.C. and Nguyen-Xuan, H., *An edge-based smoothed finite element method for visco-elastoplastic analyses of 2D solids using triangular mesh.* Computational Mechanics, 2009. **45**(1): p. 23-44.
24. Liu, G.R. and Zhang, G.Y., *A normed G space and weakened weak (W2) formulation of a cell-based smoothed point interpolation method.* International Journal of Computational Methods, 2009. **6**(1): p. 147-179.
25. Smith, I.M. and Griffiths, D.V., *Programming the finite element method.* 2004: John Wiley & Sons Inc.
26. Liu, G.R., *A G space theory and a weakened weak (W2) form for a unified formulation of compatible and incompatible methods: Part I theory.* International Journal for Numerical Methods in Engineering, 2010. **81**(9): p. 1093-1126.
27. Liu, G.R., *A G space theory and a weakened weak (W2) form for a unified formulation of compatible and incompatible methods: Part II applications to solid mechanics problems.* International Journal for Numerical Methods in Engineering, 2010. **81**(9): p. 1127-1156.
28. Zienkiewicz, O., Taylor, R. and Zhu, J., *The finite element method: its basis and fundamentals*. Vol. 1. 2005: Butterworth-Heinemann, Amsterdam, London.
29. Chen, L. *Development of smoothed numerical methods for fracture analyses and interfacial toughness characterization in thin film systems*. Department of Mechanical Engineering, 2011, Ph.D. thesis, National University of Singapore: Singapore.
30. Chen, L., Nguyen-Xuan, H., Nguyen-Thoi, T., Zeng, K. and Wu, S., *Assessment of smoothed point interpolation methods for elastic mechanics.* International Journal for Numerical Methods in Biomedical Engineering, 2010. **26**(12): p. 1635-1655.
31. Liu, G.R. and George, X.X., *A gradient smoothing method (GSM) for fluid dynamics problems.* International Journal for Numerical Methods in Fluids, 2008. **58**(10): p. 1101-1133.
32. George, X.X. *Development of Gradient Smoothing method (GSM) for Fluid Flow Problems*. Department of Mechanical Engineering, 2009, Ph.D. thesis, National University of Singapore: Singapore.

33. Chorin, A.J., *A numerical method for solving incompressible viscous flow problems*. Journal of Computational Physics, 1967. **2**(1): p. 12-26.
34. Tamamidis, P., Zhang, G. and Assanis, D.N., *Comparison of pressure-based and artificial compressibility methods for solving 3D steady incompressible viscous flows.* Journal of Computational Physics, 1996. **124**(1): p. 1-13.
35. Harlow, F.H. and Welch, J.E., *Numerical calculation of time-dependent viscous incompressible flow of fluid with free surface.* Physics of Fluids, 1965. **8**(12): p. 2182.
36. Patankar, S.V. and Spalding, D.B., *A calculation procedure for heat, mass and momentum transfer in three-dimensional parabolic flows.* International Journal of Heat and Mass Transfer, 1972. **15**(10): p. 1787-1806.
37. Patankar, S.V., *Numerical heat transfer and fluid flow*. 1980: Hemisphere Pub.
38. Arakawa, A., *Computational design for long-term numerical integration of the equations of fluid motion: Two-dimensional incompressible flow. Part I.* Journal of Computational Physics, 1966. **1**(1): p. 119-143.
39. Rhie, C.M. and Chow, W.L., *Numerical study of the turbulent flow past an airfoil with trailing edge separation.* AIAA Paper, 1983. **21**(11): p. 1525-1532.
40. Turkel, E., *Preconditioned methods for solving the incompressible and low speed compressible equations.* Journal of Computational Physics, 1987. **72**(2): p. 277-298.
41. Ohwada, T., Asinari, P. and Yabusaki, D., *Artificial compressibility method and lattice Boltzmann method: similarities and differences.* Computers & Mathematics with Applications, 2011. **61**(12): p. 3461-3474.
42. Kwak, D., Chang, J.L.C., Shanks, S.P. and Chakravarthy, S.R., *A three-dimensional incompressible Navier-Stokes flow solver using primitive variables.* AIAA Paper, 1986. **24**: p. 390-396.
43. Blazek, J., *Computational fluid dynamics: principles and applications*. 2005: Elsevier Science.
44. Roe, P.L., *Approximate Riemann solvers, parameter vectors, and difference schemes.* Journal of Computational Physics, 1981. **43**(2): p. 357-372.
45. Haselbacher, A. and Blazek, J. *On the accurate and efficient discretisation of the Navier-Stokes equations on mixed grids*. *14th Computational Fluid Dynamics Conference*. 1999. Norfolk, VA, UNITED STATES.
46. Mandal, J.C., Sonawane, C.R., Iyer, A.S. and GosaviInamdar, S.J., *Incompressible flow computations over moving boundary using a novel upwind method.* Computers & Fluids, 2010.
47. Anderson, W.K., Rausch, R.D. and Bonhaus, D.L., *Implicit/multigrid algorithms for incompressible turbulent flows on unstructured grids.* Journal of Computational Physics, 1996. **128**(2): p. 391-408.
48. Barth, T.J. and Jespersen, D.C. *The design and application of upwind schemes on unstructured meshes*. *27th Aerospace Sciences Meeting*. 1989. Reno, Nevada, UNITED STATES.
49. Luo, H., Baum, J.D. and Lohner, R. *An improved finite volume scheme for compressible flows on unstructured grids*. *33rd Aerospace Sciences Meeting and Exhibit*. 1995. Reno, NV, UNITED STATES.
50. Whitfield, D.L. and Taylor, L.K., *Numerical solution of the two-dimensional time-dependent incompressible Euler equations*, in *NASA Contractor Report*. 1994.

51. Giles, M.B., *Non-Reflecting Boundary Conditions For Euler Equation Calculations.* AIAA Paper, 1990. **28**: p. 2050-2058.
52. Ahn, H.T. *A New Incompressible Navier-Stokes method with general hybrid meshes and its application to flow/structure interactions*. 2005, Ph.D. thesis, The University of Texas at Austin: Austin.
53. Courant, R., Friedrichs, K. and Lewy, H., *Über die partiellen Differenzengleichungen der mathematischen Physik.* Mathematische Annalen, 1928. **100**(1): p. 32-74.

Chapter 3

ES-FEM-T3 for solid mechanics

As one typical smoothed method, the ES-FEM-T3 was found to possess a series of attractive properties such as super convergence, high convergence rate, accuracy and computational efficiency, stable in both spatial and temporal domains over the standard FEM-T3 and NS-FEM-T3 for solving solid mechanics [1]. This chapter extends the ES-FEM-T3 for solving two engineering problems: the 2D linear bending stress analysis of the gear tooth existing in the gear transformation and the 3D nonlinear membrane deflection analysis involving large deformations and rotations. For comparison the standard FEM-T3 models are also established in each case. The performances of the ES-FEM-T3 in these two practical areas give us confidence of further extending it for solving FSI problems in Chapter 5.

3.1 Implicit ES-FEM-T3 for 2D linear bending stress analysis

A typical engineering problem, i.e. the gear transmission problem, is considered in this section to study the loading carrying capacity of the gear tooth during the gear transmission process whereby the gear tooth withstands a tensile stress at the loaded side (drive side) and a compressive stress at the opposite side (coast side). Tooth fracture always occurs at the fillet of the loaded side, which is mainly due to the stress concentration in this region [2]. Thus an accurate estimate of the stress distributions in this region should be quite essential for ensuring the safety of the gear transmission. As previously mentioned, the standard FEM-T3 would give an “over-stiff” numerical model leading to poor accuracy in the stress field. In that case, the ES-FEM-T3 could be a better choice to accurately estimate the stress distributions in the gear tooth. Numerical innovations, e.g. replacing the concentrated transferred force *F* with a linearly distributed pressure around the loading point, are created during the formulation process of the implicit ES-FEM-T3 model in order to avoid the stress singularity at the loading region. In consideration of the superior performance of the ES-FEM-T3 in the stress field, it is further used for the gear profile optimization analysis. A series of novel asymmetric involute gears with a larger pressure angle $\alpha_d \geq 20^\circ$ in the drive side and a normal pressure $\alpha_c = 20^\circ$ in the coast side is designed and the most favorable gear profile is finally determined.

3.1.1 Formulaiton of implicit ES-FEM-T3 model

The loading carrying capacity analysis, i.e. bending strength analysis, is a linear elastic static analysis. Thus only the static model of implicit ES-FEM-T3 needs be constructed, as that in Eq. (2.22). The construction procedures are exactly the same as those established in Section 2.2. They will not be repeated and the final discrete governing equations are only presented here, as follows

$$\bar{\mathbf{K}}\mathbf{u} = \tilde{\mathbf{f}} \tag{3.1}$$

where $\bar{\mathbf{K}}$ is the smoothed stiffness matrix with its entry of $\bar{\mathbf{K}}_{IJ}$ assembled over the edge-based smoothing domains; $\mathbf{u} \in \mathbb{R}_0^{dN_n}$ is the nodal displacement vector; and $\tilde{\mathbf{f}}$ is the external force vector with its entry of the transferred force *F* generating from the contact of two gear teeth during the gear transmission process, as illustrated in Fig. 3.1. Physical meaning of the parameters labeled in this figure will be detailed later.

This transferred force *F* can be further divided into a tangent force F_t and normal force F_n as

$$\begin{cases} F_t = F \times \cos \alpha_{FM} \\ F_n = F \times \sin \alpha_{FM} \end{cases} \tag{3.2}$$

where $F = T / \left(B \times r_M \times \cos \alpha_{dM} \right)$ with $T = 9550 \times P/n$ where P is the translated power, KW, n is the speed of the gear, rpm; B is the width of the gear tooth, B=1 for 2D analysis; r_M is the radius of the circle passing point M; and α_{dM} is the pressure angle at the loading point M.

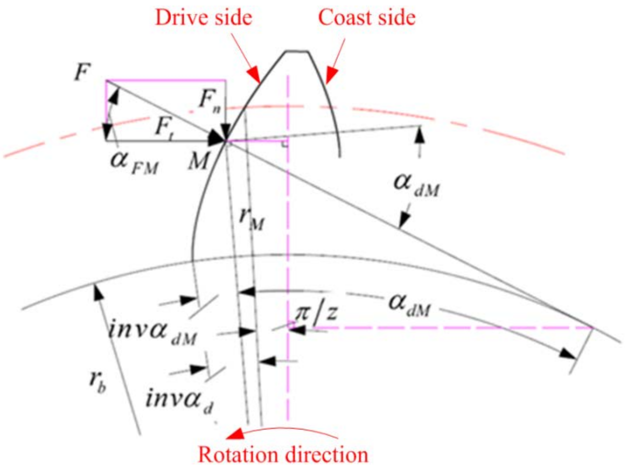

Fig. 3.1 Illustration of the transferred force *F* in the drive side of a gear tooth during the gear transmission process

It should be noted that this transferred force *F* is not always constant in one gear meshing cycle but follows a jump curve as shown in Fig. 3.2a, because the gear undergoes a “two teeth contacts→one tooth contact→two teeth contact” in a whole meshing cycle. The transferred force *F* is shared by two teeth at the “two teeth contacts” status. Accordingly, five typical contact points can be found in one meshing cycle, as illustrated in Fig. 3.2b. These are

- the lowest point of two teeth contact (*LPDTC*)---*A*
- the lowest point of one tooth contact (*LPSTC*)---*B*
- the point at the addendum circles during two teeth contact (*IPDTC*)---*C*
- the highest point of one teeth contact (*HPSTC*)---*D*
- the tip of one tooth (*TST*)---*E*

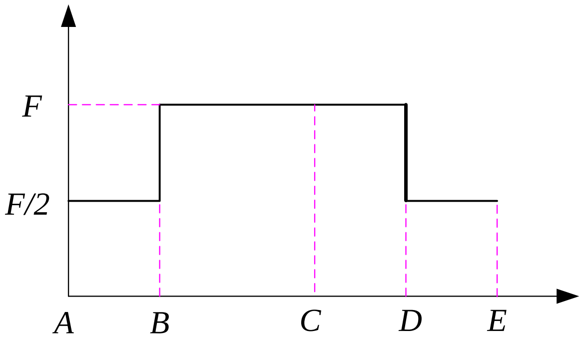

a) Transferred forces at five typical points

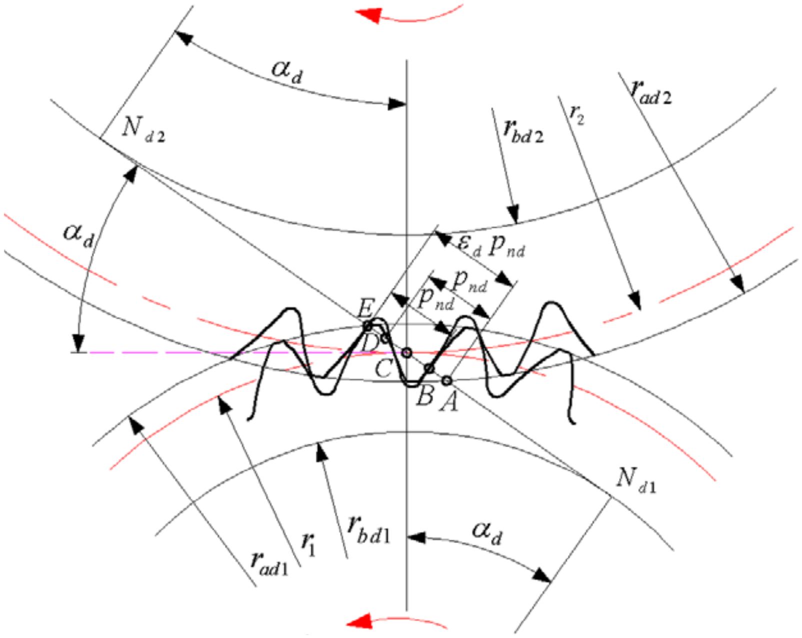

b) Illustration of the five typical points in a meshing cycle

Fig. 3.2 Illustration of the five typical points in a meshing cycle and the corresponding transferred forces

As suggested in [2, 3], the maximum bending stress occurs at the time when the gear meshing arrives at point *D* in one meshing cycle. So in the present study the transferred force *F* obtained at this status is used and assembled into the force vector $\tilde{\mathbf{f}}$ for the bending stress analysis. Accordingly, the pressure and load angles at point *D* can be calculated as

$$\alpha_{dD} = \arctan\left[\tan\alpha_{ad} - \left[2\pi\left(\varepsilon_d - 1\right)\right]/z\right] \tag{3.3}$$

$$\alpha_{FD} = \mathrm{inv}\alpha_{dD} + \alpha_{dD} - \mathrm{inv}\alpha_d - \pi/z \tag{3.4}$$

where α_{ad} is the pressure angle at the intersection point of the addendum circle and the gear tooth profile; α_{dD} is the pressure angle at point *D*; α_d is the pressure angle of the gear tooth; ε_d is the contact ratio in the drive side; and *z* is the total number of gear tooth. By substituting Eqs. (3.3) and (3.4) in Eq. (3.2), the transferred force *F* and thus the force vector $\tilde{\mathbf{f}}$ can be finally obtained.

3.1.2 Numerical verification of implicit ES-FEM-T3

A one-tooth model with the pressure angles $\alpha_d = 20^\circ / \alpha_c = 20^\circ$ in the drive and coast sides, respectively, is created, as shown in Fig. 3.3, to test three key properties of the newly proposed ES-FEM-T3, e.g. the accuracy in the stress field, the convergence property of the strain energy and the convergence rate of the strain energy norm. An implicit ES-FEM-T3 in-house code developed in MATLAB is used. For comparison the implicit FEM-T3 code is also created. The materials properties of the gear tooth are E=2.16×10^{11}Pa and v=0.3. A triangular mesh with 521 irregular nodes, as shown in Fig. 3.4a, is created as the background mesh. As the exact stress is not available for this problem, a refined mesh with 10233 irregular nodes, as shown in Fig. 3.4b, is also generated for the reference stress. Note that there is a higher node density at the fillet in the drive side in order to get more accurate stress distributions at this region. This analysis is seen as a plane strain analysis.

Both Dirichlet and Neumann boundary conditions are applied at the gear tooth, as shown in Fig. 3.3. For the Dirichlet boundary, the displacements at the relevant nodes are constrained in both *x*- and *y*-directions. For Neumann boundary condition, the loads of F_t =481551.67N and F_n =162231.99N gotten from Eq. (3.2) are applied at point *D*. In order to avoid the stress singularity, the region near the point *D* is particularly meshed, as the zoom-in part in Fig. 3.5a. The concentrated load *F* is linearly discretized to the 9 adjacent nodes on a line associated with the point *D* using Gauss integration method, as shown in Fig. 3.5b and Fig. 3.5c.

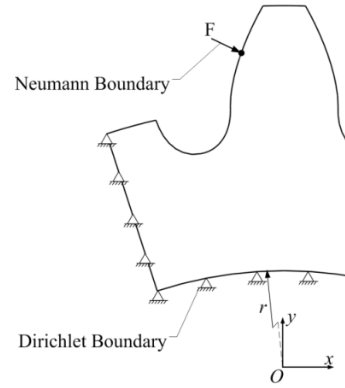

Fig. 3.3 One-tooth gear model subjecting to Dirichlet and Neumann boundary conditions

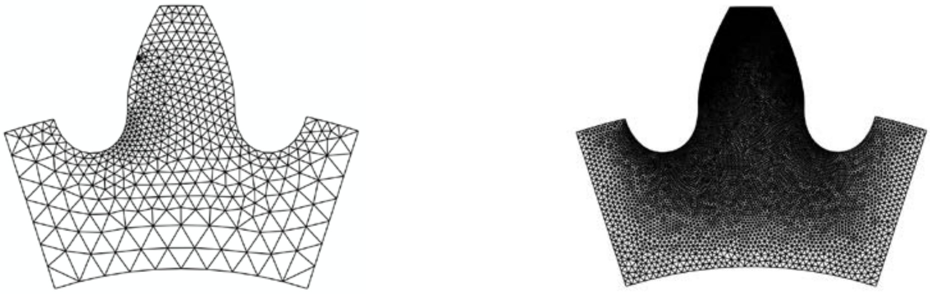

a) Mesh with 521 nodes

b) Mesh with 10233 nodes

Fig. 3.4 Generated meshes for the one-tooth gear model

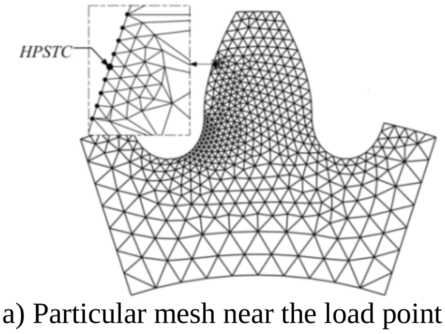

a) Particular mesh near the load point

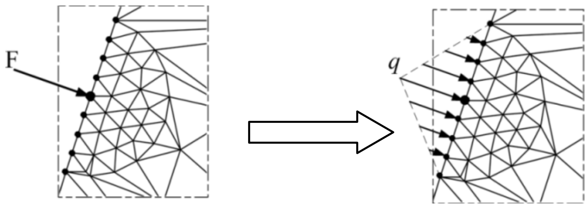

b) Concentrated load applied at the *HPSTC*

c) Distributed load applied at the 9 points associated with *HPSTC*

Fig. 3.5 Illustration of the load distribution: from a concentrated load to a distributed load

3.1.2.1 *Accuracy of the stress field*

The gear tooth usually fails at the fillet on the tensile-stress side [2]. Therefore, it is prudent to pay special attention on the stress distributions at this region. Fig. 3.6 plots the stress contours from the ES-FEM-T3, FEM-T3 and the referential solutions. The zoom-in figures in Fig. 3.6 highlight the stress distributions in the two most sensitive regions, i.e. the loading region and the stress concentration region. Comparing these three contours, it can be seen that the stress distribution from ES-FEM-T3 are much closer to the referential one than that from the standard FEM-T3 at the loading region, which indicates that the ES-FEM-T3 can deal with the concentrated load much better than the FEM-T3.

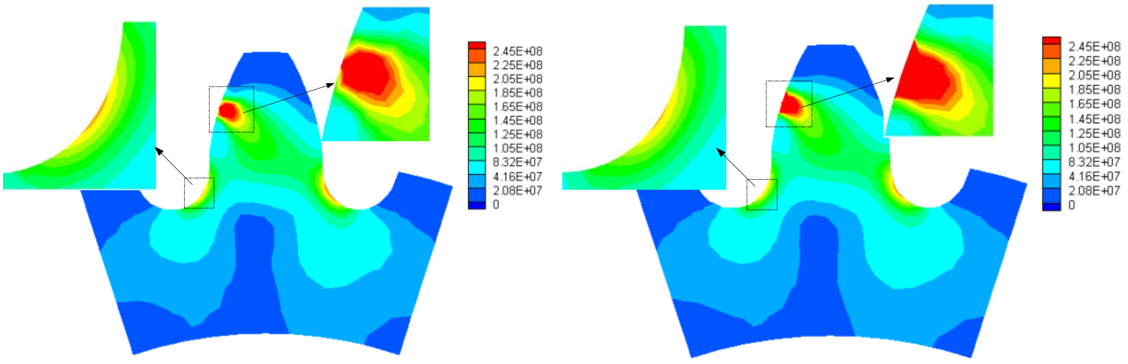

a) Contour of ES-FEM-T3 with 521 nodes b) Contour of FEM-T3 with 521 nodes

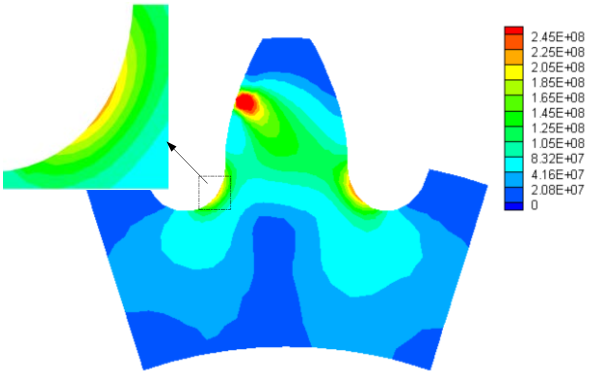

c) Contour of the referential solutions with 10233 nodes

Fig. 3.6 Contours of the Von Mises stress from ES-FEM-T3 (521 nodes), FEM-T3 (521 nodes) and the referential solutions (10233 nodes)

A further comparison of the exact stress distributions at the fillet in the drive side is plotted in Fig. 3.7. From the zoom-in part in this figure it can be seen that the resultant stress from ES-FEM-T3 is much closer to the reference than that from the standard FEM-T3. A precise comparison of the maximum bending stress in this stress concentration region shows that up to 23.67% errors are reduced by the ES-FEM-T3 on comparing with the FEM-T3.

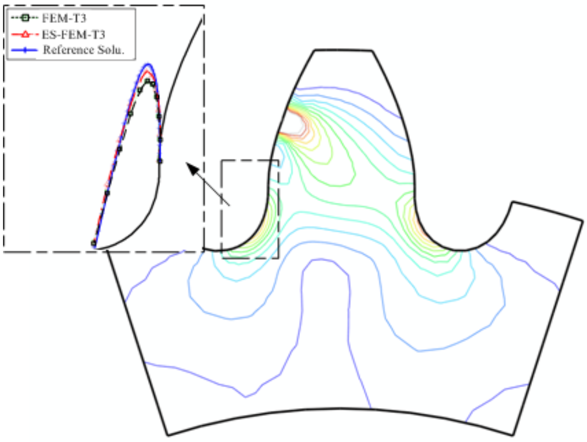

Fig. 3.7 Comparison of the Von Mises stress distributions at the fillet in the drive side from ES-FEM-T3, FEM-T3 and the referential solutions

3.1.2.2 *Convergence of the strain energy*

The strain energy indicator of a whole domain is defined as

$$e_{exact} = \frac{1}{2}\int_{\Omega} \boldsymbol{\sigma}_{exact}{}^{\mathrm{T}} \boldsymbol{\varepsilon}_{exact} \mathrm{d}\Omega = \frac{1}{2}\int_{\Omega} \boldsymbol{\sigma}_{exact}{}^{\mathrm{T}} \mathbf{D}^{-1} \boldsymbol{\sigma}_{exact} \mathrm{d}\Omega \tag{3.5}$$

where $\boldsymbol{\sigma}_{exact}$ is the exact stress vector; $\boldsymbol{\varepsilon}_{exact}$ is the exact strain vector; and $\mathbf{D}$ is the material constant matrix.

Five sets of triangular meshes (321 nodes, 521 nodes, 1102 nodes, 1984 nodes and 4225 nodes) are generated for the convergence analysis. As the exact strain energy cannot be obtained, the reference strain energy from a refined mesh of 10233 nodes represents e_{exact}.

Table 3.1 lists the strain energies from the present ES-FEM-T3, the FEM-T3 and the referential solutions. Fig. 3.8 plots the convergence process of these strain energies with the increase of the degree of freedoms (DOFs) for different models. From this figure, it can be seen that i) the strain energies of both ES-FEM-T3 and FEM-T3 converge to the reference with the increase of the DOFs; and ii) the strain energy of ES-FEM-T3 is much closer to the reference than that of FEM-T3. As expected, the FEM-T3 exhibits overly-stiff behavior and hence gives the lower bound. A softening effect has been introduced into the ES-FEM-T3 because of the use of strain smoothing operation, which allows the ES-FEM-T3 to have a very close-to-exact stiffness: the results are more accurate than those from FEM-T3.

Table 3.1 Strain energies gotten from ES-FEM-T3 and FEM-T3 with different DOFs for the gear tooth bending analysis

Case	DOF	Strain energy of ES-FEM-T3	Strain energy of FEM-T3
1	642	4.1680	3.9507
2	1042	4.2037	4.0429
3	2204	4.2945	4.1925
4	3968	4.3157	4.2385
5	8450	4.3459	4.2920
Reference	20466	4.3591	

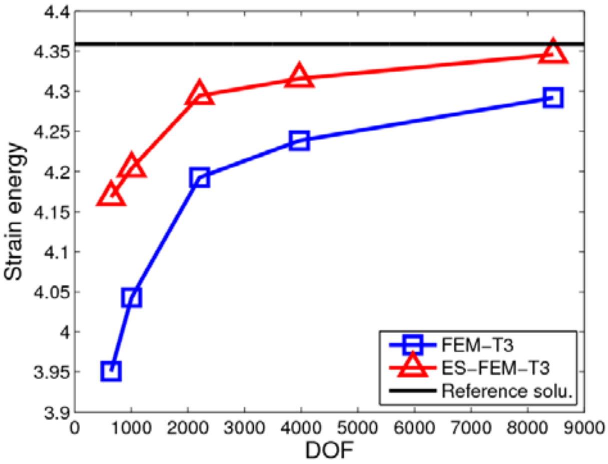

Fig. 3.8 Convergence of the strain energies to the exact solutions for the gear model using both ES-FEM-T3 and FEM-T3

3.1.2.3 *Convergence rate of strain energy norm*

The strain energy error norm indicator is defined as

$$e_e = \left[\left(e_{exact} - e_{num} \right) / e_{exact} \right]^{1/2} \tag{3.6}$$

where e_{exact} is the exact strain energy as used in Eq. (3.5); and e_{num} is the numerical strain energy.

The convergence rate in energy error norm, converging with the reducing average nodal spacing (h), is plotted in Fig. 3.9. From this figure, it can be seen that a higher slope is obtained by the ES-FEM-T3, which indicates that the ES-FEM-T3 gives a higher convergence rate than the standard FEM-T3. The convergence rate of ES-FEM-T3 is 0.99, which is much higher than 0.68 for the FEM-T3. The present ES-FEM-T3 gives a convergence rate 1.46 times higher than that of the standard FEM-T3. We know that the theoretical convergence rate in energy norm for a fully-compatible Galerkin model should be 1.0 and for a smoothed model should be between 1.0 and 2.0. A slightly lower value as found in this calculation should be because of the existence of the stress concentration at the fillet. Ever then, the ES-FEM-T3 still performs better than the standard FEM-T3.

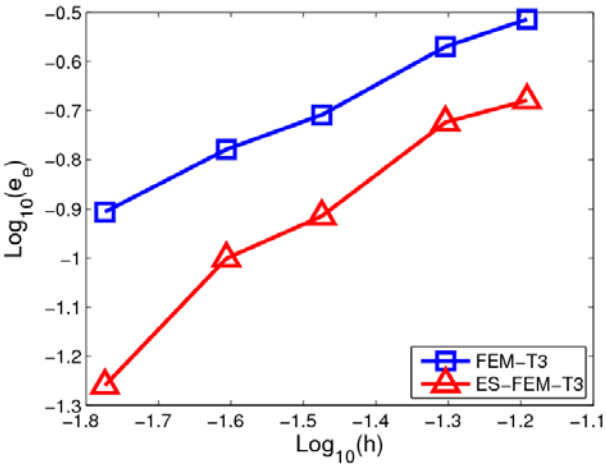

Fig. 3.9 Convergence rate of the strain energy norms for the gear model using both ES-FEM-T3 and FEM-T3

3.1.3 Implementation of implicit ES-FEM-T3 for gear tooth optimization

As pointed out by Wang in [2], the crack always occurs at the fillet in the drive side due to the high stress concentration in this region. Thus a simple idea arises that if we thicken the root in the drive side, could the maximum bending stress in this region be decreased and thus the carrying capacity of the modified gear be correspondingly improved? If it is “yes”, how thick should it be most suitable? The optimization of the gear tooth profiles presented in this section will answer these two questions.

Thickening the root of gear tooth is actually a technique of modifying the gear tooth profiles, which leads to a series of so-called asymmetric gears with different pressure angles at the drive and coast sides, respectively. By now, several kinds of asymmetric gears have been developed based on different principles. Deng *et al.* [4] made a change of the pressure angle in the coast side to increase the bending stiffness of the gear tooth. Kapelevich [5] and Kapelevich and Kleiss [6], however, suggested using a larger pressure angle in the drive side and a normal pressure angle in the coast side. Similarly, with the larger pressure angle in the drive side, Litvin *et al.* [7, 8] proposed a modified geometry of an asymmetric spur gear drive designed as a combination of an involute gear and a double crowned pinion. Muni *et al*. [9] and Kumar *et al*. [10] used a direct gear design method for the optimization of bending strength of asymmetric spur gear drives. Xiao *et al*. [11] used an asymmetric rack cutter to generate the gear pair and suggested a suitable pressure angle to be applied in the drive side via a series of analyses including the bending stress analysis, vibration analysis and thermal conduction analysis. All these researches have put significant improvements on the load carrying ability of the gear tooth during gear transmission.

In this section, a novel design of the asymmetric gear that applies a larger pressure angle in the drive side ($\alpha_d \geq 20^\circ$) and a standard pressure angle in the coast side ($\alpha_c = 20^\circ$) is presented. The optimum profile of the gear tooth is finally determined according to the stress distributions at the fillet in the drive side via the ES-FEM-T3 analysis.

3.1.3.1 *Governing equations of the gear tooth profile*

A gear tooth profile can be divided into five portions, as illustrated in Fig. 3.10, i.e. the involute (①) and trochoidal (②) potions in the drive side, the involute (③) and trochoidal (④) potions in the coast side and the addendum (⑤) connecting the two involutes. Different portions are governed by different equations, which can be derived from the mechanical relationships during the gear cutting process by an asymmetric rack cutter. The detailed derivations of the governing equations are given in Appendix A. Here these equations are directly employed to generate different asymmetric gear tooth models.

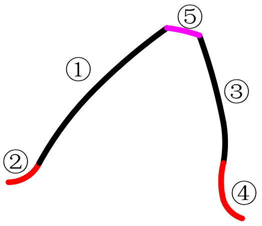

Fig. 3.10 Five portions of a gear tooth profile

3.1.3.2 *Optimization of the gear tooth profile*

Five typical asymmetric gear models with pressure angles of α_d =20°, 25°, 30°, 35° and 40°, respectively, in the drive side and a standard pressure angle of α_c =20° in the coast side are created, as shown in Fig. 3.11b, all of which are cut by the corresponding asymmetric rack cutters as shown in Fig. 3.11a. These five models have the module m=5mm and the addendum coefficient $h_{ac}^{*}=1$. With these five models it is our intent to find some potential relationships between the pressure angles and the stress distributions at the fillet in the drive side, so as to find the set of optimum pressure angles leading to the lowest stress concentration at the fillet region for the same gear transmission.

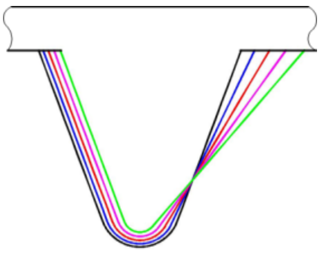

a) Asymmetric rack cutters used for cutting the five typical gear models: curves from the left to the right corresponds to the set of pressure angles: 20°/20°, 25°/20°, 30°/20°, 35°/20° and 40°/20°

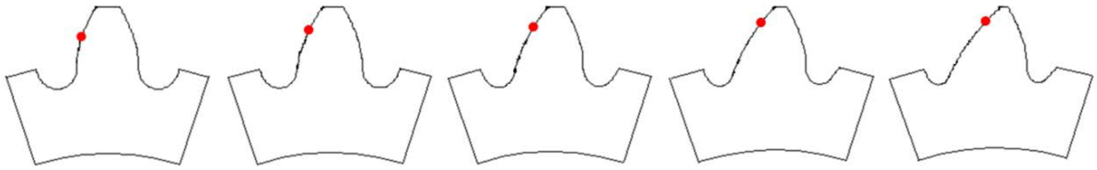

b1) model with 20°/20°
b2) model with 25°/20°
b3) model with 30°/20°
b4) model with 35°/20°
b5) model with 40°/20°

Fig. 3.11 Rack cutters with different pressure angles and the corresponding asymmetric gear teeth with a highlighted point at the *HPSTC*

The gear tooth is assumed to be linearly elastic with Young's modulus $E=2\times 10^{11}$Pa and Poisson's ratio v=0.25 undergoing a transmission with input power P=50KW at the rotation velocity n=1000rpm. The transferred forces are different for different models and they are all listed in Table 3.2 based on Eq. (3.2). These forces are respectively applied at the *HPSTC* (as highlighted in Fig. 3.11b) of these five models. These five gear models are discretized with equivalent number of nodes as listed in Table 3.3. Correspondingly, five more sets of refined meshes are generated for the reference purpose. The Dirichlet and Neumann boundary conditions used are the same as those outlined in Section 3.1.2.

Table 3.2 Transferred forces applied at the *HPSTC* for different asymmetric gear models: N

Gear model	Total force F	Tangent force F_t	Normal force F_n
20°/20°	508144.89	481551.68	162231.99
25°/20°	526862.96	476574.41	224636.17
30°/20°	551369.51	471014.73	286624.24
35°/20°	582919.87	465552.06	350794.59
40°/20°	623331.98	460744.50	419830.04

Table 3.3 Node information of the five asymmetric gear models

Gear model	Node number for comparison	Node number for reference
20°/20°	521	10233
25°/20°	524	11100
30°/20°	519	11061
35°/20°	510	10919
40°/20°	500	10928

Fig. 3.12 gives a comparison of the Von Mises stress contours of these five asymmetric gear models. Correspondingly, Fig. 3.13 plots the stress distributions at the fillet in the drive side for these five models. From these figures it can be seen that with different pressure angles in the drive side, the resulting stress fields are different, which indicates that modifying the tooth profile do affect the stress distributions in the gear tooth. An obvious trend can be found from Fig. 3.13 that with the increase of pressure angle in the drive side, the maximum bending stress decreases while the location of the fillet moves to the negative direction of the *x*-axis. The length of fillet seems also to become shorter with this trend.

A precise comparison of these maximum bending stresses is plotted in Fig. 3.14a, in which the results from the standard FEM-T3 is also presented. From this figure it can be seen that the maximum bending stresses from ES-FEM-T3 are much closer to the reference than those from FEM-T3, which again shows that the ES-FEM-T3 could give more accurate solutions than the FEM-T3. The reduced errors are respectively 23.67%, 26.31%, 25.90%, 25.41% and 29.73%.

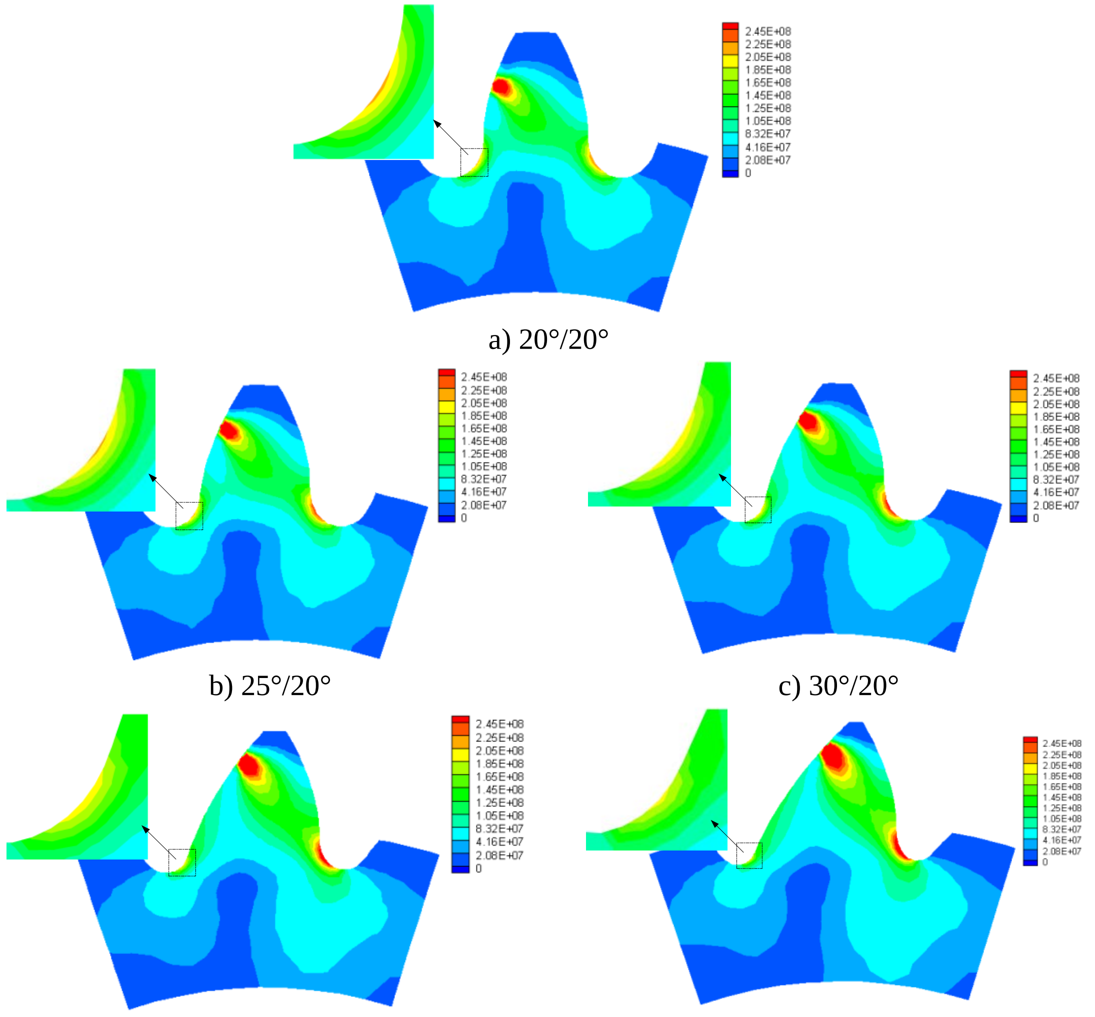

a) 20°/20°

b) 25°/20°

c) 30°/20°

d) 35°/20°

e) 40°/20°

Fig. 3.12 Von Mises stress contours from ES-FEM-T3 for the five asymmetric gear models with pressure angles of 20°/20°, 25°/20°, 30°/20°, 35°/20°, 40°/20°

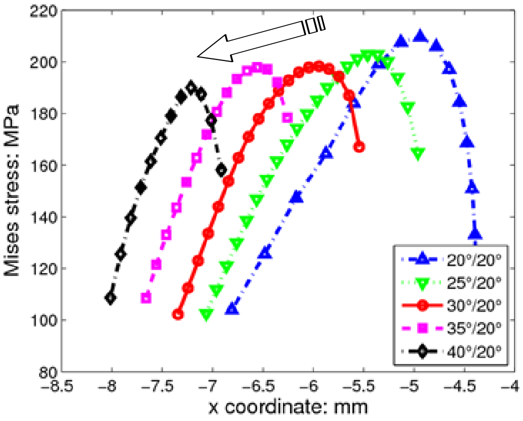

Fig. 3.13 Stress distributions at the fillet of the drive side of the five asymmetric gear models based on ES-FEM-T3

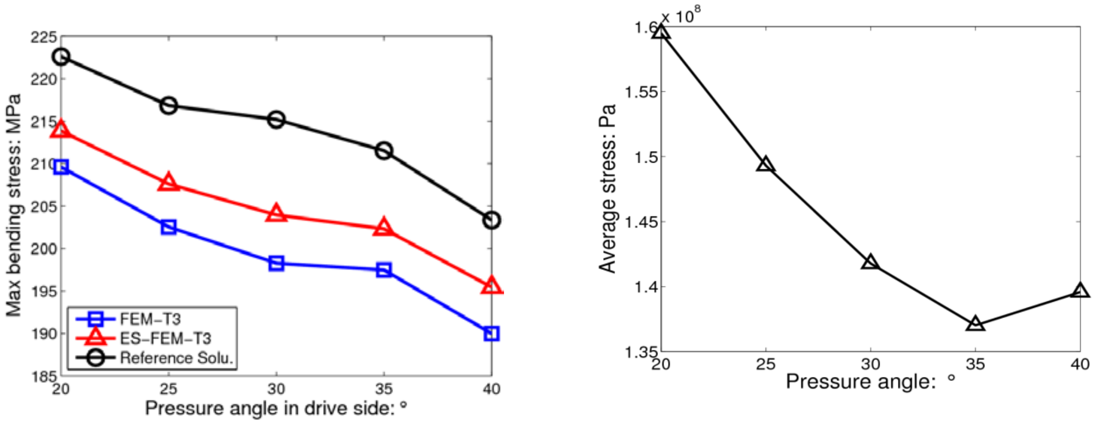

a) Trend of the maximum bending stress

b) Trend of the average bending stresses in the fillet region

Fig. 3.14 The bending stresses and their average with different pressure angles when the force is applied at *HPSTC*

From Fig. 3.14a it can be further seen that the maximum bending stress linearly decreases with the increase of the pressure angle and approximated by a straight line as

$$\sigma_{Max} = -0.877\alpha_d + 245.22 \tag{3.7}$$

where α_d is the pressure angle at the drive side; σ_{Max} is the maximum bending stress with the unit MPa. This equation gives the maximum bending stress as a function of the pressure angle for the asymmetric gear.

Fig. 3.14b gives a comparison of the average bending stresses in the fillet (total stress/length of the fillet). Different from the purely decreased trend of the maximum bending stresses, the averages stresses do not just decrease monotonically but have a minimum value at $\alpha_d = 35^\circ$. In this consideration, it seems that the pressure angle in the drive side should not be too larger. In order to select the most favorite pressure angle in the drive side, we shall consider another important indicator during the gear transmission: the contact ratio ε_d in the drive side. Theoretically, a larger contact ratio will give a smoother transmission with lower noise. From Fig. 3.11b it can be seen that with the increase of the pressure angles in the drive side, the top of the gear tooth becomes narrower thereby leading to a smaller contact ratio. This means that with the increase of the pressure angle in the drive side, on the one hand the bending strength of the gear tooth will be improved, on the other hand the contact ratio then becomes smaller leading to an unfavorable transmission condition with higher noise. Comprehensive consideration of the maximum stress, average stress and the contact ratio, we may proposed that the pressure angle of $\alpha_d = 35^\circ$ serves as the optimal choice for the drive side, resulting in a low maximum bending stress, the lowest average stress and a reasonable contact ratio.

3.1.4 Some remarks

ES-FEM-T3 possesses significant advantages than the standard FEM-T3 in solving the bending stresses of the gear tooth. Higher accuracy in stress field especially in the two most sensitive regions, e.g. the loading and stress concentration regions, is achieved by the ES-FEM-T3. Better convergence and higher convergence rate of the strain energy error are achieved by the ES-FEM-T3. After implementing the ES-FEM-T3 to determine an optimized asymmetric gear, it is found that the pressure angle of $\alpha_d = 35^\circ$ as applied in the drive side of the gear tooth allows performing best in terms of both the stress distributions in the fillet and the transmission ability. The ES-FEM-T3 is deemed well suited for the bending stress analysis of the gear tooth involving both stress concentration in the fillet and concentration load at the loading point. Some assumptions are made in the numerical calculations, e.g. the 2D simplification. This may lead to differences between the numerical and experimental results. Further to check whether the $\alpha_d = 35^\circ$ is the most suitable pressure angle for the drive side, other considerations like vibration analysis, thermal conduction analysis and the contact analysis have to be accounted for.

3.2 Explicit ES-FEM-T3 for 3D nonlinear membrane deflection analysis

In the previous section, the implicit ES-FEM-T3 has been successfully implemented in the 2D linear elastic analysis. In this section, the explicit ES-FEM-T3 is further proposed for solving the more challenging 3D nonlinear spatial membrane deflection problem. The implementation details of ES-FEM-T3 in the 3D nonlinear analysis are somewhat different from those in the 2D linear plane strain analysis; here, it involves large deflections and rotations in the 3D space and thus the gradient smoothing operation should be expressed in the 3D Cartesian coordinate system.

The study of membrane structure in this section has wide applications such as in the coverings in architecture, diaphragms in transducers, artificial arteries and organs in biomedical prosthesis, radio antennas and optical reflectors in airships [12, 13], due to its attractive properties of lightweight, flexibility and highly susceptible to the external action [14]. Various issues like excessive stretching, rupturing and tearing of the membrane structure may occur if excessive force is applied [15-18]. As such, accurate prediction of the membrane stretching becomes important to avoid its catastrophic failure.

Either the analytical or numerical model can be established to predict the ballooning shape of the stretched membrane structure. Through carefully examining a typical analytical (mechanical) model proposed by Shi *et al*. in [15] in Section 3.2.1, we hope to point out the main challenges in the analytical model and thus the motivation to employ numerical approach like ES-FEM-T3 to analyze and study the membrane deflections. As a continuous of the work in [19], the formulation of the explicit ES-FEM-T3 membrane model is summarized in Section 3.2.2. A verification of the proposed explicit ES-FEM-T3 membrane model is done in Section 3.2.3 in predicting the deflections of a square membrane. Results from the experiment, the analytical (mechanical) model in [15], the FEM-T3 membrane model and FEM-T3 shell model are also obtained for a thorough comparison in this section, so as to arrive at the superior performance of the ES-FEM-T3 membrane model for membrane deflection analysis. Two factors, i.e. the pressure fluctuations in the experiment and the boundary constraints in the numerical models, are checked to illustrate the slight differences observed between the numerical and experimental results.

3.2.1 Why to construct the numerical membrane model with ES-FEM-T3?

3.2.1.1 *Not easy to get analytical solutions*

Theoretically determining the ballooning shape (or deformation) of the membranes is usually very challenging. Analytical solutions are only available for homogeneous isotropic membrane with very simple geometrics and loading conditions, such as circular membrane under axisymmetric loading where the problem can degenerate as a one-dimensional (1D) problem [12]. In order to determine the ballooning shape of membrane with complex geometries, simplified models are often built [20-23]. Shi *et al*. built two mechanical models to estimate the deformations of the square membrane: one is the 2D model with the two opposite edges being continuously constrained [23] and the other is the 3D model with all the four vertexes being fully constrained [15]. In these two models, the deformed profile of the membrane was assumed to be governed by parabolic equations. The requirements of the force equilibrium, deformation compatibility and stress-strain relationship should be all satisfied during deriving the governing equations. Baskaran *et al*. [16] compared the predicted maximum deflections by this 2D model with experimental results and concluded that the 2D model always underestimates the maximum deflections. However, the 3D model has not been examined and verified as yet. As this 3D model is a typical one through literature reviews, it is used as a benchmark to assess the main difficulties for analytically predicting the membrane deflections, as can be seen in that the nonlinear terms present in the strains greatly affect the membrane deflections. It is these nonlinear terms preventing the analytical solving of the membrane deflections. Thus numerical analysis appears to be the only alternative.

The mechanical model built by Shi *et al.* [15] is used to estimate the deflections of a square membrane constrained by regularly spaced staples or cap nails under a static pressure, as shown in Fig. 3.15. The equation of estimating the deflections is derived as

$$\frac{l}{H}\left(m+\ln n\right)-\frac{pl^2\left[1-v\right]}{8HEh}-1=0 \tag{3.8}$$

where H is the maximum deflection of the membrane, i.e. deflection at the centre of the membrane; l is the edge length of the membrane; h is the thickness of the membrane; E and v are the Young’s modulus and Poisson’ ratio of the membrane, respectively; p is the static pressure; and m and n are the functions of H and l donated as

$$m=\frac{2H}{l}\sqrt{1+\frac{4H^2}{l^2}} \tag{3.9}$$

$$n=\frac{2H}{l}+\sqrt{1+\frac{4H^2}{l^2}} \tag{3.10}$$

Fig. 3.16a illustrates the experimental setup in [15], and Fig. 3.16b gives the simplified model of this experiment. The points E_1, E_2,… , E_8 and D_1, D_2,…, D_8 in Fig. 3.16b indicate the tested points in the experiment. A membrane named Tyvek^{TM} Homewrap with the dimension of 406mm×406mm is chosen in this experiment. The thickness of the membrane is h=0.16mm, and the material properties of the membrane are: Young's modulus E=875MPa and Poisson's ratio v=0.24. Four sets of static pressures, i.e. p=25Pa, 50Pa, 100Pa, 150Pa, are applied perpendicularly on the membrane. Both the maximum deflection H and the deflections along the diagonal and the edge are detected under these applied pressures.

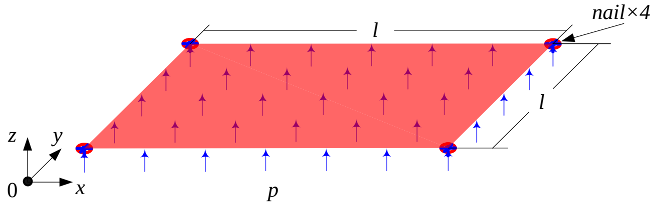

a) A membrane withstanding static pressure

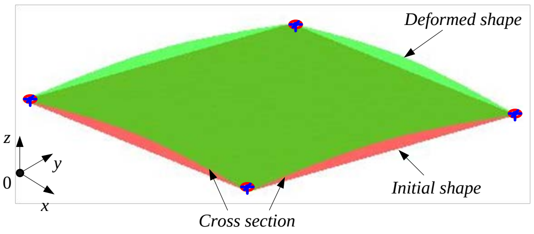

b) The initial and deformed shapes of the membrane

Fig. 3.15 A square membrane constraining the four vertexes subjects to static pressure

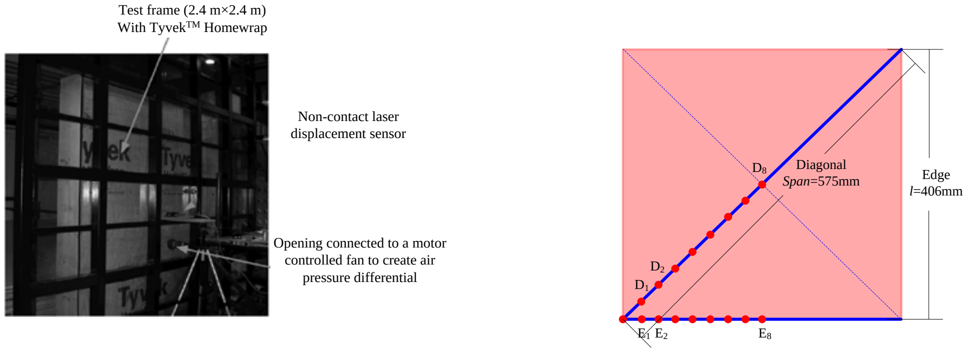

a) Experimental setup [15] b) Displacement measurement locations

Fig. 3.16 Experiment of the membrane deformation in the wall systems

A comparison of the maximum deflections from the experiment and the mechanical model under these four sets of pressures are listed in Table 3.4. And the comparisons of the deflections along the diagonal and the edge under a pressure of p=100Pa are presented in Table 3.5 and Table 3.6, respectively. Note that the notations of “Shi *et al.*” in these three tables indicate the results from the mechanical model of Eq. (3.8). Comparing the data listed in these three tables, it can be seen that although the mechanical model can give approximate solutions in relation to the experiment, significant differences still exist between the experimental and predicted deflections, especially for the maximum deflections under higher pressures (p=50Pa, 100Pa and 150Pa) in Table 3.4 and the deflections at the mid-portions of the diagonal and edge, i.e. D_5-D_8 and E_5-E_8 in Table 3.5 and Table 3.6, respectively. The deflections are always underestimated by the mechanical model, which is identical to the conclusions drawn from the 2D mechanical model [16, 23].

Table 3.4 Maximum deflections (H: mm) of the 3D ballooning membrane under four sets of pressures: p=25Pa, 50Pa, 100Pa and 150Pa

Pressure: Pa	H: experimental	H: Shi *et al.*
25	9.2	8.8
50	17.6	11.2
100	21.5	14.1
150	23.8	16.1

Table 3.5 Deflections (mm) of the 3D ballooning membrane along the diagonal under the pressure of p=100Pa

Point: D	1	2	3	4	5	6	7	8
Experimental	1.6	5.3	9.6	13.7	16.2	20.1	20.4	21.5
Shi *et al.*	3.3	6.2	8.6	10.6	12.1	13.2	13.9	14.1

Table 3.6 Deflections (mm) of the 3D ballooning membrane along the edge under the pressure of p=100Pa

Point: E	1	2	3	4	5	6	7	8
Experimental	0.9	3.6	4.1	6.5	9.3	10.4	11.1	11.7
Shi *et al.*	1.7	3.1	4.3	5.3	6.1	6.6	6.9	7.1

One possible reason that accounts for the large difference of the deflections observed between the experiment and the mechanical model could be attributed to the strain assumption made in the derivation of the differential equations in [15]. The deformation compatibility is required in the derivation of these differential equations, in which the strains along the diagonal were obtained as follows: selecting an arbitrary point *E* located at the diagonal, a line *EF* paralleling to the *x* axis in a non-deformed membrane was assumed to perpendicularly transfer to *E'F'* in the deformed membrane subject to a static pressure, as shown in Fig. 3.17a. Thus the strain at the point *E* along the *x*- and *y*-directions can be expressed, respectively, as

$$\varepsilon_x = \frac{\left|E^{'}F^{'}\right| - \left|EF\right|}{\left|EF\right|} = \sqrt{1+\left(\frac{\partial u_z}{\partial x}\right)^2} - 1 \tag{3.11}$$

$$\varepsilon_y = \frac{\left|E^{'}G^{'}\right| - \left|EG\right|}{\left|EG\right|} = \sqrt{1+\left(\frac{\partial u_z}{\partial y}\right)^2} - 1 \tag{3.12}$$

where u_z is the assumed deflection at that arbitrary point *E* in *z*-direction. The shear strain is equal to zero ($\varepsilon_{xy} = 0$) at that point because of the symmetric property of the deformed membrane.

It should be noted that the derivations of the strains above are based on the small deformation assumption. However, in the previous experiment the membrane can undergo large deformations with highly geometric nonlinearity under especially higher pressures, as shown in Fig. 3.17b. This would cause the arbitrary line *EF* no longer perpendicularly transfer to *E'F'*. The displacements of *E* in both *x*- and *y*-directions (u_x and u_y) are thus induced, as shown in Fig. 3.17c. In that case the nonlinear terms, which are functions of the spatial derivatives of u_x and u_y, should be added into the original strains, i.e. into Eq. (3.11) and Eq.(3.12), as follows

$$\varepsilon_x = \underbrace{\frac{\partial u_x}{\partial x}}_{term1} + \underbrace{\sqrt{1+\left(\frac{\partial u_z}{\partial x}\right)^2} - 1}_{term2} \tag{3.13}$$

$$\varepsilon_y = \underbrace{\frac{\partial u_y}{\partial y}}_{term1} + \underbrace{\sqrt{1+\left(\frac{\partial u_z}{\partial y}\right)^2} - 1}_{term2} \tag{3.14}$$

where the *term* 1 is the nonlinear term, and the *term* 2 is the strain of Eq. (3.11) or Eq.(3.12) called linear term here.

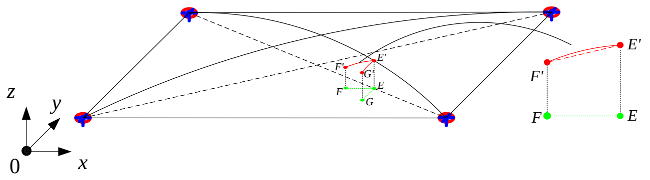

a) Illustration of the strain derivation in the mechanical model

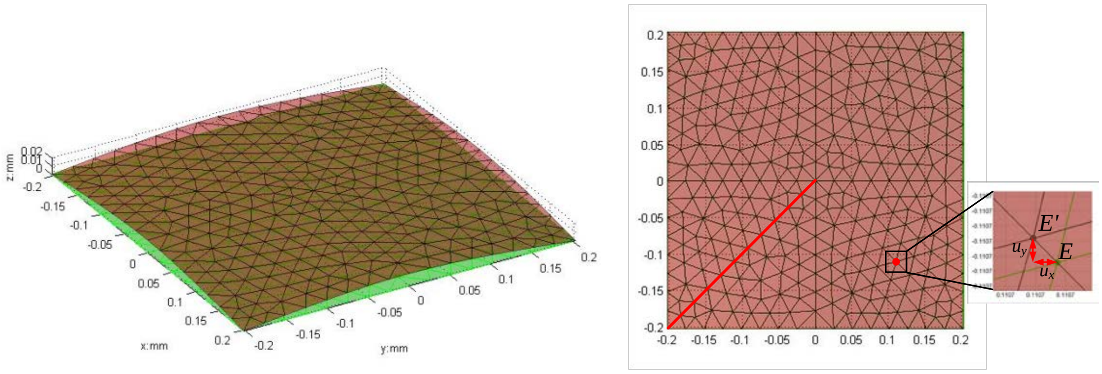

b) General profile of membrane undergoing a large deformation

c) Displacements at point E (u_x and u_y) in a large deformation configuration

Fig. 3.17 Illustration of the strain derivations in both linear and nonlinear forms

Taking ε_x as an example, the calculated linear and nonlinear strains along the diagonal are shown in Fig. 3.18, which are obtained base on Eq. (3.11) and Eq. (3.13) under the pressure of p=100Pa, respectively. From this figure it can be seen that there is a large difference between the linear strain and the nonlinear strain, which is apparently due to the adding of the nonlinear term (*term* 1). This is the possible reason for the underestimations of membrane deflections by the differential equations in [15]. If the strains of Eq. (3.11) and Eq. (3.13) are replaced by the strains of Eq. (3.12) and Eq. (3.14), the newly predicted membrane deflections by the mechanical model should be much closer to the experimental results, and thus the underestimations of the deflections can then be avoided. However, the effects of the nonlinear strains should be verified.

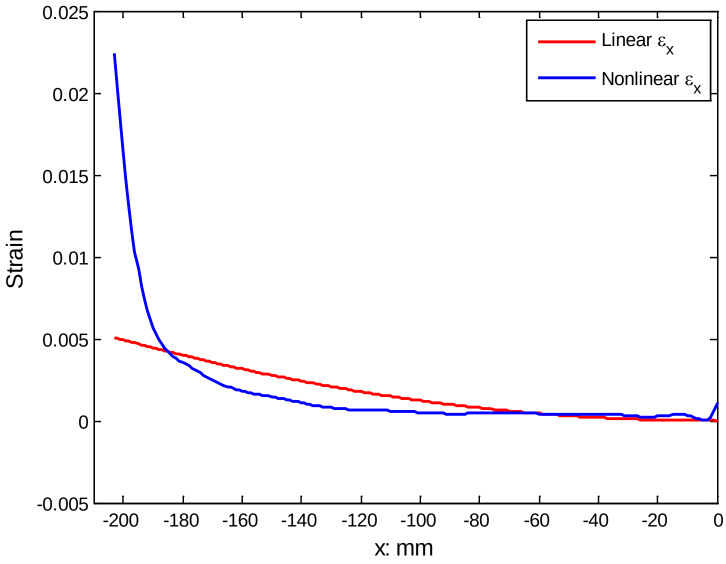

Fig. 3.18 Comparisons of the linear and nonlinear strains under the pressure of *p*=100MPa

In the calculation of the nonlinear strain ε_x, one major problem is encountered, i.e. how to theoretically express u_x. The *term* 2 in the nonlinear strain can be obtained easily, however, the *term* 1 cannot be obtained so easy because of the unknown u_x which is a function of geometry, material properties of the membrane and the external applied pressures, etc. In the calculation of the nonlinear strain ε_x above, the distribution of u_x can be obtained through a more convenient way, i.e. numerical simulation:

i) Get the u_x at the discrete points along the diagonal numerically

ii) Interpolate these discrete displacements using polynomials, as shown in Fig. 3.19

iii) Substitute the approximate u_x into Eq. (3.13) to get the nonlinear strain

However, the order of the approximating polynomial function of u_x is up to 10, which may cause difficulties to be theoretically analyzed. As such, the numerical simulation which deals with the nonlinear term much easier appears better suited to simulate the large deformation of the membrane.

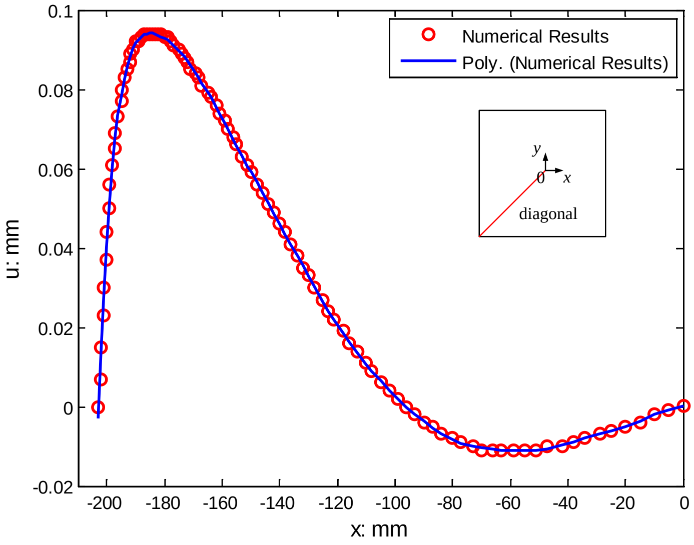

Fig. 3.19 Numerical results for displacement u_x and their approximations by polynomial along the diagonal

3.2.1.2 *ES-FEM-T3 superior to FEM-T3 for membrane deflection analysis*

The standard FEM is frequently used to determine the ballooning shapes of these deformed membranes. We has already shown that the standard FEM-T3 can give rise to “over-stiff” numerical model and lead to poor accuracy in the stress field. Comparatively, the ES-FEM-T3 was found particularly superior in convergence, accuracy, computational efficiency and stability using the same mesh. In this study, the ES-FEM-T3 is employed for the numerical simulation of the membrane deformation, in which the displacement gradient is smoothed using edge-based smoothing domains in 3D global Cartesian coordinate system, and the explicit time integration and Dynamic Relaxation Method (DRM) are used to obtain the steady-state solutions of the membrane structure. The novel ES-FEM-T3 membrane model was firstly proposed by Zhang *et al*. in [19]. As a continuation of this work, the ES-FEM-T3 membrane model is further explored here to check its properties, and especially on solving the practical membrane deformation problem in engineering. A summary of the formulation procedure for the ES-FEM-T3 membrane model is presented in next section for its implementation in Section 3.2.3.

3.2.2 Formulation of explicit ES-FEM-T3 membrane model

3.2.2.1 *Co-rotational local coordinate system*

A membrane element can be seen to degenerate from a flat shell element based on the Mindlin-Reissner assumption [24, 25], which is actually its membrane part without bending stiffness. The external forces (mainly the pressures) are undertaken by the membrane structure via its in-plane stretches and out of plane rotations [18].

Because of the lack of bending stiffness, the displacements throughout the thickness of the membrane are the same and thus the thickness *h* of the membrane is constant in the whole deformation process. In this case, the deformations of the membrane structure can be described with only the deformations of a plane, e.g. the mid-plane, paralleling to the membrane surface. And the elemental stress in the plane can be seen as a state of plane stress [18]. However, different from the "real" plane stress problem where the deformation occurs in the 2D space, the deformation of the mid-plane of the membrane occurs in the 3D space where the nodal displacement in this plane has three degree of freedoms.

If we discretize the mid-plane of the membrane with a set of triangular mesh, as shown in Fig. 3.20, the smoothed gradient of the displacement vector **u** in the 3D space (global Cartesian coordinate system) can be approximated with the ES-FEM-T3 according to Eqs. (2.5) and (2.7) proposed in Chapter 2 as

$$\nabla \mathbf{u}\left(\mathbf{x}_k\right) \approx \frac{1}{A_k^{\mathrm{sd}}} \int_{\Gamma_k^{\mathrm{sd}}} \mathbf{u}\left(\mathbf{x}\right)\mathbf{n}\,\mathrm{d}\Gamma \approx \frac{1}{A_k^{\mathrm{sd}}} \sum_{m=1}^{N_{seg}} \left[\sum_{n=1}^{N_{gau}} w_{mn}\mathbf{u}\left(\mathbf{x}_{mn}\right)\mathbf{n}\left(\mathbf{x}_{mn}\right) \right] \tag{3.15}$$

or

$$\bar{u}_{i,j}\left(\mathbf{x}_k\right) \approx \frac{1}{A_k^{\mathrm{sd}}}\int_{\Gamma_k^{\mathrm{sd}}} u_i\left(\mathbf{x}\right) n_j \mathrm{d}\Gamma \approx \frac{1}{A_k^{\mathrm{sd}}}\sum_{m=1}^{N_{seg}}\left[\sum_{n=1}^{N_{gau}} w_{mn}\bar{u}_i\left(\mathbf{x}_{mn}\right) n_j\left(\mathbf{x}_{mn}\right)\right],\quad i,j = x,y,z\,.$$

The physical meanings of the parameters in Eq. (3.15) are exactly the same as those described in Eqs. (2.5) and (2.7). $\mathbf{u}\left(\mathbf{x}_{mn}\right)$ is the displacement vector at point $\mathbf{x}_{mn}$ that can be interpolated using the simplest linear shape function $\mathbf{N}_I(\mathbf{x})$ of the standard T3 element as

$$\mathbf{u}\left(\mathbf{x}_{mn}\right) = \sum_{I\in S_k^{\mathrm{sd}}} \mathbf{N}_I\left(\mathbf{x}_{mn}\right)\mathbf{u}_I$$

or (3.16)

$$u_i\left(\mathbf{x}_{mn}\right) = \sum_{I\in S_k^{\mathrm{sd}}} N_I\left(\mathbf{x}_{mn}\right)u_{Ii},\quad i=x,y,z$$

Here, S_k^{sd} is the group of nodes supporting the smoothing domain Ω_k^{sd}, the same as that in Eq. (2.12); and $\mathbf{u}_I$ is the displacement vector at the node.

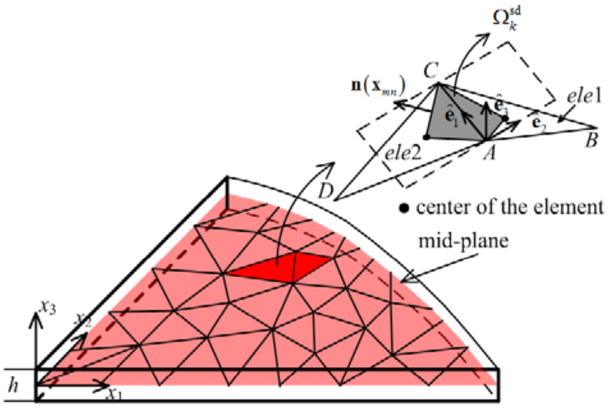

Fig. 3.20 Description of edge-based smoothing domain for 3-node spatial triangular membrane element degenerated from solid prism element and highlight of an edge-based surface smoothing domain for an edge of a linear triangular mesh, and the embedded local co-rotational coordinate system

By substituting Eq. (3.16) back into Eq. (3.15), this leads to the formulation of the smoothed gradient of displacement field in a smoothing domain in the mid-plane as

$$\nabla\mathbf{u}\left(\mathbf{x}_k\right) \approx \sum_{I\in S_k^{\mathrm{sd}}}\left(\frac{1}{A_k^{\mathrm{sd}}}\int_{\Gamma_k^{\mathrm{sd}}}\mathbf{N}_I\left(\mathbf{x}\right)\mathbf{n}\mathrm{d}\Gamma\mathbf{u}_I\right) = \sum_{I\in S_k^{\mathrm{sd}}}\nabla\bar{\mathbf{N}}_I\left(\mathbf{x}\right)\mathbf{u}_I \qquad (3.17)$$

or

$$u_{i,j}\left(\mathbf{x}_k\right) \approx \sum_{I\in S_k^{\mathrm{sd}}} \left(\frac{1}{A_k^{\mathrm{sd}}} \int_{\Gamma_k^{\mathrm{sd}}} N_I\left(\mathbf{x}\right)\mathbf{n}\mathrm{d}\Gamma u_{Ii} \right) = \sum_{I\in S_k^{\mathrm{sd}}} \bar{\mathbf{N}}_{I,j}\left(\mathbf{x}\right) u_{Ii}, \quad i,j = x,y,z$$

where $\nabla\bar{\mathbf{N}}_I$ is the smoothed derivatives of the shape function in global coordinate.

It should be noted that the nodal displacement vector $\mathbf{u}_I$ in Eq. (3.17) includes components of both rigid body motions (i.e. translations and rotations) and in-plane stretches in the 3D space. As the rigid body motions have no contribution to the strain and stress states, they should be eliminated from the displacement vector $\mathbf{u}_I$ so that the remaining part (denoted as $\hat{\mathbf{u}}_I$) can be directly used for calculating the smoothed strains, the smoothed stresses and finally the smoothed internal nodal forces to balance the equilibrium equations.

In order to achieve this elimination, the local co-rotational coordinate systems attached to each smoothing domain need be predefined. And the corresponding transformation matrix **T** associates with these local co-rotational coordinate systems need be constructed. By using this transformation matrix **T**, any field variables (not limited to the displacement vector $\mathbf{u}_I$) can be transformed from the global to the local co-rotational coordinate systems, so that the smoothed strain and stress can be properly evaluated in this local co-rotational coordinate system with $\hat{\mathbf{u}}_I$.

As illustrated in Fig. 3.20, for an inner smoothing domain Ω_k^{sd} with two neighboring membrane elements, i.e. element *ele*1 and *ele*2 sharing a common edge *k*, its basis orientation vectors of local co-rotational coordinates $\hat{\mathbf{x}} = \left\{\hat{x}, \hat{y}, \hat{z}\right\}^{\mathrm{T}}$ are

$$\hat{\mathbf{e}}_1 = \frac{\mathbf{x}_C - \mathbf{x}_A}{\left\|\mathbf{x}_C - \mathbf{x}_A\right\|}\ , \hat{\mathbf{e}}_2 = \mathbf{n}_k^s / \left\|\mathbf{n}_k^s\right\|\ ,\ \hat{\mathbf{e}}_3 = \frac{\hat{\mathbf{e}}_1 \times \hat{\mathbf{e}}_2}{\left\|\hat{\mathbf{e}}_1 \times \hat{\mathbf{e}}_2\right\|} \tag{3.18}$$

where $\mathbf{x}_I$ (I=A, B, C, D) is to the global Cartesian coordinates of the four nodes supporting Ω_k^{sd}, in which $\mathbf{x}_A$ is set as the origin of this local co-rotational coordinate system; and $\mathbf{n}_k^{\mathrm{sd}}$ denotes the smoothed (averaged) normal vector of the normal vectors of the two neighboring elements, i.e.

$$\mathbf{n}_k^{\mathrm{sd}} = \left[Area\left(ele1\right)\mathbf{n}^{ele1} + Area\left(ele2\right)\mathbf{n}^{ele2} \right] / \left[Area\left(ele1\right) + Area\left(ele2\right) \right] \quad (3.19)$$

in which $\mathbf{n}^{ele1}$ and $\mathbf{n}^{ele2}$ denote the outward surface normal vectors of the T3 membrane element *ele*1 and *ele*2, respectively; and *Area*(*ele*1) and *Area*(*ele*2) denote the areas of the membrane element *ele*1 and *ele*2, respectively.

The transformation matrix **T** can thus be constructed with the basis orientation vectors as

$$\mathbf{T} = \left\{ \hat{\mathbf{e}}_1, \hat{\mathbf{e}}_2, \hat{\mathbf{e}}_3 \right\} . \quad (3.20)$$

With the help of the transformation matrix **T**, the global displacement vector $\mathbf{u}_I$ can be transformed from the global to the local coordinate system as

$$\hat{\mathbf{u}}_I = \mathbf{T}\mathbf{u}_I . \quad (3.21)$$

After substituting Eq. (3.21) into Eq. (3.17), the smoothed gradient of the displacement field with ES-FEM-T3 in the local co-rotational coordinate system can be finally obtained. This smoothed gradient will be used to calculate the smoothed internal nodal force $\bar{\hat{\mathbf{f}}}_I^{int}$ in the local coordinate system. Then the $\bar{\hat{\mathbf{f}}}_I^{int}$ is transformed back into the global coordinate system for the force assembly. Details on constructing $\bar{\hat{\mathbf{f}}}_I^{int}$ can be found in the next section.

3.2.2.2 *Formulation of membrane with explicit ES-FEM-T3*

In solving a membrane problem, its static state should be purchased. However, the static solutions of membrane deformation cannot be gotten straightforward due to the impending rigid body motions which leads to the stiffness matrix ill conditioned or singular [18]. Therefore, the dynamic relaxation technique is adopted [18, 26]. In this technique a pseudo damping force with a positive damping coefficient is added into the motion equation resulting in the dissipation of kinetic energy. In the end one can obtain the steady state of the deformed membrane and examine the displacement and strain energy with the admissible minimum influences of the transient response [19]. Similar to the motion equation proposed in Eq. (2.17), the discrete governing equation of the membrane deformation with dynamic relaxation technique can be written as

$$\tilde{\mathbf{M}}\ddot{\mathbf{u}} = \tilde{\mathbf{f}}^{ext} - \bar{\mathbf{f}}^{int} - \tilde{\mathbf{f}}^{damp} \tag{3.22}$$

in which all the variable are evaluated in the global Cartesian coordinate.

Either the implicit (e.g the Newmark β-method) or explicit methods (e.g. the central difference method) can be used for the time integration of Eq. (3.22). Here, we choose the central difference explicit time integration method because of its attractive feature of avoiding solving large-scale equations [24].

In the explicit time integration implementation, the time of simulation $0 \le t \le t^E$ is subdivided into a series of time steps Δt^n, n=1 *to* n_{TS} where n_{TS} is the total number of time steps. Accordingly, Eq. (3.22) at time step n can be expressed as

$$\tilde{\mathbf{M}}\,{}^{n}\ddot{\mathbf{u}} = {}^{n}\tilde{\mathbf{f}}^{ext}\left({}^{n}\mathbf{u}\right) - {}^{n}\bar{\mathbf{f}}^{int}\left({}^{n}\mathbf{u}\right) - {}^{n}\tilde{\mathbf{f}}^{damp}\left({}^{n}\dot{\mathbf{u}}\right) \tag{3.23}$$

where $\tilde{\mathbf{M}}$ is the lumped mass matrix that only need to be evaluated once at the initial time t=0; ${}^{n}\ddot{\mathbf{u}}$, ${}^{n}\tilde{\mathbf{f}}^{ext}$ and ${}^{n}\bar{\mathbf{f}}^{int}$ are the acceleration, external force and smoothed internal force vectors, respectively, at time step t^n; and ${}^{n}\tilde{\mathbf{f}}^{damp}$ is the damping force vector evaluated as [18]

$${}^{n}\tilde{\mathbf{f}}^{damp} = \mu\mathbf{M}\,{}^{n}\dot{\mathbf{u}} \tag{3.24}$$

where μ is the damping coefficient and ${}^{n}\dot{\mathbf{u}}$ is the velocity vector at time step t^n.

In our ES-FEM-T3 membrane model, both the mass matrix $\tilde{\mathbf{M}}$ and external force vector ${}^{n}\tilde{\mathbf{f}}^{ext}$ are evaluated by the same way as in the standard FEM-T3. Only the smoothed internal force vector ${}^{n}\bar{\mathbf{f}}^{int}$ is evaluated with the ES-FEM-T3 over the edge-based smoothing domains. In other words, the ES-FEM-T3 membrane model only modifies the formulation of internal force vector, which concurs with the statement that "*the S-FEM models change only the stiffness matrix.*" in Chapter 2. Thus the formulation of the smoothed internal force vector ${}^{n}\bar{\mathbf{f}}^{int}$ with ES-FEM-T3 only be detailed here.

1) *Constructing the smoothed nodal force in local coordinates with ES-FEM-T3*

In the explicit time integration process, the membrane deformation is assumed to undergo a series of spatial configurations. The kinetic relationships should be satisfied in each spatial configuration, and the kinematic relationships are described with the total Lagrangian (TL) formulation [24] which uses only the initial configuration as the reference configuration. Accordingly, a kinematic description of the ES-FEM-T3 membrane model is illustrated in Fig. 3.21.

At the initial configuration (time t=0), the smoothing domain is denoted by ${}^{0}\Omega_{k}^{\mathrm{sd}}$ in which the left superscript denotes the time step. The coordinates of its four supporting nodes are denotes by $\hat{\mathbf{X}}_I$ (e.g. $I \in S_k^{\mathrm{sd}} = \{A, B, C, D\}$ as in Fig. 3.20) in the local coordinates and $\mathbf{X}_I$ in global coordinates. The basis vectors ${}^{0}\hat{\mathbf{e}}_i, i = 1, 2, 3$ of this local coordinate system are determined by substituting $\hat{\mathbf{X}}_I$ into Eq. (3.18). Through the motion $\mathbf{x} = f\left(\mathbf{X}, t\right)$ the membrane is transformed from the initial configuration ${}^{0}\Omega$ to the current configuration ${}^{n}\Omega$ at time t^n. Consequently, ${}^{0}\Omega_{k}^{\mathrm{sd}}$ is transformed to

$^{n}\Omega_k^{\text{sd}}$. The coordinates of the nodes supporting $^{n}\Omega_k^{\text{sd}}$ are denotes as $\hat{\mathbf{x}}_I$ in the local coordinates and $\mathbf{x}_I$ in global coordinates. The basis vectors $^{n}\hat{\mathbf{e}}_i$, $i=1,2,3$ at time t^n are determined by substituting $\hat{\mathbf{x}}_I$ into Eq. (3.18). It should be noted that when $t^{n=1}$ =0, $\hat{\mathbf{X}}_I=\hat{\mathbf{x}}_I$ and $\mathbf{X}_I=\mathbf{x}_I$.

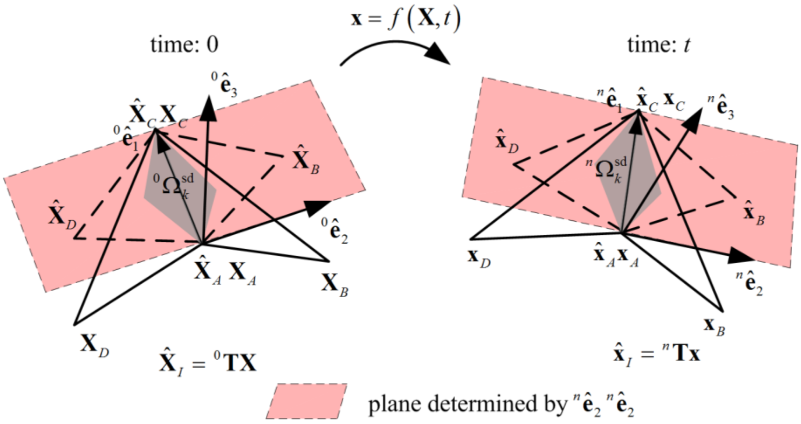

Fig. 3.21 The kinematics of the ES-FEM-T3 model for spatial membrane structures in the total Lagrangian formulation

The transformation matrices $^{0}\mathbf{T}$ and $^{n}\mathbf{T}$ corresponding to time t=0 and t=t^n can be obtained with $^{0}\hat{\mathbf{e}}_i$ and $^{n}\hat{\mathbf{e}}_i$, respectively, according to Eq. (3.20). With the help of these two transformation matrices, coordinates between global and local systems at any time can be calculated as

$$\hat{\mathbf{X}}_I={}^{0}\mathbf{T}\left(\mathbf{X}_k\right)\cdot\mathbf{X}_I \tag{3.25}$$

$$\hat{\mathbf{x}}_I={}^{n}\mathbf{T}\left(\mathbf{x}_k\right)\cdot\mathbf{x}_I\,. \tag{3.26}$$

By using these two equations, the rigid body motions (rotations) part of the nodal displacement is eliminated, as illustrated in Fig. 3.22. The resultant in-plane nodal displacements can then be obtained in the local coordinate system as

$${}_{0}^{n}\hat{u}_{Ii}=\hat{x}_{Ii}-\hat{X}_{Ii}\quad\left(I\in S_k^{\text{sd}};\,i=1,2\right) \tag{3.27}$$

where the left subscript in ${}_{0}^{n}\hat{u}_{Ii}$ denotes the time for the reference configuration, i.e. the displacement is measured at time t with respect to the reference configuration at time 0 (initial configuration). Note that in the TL formulation all the parameters are measured referring to the reference configuration, hence the left subscript “0” in these parameters will be omitted below for the sake of simplification. For example, ${}_0^n\hat{u}_{Ii}$ is written as ${}^n\hat{u}_{Ii}$.

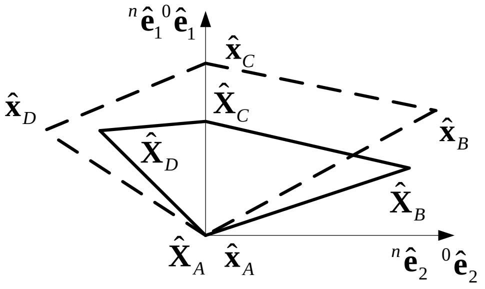

Fig. 3.22 In-plane deformation in the local coordinate plane $\hat{X}_1\hat{X}_2$ after coordinate transformation

By using the displacement vector ${}^n\hat{u}_{Ii}$, the in-plane smooth deformation gradient ${}^n\bar{\hat{\mathbf{F}}}\left(\mathbf{X}_k\right)$ is computed so as to measure the in-plane strain ${}^n\bar{\hat{\mathbf{E}}}$, as

$$ {}^n\bar{\hat{F}}_{ij}\left(\mathbf{X}_k\right) = {}^n\hat{u}_{i,j}\left(\mathbf{X}_k\right)+\delta_{ij} = \sum_{I\in S_k^{\mathrm{sd}}} {}^0\bar{\hat{N}}_{I,j}\left(\mathbf{X}_k\right){}^n\hat{u}_{Ii}+\delta_{ij}, \quad i, j = x, y \tag{3.28}$$

where ${}^0\bar{\hat{N}}_{I,j}$ are the smoothed derivatives of the smoothed function in ${}^0\Omega_L^{\mathrm{sd}}$.

The smoothed Green-Lagrangian membrane strain ${}^n\bar{\hat{\mathbf{E}}}$ in the local coordinates system can then be calculated as

$$ {}^n\bar{\mathbf{E}}_k = \frac{1}{2}\left({}^n\bar{\mathbf{F}}^{\mathrm{T}}\,{}^n\bar{\mathbf{F}}-\mathbf{I}\right). \tag{3.29}$$

For most of the nonlinear elastic materials, the second Piola-Kirchhoff (PK2) membrane stress ${}^n\bar{\hat{\mathbf{S}}}_k$ in local coordinates can be expressed as the function of smoothed Green-Lagrangian membrane strain ${}^n\bar{\hat{\mathbf{E}}}_k$ as

$$ {}^n\bar{\hat{\mathbf{S}}}_k = \mathbf{D}\,{}^n\bar{\hat{\mathbf{E}}}_k \tag{3.30}$$

where **D** is the material response tensor of the isotropic St. Venant-Kirchhoff material under the plane stress condition.

Using the smoothed strain and stress tensors of Eqs. (3.29) and (3.30), the smoothed internal force vector ${}^{n}\bar{\hat{\mathbf{f}}}_{k}^{int}$ corresponding to the k^{th} smoothing domain ${}^{n}\Omega_{k}^{\mathrm{sd}}$ in local co-rotational coordinates can be calculated as

$$ {}^{n}\bar{\hat{\mathbf{f}}}_{k}^{int} = \left[{}^{n}\bar{\hat{\mathbf{B}}}_{k} \right]^{\mathrm{T}} \left\{ {}^{n}\bar{\hat{\mathbf{S}}}_{k} \right\} {}^{0}A_{k}^{\mathrm{sd}} \tag{3.31} $$

where $\left[{}^{n}\bar{\hat{\mathbf{B}}}_{k} \right]$ is the smoothed strain-displacement matrix associated with the smoothing domain ${}^{n}\Omega_{k}^{\mathrm{sd}}$; and $\left\{ {}^{n}\bar{\hat{\mathbf{S}}}_{k} \right\}$ is the smoothed PK2 stress vector of the smoothing domain ${}^{n}\Omega_{k}^{\mathrm{sd}}$. Assuming the indices of the supporting nodes of the smoothing domain Ω_{k}^{sd} are *I*=*A*, *B*, *C*, *D* as illustrated in Fig. 3.20, the matrices and vectors in Eq. (3.31) are

$$ \left[{}^{n}\bar{\hat{\mathbf{B}}}_{k} \right] = \left[{}^{n}\bar{\hat{\mathbf{B}}}_{A}(\mathbf{X}) \;\vdots\; {}^{n}\bar{\hat{\mathbf{B}}}_{B}(\mathbf{X}) \;\vdots\; {}^{n}\bar{\hat{\mathbf{B}}}_{C}(\mathbf{X}) \;\vdots\; {}^{n}\bar{\hat{\mathbf{B}}}_{D}(\mathbf{X}) \right] \tag{3.32} $$

$$ \left[{}^{n}\bar{\hat{\mathbf{B}}}_{I}(\mathbf{X}) \right] = \begin{bmatrix} {}^{0}\bar{\hat{N}}_{I,1} & 0 \\ 0 & {}^{0}\bar{\hat{N}}_{I,2} \\ {}^{0}\bar{\hat{N}}_{I,2} & {}^{0}\bar{\hat{N}}_{I,1} \end{bmatrix} + \begin{bmatrix} {}^{n}\bar{\hat{u}}_{1,1}\,{}^{0}\bar{\hat{N}}_{I,1} & {}^{n}\bar{\hat{u}}_{2,1}\,{}^{0}\bar{\hat{N}}_{I,1} \\ {}^{n}\bar{\hat{u}}_{1,2}\,{}^{0}\bar{\hat{N}}_{I,2} & {}^{n}\bar{\hat{u}}_{2,2}\,{}^{0}\bar{\hat{N}}_{I,2} \\ {}^{n}A_{I1} & {}^{n}A_{I2} \end{bmatrix} \tag{3.33} $$

$$ {}^{n}A_{Ii} = {}^{n}\bar{\hat{u}}_{i,1}\,{}^{0}\bar{\hat{N}}_{I,2} + {}^{n}\bar{\hat{u}}_{i,2}\,{}^{0}\bar{\hat{N}}_{I,1}, \quad i\text{=}1,2 \tag{3.34} $$

$$ \left\{ {}^{n}\bar{\hat{\mathbf{S}}}_{k} \right\} = \left\{ {}^{n}\bar{\hat{S}}_{k11} \quad {}^{n}\bar{\hat{S}}_{k22} \quad {}^{n}\bar{\hat{S}}_{k12} \right\} \tag{3.35} $$

$$ {}^{n}\bar{\hat{\mathbf{f}}}_{k}^{int} = \left[{}^{n}\bar{\hat{f}}_{A1}^{int} \quad {}^{n}\bar{\hat{f}}_{A2}^{int} \;\vdots\; {}^{n}\bar{\hat{f}}_{B1}^{int} \quad {}^{n}\bar{\hat{f}}_{B2}^{int} \;\vdots\; {}^{n}\bar{\hat{f}}_{C1}^{int} \quad {}^{n}\bar{\hat{f}}_{C2}^{int} \;\vdots\; {}^{n}\bar{\hat{f}}_{D1}^{int} \quad {}^{n}\bar{\hat{f}}_{D2}^{int} \right]^{\mathrm{T}}. \tag{3.36} $$

It should be noted that the edge-based smoothing domain located at the boundary of the solution domain only has three supporting nodes. Hence, the size of the above equations will be correspondingly reduced.

2) *Transforming the smoothed nodal force from local to global coordinates*

By using coordinate transformation, the smoothed internal force vector in global Cartesian coordinates can be transformed back as

$$ {}^{n}\bar{\mathbf{f}}^{int} = \sum_{i=1}^{N_{sd}} \left[{}^{n}\mathbf{T}\left(\mathbf{X}\right) \right]^{\mathrm{T}} \, {}^{n}\hat{\bar{\mathbf{f}}}_{k}^{int} \, . \tag{3.37} $$

After substituting Eq. (3.37) in Eq. (3.23), the discrete dynamic equations governing the membrane deformations can be finally gotten. In order to find the unique solution of Eq. (3.23), boundary conditions, i.e.

$$ g_{ibc}\left({}^{n}\dot{\mathbf{u}} \right) = 0 \; , \; ibc = 1 \text{ to } n_{bc} \tag{3.38} $$

should be subjected, in which $g_{ibc}\left({}^{n}\dot{\mathbf{u}} \right) = 0$ is the velocity boundary conditions at time *t*, and n_{bc} is the number of the boundary conditions.

Detailed procedures to solve the equation of motion using dynamic relaxation method based on the central difference explicit time integration algorithm are summaried in the flowing flowchart.

Flowchart for explicit time integration of the membrane deformation problem

(1) Construct the edge-based smoothing domains ${}^{0}\Omega_{k}^{\mathrm{sd}}$, $k=1,\cdots,N_{sd}$
(2) Initial conditions and initialization of parameters
  (2.1) Set initial conditions ${}^{0}\hat{\bar{\mathbf{S}}}_{k}$, ${}^{0}\dot{\bar{\mathbf{u}}}$, ${}^{0}\bar{\mathbf{u}} = \mathbf{0}$, t=0 and the counter n=0
  (2.2) Loop over all smoothing domains ${}^{0}\Omega_{k}^{\mathrm{sd}}$ to compute the transformation matrices ${}^{0}\mathbf{T}\left(\mathbf{X}_{I}\right)$, the local material coordinates $\hat{\mathbf{X}}_{I} = {}^{0}\mathbf{T}\left(\mathbf{X}_{I}\right)\cdot\mathbf{X}_{I}$ for all supporting nodes of the k^{th} smoothing domain and the smoothed derivatives of the shape function ${}^{0}\hat{\bar{N}}_{I,i} = {}^{0}\mathbf{T}\left(\mathbf{X}_{I}\right)\cdot {}^{0}\bar{N}_{I,i}\left(\mathbf{X}_{I}\right)$
  (2.3) Compute the lumped mass matrix $\tilde{\mathbf{M}}$
  (2.4) Call subroutine *Cal_Internal_Force* to compute the global nodal force vector ${}^{0}\mathbf{f}$ where ${}^{0}\mathbf{f} = {}^{0}\tilde{\mathbf{f}}^{ext} - {}^{0}\bar{\mathbf{f}}^{int} - {}^{0}\tilde{\mathbf{f}}^{damp}$
  (2.5) Compute the accelerations ${}^{0}\ddot{\mathbf{u}} = \tilde{\mathbf{M}}^{-1}\,{}^{0}\mathbf{f}$
(3) Time update $t^{n+1} = t^{n} + \Delta t$, $t^{n+1/2} = \left(t^{n} + t^{n+1}\right)\big/2$
(4) First partial update nodal velocities ${}^{n+1/2}\dot{\mathbf{u}} = {}^{n}\dot{\mathbf{u}} + \Delta t \cdot {}^{n}\ddot{\mathbf{u}}\big/2$
(5) Enforce velocity boundary conditions $g_{ibc}\left({}^{n+1/2}\dot{\mathbf{u}} \right) = 0$, $ibc = 1 \text{ to } n_{bc}$

```
(6)  Update the nodal displacements ${}^{n+1}\mathbf{u} = {}^{n}\mathbf{u} + \Delta t \cdot {}^{n+1/2}\dot{\mathbf{u}}$
(7)  Call subroutine Cal_Internal_Force to compute the internal force vector ${}^{n+1}\mathbf{f}$ using the nodal displacements
(8)  Compute nodal accelerations ${}^{n+1}\ddot{\mathbf{u}} = \mathbf{M}^{-1} \cdot {}^{n+1}\mathbf{f}$
(9)  Second partial update nodal velocities ${}^{n+1}\dot{\mathbf{u}} = {}^{n+1/2}\dot{\mathbf{u}} + \Delta t \cdot {}^{n+1}\ddot{\mathbf{u}} / 2$
(10) Check convergence according to Eq. (3.39). If these conditions are satisfied, the steady solution is obtained. If NOT, update the counter $n \leftarrow n+1$ and go to Step (3).

Subroutine Cal_Internal_Force

(S.1) Initialization ${}^{0}\mathbf{f}$ , $\Delta t_{crit} = \infty$
(S.2) Compute the global external nodal force ${}^{n}\tilde{\mathbf{f}}^{ext}$ and pseudo damping force ${}^{n}\tilde{\mathbf{f}}^{damp}$
(S.3) Loop all smoothing domains ${}^{n}\Omega_k^{\mathrm{sd}}$ , $k = 1, \cdots, N_{sd}$
      i)    Get the current nodal coordinates $\mathbf{x}_I = \mathbf{X}_I + {}^{n}\mathbf{u}_I$ for all supporting nodes
      ii)   Compute ${}^{n}\hat{\mathbf{e}}_k$ of the local spatial coordinate systems
      iii)  Compute coordinate transformation matrix ${}^{n}\mathbf{T}(\mathbf{x}_I)$
      iv)   Compute $\hat{\mathbf{x}}_I = {}^{n}\mathbf{T}(\mathbf{x}_I) \cdot \mathbf{x}_I$ for all supporting nodes
      v)    Compute ${}^{n}\hat{\mathbf{u}}_I = \hat{\mathbf{x}}_I - \hat{\mathbf{X}}_I$
      vi)   Compute the smoothed PK2 stresses $\left\{ {}^{n}\hat{\bar{\mathbf{S}}}_k^{\mathrm{sd}} \right\}$
      vii)  Compute ${}^{n}\bar{\mathbf{f}}_k^{int}$ according to Eq. (3.31)
      viii) Scatter ${}^{n}\bar{\mathbf{f}}_k^{int}$ to the global ${}^{n}\bar{\mathbf{f}}^{int}$ according to Eq. (3.37)
      ix)   ${}^{n}\mathbf{f} = {}^{n}\tilde{\mathbf{f}}^{ext} - {}^{n}\bar{\mathbf{f}}^{int} - {}^{n}\tilde{\mathbf{f}}^{damp}$
      x)    Compute $\Delta t_{crit}^{\mathrm{sd}}$, if $\Delta t_{crit}^{\mathrm{sd}} < \Delta t_{crit}$ then $\Delta t_{crit} = \Delta t_{crit}^{\mathrm{sd}}$
(S.4) End loop over smoothing domains
(S.5) Time step in next iteration $\Delta t = \alpha \Delta t_{crit}$
```

From this flowchart it can be seen that the explicit time integration can be easily implemented and a major part of this integration procedure is the calculation of the nodal force as done in the subroutine "*Cal_Internal_Force*". There are two essential computational aspects that should be pointed out during the explicit time integration.

i) The stoppage of the iterations

The admissible error ε_U in Eq. (3.39) is defined to determine if the membrane structure has reached the steady state. ε_{IJ} is suggested to be set very small, e.g.

1×10^{-10}, so as to get steady state solutions with the admissible minimal influences of the transient responses [19]:

$$\left\| {}^{n+1}\mathbf{u} - {}^{n}\mathbf{u} \right\|_{L2} / \left\| {}^{n}\bar{\mathbf{u}} \right\|_{L2} < \varepsilon_U \, . \tag{3.39}$$

ii) Critical time step

The explicit time integration algorithm is conditionally stable. If the time step Δt exceeds a critical value Δt_{crit}, the solution will grow unboundedly [24]. A stable time step for a standard FEM-T3 model with rate-independent materials is given by

$$\Delta t = \alpha \Delta t_{crit} \;\; , \;\; \Delta t_{crit} = \frac{2\pi}{\omega_{\max}} \le \min_{e,I} \frac{2}{\omega_I^e} = \min_{e} \left(\frac{\ell_e}{c_e} \right) \tag{3.40}$$

where $\omega_{\max}$ is the maximum frequency of the linearized system; ℓ_e is the characteristic length of the element *e*, which usually defined as $\ell_e = 2\sqrt{\sqrt{3} Area_e / 3}$; c_e is the current wave speed in element *e*, which is usually set constant for all the elements, $c_e = \sqrt{E \Big/ \left[\left(1 - \upsilon^2 \right) \rho \right]}$; and α is a reduction factor that accounts for the destabilizing effects of nonlinearities. As suggested in [24], a good choice for α is between 0.8 and 0.98.

According to the “soft effect” theory as stated in Chapter 2, an S-FEM model (including our ES-FEM-T3) is always softer than the FEM-T3 model, hence using the above critical time step in the ES-FEM-T3 should be on the conservative side.

3.2.3 Implementation of explicit ES-FEM-T3 for 3D membrane deflection analysis

The explicit FEM-T3 membrane and shell models are also established in the present study so as to further check the effects of different element types on the membrane deflections. In summary, a total of three numerical models are established

- Membrane model with ES-FEM-T3, i.e. ES-FEM/Membrane model
- Membrane model with FEM-T3, i.e. FEM/Membrane model
- Shell model with FEM-T3, i.e. FEM/Shell model

The ES-FEM/Membrane and FEM/Membrane models are from the in-house code, and the FEM/Shell model is constructed in the commercial software: Abaqus. The 3D spatial square membrane deformation problem introduced in Section 3.2.1 is calculated with different numerical models and the experimental results are used as a benchmark. The material of the membrane is assumed to be linear elastic and the material properties are chosen the same as those used in the experiment. The four vertexes of the square membrane are totally constrained, i.e. the displacements in *x*-, *y*- and *z*-directions are all constrained for the ES-FEM/Membrane model and FEM/Membrane model, and only the displacements in *x*-, *y*- and *z*-directions are constrained for the FEM/Shell model, as shown in Fig. 3.15b. The pressures of p=25Pa, 50Pa, 100Pa, 150Pa are perpendicularly applied on the membrane, respectively.

3.2.3.1 *Mesh convergence analysis*

Theoretically the numerical results will converge to the exact ones with the increase of the DOFs [27-29]. So the mesh convergence analysis should be carried out firstly in order to avoid the effect of DOFs on the final results. In the present analysis five sets of meshes are created (507, 963, 2118, 4320 and 7842 DOFs), as shown in Fig. 3.23a, in which the latter mesh has a relationship of approximate 2 times DOFs of the former. Fig. 3.23b plots the calculated maximum deflections by the ES-FEM/Membrane model based on these five sets of meshes under different pressures. From Fig. 3.23b, it can be seen that the maximum deflections increase with the increase of the DOFs, however, the difference between the two neighboring curves becomes smaller, which means that the deflection will become mesh independent when the DOFs are large enough. However, more computation time will be consumed when more DOFs are used in the simulation. So after considering both the computational accuracy and efficiency, the set of mesh with 4320 DOFs is chosen in the following analysis.

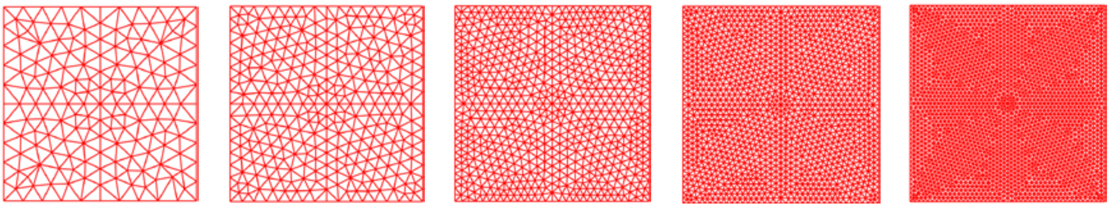

a. 507 DOFs b. 963 DOFs c. 2118 DOFs d. 4320 DOFs e. 7842 DOFs

a) Meshes with different DOFs

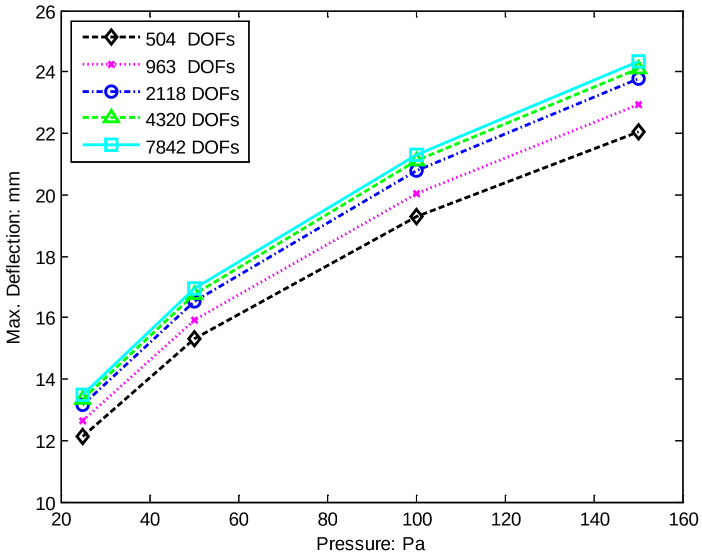

b) Mesh convergence analysis

Fig. 3.23 Five sets of meshes and the corresponding mesh convergence analysis based on the maximum deflections of the membrane by the ES-FEM/Membrane model

3.2.3.2 *Computational accuracy*

a) Calculated deflections from the numerical models

The maximum deflections of the membranes from the models of ES-FEM/Membrane, FEM/Membrane and FEM/Shell under the four sets of static pressures are listed in Table 3.7. And the deflections at the points D_1, D_2,…, D_8 along the diagonal and E_1, E_2,…, E_8 along the edge under a typical pressure of p=100MPa are listed in Table 3.8 and Table 3.9, respectively. At the same time the deformed membranes calculated by the model of ES-FEM/Membrane under different static pressures are plotted in Fig. 3.24a. One typical deformed contour plot of the membrane under the pressure of p=100Pa is plotted in Fig. 3.24b. Different colors used in these figures illustrate different deflection magnitudes of the membrane and the legends on the right of these figures give the values corresponding to these colors. Note that the shapes of the deformed membrane from the models of FEM/Membrane and FEM/Shell are quite similar to that from the model of ES-FEM/Membrane, so only the deformed contour plot from the model of ES-FEM/Membrane is plotted here.

Table 3.7 Maximum deflections (*H*: mm) of the 3D ballooning membrane under four sets of pressures: *p*=25Pa, 50Pa, 100Pa and 150Pa

Pressure: Pa		25	50	100	150
Maximum deflection *H*: mm	ES-FEM/Membrane	13.3	16.8	21.1	24.1
	FEM/Membrane	13.2	16.6	20.9	23.9
	FEM/Shell	13.2	15.7	19.9	22.8

Table 3.8 Numerical deflections (mm) of the 3D ballooning membrane along the diagonal under the pressure of *p*=100Pa

Point: D	1	2	3	4	5	6	7	8
ES-FEM/Membrane	4.4	8.6	12.4	15.7	18.2	19.9	20.8	21.1
FEM/Membrane	4.4	8.7	12.6	15.8	18.1	19.7	20.6	20.9
FEM/Shell	4.2	8.0	11.6	14.7	17.1	18.7	19.6	19.9

Table 3.9 Numerical deflections (mm) of the 3D ballooning membrane along the edge under the pressure of *p*=100Pa

Point: E	1	2	3	4	5	6	7	8
ES-FEM/Membrane	2.9	5.7	8.4	10.8	12.8	14.4	15.5	15.9
FEM/Membrane	2.8	5.6	8.3	10.7	12.7	14.3	15.3	15.6
FEM/Shell	2.7	5.3	7.78	10.1	12.0	13.6	14.6	15.0

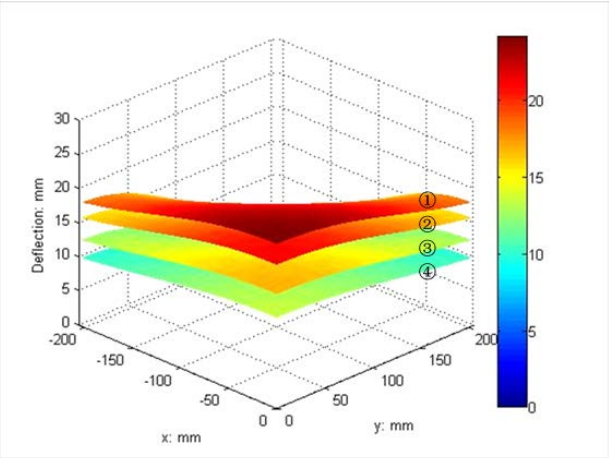

①: *p*=150Pa ②: *p*=100Pa ③: *p*=50Pa ④: *p*=25Pa

a) Deformed profiles of the membrane under static pressures: *p*=25Pa, 50Pa, 100Pa and 150Pa

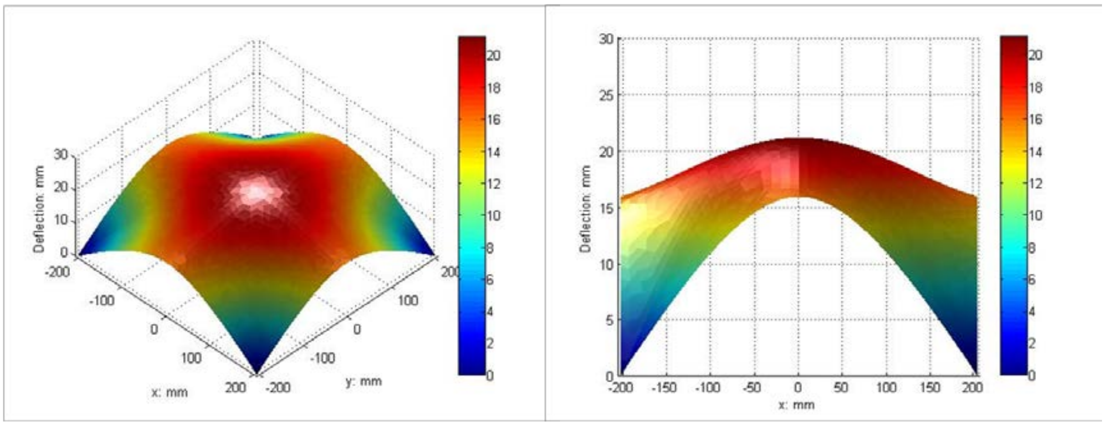

b) Deformed profile of the membrane under static pressures of *p*=100Pa

Fig. 3.24 Membrane deformation based on the ES-FEM/membrane model

b) Verification of the maximum deflections

The maximum deflections, which are from the experiment, the mechanical model and the numerical models, have already been listed in Table 3.4 and Table 3.7, respectively. Fig. 3.25a plots the comparisons of the maximum deflections based on these data. An approximate trend of these maximum deflections can be found from these curves: i) the maximum deflection nonlinearly increases with the increase of the applied pressure; ii) the numerical models can give much closer maximum deflections to the experiment than the mechanical model, although there are still some differences; iii) there is a jump in the experimental curve from *p*=25Pa to *p*=50Pa.

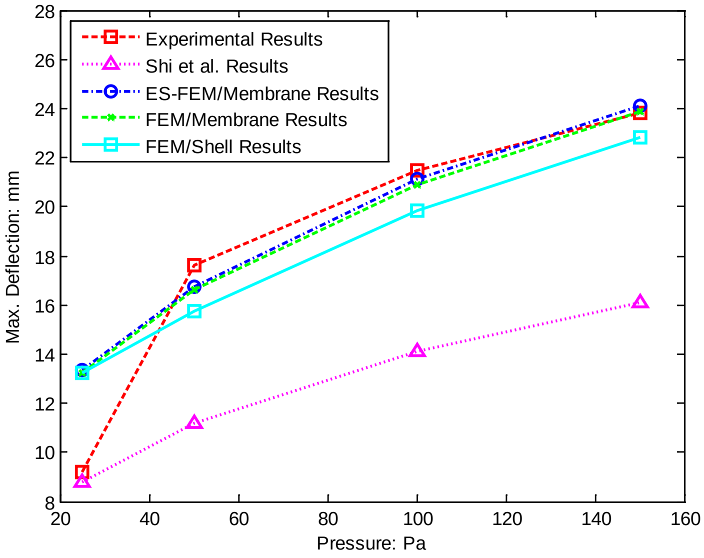

a) Comparison of the maximum deflections

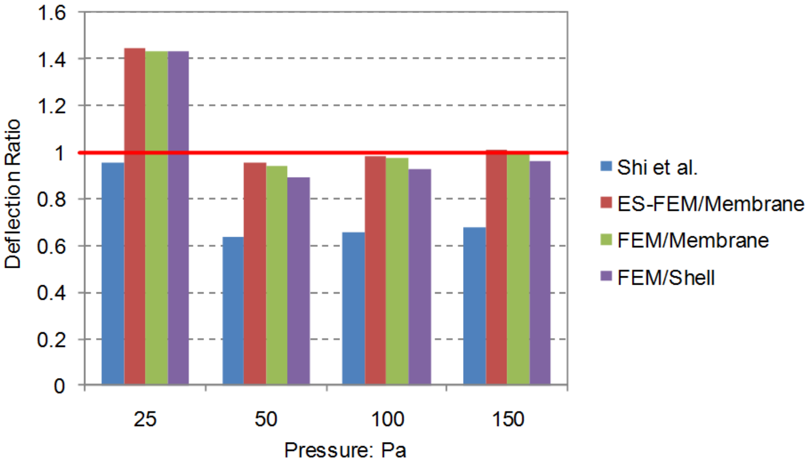

b) Comparison of the deflection ratios

Fig. 3.25 Comparisons of the maximum membrane deflections and the corresponding deflection ratios under different pressures

To provide more clear and fair comparisons for these maximum deflections, the deflection ratio is further introduced by dividing the maximum deflections (both from the mechanical and numerical models) with those from the experiment. A ratio close to 1 indicates that the maximum deflections predicted by the models can correlate well with the experimental data.

Fig. 3.25b plots the deflection ratios obtained from these models under the four sets of pressures. From this figure it can be seen that:

i) The deflection ratios from the numerical models (models of ES-FEM/Membrane, FEM/Membrane and FEM/Shell) are all closer to 1 than the mechanical model except for the case *p*=25Pa, which means that after introducing the nonlinear strains in the numerical models the calculated maximum deflections are much closer to the experiment than those from the mechanical model considering only linear strains. This indicates that the nonlinear strain is indeed a key factor to affect the accurate prediction of the deflections. As shown in Fig. 3.25b, the ratios from the numerical models are all in the range of $\left[0.89, 1.01\right]$, however, those from the mechanical model are just in the range of $\left[0.63, 0.68\right]$.

ii) For the numerical models, the ES-FEM/Membrane model always gives much closer deflections to the experiment than the other two models, and the FEM/Shell model always gives the lower bound results. This is mainly due that the ES-FEM/Membrane model behaves much softer than the standard FEM/Membrane model, and the bending property of the shell element makes the FEM/Shell model even stiffer than the other two membrane models [19]. It is better to choose the ES-FEM/Membrane model to estimate the maximum defections of the membrane in a numerical analysis.

iii) There is a jump of the maximum deflection from *p*=25Pa to *p*=50Pa in the experimental curve as shown in Fig. 3.25a. Comparing the trend of this curve with those from the mechanical model and numerical models, we suspect that there may be a measurement error in the experiment under the pressure of *p*=25Pa.

c) Verification of the deflections along the diagonal and the edge

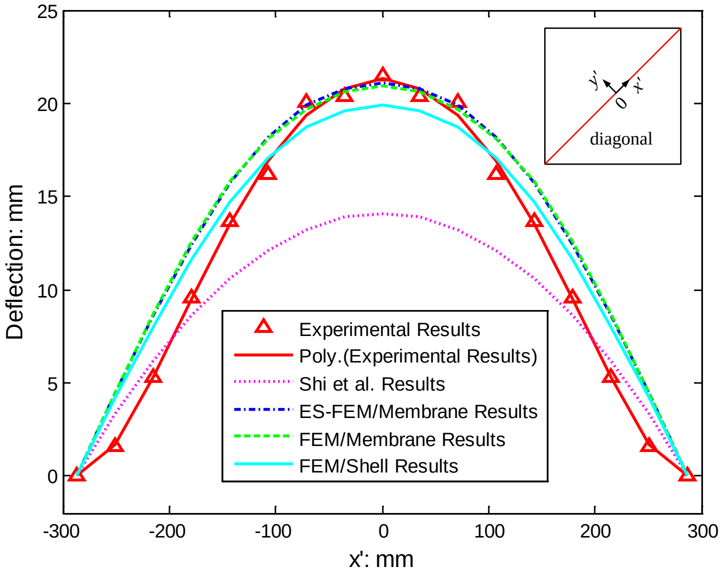

a) Comparison of the deflections along the diagonal

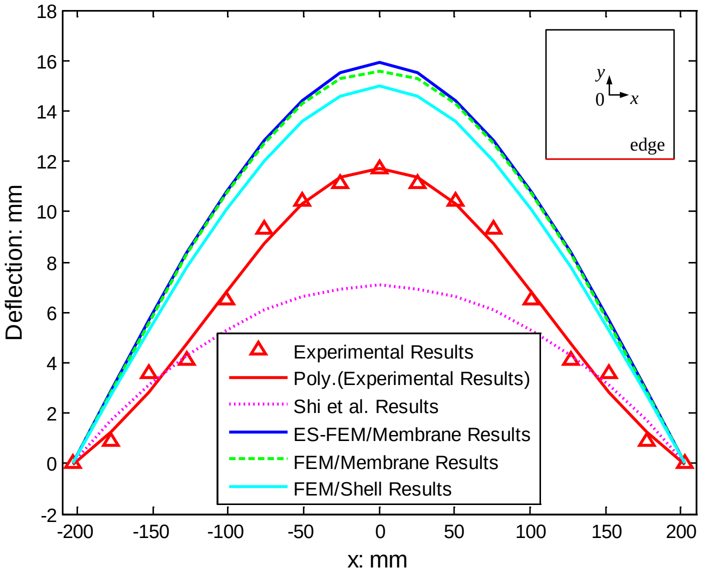

b) Comparison of the deflections along the edge

Fig. 3.26 Comparisons of the membrane deflections along the diagonal and the edge based on the mechanical model, numerical models and experiment under the pressure of p=100Pa

The deflections along the diagonal and the edge are plotted in Fig. 3.26a and Fig. 3.26b based on the data listed in Table 3.5, Table 3.6, Table 3.8 and Table 3.9, respectively. From Fig. 3.26a, it can be seen that the numerical models can give much closer curves to the experiment than the mechanical model along the diagonal. It again verifies that the use of nonlinear strains in the simulation is so important to correctly predict the deflection. The ES-FEM/Membrane model and FEM/Membrane give quite similar deflections, and the FEM/Shell model gives smaller deflections than these two models. The reason for this is similar to those mentioned in the discussion b). The mechanical model underestimates the deflections along the diagonal. From Fig. 3.26b, it can be seen that although the shapes of the deformed curves from the numerical models are similar with that from the experiment, the deflections are overestimated by these numerical models. The mechanical model still gives underestimated results.

3.2.3.3 *Aspects influencing the deflections*

From the comparisons of both the maximum deflections and deflections along the diagonal and the edge discussed in the section above, it can be seen that the numerical models involving nonlinear strains can give much closer deflection to the experiment than the mechanical model with just linear strains. This suggests that the strain expressed in nonlinear form is quite essential for the accurate calculation of membrane undergoing large deformations. However, there are still some differences of the deflections between the numerical and experimental results, especially for the deflections along the edge. Several factors may cause the differences, which may be from the setting of the experiment or the numerical models. These factors will be discussed in the following text.

a) Effect of the reproducibility on the maximum deflections

Some pressure fluctuations are inevitable in an experiment because of the accuracy of the used sensor or the tightness of the equipment. So the reproducibility of the experimental results is important. However, this kind of test was not done in [15]. In the experiment by Baskaran *et al*. [30], the reproducibility test for the membrane deformation under different static pressures was done and it was concluded that the deflections are repeatable within an error of ±5%. Here if we also introduce an error quantity for the deflection in the experiment of Shi *et al*. [15] by assuming a tolerance of ±5% (see Fig. 3.27). From this figure it can be seen that:

i) The curves corresponding to both the ES-FEM/Membrane model and FEM/Membrane model fall within this error band, which indicates that the inaccuracies associated with the numerical models are deemed acceptable, and these two numerical models are able to accurately predict the maximum deflections. However, if the error band is not considered, the numerical curves will be "beyond" the experimental curve.

ii) Even considering the error band of the experimental measurements, the curves corresponding to both the FEM/Shell model and the mechanical model do not lie within this band. This shows that these two mentioned models possess much larger inaccuracies and may not so suitable to predict the maximum deflections of the membrane undergoing large deformations.

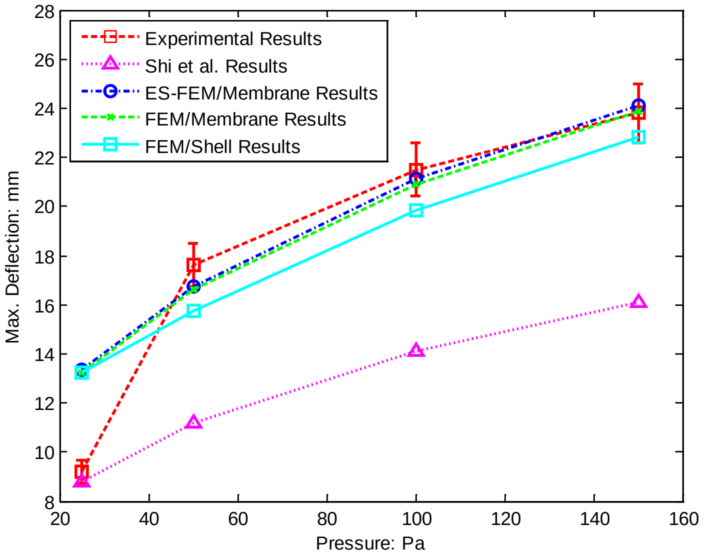

Fig. 3.27 Comparisons of the maximum deflections of the membrane under different pressures

b) Effect of the boundary constraints on the deflections along the diagonal and the edge

The boundary constraints in the numerical model and the experiment should be set the same, otherwise the calculated results cannot match the experimental results very well.

In the experiment by Shi *et al*. [15], a special type of nail with a small and fairly round edge cap was chosen to avoid the effect of the edge on the tested results, but the exact radius of the cap was not mentioned. In the previous simulations, the radius of the round edge cap is set to be zero (R=0 as shown in Fig. 3.28), however, some differences between the numerical and experimental deflections are found, either along the diagonal or along the edge. So the different settings of the radius of the round edge cap between the experiment and numerical models may be a factor causing these differences. Here a slight change of the radius of the round cap (R=4.5mm, 9mm, 18mm) is made to check their effects on the deflections.

Fig. 3.29a-d and Fig. 3.30a-d plot the calculated deflections by ES-FEM/Membrane model, the mechanical model and the corresponding experiment along the diagonal and the edge, respectively. From these figures, we can see that:

i) The radius of the round edge cap do affect the deflection of the membrane: with the increase of the radius of the cap, the deflection will decrease along both the diagonal and edge, which can be attributed to the span of the membrane decreases with the increase of the radius of the round edge cap.

ii) When R=0, the curve of the numerical model can match the experimental one well along the diagonal. When R=18mm the curve of the numerical model can match the experimental one well along the edge. However, there seems to be no one where the curves of the numerical model can simultaneously match the experiment well along both the diagonal and edge. With the increase of the radius, the difference between the numerical and experimental deflections increases along the diagonal. However, the difference decreases along the edge. If the same difference is chosen along the diagonal and the edge, a radius of R=4.8mm can be obtained, as shown in Fig. 3.31.

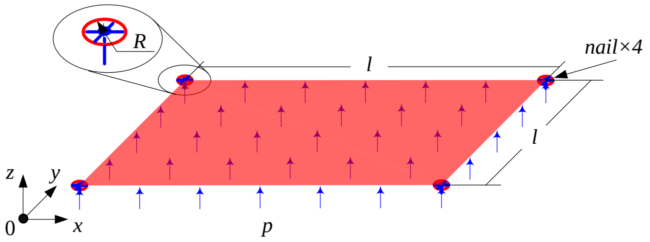

Fig. 3.28 Constrained membrane with round edge cap of radius R: R=0, 4.5mm, 9mm and 18mm

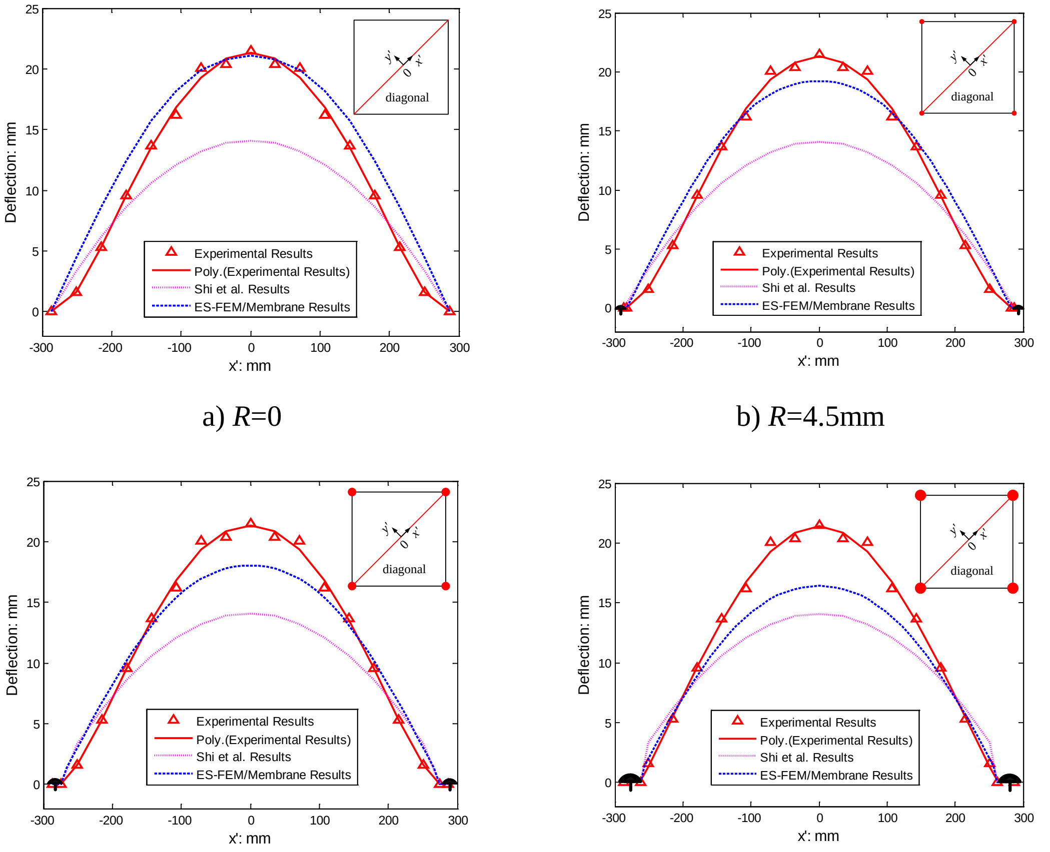

a) R=0

b) R=4.5mm

c) R =9mm

d) R =18mm

Fig. 3.29 Membrane deflections along the diagonal with different R: R=0, 4.5mm, 9mm and 18mm

The boundary constraint is a factor which affects the numerical result, and it should be dealt with carefully to minimum the difference between the numerical and experimental results.

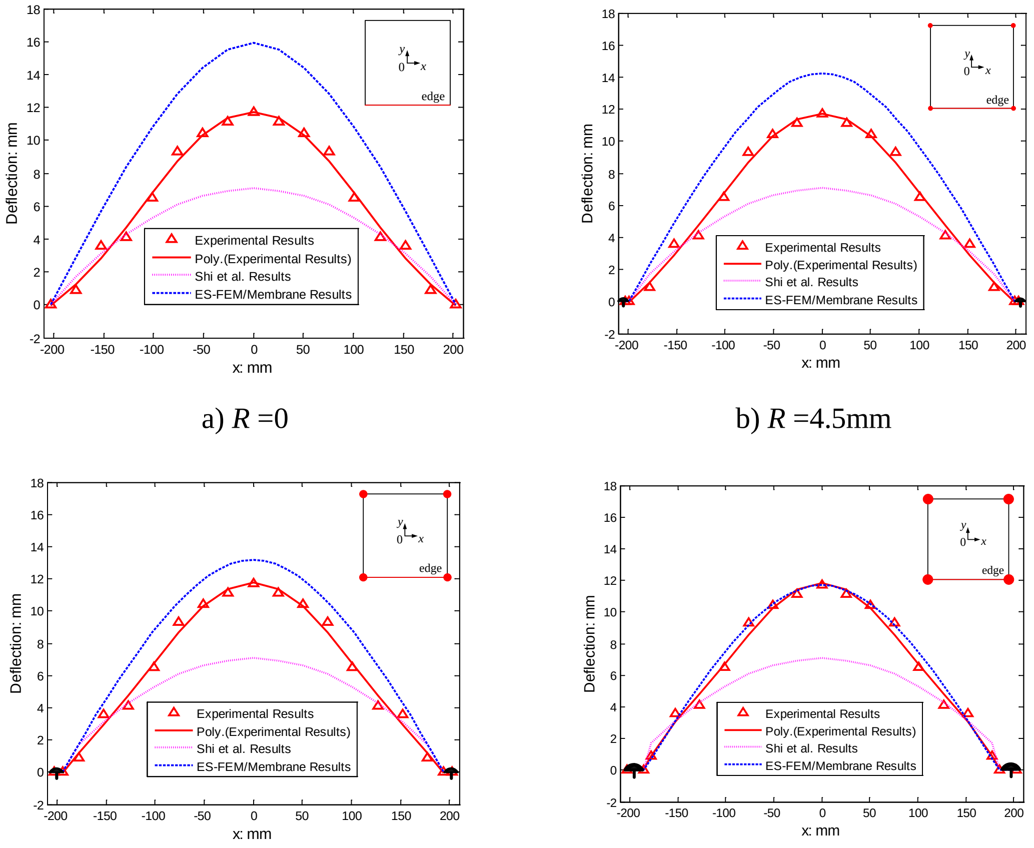

a) *R* =0

b) *R* =4.5mm

c) *R*=9mm

d) *R*=18mm

Fig. 3.30 Membrane deflections along the edge with different *R*: *R*=0, 4.5mm, 9mm and 18mm

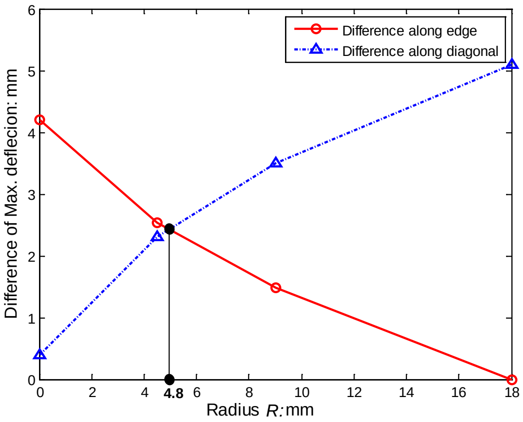

Fig. 3.31 Differences of the maximum membrane deflections along the diagonal and edge

3.2.4 Some remarks

The nonlinear simulations for the membrane deformation based on both membrane and shell models using the ES-FEM-T3 and FEM-T3 are presented and two factors, i.e. pressure fluctuations in the experiment and boundary constraints in the numerical models, are carefully checked to determine their influence on the slight difference observed between the numerical and experimental results. From the above formulations and discussions, we found that:

i) The 3D mechanical model proposed by Shi *et al*. [15] always underestimates the membrane deflections, whether it is for the maximum deflections or the deflections along the diagonal and the edge. One possible reason for this underestimation is its linear strain assumption. The 3D mechanical model is only effective for the membrane with a small deformation. In order to accurately predict the membrane with a larger deformation, the nonlinear term should be added into the strain. As the theoretical treatment of the nonlinear term is complex, numerical simulation appears to be the viable approach.

ii) Numerical simulation is a good choice to calculate the membrane with a large deformation. The numerical results from the membrane model agree much better with the experiment in contrast to the shell model. So the membrane model is the preferred model to simulate the membrane’s deformations.

iii) The ES-FEM/Membrane model can give much closer results to the experiment than either the FEM/Membrane model or FEM/Shell model.

iv) If one would use the experimental data as a benchmark to evaluate the numerical results, a reproducibility test is suggested to determine the experimental uncertainty. The boundary constraints should be carefully set in the numerical simulations to make sure that they are the same as those in the experiment.

3.3 Concluding remarks for Chapter 3

In this chapter, both the linear and nonlinear ES-FEM-T3 models are successfully established and implemented for solving two practical engineering problems. Not only are the numerical properties of the ES-FEM-T3 confirmed (as concluded in [1]) by these simulations, some other conclusions are also drawn. The ES-FEM-T3 gives more accurate solution irrespective of the linear elastic bending stress analysis or the nonlinear membrane deflection analysis. These findings give us confidence to further extend it for solving other more complex FSI problems. A detailed procedure of coupling the ES-FEM-T3 with GSM/ALE (detailed sooner) for solving FSI problems will be presented in Chapter 5.

References for Chapter 3

1. Liu, G.R. and Nguyen, T.T., *Smoothed finite element methods*. 2010: CRC Pr I Llc.
2. Wang, M.J., *A new photoelastic investigation of the dynamic bending stress of spur gears.* Journal of Mechanical Design, 2003. **125**(2): p. 365-372.
3. Bibel, G.D., Reddy, S.K., Savage, M. and Handschuh, R.F. *Effects of rim thickness on spur gear bending stress*. *27th Joint Propulsion Conference*. 1991. Sacramento, California, United States.
4. Deng, G., Nakanishi, T. and Inoue, K., *Bending load capacity enhancement using an asymmetric tooth profile.* JSME International Journal Series C, 2003. **46**(3): p. 1171-1177.
5. Kapelevich, A., *Geometry and design of involute spur gears with asymmetric teeth.* Mechanism and Machine Theory, 2000. **35**(1): p. 117-130.
6. Kapelevich, A.L. and Kleiss, R.E., *Direct gear design for spur and helical involute gears.* Gear Technology, 2002. **19**(5): p. 29-35.
7. Litvin, F.L., Lian, Q. and Kapelevich, A.L., *Asymmetric modified spur gear drives: reduction of noise, localization of contact, simulation of meshing and stress analysis.* Computer Methods in Applied Mechanics and Engineering, 2000. **188**(1): p. 363-390.
8. Litvin, F.L., Fuentes, A. and Howkins, M., *Design, generation and TCA of new type of asymmetric face-gear drive with modified geometry.* Computer Methods in Applied Mechanics and Engineering, 2001. **190**(43): p. 5837-5865.
9. Muni, D.V., Kumar, V.S. and Muthuveerappan, G., *Optimization of asymmetric spur gear drives for maximum bending strength using direct gear design method.* Mechanics Based Design of Structures and Machines, 2007. **35**(2): p. 127-145.
10. Senthil Kumar, V., Muni, D.V. and Muthuveerappan, G., *Optimization of asymmetric spur gear drives to improve the bending load capacity.* Mechanism and Machine Theory, 2008. **43**(7): p. 829-858.
11. Xiao, W.Q. *Investigation on meshing theory and load capacity of high performance unsymmetrical gear with double pressure angles*. Department of Mechanical Engineering, 2008, Ph.D. thesis, University of Science and Technology Beijing: Beijing, China.
12. Jenkins, C.H.M. and Korde, U.A., *Membrane vibration experiments: An historical review and recent results.* Journal of Sound and Vibration, 2006. **295**(3): p. 602-613.
13. Miyamura, T., *Wrinkling on stretched circular membrane under in-plane torsion:: bifurcation analyses and experiments.* Engineering Structures, 2000. **22**(11): p. 1407-1425.
14. Wu, Y., Sun, X. and Shen, S., *Computation of wind–structure interaction on tension structures.* Journal of Wind Engineering and Industrial Aerodynamics, 2008. **96**(10): p. 2019-2032.
15. Shi, X. and Burnett, E., *Mechanics and test study of flexible membranes ballooning in three dimensions.* Building and Environment, 2008. **43**(11): p. 1871-1881.
16. Baskaran, A., Murty, B. and Wu, J., *Calculating roof membrane deformation under simulated moderate wind uplift pressures.* Engineering Structures, 2009. **31**(3): p. 642-650.

17. Baskaran, B. and Molleti, S., *Application of numerical models to evaluate wind uplift ratings of roofs. Part II.* Wind & Structures, 2005. **8**(3): p. 213-233.
18. Wu, T.Y. and Ting, E.C., *Large deflection analysis of 3D membrane structures by a 4-node quadrilateral intrinsic element.* Thin-Walled Structures, 2008. **46**(3): p. 261-275.
19. Zhang, Z.Q. and Liu, G.R., *An edge-based smoothed finite element method (ES-FEM) using 3-node triangular elements for 3D non-linear analysis of spatial membrane structures.* International Journal for Numerical Methods in Engineering, 2011. **86**(2): p. 135-154.
20. Szyszkowski, W. and Glockner, P.G., *Spherical membranes subjected to concentrated loads.* Engineering Structures, 1987. **9**(1): p. 45-52.
21. Zingoni, A., *Stresses and deformations in egg-shaped sludge digestors: membrane effects.* Engineering Structures, 2001. **23**(11): p. 1365-1372.
22. Rahal, K.N., *Simplified design and capacity calculations of shear strength in reinforced concrete membrane elements.* Engineering Structures, 2008. **30**(10): p. 2782-2791.
23. Shi, X., Liang, J. and Burnett, E., *Mechanics and test study of two-dimensional flexible membranes.* Journal of Architectural Engineering, 2006. **12**: p. 93.
24. Belytschko, T., Liu, W.K. and Moran, B., *Nonlinear finite elements for continua and structures*. 2000: John Wiley & Sons Ltd., Baffins Lane, Chichester, West Sussex, PO191 UD, England.
25. Liu, G.R., *Meshfree methods: moving beyond the finite element method, 2nd Edition*. 2009: CRC.
26. Sauve, R.G. and Metzger, D.R., *Advances in dynamic relaxation techniques for nonlinear finite element analysis.* Journal of Pressure Vessel Technology, 1995. **117**: p. 170.
27. Zienkiewicz, O., Taylor, R. and Zhu, J., *The finite element method: its basis and fundamentals*. Vol. 1. 2005: Butterworth-Heinemann, Amsterdam, London.
28. Bathe, K.J., *Finite element procedures.* Englewood Cliffs, New Jersey, 1996.
29. Liu, G.R. and Quek, S., *The finite element method: a practical course*. 2003: Butterworth-Heinemann.
30. Baskaran, A., Lee, W. and Richardson, C., *Dynamic evaluation of thermoplastic roofing system for wind performance.* Journal of Architectural Engineering, 1999. **5**(1): p. 16-24.

Chapter 4

GSM/ALE for incompressible fluid flows over moving mesh

As an important part of the smoothed family, the ES-FEM-T3 has already been successfully implemented for solving solid mechanics in the previous chapter. In this chapter, another important part of this smoothed family, i.e. the GSM, will be explored for solving the fluid flows over moving mesh due to the oscillation of the rigid body immersed in it. Accordingly, the novel GSM/ALE, i.e. the implementation of GSM into the ALE form of Navier-Stokes equations, is proposed. This newly proposed GSM/ALE will be the basis of further solving the fluid-deformable structure interaction problems in Chapter 5.

Different from the GSM for solving fluid flows over fixed mesh [1-3], the GSM/ALE is performed over moving mesh in which the velocities of the moving grid points are involved. Accurately determining these velocities are quite essential to preserve the conservations of mass and momentum on the moving mesh, thus to ensure the accuracy of the proposed GSM/ALE. For a general problem the grid positioning quantities are usually available as a function of time, particularly in the case that the grid movement is governed by the PDEs. The grid velocities are approximated by finite difference interpolations of these positioning quantities [4].

During the determination of the positioning quantities and velocities of the moving grid, the so-called geometric conservation law (GCL) is suggested to be obeyed. The GCL states that no disturbance should be introduced by any arbitrary mesh motion for a uniform flow [5]. Obey the GCL in an ALE formulation: i) can increase the accuracy of the solutions [6, 7]; ii) is sufficient for achieving at least 1st-order accuracy [8]; and iii) is necessary for preserving the non-linear stability of the underlying time-integration scheme [8]. Literature reveals that there are roughly two approaches to determine the geometric parameters to enforce the GCL:

i) By adding an extra term derived directly from the GCL into the discretized governing equations [6, 9, 10], the GCL can be satisfied automatically regardless of the mesh movement;

ii) Different intermediate mesh configurations between $\left[t^n,\ t^{n+1}\right]$ are constructed and the governing equations are discretized on these mesh configurations [4, 8, 11]. For different time integration methods, e.g. the *n*th order central difference method [4, 8, 11] and the *n*th stage Runge-Kutta method [4], the intermediate mesh configurations may be chosen at different intervals between $\left[t^n,\ t^{n+1}\right]$.

It is argued that the derivation procedure for the first approach does not strictly satisfy the strong conservations of mass and momentum in time and may not be suitable for rapidly moving strong shock problems [6]. However, for problems without rapidly moving strong shocks, the first approach is much more efficient and the relevant results are of sufficient accuracy. In the present study, this approach is chosen to construct the GSM/ALE for the incompressible fluid flow problems.

Referring to the time integration of the GSM for solving incompressible fluid flows over fixed mesh, the artificial compressibility method is again utilized by the GSM/ALE and the dual time stepping approach is employed for the time integration of the transient/steady incompressible fluid flows over moving mesh. In comparison with the single global time stepping approach, larger physical time step is allowed in the properly devised dual time stepping approach, which can help to achieve not only fast convergence but also high stability in the solution process. To circumvent the upwinding effect, the second order Roe flux differencing splitting unwinding scheme (Roe2) is adopted, and a Riemann problem is solved at the cell interface to evaluate the numerical fluxes [12].

In this chapter, the general idea of ALE is firstly introduced. Then the detailed derivations of the GSM/ALE in both spatial and temporal domains are presented. The verifications of the convergence, accuracy and robustness of this newly proposed GSM/ALE is demonstrated through solving a series of benchmark tests. Some concluding remarks are given in the end of this chapter.

4.1 ALE formulation based on GSM framework

4.1.1 A brief on ALE formulation

As reviewed in Chapter 1, the ALE description is a hybrid technique that combines the advantages of both the Lagrangian and Eulerian descriptions while minimizing their disadvantages [13]. In the ALE description an extra reference configuration that coincides with the moving mesh domain $\hat{\Omega}$ is introduced except the material (initial) and spatial configurations. The kinematics of the material particles is described referring to this configuration. Thus in formulating the continuous media with ALE, a total of two motions, i.e. the mesh and material motions, should be described and the kinematic relationships between these two motions should be established.

The descriptions of these two motions can be, respectively, defined as

$$\mathbf{x} = \phi\left(\mathbf{X}, t\right) \tag{4.1}$$

$$\mathbf{x} = \hat{\phi}\left(\chi, t\right) \tag{4.2}$$

where **x** is the coordinates in the spatial domain Ω; **X** is the material coordinates in the initial domain ${}^0\Omega$; χ is the mesh (reference) coordinates in the reference domain $\hat{\Omega}$; $\phi\left(\mathbf{X},t\right)$ is the kinematic equation that maps the material particle **X** to the spatial point **x**; and $\hat{\phi}\left(\chi,t\right)$ is the kinematic equation that maps the mesh point χ to the spatial point **x**.

By compositing Eqs. (4.1) and (4.2), the kinematic relationship of position quantities of material coordinates **X** and mesh coordinates χ can be established at an arbitrary time *t* as

$$\mathbf{x}=\hat{\phi}\left(\chi,t\right)=\phi\left(\mathbf{X},t\right)\Rightarrow\chi=\Psi\left(\mathbf{X},t\right)=\hat{\phi}^{-1}\circ\phi \tag{4.3}$$

where $\Psi\left(\mathbf{X},t\right)$ describes the movements of the material particles by referring to the reference domain $\hat{\Omega}$. For simplification, at the initial time *t*=0 the reference domain $\hat{\Omega}$ is usually set to be identical with the initial domain ${}^0\Omega$, i.e. $\chi\left(\mathbf{X},0\right)=\mathbf{X}$. A clear illustration for these relationships is shown in Fig. 4.1.

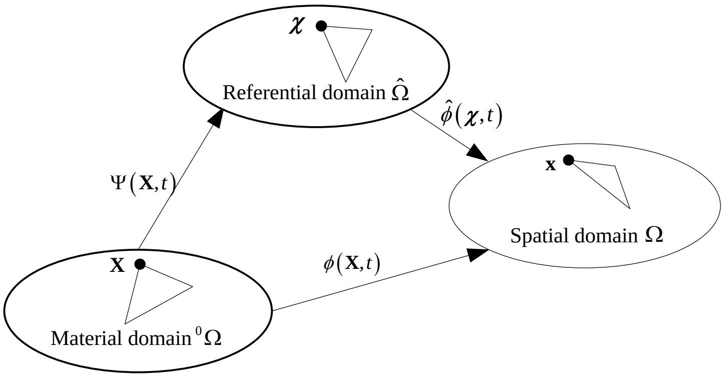

Fig. 4.1 Mappings between Lagrangian, Eulerian, ALE descriptions

Analogously, the kinematic relationship of the velocities of the material particles and mesh points can be established at an arbitrary time *t* as

$$\begin{aligned}\dot{\mathbf{x}} = \mathbf{v} = \frac{\partial \phi(\mathbf{X},t)}{\partial t} &= \left.\frac{\partial \hat{\phi}(\boldsymbol{\chi},t)}{\partial t}\right|_{\chi} + \left.\frac{\partial \hat{\phi}(\boldsymbol{\chi},t)}{\partial \boldsymbol{\chi}}\frac{\partial \Psi(\mathbf{X},t)}{\partial t}\right|_{\mathrm{X}} \\ &= \mathbf{v}_g + \frac{\partial \hat{\phi}(\boldsymbol{\chi},t)}{\partial \boldsymbol{\chi}} \cdot \mathbf{w}\end{aligned} \tag{4.4}$$

where **v** is the velocity of the material particle; $\mathbf{v}_g$ is the velocity of the mesh point; and **w** is the velocity of the material particle seen from the referential domain $\hat{\Omega}$.

Theoretically, the velocity **w** can explicitly appear in the ALE form of the governing equations. In that case the gradients of the fluid quantities (i.e. ρ and $\rho\mathbf{v}$) should be evaluated according to the reference domain $\hat{\Omega}$. However, in computational mechanics it is usually much more convenient to work in the spatial domain Ω or the material domain ${}^{0}\Omega$. Particularly, in fluid mechanics, the constitutive relationships are naturally expressed in the spatial domain and the Cauchy stress tensor is a natural measure for stress [14]. For this purpose, another velocity parameter, i.e. the so-called convective velocity **c** which is the material particle velocity seen from the spatial domain Ω, is introduced to replace **w** in the ALE form of governing equations. In that case, the gradients of the fluid quantities (i.e. ρ and $\rho\mathbf{v}$) are evaluated according to the spatial domain Ω.

After rewriting Eq. (4.4), the so-called convective velocity **c** can be easily gotten as

$$\mathbf{c} = \mathbf{v} - \mathbf{v}_g = \frac{\partial \hat{\phi}(\boldsymbol{\chi},t)}{\partial \boldsymbol{\chi}} \cdot \mathbf{w}\,. \tag{4.5}$$

It should be noted that the **w** and **c** can be identical if and only if the mesh motion is purely translational, i.e. $\partial \hat{\phi}(\boldsymbol{\chi},t) / \partial \boldsymbol{\chi} = \mathbf{I}$ where **I** denotes the identity tensor [14]. An illustration of different velocities is shown in Fig. 4.2.

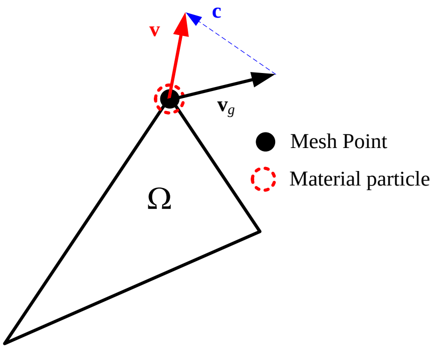

Fig. 4.2 Illustration of the relationship among the material velocity, mesh velocity and convective velocity

4.1.2 Governing equations in ALE form

In a general ALE formulation the material and mesh motions do not coincide with each other. This will lead to the flux of the field variables across the surface of the moving volume. Thus an extra convection term should be added into the governing equations to ensure the conservations. As is known in the Eulerian description the integral form of the conservation equations can be derived according to the Reynolds transport theorem over the fixed mesh [13]. Similarly, the Reynolds transport theorem over an arbitrary moving volume can be written as [13, 14]

$$\left.\frac{\partial}{\partial t}\right|_{\chi}\int_{\Omega(t)} f\left(\mathbf{x},t\right)\mathrm{d}V = \underbrace{\int_{\Omega(t)} \left.\frac{\partial f\left(\mathbf{x},t\right)}{\partial t}\right|_{\mathbf{x}} \mathrm{d}V}_{term\ 1} + \underbrace{\int_{\partial\Omega(t)} f\left(\mathbf{x},t\right)\mathbf{v}_g\cdot\mathbf{n}\,\mathrm{d}S}_{term\ 2} \tag{4.6}$$

where $\Omega(t)$ denotes the time varying moving volume; $f\left(\mathbf{x},t\right)$ denotes an arbitrary field variable that can be the density ρ or momentum component ρv_x and ρv_y described with the spatial coordinates **x**; **n** denotes the unit outward normal of the surface $\partial\Omega(t)$ bounding the moving volume $\Omega(t)$, $\mathbf{n}=n_x\mathbf{i}+n_y\mathbf{j}$ in 2D; the *term* 1 in the right hand side (RHS) is the local time derivative of the volume integral with time t

fixed; and the *term* 2 represents the relative flux of $f\left(\mathbf{x},t\right)$ across the surface $\partial\Omega\left(t\right)$ at this fixed time *t*.

If we replace the scalar $f\left(\mathbf{x},t\right)$ in Eq. (4.6) by the fluid density ρ and momentum component ρv_x and ρv_y , and replace the spatial time derivative $\partial f\left(\mathbf{x},t\right)/\partial t$ with the expressions in Eq. (2.27), the ALE integral form of the governing equations can be finally obtained as

$$\left.\frac{\partial}{\partial t}\right|_{\chi} \int_{\Omega(t)} \mathbf{U}\mathrm{d}V + \int_{\partial\Omega(t)} \left(\overline{\mathbf{F}}_c^{ale} - \overline{\mathbf{F}}_v\right)\mathrm{d}S = \mathbf{0} \tag{4.7}$$

where $\overline{\mathbf{F}}_c^{ale}$ is in the form of

$$\overline{\mathbf{F}}_c^{ale} = \begin{bmatrix} \rho\mathbf{c}\cdot\mathbf{n} \\ \rho v_x \mathbf{c}\cdot\mathbf{n} + p n_x \\ \rho v_y \mathbf{c}\cdot\mathbf{n} + p n_y \end{bmatrix} = \begin{bmatrix} \rho\Theta \\ \rho v_x \Theta + p n_x \\ \rho v_y \Theta + p n_y \end{bmatrix} = \underbrace{\begin{bmatrix} \rho V_s \\ \rho v_x V_s + p n_x \\ \rho v_y V_s + p n_y \end{bmatrix}}_{\overline{\mathbf{F}}_c^s} - \underbrace{\begin{bmatrix} \rho V_g \\ \rho v_x V_g \\ \rho v_y V_g \end{bmatrix}}_{\overline{\mathbf{F}}_c^a} \tag{4.8}$$

in which $\overline{\mathbf{F}}_c^s$ is exactly the same as $\overline{\mathbf{F}}_c$ defined in Eq. (2.38). An additional superscript "*s*" is added to distinguish it with the extra flux $\overline{\mathbf{F}}_c^a$ that is due to the effect of the mesh movement; V_g in $\overline{\mathbf{F}}_c^a$ is the contravariant velocity of mesh movement, i.e. $V_g = \mathbf{v}_g \cdot \mathbf{n}$; and $\Theta = V_s - V_g$.

Taking a cell average of the field variables **U** in Eq. (4.7), i.e. $\mathbf{U} = \frac{1}{A}\int_{\Omega(t)} \mathbf{U}\mathrm{d}V$ where *A* stands for the area of the control volume $\Omega\left(t\right)$, it can be rewritten as

$$\frac{\partial}{\partial t}\left(\mathbf{U}A\right) + \int_{\partial\Omega(t)} \left(\overline{\mathbf{F}}_c^{ale} - \overline{\mathbf{F}}_v\right)\mathrm{d}S = \mathbf{0}\,. \tag{4.9}$$

Comparing Eqs. (2.28) and (4.9) we can see that the main difference between the standard Eulerian formulation and the ALE formulation is the introduction of the extra "ALE" flux $\overline{\mathbf{F}}_c^a$ which is a function of the positioning quantities and velocities of the moving grid points. Thus the general procedures of solving Eq. (4.7) with GSM are similar with those of solving Eq. (2.28) over fixed mesh, except an additional effort for evaluating the ALE convective flux $\overline{\mathbf{F}}_c^a$.

It has already been shown (and will be further shown in Section 4.2) that the computation of positioning quantities and velocities of the moving grid points in the ALE formulation must be performed in such a way that the ALE numerical scheme preserves the state of a uniform flow [5], i.e. obeying the GCL. As reviewed previously, there are in the literature mainly two different approaches to deal with the temporal term $\partial(\mathbf{U}A)/\partial t$ in Eq. (4.9) to ensure the satisfactory of the GCL by the ALE, thus to determine the geometric parameters.

i) Temporal term with an expansion

Since the area of $\Omega(t)$ and cell average of the field variables **U** are smooth with respect to time [9], the temporal term $\partial(\mathbf{U}A)/\partial t$ can be expanded as

$$\mathbf{U}\frac{\partial A}{\partial t}+A\frac{\partial \mathbf{U}}{\partial t}+\int_{\partial\Omega(t)}\left(\overline{\mathbf{F}}_c^{ale}-\overline{\mathbf{F}}_v\right)\mathrm{d}S=0. \tag{4.10}$$

For flows with constant density and velocities Eq. (4.10) degenerates to

$$\frac{\partial A}{\partial t}-\int_{\partial\Omega(t)}\left(\mathbf{v}_g\cdot\mathbf{n}\right)\mathrm{d}S=0. \tag{4.11}$$

Either replacing $\frac{\partial A}{\partial t}$ in Eq. (4.10) with $\frac{\partial A}{\partial t}=\int_{\partial\Omega(t)}\left(\mathbf{v}_g\cdot\mathbf{n}\right)\mathrm{d}S$ [6, 9] or substitute Eq. (4.11) directly into the RHS of Eq. (4.10) [10], the GCL can be automatically satisfied regardless of the movement of the fluid mesh.

ii) Temporal term without an expansion

If the temporal term $\partial\left(\mathbf{U}A\right)/\partial t$ is discretized directly in time by using either the n^{th} order central difference method [4, 8, 11] or the n^{th} stage Runge-Kutta method [4], the GCL will be satisfied with the geometric parameters at different intermediate configurations between time levels t^n and t^{n+1}. For example, if we use the BDF2 to discrete the temporal term, it becomes

$$\frac{3\,{}^{n+1}\left(A\mathbf{U}\right)-4\,{}^{n}\left(A\mathbf{U}\right)+{}^{n-1}\left(A\mathbf{U}\right)}{2\Delta t}+\int_{\partial\Omega(\mathbf{x},t)}\left(\overline{\mathbf{F}}_c^{ale}-\overline{\mathbf{F}}_v\right)\mathrm{d}S=0 \tag{4.12}$$

For a flow with constant density and velocities Eq. (4.12) degenerates to

$$\frac{3\,{}^{n+1}A-4\,{}^{n}A+{}^{n-1}A}{2\Delta t}-\int_{\partial\Omega(\mathbf{x},t)}\left(\mathbf{v}_g\cdot\mathbf{n}\right)\mathrm{d}S=0 \tag{4.13}$$

In order to satisfy the GCL, the first term in Eq. (4.13) should be accurately evaluated. Thus evaluations of the second term in Eq. (4.13) and the fluxes in Eq. (4.12) are constrained either on a set of intermediate mesh configurations at each time interval $\left[t^n,\ t^{n+1}\right]$ and time-averaging of each set of these numerical quantities, or on a unique computational mesh configuration in the time interval $\left[t^n,\ t^{n+1}\right]$ by time-averaging the intermediate mesh configurations themselves, rather than simply evaluating them on the mesh configuration t^{n+1} [4, 8, 11].

Comparing these two approaches, the first one has less constraint on the geometric parameters and is thus more efficient in the calculation process. It is used in the present study, which leads to the governing equations in the final form as

$$A\frac{\partial\mathbf{U}}{\partial t}+\mathbf{U}\int_{\partial\Omega(\mathbf{x},t)}\mathbf{v}_g\cdot\mathbf{n}\mathrm{d}S+\int_{\partial\Omega(t)}\left(\overline{\mathbf{F}}_c^{ale}-\overline{\mathbf{F}}_v\right)\mathrm{d}S=0 \tag{4.14}$$

where the second term is called the moving mesh source term [9].

To numerically solve the ALE form of the incompressible Navier-Stokes equations, i.e. Eq. (4.14), the 1st order (convective) and 2nd order (viscous) spatial derivatives of the field variables in it are discretized with the proposed GSM of Eqs. (2.33), (2.34) and (2.35), and the physical time derivation is discretized with the second-order three-level backward differencing scheme (BDF2). With the help of artificial compressibility method, a dual time stepping procedure is constructed in the time domain, where the steady state solutions with respect to pseudo time ($\Delta\tau$) is pursued at each physical time interval (Δt) by using the iterative time marching method. Details about the spatial and temporal discretizations will be presented in the following two sections.

4.1.3 Spatial discretization of the governing equations with GSM

4.1.3.1 *Convective flux*

The convective fluxes $\overline{\mathbf{F}}_c^s$ and $\overline{\mathbf{F}}_c^a$ are evaluated separately. The evaluation of the stationary convective flux $\overline{\mathbf{F}}_c^s$ can follow exactly the same way as that in Eq. (2.41) where a Riemann problem is solved at the volume interface in order to avoid the unexpected high frequency spurious oscillations due to the high Reynolds number. The stationary convective flux at interface ij_k can be approximated according to Eq. (2.41) as

$$\left(\overline{\mathbf{F}}_c^s\right)_{ij_k} = \frac{1}{2}\left[\overline{\mathbf{F}}_c^s\left(\mathbf{Q}_{ij_k}^L\right) + \overline{\mathbf{F}}_c^s\left(\mathbf{Q}_{ij_k}^R\right) + \left|\overline{\mathbf{A}}_{Roe}\right|\left(\mathbf{Q}_{ij_k}^L - \mathbf{Q}_{ij_k}^R\right)\right]. \tag{4.15}$$

where the physical meanings of the parameters are exactly the same as those in Eq. (2.41). The approximation of the stationary convective flux $\overline{\mathbf{F}}_c^s$ at the node i can then be expressed as

$$\int_{\partial\Omega(t)} \overline{\mathbf{F}}_{ci}^s \mathrm{d}S \approx \sum_{k=1}^{N_{sup}} \left(\overline{\mathbf{F}}_c^s\right)_{ij_k} \left(\Delta S\right)_{ij_k} \tag{4.16}$$

where N_{sup} is the total number of supporting nodes surrounding the node i.

The grid velocities at mid-point of the edge in the ALE convective flux $\overline{\mathbf{F}}_c^a$ is approximated with a central difference scheme

$$\mathbf{v}_g^m = \frac{1}{2}\left(\mathbf{v}_g^L + \mathbf{v}_g^R\right) \tag{4.17}$$

where $\mathbf{v}_g^L$ and $\mathbf{v}_g^R$ corresponds to the grid velocities at node *i* and j_k, respectively.

Finally, the total convective flux at the node *i* can be approximated as

$$\int_{\partial\Omega(\mathbf{x},t)} \left(\overline{\mathbf{F}}_{ci}^s + \overline{\mathbf{F}}_{ci}^a\right) \mathrm{d}S \approx \sum_{k=1}^{N_{sup}} \left(\overline{\mathbf{F}}_c^s + \overline{\mathbf{F}}_c^a\right)_{ij_k} \left(\Delta S\right)_{ij_k} = \mathbf{C}_i\left(\mathbf{Q}, \mathbf{x}(t), \dot{\mathbf{x}}(t)\right) \tag{4.18}$$

4.1.3.2 *Viscous flux*

The evaluation of the viscous flux corresponding to node *i* also follows exactly the same form as in Eq. (2.44),

$$\int_{\partial\Omega(t)} \overline{\mathbf{F}}_{vi} \mathrm{d}S \approx \sum_{k=1}^{N_{sup}} \left(\overline{\mathbf{F}}_v\right)_{ij_k} \left(\Delta S\right)_{ij_k} = \mathbf{D}_i\left(\mathbf{x}(t), \dot{\mathbf{x}}(t)\right) \tag{4.19}$$

where $\left(\overline{\mathbf{F}}_v\right)_{ij_k}$ is associated with the velocity gradients (∇v_x and ∇v_y) at the mid-point of an edge ij_k that is calculated according to Eqs. (2.33) and (2.34).

4.1.3.3 *Moving mesh source term*

The moving mesh source term of $\mathbf{S} = \mathbf{U}\int_{\partial\Omega(\mathbf{x},t)} \mathbf{v}_g \cdot \mathbf{n} \mathrm{d}S$ contains the grid velocities. It can be integrated along the edge of nGSD corresponding to node *i*,

$$\mathbf{S}_i\left(\mathbf{Q}, \mathbf{x}(t), \dot{\mathbf{x}}(t)\right) = \mathbf{U}_i \int_{\partial\Omega(t)} \mathbf{v}_g \cdot \mathbf{n} \mathrm{d}S \approx \mathbf{U}_i \sum_{k=1}^{N_{sup}} \left(\mathbf{v}_g \cdot \mathbf{n}\right)_{ij_k} \left(\Delta S\right)_{ij_k} . \tag{4.20}$$

By substituting the discretized forms of Eqs. (4.18), (4.19) and (4.20) back into Eq. (4.14), the semi-discrete form of the Navier-Stokes equations can be finally obtained as

$$
\begin{aligned}
{}^{ale}\mathbf{R}_i^*\left(\mathbf{Q},\mathbf{x}(t),\dot{\mathbf{x}}(t)\right) = A_i \frac{\partial \mathbf{U}_i}{\partial t} \\
+\mathbf{S}_i\left(\mathbf{Q},\mathbf{x}(t),\dot{\mathbf{x}}(t)\right)+\mathbf{C}_i\left(\mathbf{Q},\mathbf{x}(t),\dot{\mathbf{x}}(t)\right)-\mathbf{D}_i\left(\mathbf{x}(t),\dot{\mathbf{x}}(t)\right)=\mathbf{0}\ .
\end{aligned}
\tag{4.21}
$$

4.1.4 Temporal discretization of the governing equations with dual time stepping approach

By adding a pseudo time term into Eq. (4.14), the ALE form of the governing equations with artificial compressibility can be constructed as

$$
\mathbf{P}\frac{\mathrm{d}}{\mathrm{d}\tau}\left(\mathbf{Q}_i A_i\right)+{}^{ale}\mathbf{R}_i^*\left(\mathbf{Q},\mathbf{x}(t),\dot{\mathbf{x}}(t)\right)=\mathbf{0}\,. \tag{4.22}
$$

This equation has the similar form with Eq. (2.46) except the expression of semi-discrete transient ${}^{ale}\mathbf{R}_i^*\left(\mathbf{Q},\mathbf{x}(t),\dot{\mathbf{x}}(t)\right)$ in which an extra ALE convective flux $\overline{\mathbf{F}}_c^a$ is added comparing with $\mathbf{R}_i^*\left(\mathbf{Q},\mathbf{x}\right)$ in Eq. (2.46). By using the BFD2 to discretize the physical time term in the unsteady residual ${}^{ale}\mathbf{R}_i^*\left(\mathbf{Q},\mathbf{x}(t),\dot{\mathbf{x}}(t)\right)$, it becomes

$$
\begin{aligned}
{}^{ale}\mathbf{R}_i^*\left(\mathbf{Q},{}^{n+1}\mathbf{x},{}^{n+1}\dot{\mathbf{x}}\right)={}^{n+1}A_i\left(\frac{3\mathbf{U}_i-4\,{}^{n}\mathbf{U}_i+{}^{n-1}\mathbf{U}_i}{2\Delta t}\right) \\
+\mathbf{S}_i\left(\mathbf{Q},{}^{n+1}\mathbf{x},{}^{n+1}\dot{\mathbf{x}}\right)+\mathbf{C}_i\left(\mathbf{Q},{}^{n+1}\mathbf{x},{}^{n+1}\dot{\mathbf{x}}\right)-\mathbf{D}_i\left({}^{n+1}\mathbf{x},{}^{n+1}\dot{\mathbf{x}}\right)=\mathbf{0}
\end{aligned}
\tag{4.23}
$$

where ${}^{ale}\mathbf{R}_i^*\left(\mathbf{Q},\mathbf{x}(t),\dot{\mathbf{x}}(t)\right)$ is evaluated at time t^{n+1}; $\mathbf{U}_i$ is evaluated at the "*k*-1" level of RK5 method in the pseudo time level as illustrated below; and the mesh velocity ${}^{n+1}\mathbf{v}_g$ is evaluated with the same way as for the physical time term [6, 9]

$$
{}^{n+1}\mathbf{v}_g={}^{n+1}\dot{\mathbf{x}}=\frac{3\,{}^{n+1}\mathbf{x}-4\,{}^{n}\mathbf{x}+{}^{n-1}\mathbf{x}}{2\Delta t}\,. \tag{4.24}
$$

Other terms in the unsteady residual can be expressed as

$$
\mathbf{S}_i\left(\mathbf{Q},{}^{n+1}\mathbf{x},{}^{n+1}\dot{\mathbf{x}}\right)=\mathbf{U}_i\int_{\partial\Omega\left({}^{n+1}\mathbf{x}\right)}{}^{n+1}\mathbf{v}_g\cdot{}^{n+1}\mathbf{n}\ \mathrm{d}S \tag{4.25}
$$

$$
\mathbf{C}_i\left(\mathbf{Q},{}^{n+1}\mathbf{x},{}^{n+1}\dot{\mathbf{x}}\right)-\mathbf{D}_i\left({}^{n+1}\mathbf{x},{}^{n+1}\dot{\mathbf{x}}\right)=\int_{\partial\Omega\left({}^{n+1}\mathbf{x}\right)}\left[{}^{ale}\overline{\mathbf{F}}_c\left(\mathbf{U}_i,{}^{n+1}\mathbf{x},{}^{n+1}\dot{\mathbf{x}}\right)-\overline{\mathbf{F}}_v\left(\mathbf{U}_i,{}^{n+1}\mathbf{x}\right)\right]\mathrm{d}S\ . \tag{4.26}
$$

The RK5 method with residual smoothing is used in the pseudo time level [3, 15] for its high efficiency of the steady-state solver. The general form for RK5 method with residual smoothing applied to Eq. (4.22) can be derived as

$$ {}^{k}\mathbf{Q}_i = {}^{0}\mathbf{Q}_i - \frac{\alpha_k\lambda}{1+\alpha_k\lambda}\left[{}^{0}\mathbf{Q}_i + \frac{2}{3}\frac{\Delta t}{{}^{n+1}A_i}\,{}^{k-1}\left({}^{ale}\mathbf{R}_i^{*}\right) - {}^{k-1}\mathbf{Q}_i \right], \quad k=1,...,5 \qquad (4.27) $$

where $\lambda = \mathrm{CFL}\times\Delta\tau/(2\Delta t)$; and α_k (α_1=0.0695, α_2=0.1602, α_3=0.2898, α_4=0.5060, α_5=1.0) is the optimized coefficients for convergence acceleration to steady state.

According to this dual time stepping integration, a summary of the computational procedures with GSM for solving both steady-state and transient fluid flows is listed in the following flowchart.

Flowchart for solving the incompressible flows with GSM/ALE

```
(1)  Construct the nGSD and mGSD
(2)  Initial geometry quantities and flied variables
     (2.1)  Calculate the initial quantities in Eqs. (2.33)-(2.35)
     (2.2)  Initial the flow field, ${}^{-1}\mathbf{U}={}^{0}\mathbf{U}=\mathbf{0}$
     (2.3)  Initial physical time, $n$=0 and $t^0$=0
(3)  Apply the boundary conditions
(4)  Solver for transient and steady flows
     (4.1)  For transient flow, call subroutine Transient_solver
     (4.2)  For steady flow, call subroutine Steady_solver
```

Subroutine *Transient_solver*

```
(4.1.1)  Update the positions and velocities of the moving mesh, ${}^{n+1}\mathbf{x}$, ${}^{n+1}\mathbf{v}_g$
(4.1.2)  Update the geometry quantities, ${}^{n+1}A$ and quantities in Eqs. (2.42)-(2.44)
(4.1.3)  Update the moving mesh source terms, $\mathbf{S}_i = {}^{n+1}\mathbf{U}_i \int_{\partial\Omega\left({}^{n+1}\mathbf{x}\right)} {}^{n+1}\mathbf{v}_g \cdot {}^{n+1}\mathbf{n}\,\mathrm{d}S$
(4.1.4)  Initial the pseudo time counter, $m$=1
(4.1.5)  Transfer ${}^{n+1,m}\mathbf{Q} = f\left({}^{n}\mathbf{U}\right)$
(4.1.6)  Transfer ${}^{n+1,0}\mathbf{Q} = {}^{n+1,m}\mathbf{Q}$
(4.1.7)  Loop over RK steps $k$=1, 5
             ${}^{k}\mathbf{R}' = \frac{\alpha_k\lambda}{(1+\alpha_k\lambda)}\left[ {}^{n+1,0}\mathbf{Q} - \frac{2\Delta t}{3\,{}^{n+1}A}\,{}^{ale}\mathbf{R}^{*}\left({}^{n+1,m,k-1}\mathbf{Q}, {}^{n}\mathbf{U}, {}^{n-1}\mathbf{U}\right) - {}^{n+1,m,k-1}\mathbf{Q} \right]$
             ${}^{n+1,m,k}\mathbf{Q} = {}^{0}\mathbf{Q} - {}^{k}\mathbf{R}'$
         End loop $k$
(4.1.8)  Update ${}^{n+1,m+1}\mathbf{Q} = {}^{n+1,m,5}\mathbf{Q}$, ${}^{n+1}\mathbf{U} = f^{-1}\left({}^{n+1,m+1}\mathbf{Q}\right)$
```

```
(4.1.9)   Apply the boundary conditions to ${}^{m+1}\mathbf{U}$
(4.1.10)  If error_transient < tol
              Break the loop over pseudo time, go to step (4.1.11)
          Else
              Update counter $m \leftarrow m+1$ and go to step (4.1.6)
          End If
(4.1.11)  Update counter $n \leftarrow n+1$ and go to step (4.1.1)
```

Subroutine *Steady_solver*

```
(4.2.1)   Initial the pseudo time counter, $m=0$
(4.2.2)   Update the positions and velocities of the moving mesh, ${}^{m+1}\mathbf{x}$, ${}^{m+1}\mathbf{v}_g$
(4.2.3)   Update the geometry quantities, ${}^{m+1}A$ and quantities in Eqs. (2.42)-(2.44)
(4.2.4)   Update the moving mesh source terms, $\mathbf{S}_i = {}^{m+1}\mathbf{U}_i \int_{\partial\Omega({}^{m+1}\mathbf{x})} {}^{m+1}\mathbf{v}_g \cdot {}^{m+1}\mathbf{n} \mathrm{d}S$
(4.2.5)   Transfer ${}^{m}\mathbf{Q} = f\left({}^{m}\mathbf{U}\right)$
(4.2.6)   Transfer ${}^{0}\mathbf{Q} = {}^{m}\mathbf{Q}$
(4.2.7)   Loop over RK steps $k=1, 5$
              ${}^{k}\mathbf{R}' = \frac{\alpha_k \lambda}{(1+\alpha_k \lambda)} \left[ \mathbf{Q}^0 - \frac{2\Delta t}{3\,{}^{m+1}A} {}^{ale}\mathbf{R}^*\left({}^{m,k-1}\mathbf{Q}, {}^{m}\mathbf{U}, {}^{m-1}\mathbf{U}\right) - {}^{m,k-1}\mathbf{Q} \right]$
              ${}^{m,k}\mathbf{Q} = {}^{0}\mathbf{Q} - {}^{k}\mathbf{R}'$
          End loop k
(4.2.8)   Update ${}^{m+1}\mathbf{Q} = {}^{m,5}\mathbf{Q}$, ${}^{m+1}\mathbf{U} = f^{-1}\left({}^{m+1}\mathbf{Q}\right)$
(4.2.9)   Apply the boundary conditions to ${}^{m+1}\mathbf{U}$
(4.2.10)  If error_steady< tol
              Steady state is gotten, break the loop m
          Else
              Update counter $m \leftarrow m+1$ and go  to step (4.2.2)
          End If
```

where *tol* donates the tolerant error in the calculation and *error_transient* donates the numerical error in each pseudo time step defined the same as Eq. (2.49), and *error_steady* is defined as

$$error\_steady = \sqrt{\sum_{i=1}^{N_{node}} \left({}^{m+1}\mathbf{U}_i - {}^{m}\mathbf{U}_i \right) \Big/ \sum_{i=1}^{N_{node}} {}^{m+1}\left(\mathbf{U}_i - {}^{1}\mathbf{U}_i \right)} . \tag{4.28}$$

As is pointed out in Chapter 2, the transient solutions of the fluid flows can be obtained efficiently with the help of dual time stepping technique with the *Transient_solver*. However, if only the steady-state solution is required, those physical temporal terms occurring in the respective systems of equations are neglected but the pseudo time terms are still retained, as in the subroutine *Steady_solver,* in which the RK 5 method is then used for the time integration.

4.2 Verification of GSM/ALE

A set of flow problems involving moving meshes/boundaries has been considered to demonstrate the validity and performance of the proposed GSM/ALE. The recovery of uniform flow is firstly considered to verify that the GSM/ALE obeys the GCL regardless of the moving of the mesh. The Poisson’s problems which have analytical solutions are then presented to show the spatial/temporal convergence properties of the proposed GSM/ALE. The effect of the mesh distortion on the solution is also discussed to verify the robustness of the GSM/ALE on extremely distorted meshes. Benchmarks examples of lid-driven cavity flows and flow passed a stationary/cross-line/in-line oscillating cylinders are finally tested to demonstrate the global applicability of the proposed GSM/ALE. The results from the GSM on fixed mesh are calculated in some cases for purpose of comparison.

4.2.1 Recovery of uniform flow

The uniform flow in a square with randomly moving mesh in the domain is carried out to verify that the proposed GSM/ALE can preserve the uniform state of flow irrespective of the mesh movement, i.e. conforming to the GCL [16-18]. Configuration of the problem is shown in Fig. 4.3a. The grid inner domain is driven harmonically with a non-dimensional frequency and given as

$$\begin{cases} x = x_0 + A_x a \\ y = y_0 + A_y a \end{cases}. \tag{4.29}$$

Here x_0 and y_0 are the initial coordinates of the grid in the square; a controls the movement of the mesh where $a = \sin\left(2\pi ft\right)\times\sin\left(2\pi x_0/l_x\right)\times\sin\left(2\pi y_0/l_y\right)$, in which f is the frequency of the mesh movement, l_x and l_y are the length of the square's edge in x- and y-directions, respectively; A_x and A_y are the amplitude of the mesh movement in x- and y-directions, respectively; and t is the physical time, $t = n\Delta t$ where n denotes the n^{th} time step.

Parameters of the grid deformation are taken as follows: $A_x = A_y = 0.1$, and the physical time interval is $\Delta t = 0.01s$. A set of frequencies, i.e. $f=0.5$, $f=1$, $f=2$ and $f=5$, are selected to verify the independence of the solutions on the grid velocities.

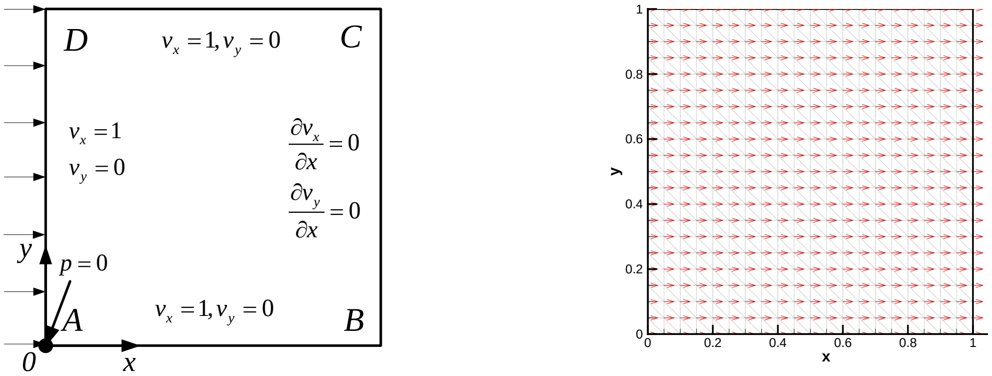

a) Boundary condition b) Initial velocity contour and mesh

Fig. 4.3 Illustration of a uniform flow passing a square

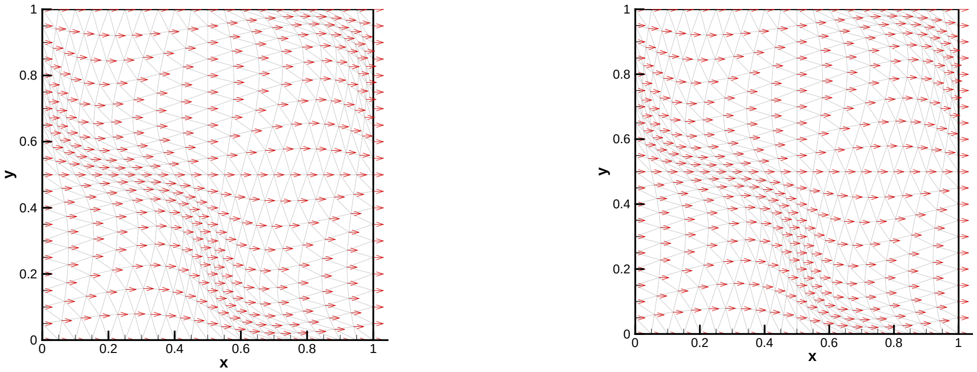

a) $f=1$ b) $f=5$

Fig. 4.4 Velocity contours and mesh configurations of two selected cases in the problem of a uniform flow passing a square

The initial mesh/velocity vector contour is shown in Fig. 4.3b. Two selected instant mesh configurations together with the calculated velocity vectors are plotted in Fig. 4.4, corresponding to *f*=1 and *f*=5, respectively. From these two figures it can be seen that the calculated velocities are constant in space and the uniform velocity field has been recovered by GSM/ALE, regardless of the velocity of mesh movement.

A quantitative comparison of the calculated results under these frequencies is presented based on the L_2 relative error norm given in Eq. (4.30) which measures the difference of the numerical and analytical results at every nodal point,

$$error = \left[\sum_{i=1}^{N_{node}} \left(\mathbf{U}_i - \hat{\mathbf{U}}_i \right)^2 \Big/ \sum_{i=1}^{N_{node}} \hat{\mathbf{U}}_i^2 \right]^{1/2} . \tag{4.30}$$

Here $\mathbf{U}_i$ and $\hat{\mathbf{U}}_i$ are the numerical and analytical results at node *i*, respectively.

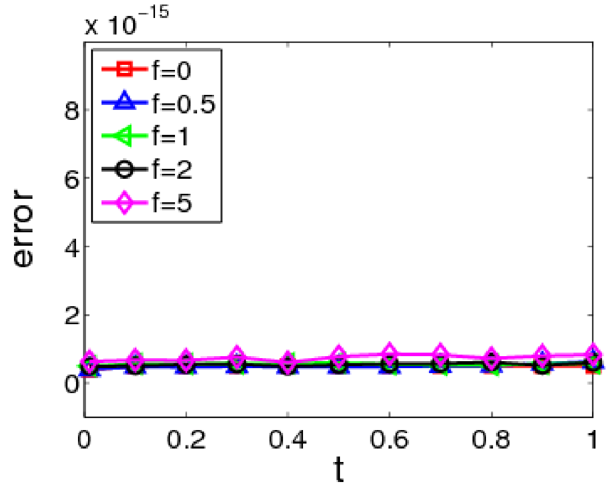

Fig. 4.5 Comparison of the L_2 relative error norms of the calculated solutions under different *f* for the uniform flow problem

Fig. 4.5 compares the numerical errors under these frequencies. From this figure it can be seen that these errors are extremely small and quite close to each other, which verifies that the proposed GSM/ALE satisfies the GCL regardless of the mesh movement and it can recover the uniform flow to a machine tolerance.

4.2.2 Poisson's problem

Poisson's equation governs many physical problems, such as heat conduction problems with sources sinks. In this section numerical tests for 2D Poisson's equation in a square computational domain, as shown in Fig. 4.6, are conducted to check the accuracy, spatial/temporal convergences and robustness in response to cell irregularity in the present GSM/ALE.

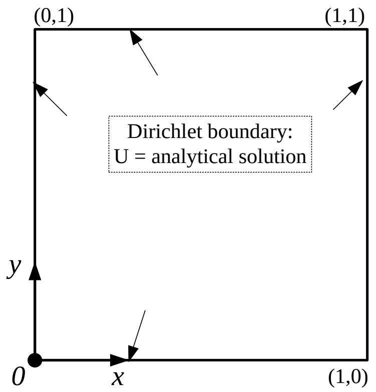

Fig. 4.6 Illustration of the Poisson problem

The governing equation under investigation takes the following form

$$\frac{\partial U}{\partial t}=\frac{\partial^2 U}{\partial x^2}+\frac{\partial^2 U}{\partial y^2}-f\left(x,y,t\right),\quad \left(0\le x\le 1,\ 0\le y\le 1\right) \tag{4.31}$$

where U is a scalar variable with any reasonable physical meanings; $f(x,y,t)$ is the source term of the corresponding governing equation. The steady-state solutions of U is calculated by adopting the pseudo-transient approach.

Two Poisson problems with variations in source and boundary conditions are studied here. For the first Poisson problem, the source and initial conditions are prescribed as

$$\left.\begin{array}{r} f\left(x,y,t\right)=13\exp\left(-2x+3y\right) \\ U\left(x,y,0\right)=0 \end{array}\right\},\quad \left(0\le x\le 1,\ 0\le y\le 1\right)\ . \tag{4.32}$$

As plotted in Fig. 4.7a, the analytical solution to this problem is given as

$$U\left(x,y\right)=\exp\left(-2x+3y\right),\quad \left(0\le x\le 1,\ 0\le y\le 1\right)\ . \tag{4.33}$$

For the second Poisson problem, the source, initial conditions and analytical solution are given as

$$\left.\begin{aligned} f\left(x,y,t\right) &= \sin(\pi x)\sin(\pi y) \\ U\left(x,y,0\right) &= 0 \end{aligned}\right\}, \quad \left(0 \le x \le 1,\ 0 \le y \le 1\right) \tag{4.34}$$

$$U\left(x,y\right) = -\frac{1}{2\pi^2}\sin(\pi x)\sin(\pi y), \quad \left(0 \le x \le 1,\ 0 \le y \le 1\right) \ . \tag{4.35}$$

The contour plot of the analytical solution to the second problem is shown in Fig. 4.7b.

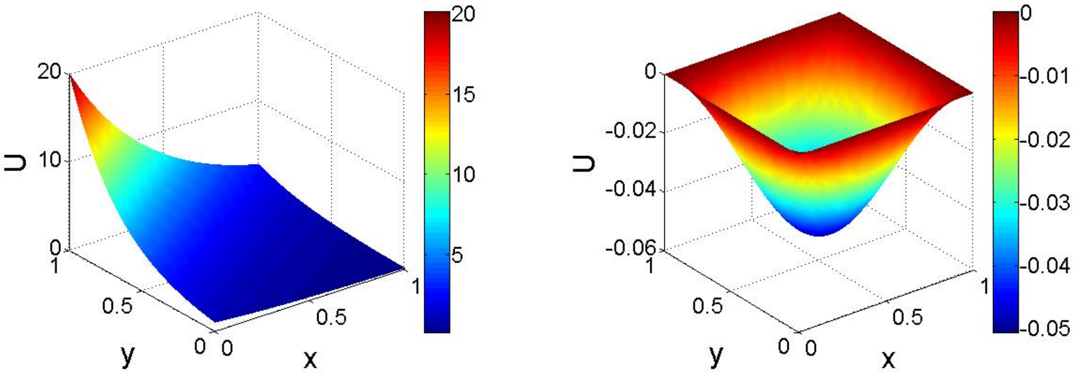

a) The first Poisson problem b) The second Poisson problem

Fig. 4.7 Contour plots of the exact solutions of the two Poisson problems

In a numerical calculation, the analytical solution given in either Eq. (4.33) or Eq. (4.35), is directly applied on the four edges of the square domain with the Dirichlet boundary conditions.

Spatial convergence of the present GSM/ALE is firstly conducted by using three sets of uniform triangular meshes of 30×30, 45×45 and 60×60. These meshes are artificially driven to deform according to Eq. (4.29) in the calculation. Parameters of the grid deformation are taken as follows: A_x= A_y=0.05, $\Delta t = 0.0005s$ and f=1. The L_2 relative error norm defined in Eq. (4.30) is used to measure the difference between the numerical and exact solutions.

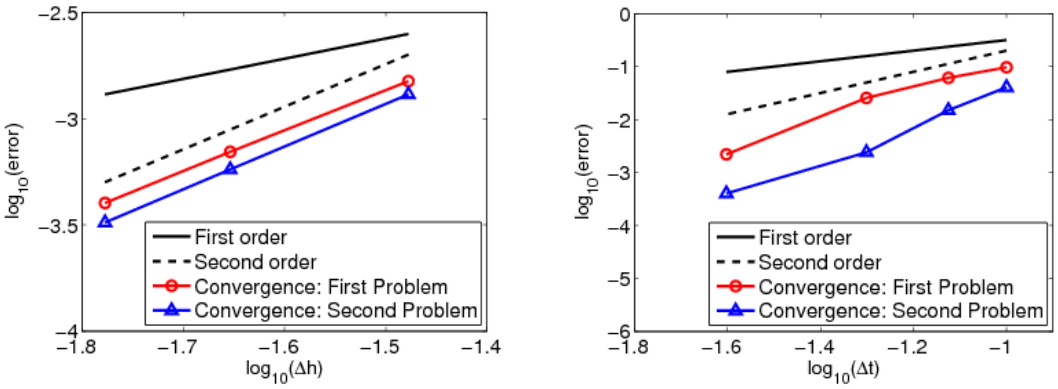

a) Spatial convergence b) Temporal convergence

Fig. 4.8 Convergence rates of the GSM/ALE in both spatial and temporal domains for the two Poisson problems

Fig. 4.8a plots the grid-convergence property of the present GSM/ALE. The solid and dashed lines indicate the first and second order accuracy slopes, respectively. From this figure, we can see that the L_2 relative error norms for both the first and second Poisson problems decrease asymptotically with Δh^2 in a manner supporting the expected second-order spatial accuracy of the present method, which is consistent with the truncation error analyses of the GSM on a fixed mesh [3].

The time step refinement study is then presented to evaluate the temporal convergence of the GSM/ALE. The mesh of 60×60 is used, and mesh movement parameters are A_x= A_y=0.05 and f=0.1. A series of successively refined time-steps (Δt =0.1s, 0.075s, 0.05s and 0.025s) are selected for the time refinement study. The L_2 relative error norms corresponding to each time steps are computed at the time $t = 0.4s$ when the field is still unsteady.

Fig. 4.8b shows the decay of the error as the time step is refined. The solid and dashed lines indicate the first and second order time accuracy slopes, respectively. Again a second order temporal accuracy of the present GSM/ALE is achieved for both the first and second Poisson problems. It is consistent with the second order accuracy of the BFD2 on fixed meshes [3, 9].

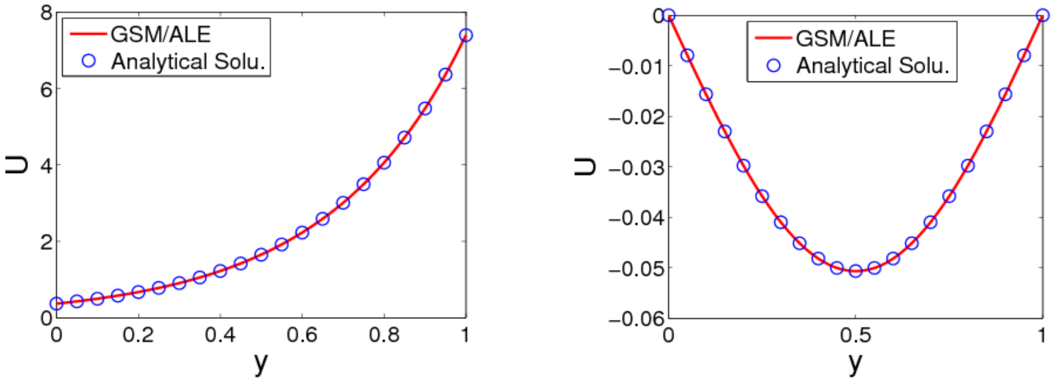

a) The first Poisson problem b) The second Poisson problem

Fig. 4.9 Comparisons of the numerical and analytical solutions along the vertical line across the center of the computational domain for the two Poisson problems

To further examine the calculated steady state solutions by GSM/ALE, comparisons with the analytical solutions along the vertical line across the geometric center of the domain are presented for both the first and second Poisson problems, as shown in Fig. 4.9. From this figure we can clearly see that the numerical solutions match very well with the analytical solutions, which indicates that the present GSM/ALE can give accurate results.

In the previous study [3, 19], it was found that the GSM on fixed mesh is remarkably robust and insensitive to cell irregularity which is attributed to the consistent use of smoothing techniques. In the present study the robustness of the present GSM/ALE to the irregularity of the cells is discussed to illustrate that the present GSM/ALE can also give accurate results even with very large mesh distortion. This is important because in the FSI problems especially where there are large deformations in solid domain the mesh condition is highly non-uniform. A method that can give accurate and stable results on those extremely distorted meshes will avoid or minimize the time consuming re-meshing process and the corresponding less accurate numeral interpolation procedure.

To indicate the distortions of the mesh, the coefficient of irregularity for all triangular cells in the computational domain, γ, is defined as [3, 20]

$$\gamma = \left[\sum_{i=1}^{N_{ele}} \frac{(a_i - b_i)^2 + (b_i - c_i)^2 + (c_i - a_i)^2}{a_i^2 + b_i^2 + c_i^2} \right] \Big/ N_{ele} \tag{4.36}$$

where a_i, b_i and c_i denote the lengths of the cell edges of a triangular cell, respectively; and N_{ele} stands for the total number of cells in the overall domain. A higher irregularity number means a worse (distorted) mesh condition.

A_x and A_y in Eq. (4.29) controls the amplitude of the mesh movement, thus the irregularity of the mesh. A series of A_x and A_y (A_x= A_y=0.025, 0.05, 0.075 and 0.1) are chosen here to deform the mesh. The corresponding maximum mesh deformations are shown in Fig. 4.10. The stretching and skewing of the mesh become significant with the increase of the amplitude. Contours of the calculated results based on these meshes are plotted in Fig. 4.11 and Fig. 4.12. From these two figures we can find that there is no significant difference among the contours for each problem, which indicates that the present GSM/ALE can give reasonable steady state solutions regardless of mesh distortion.

Table 4.1 L_2 relative error norms of the computed results under different mesh irregularities for the first/second Poisson problems

	Irregularity			
	0.0887	0.0979	0.1160	0.1499
First Problem	2.0520e-4	4.0076e-4	5.9985e-4	8.2594e-4
Second Problem	2.5557e-4	3.2436e-4	4.1677e-4	4.5501e-4

To quantify the effect of mesh distortion on the calculated results, the L_2 relative error norms of the numerical solutions based on different distorted meshes are listed in Table 4.1. From this table we can conclude that:

i) The L_2 relative error norms of the solutions on these highly distorted and rapidly moving meshes are of the same order and remain fairly small.

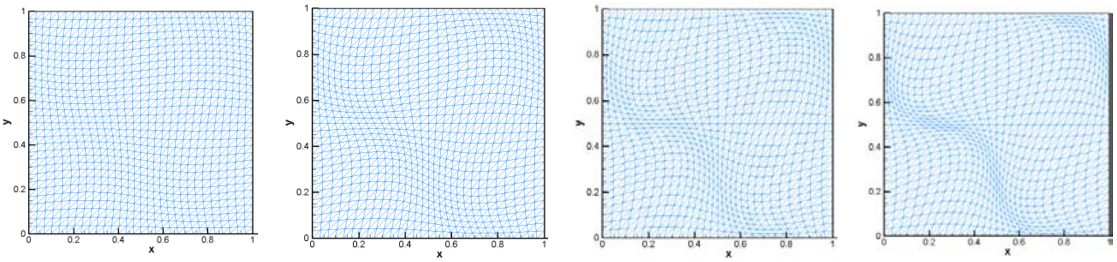

a) γ=0.0887 b) γ=0.0980 c) γ=0.1160 d) γ=0.1494

Fig. 4.10 Mesh of 30×30 with different irregularities for the two Poisson problems

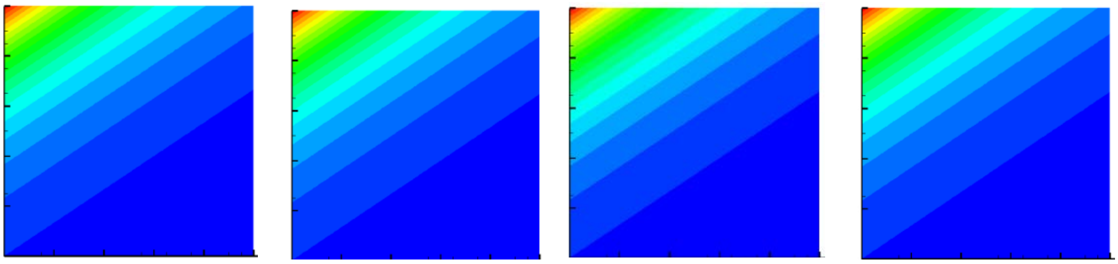

a) γ=0.0887 b) γ=0.0980 c) γ=0.1160 d) γ=0.1494

Fig. 4.11 Contour plots of the steady results for the first Poisson problem based on mesh of 30×30 with different irregularities

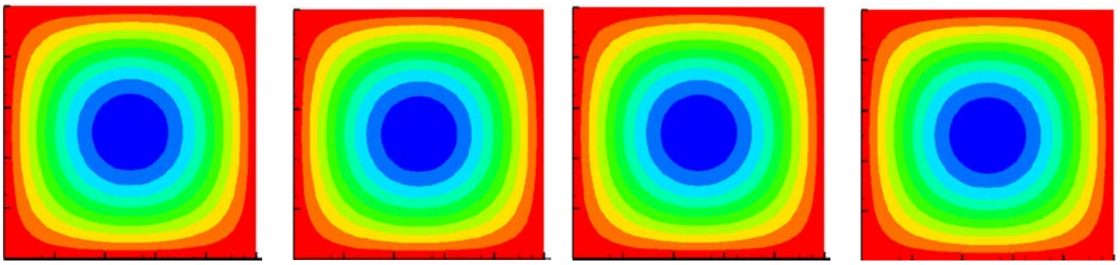

a) γ=0.0887 b) γ=0.0980 c) γ=0.1160 d) γ=0.1494

Fig. 4.12 Contour plots of the steady results for the second Poisson problem based on mesh of 30×30 with different irregularities

ii) With the increase of the irregularity, the L_2 relative error norm increases slightly, implying that the irregularity can affect the accuracy of the numerical solutions. Of course this effect is reasonable and limited in the calculations, and is also observed on the numerical calculations with fixed meshes in [3]. It thus suggests that the condition of element must not be extremely distorted, otherwise the re-meshing process is better suited to ensure a more accurate solution. Anyway, the GSM/ALE can still ensure reasonable accuracy in the presence of much distorted mesh.

iii) With the increase of the irregularity, a smaller time step is suggested to be used in the time integration process to ensure the stability and convergence of the calculation. This is because the critical time step in an explicit method is proportional to the characteristic length of an element. As the mesh becomes more and more distorted, the characteristic length of the quite distorted element becomes smaller, thus a smaller time step should be chosen to ensure the stability of the calculation.

iv) The CFL is important to ensure the stability of the numerical results. In the present CFL=0.2 is chosen for the case of γ=0.0887, 0.0980, 0.1160 and CFL=0.1 for γ=0.1494.

4.2.3 Lid-driven cavity flow

The lid-driven cavity flow is a benchmark problem designed to evaluate the behavior of the algorithms that deal with incompressible viscous flows [21-23]. The purpose of testing this problem in this subsection is to verify that the present GSM/ALE can give steady-state flows in the midst of arbitrarily mesh movement during the calculation.

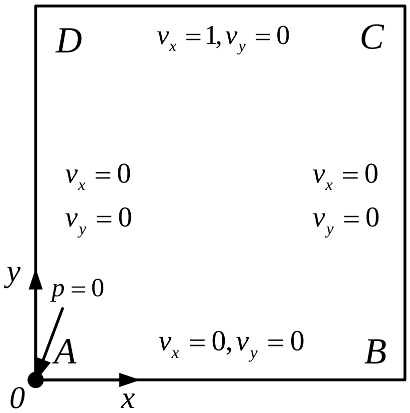

Fig. 4.13 Illustration of the lid-driven cavity problem

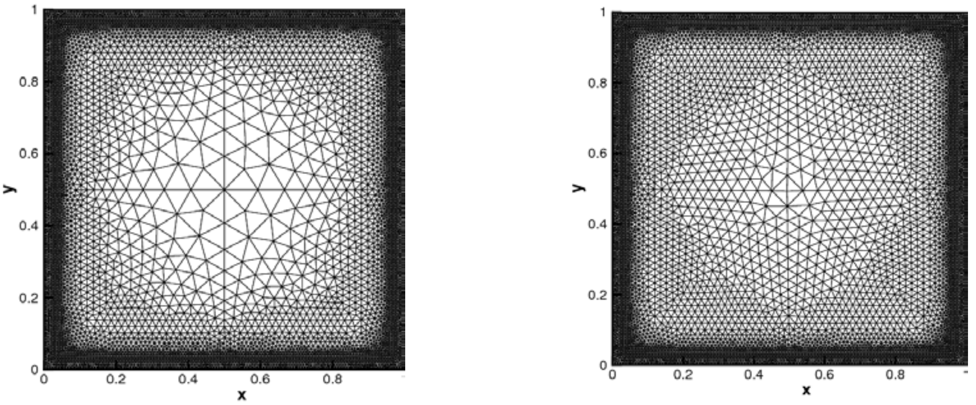

a) Initial coarse grid (n_{node}=3618) b) Initial fine grid (n_{node}=8151)

Fig. 4.14 Meshes used in the lid-driven cavity problem

Fig. 4.13 shows the geometric layout of the lid-driven cavity with the dimension of [0,1]×[0,1]. Incompressible viscous fluid is confined within a squared cavity in which only the upper edge is allowed to tangentially slide at a prescribed velocity (v_x=1 in this test). Meanwhile, non-slip conditions (v_x=v_y=0) are applied to the rest of the walls. Reference pressure is prescribed to be zero at the bottom left corner. Two sets of meshes are studied: the coarser mesh is used for lower Reynolds number flows (Re<1000), while the finer grid is adopted for larger Reynolds number flows (Re≥1000) where the more steeper boundary layers near walls are essentially required to be resolved by employment of finer grids, as shown in Fig. 4.14. The meshes inside the domain are driven to deform according to Eq. (4.29), the same as those in Subsections 4.1 and 4.2.

As a Hopf bifurcation will appear for larger Reynolds numbers (usually the critical Re =10000), Reynolds numbers below this critical value, i.e. Re=10, 100, 1000, 5000, are selected in this study to ensure a steady solution. In this test, CFL>10 is used. A much lower CFL (especially lower than 1) appears to induce unstable solutions.

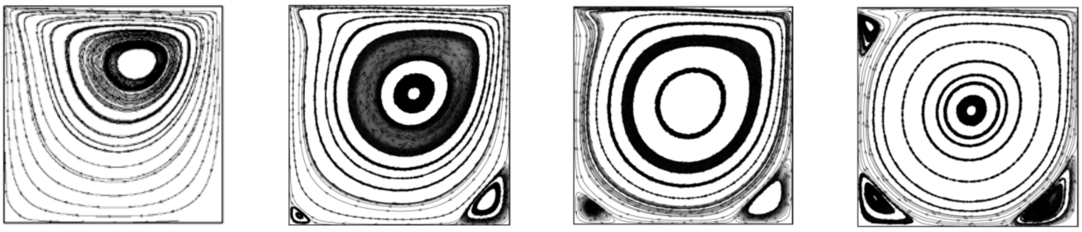

a) *Re*=100 b) *Re*=400 c) *Re*=1000 c) *Re*=5000

Fig. 4.15 Plots of streamlines for various Reynolds numbers of the lid-driven cavity problem

Numerical results by GSM/ALE on the streamfunctions for various Reynolds numbers are shown in Fig. 4.15. As is well known, the details about the vertical flow structures depend highly on Reynolds numbers. For cases of $Re \leqslant 1$, the flow is almost symmetric with respect to the central vertical line. As the Reynolds number increases, the position of the central vortex moves towards the top right corner before it returns again to the centre of the cavity at higher Reynolds numbers. The bottom right and left vortices begin to develop at low Reynolds numbers, and continuously increase in scale and shift their position, as Reynolds number increases. A secondary vortex is developed near the top left corner at *Re*=5000 approximately. All the above phenomena are well re-captured by the proposed GSM/ALE solver, as shown in Fig. 4.15.

The steady velocity components v_x and v_y along the vertical and horizontal lines through geometric center of cavity are plotted in Fig. 4.16 and Fig. 4.17, respectively, in which the results from GSM/ALE are compared with those from the GSM on fixed mesh as well as other references. From these figures it can be seen that the curves of GSM/ALE and GSM are extremely close to each other and both are close to the references. The wall boundary layer becomes thinner with the increase of *Re*, and the near-linearity of these velocity profiles in the central core of the cavity is indicative of the uniform vorticity region that develops here at large *Re* [21]. A slight difference of the curves between the GSM/ALE and GSM at *Re*=5000 should be due to the deformation of the mesh, as discussed in Section 4.2.

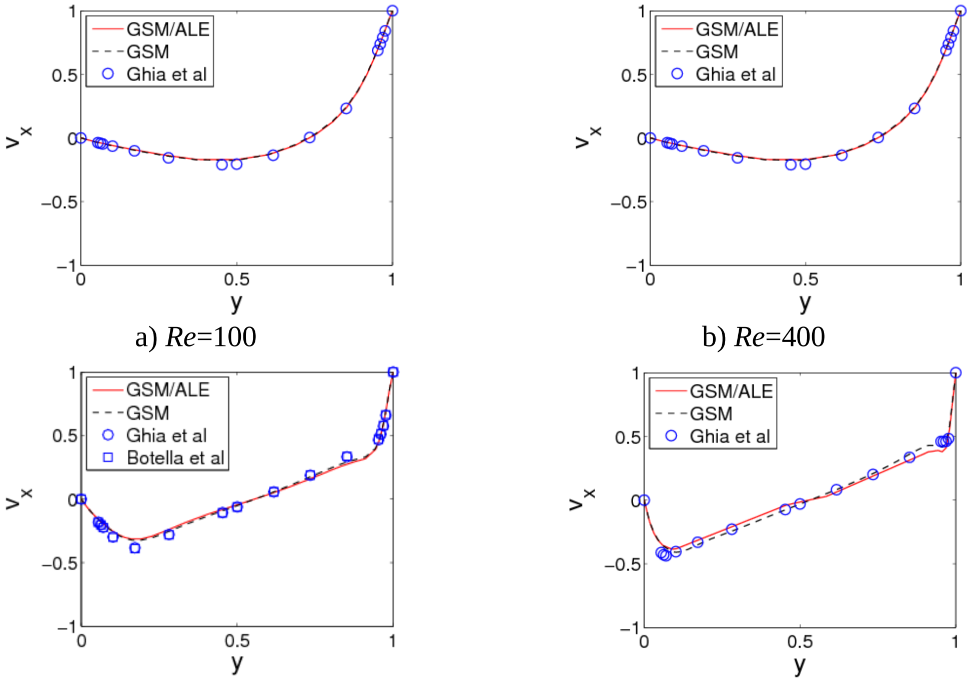

a) *Re*=100 b) *Re*=400

c) *Re*=1000 d) *Re*=5000

Fig. 4.16 Comparison of profiles of v_x along vertical line through geometric center of the cavity

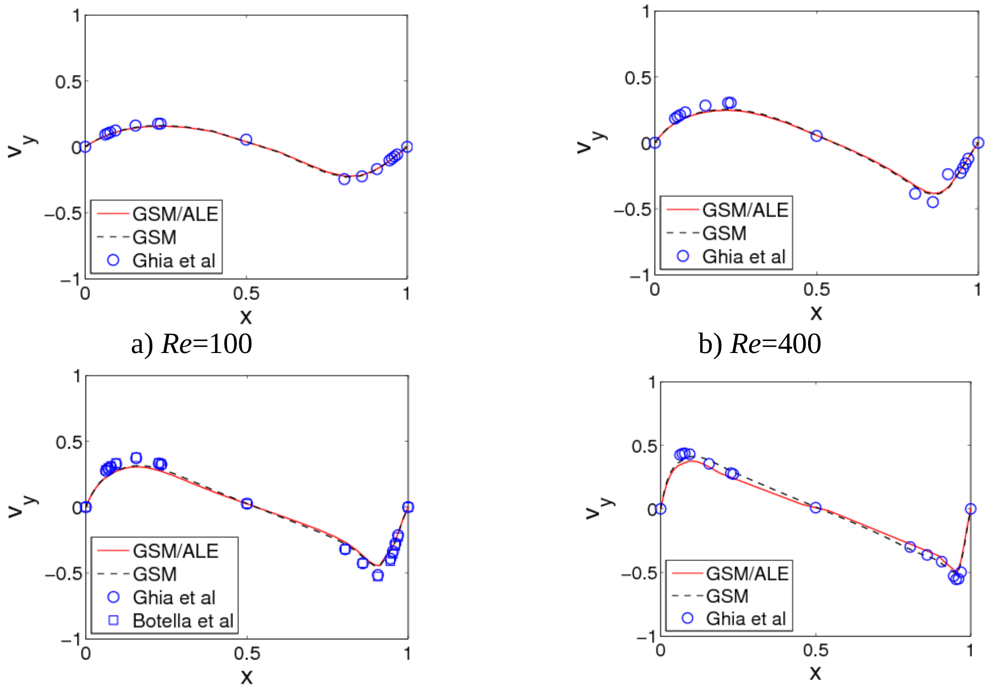

a) *Re*=100 b) *Re*=400

c) *Re*=1000 d) *Re*=5000

Fig. 4.17 Comparison of profiles of v_y along horizontal line through geometric center of the cavity

4.2.4 Flow past a cylinder

The rigid cylinder immersed in a uniform flow stream has been widely studied as a benchmark problem, in which the cylinder can be either fixed in space or forced cross-line/in-line oscillations with respect to the free stream direction. For a fixed cylinder, there is no interaction between the fluid and solid. However, for the forced cross-line/in-line oscillation cylinders, a nonlinear interaction will occur as the cylinder oscillation frequency approaches the vortex shedding frequency. The Strouhal shedding frequency (S_t for a fixed cylinder) will be suppressed and the vortex sheds according to the cylinder oscillation frequency over a range of flow velocities. If the cylinder oscillation frequency is near twice the S_t, both the drag and lift coefficients will increase greatly, called the phasing-locking phenomenon [24-26].

In the present section, both the stationary and cross-line/in-line oscillation cylinders immersed in a uniform flow are studied to verify that the current GSM/ALE can give correct steady-state and transient solutions with grid movement during the calculation. Experimental and other numerical results are sourced for comparison to the present calculation.

4.2.4.1 ***Flow past a stationary cylinder***

The uniform flow ($v_{x\infty}=1, v_{y\infty}=0$) past a stationary cylinder of radius r=0.5 is firstly studied, as shown in Fig. 4.18a. Characteristic based farfield boundary conditions are imposed at the external boundary of the computational domain (R=15r), and non-slip wall boundary conditions are imposed onto the surface of the cylinder. Initially, the independent variables in the fluid domain are set to be v_x=1, v_y=0 and p=0.

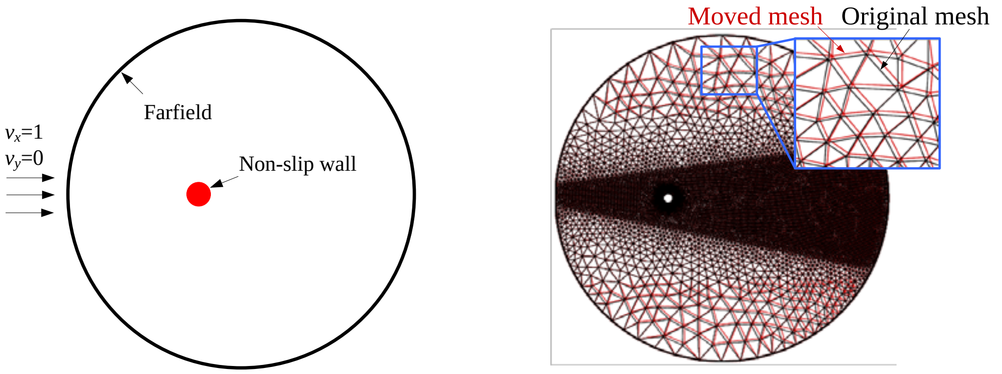

a) Geometry b) Original/moved unstructure meshes

Fig. 4.18 Illustration of the uniform flow over a stationary/cross-line/in-line oscillating cylinder

A set of unstructured triangular meshes (10079, 14152, 29770 and 38321 nodes) with a higher grid density near the surface of the cylinder are generated. To derive these meshes in the fluid domain, the excitation function similar with Eq. (4.29) is imposed,

$$\begin{cases} x = x_0 + A_x a \\ y = y_0 + A_y a \end{cases}. \tag{4.37}$$

The physical interpretation of the parameters in Eq.(4.37) are exactly the same as those in Eq. (4.29) except that $a = l_{io} \sin\left(2\pi ft\right) / R$, in which l_{io} is the distance of the arbitrary point i to the origin o, R is the radius of the outward circle. The parameter values of A_x=A_y=0.2, f=10 and Δt=0.01s are used in the calculation. It is found that the solutions converge on the mesh of 29770 and 38321 nodes with almost identical solutions. Thus in the following simulations, the set of mesh of 29770 nodes is used. One configuration of this deformed mesh is plotted in Fig. 4.18b.

During the simulation the drag/lift coefficients and the Strouhal number are used as a criterion to judge the performance of the numerical method,

$$C_D = \frac{F_D}{0.5\rho v_{x\infty}^2 D} \tag{4.38}$$

$$C_L = \frac{F_L}{0.5\rho v_{x\infty}^2 D} \tag{4.39}$$

where ρ is the density of the fluid; D is the characteristic length of the cylinder; $v_{x\infty}$ is the farfield velocity of the fluid for the stationary cylinder case; and F_D and F_L are the drag and lift force, respectively, which arise from two sources, i.e. the shear stress τ_{ij} and the pressure p distribution along the surface of the body,

$$F_i = \sum_{k=1}^{N_{wall}} \left(f_i \right)_k = \sum_{k=1}^{N_{wall}} \left\{ \left[-p\delta_{ij} + \mu \left(\frac{\partial v_i}{\partial x_j} + \frac{\partial v_j}{\partial x_i} \right) \right] n_j l \right\}_k . \tag{4.40}$$

Parameter f_i is the surface force component in x_i direction; i, j=1 or 2 denotes the direction of x or y, corresponding to F_D and F_L, respectively; n_j is the direction cosine of **n** in x_j direction; N_{wall} denotes the total number of elements on the wall; and l_k is the length of the k^{th} edge.

When the flow becomes oscillatory, the originally stationary vortices behind the cylinder start moving downstream and shed alternatively with frequency f_o. The Strouhal number (S_t) is the dimensionless frequency of vortex shedding, defined as

$$S_t = \frac{f_o D}{v_{x\infty}} \tag{4.41}$$

where f_o is the frequency of vortex shedding, which is obtained from the dimensionless time period T_o during vortices shedding, $f_o = 1/T_o$.

As is well known, the uniform flow with a fixed cylinder is characterized by the Reynolds number. In general, as $Re \leqslant 40$, there is a steady state solution in which two symmetrical eddies develop behind the cylinder. As the Reynolds number increases further, the flow becomes unstable and a periodic vortex shedding, known as Von Karman Vortex Street, forms behind the cylinder. Both phenomena resulting from varied Reynolds number have been simulated in the current study.

i) Steady state flow

The steady state flow with *Re*=30 is studied in this subsection. Fig. 4.19 shows the evolution of eddies behind the cylinder in term of streamlines by both GSM and GSM/ALE. As schematically illustrated in Fig. 4.19a, the reattachment length (S), which is measured from the right end point of the cylinder to the reattachment point where the two eddies end is monitored, and the normalized attachment lengths by the diameter of the cylinder are summarized in Table 4.2. In comparison with the experiment data by Teneda [27], numerical results with domain decomposition method from Huang *et al* [28] and the numerical results from the GSM on fixed mesh, it is clear that the GSM/ALE gives the same results as the GSM and matches quite well with the references. Comparing the drag and lift coefficients, as plotted in Fig. 4.20, we can see that constant drag and lift coefficients (C_D=1.72 and C_L=0) are obtained for the steady flow and these coincide with those from GSM, which confirms that the present GSM/ALE can give accurate results regardless of mesh movement.

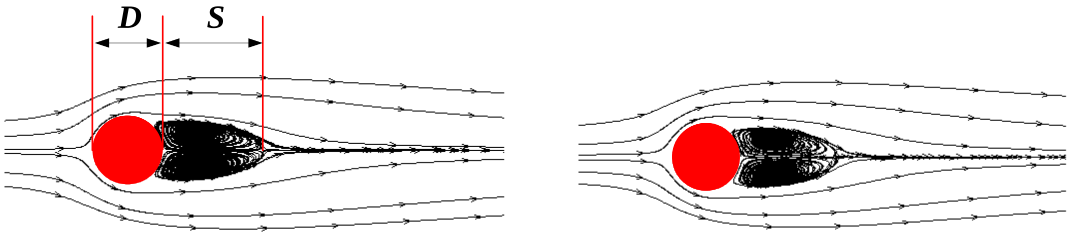

a) Streamline from GSM b) Streamline from GSM/ALE

Fig. 4.19 The streamlines of the flow over a stationary cylinder at *Re*=30

Table 4.2 Comparisons of the predicted reattachment length ratios S/D at *Re*=30 of a stationary cylinder in uniform flow

Re	Present	GSM [3]	Exp [27]	DDM [28]
30	1.5	1.5	1.49	1.27

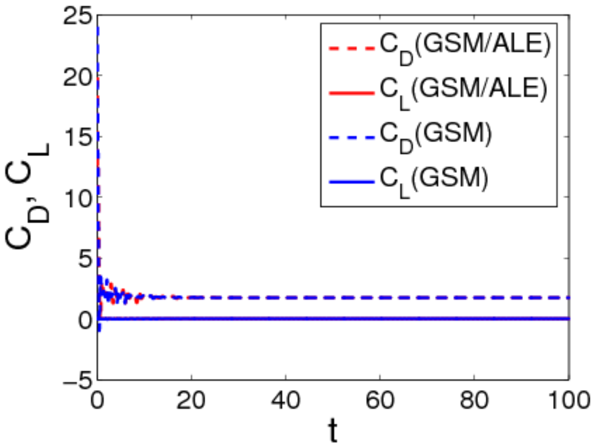

Fig. 4.20 Variation of drag and lift coefficients (C_D and C_L) with time in the case of uniform flow over a stationary cylinder at *Re*=30

ii) Time-dependent flow

The setting of time-dependent flow is the same as that in the last section except at hither *Re*=150. Key parameters depicting the vortex shedding change, i.e. the lift and drag coefficients and the Strouhal number, are calculated. Fig. 4.21 plots the time history of the drag and lift coefficients. The oscillating behavior of the time-dependent flow is related to the vortex shedding change. The lift coefficient settles to a regular sinusoidal function after the onset of wake instability leads to vortex shedding, as shown in the enlarged part of Fig. 4.21. Table 4.3 lists a detailed comparison of these three parameters with the reference data. From these comparisons, it is clear that the calculated three parameters by GSM/ALE are the same as those by the GSM, and they match quite well with the references. The GSM/ALE can give the correct transient results for this unsteady flow problem.

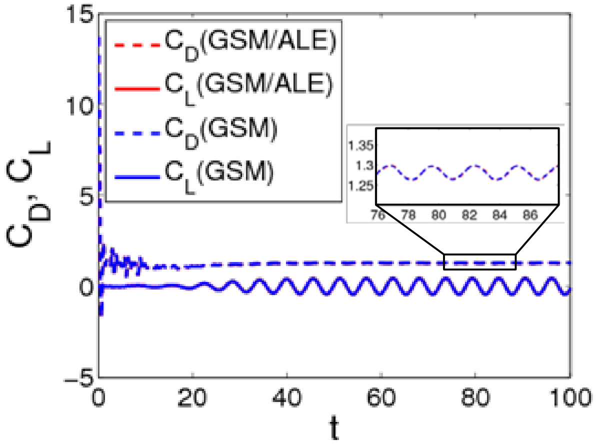

Fig. 4.21 Variation of drag and lift coefficients (C_D and C_L) with time in the case of uniform flow over a stationary cylinder at *Re*=150

Table 4.3 Comparisons of the predicted C_D, C_L and S_t at *Re*=150 in the case of a stationary cylinder in a uniform flow

	Present	GSM [3]	Lin [29]	Kallinderis and Ahn [30]	Belov [31]	Relf (exp) [32]
C_D	1.28±0.02	1.28±0.02	1.380±0.027	1.166±0.023	1.168±0.025	1.33
C_L	±0.45	±0.45	±0.561	±0.477	±0.486	-
S_t	0.18	0.18	0.19	0.18	0.18	-

4.2.4.2 *Cross-line oscillating cylinder in a free stream*

The uniform flow past a circular cylinder oscillating in the direction normal to the incoming flow is a classical test [18, 25], as shown in Fig. 4.22. Transverse oscillation of the cylinder in *y* direction is defined as

$$v_c = 2\pi\left(\frac{f_e}{f_o}\right)A_m S_t \cos\left[2\pi\left(\frac{f_e}{f_o}\right)S_t t\right] \tag{4.42}$$

where v_c is the transverse velocity; A_m is the amplitude of the transverse, $A_m = a_m / D$; S_t is the Strouhal number, $S_t = f_o D / U_\infty$; f_e is the frequency of oscillating cylinder and f_o is the natural shedding frequency the same as illustrated in the previous subsection; and *t* is the physical time.

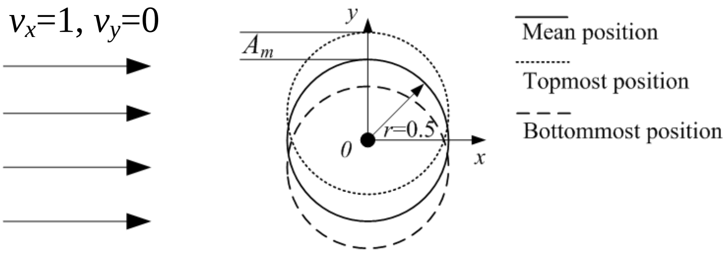

Fig. 4.22 Illustration of the cross-line oscillation of the cylinder in a uniform flow

Parameters governing this flow is chosen as follows: the Reynolds number is fixed at Re=185 and the Strouhal number is taken as S_t=0.19, similar with those in [18, 25]. Amplitude of the transverse (A_m) is set to be 0.2. Three different frequency ratios, i.e. f_e/f_o=0.9,1.0,1.1, are chosen to examine the dynamic response of the flow problems. The physical time interval of $\Delta t = 0.01s$ is used to march in the temporal domain. Since the flow is unsteady, the calculation will not be terminated until obvious transients died out and then for a time roughly equivalent to the time required for steady state in the lock-in cases. The wake characteristics generated by the cylinder are compared with the numerical results in [18, 25] through time series analysis and examination of instantaneous streamline and vorticity patterns.

Fig. 4.23 shows the time history of drag/lift coefficients at different frequency ratios. From this figure it is found that fairly regular drag/lift coefficients are generated once vortex shedding is established. For the value of f_e/f_o=0.9 and 1.0, the drag/lift coefficients exhibit sine/cosine behaviors. For the value of f_e/f_o=1.1, the drag/lift coefficients exhibit regular signs of the influence of a higher harmonic. A comparison of the peak lift coefficient, and the peak and average drag coefficient under different frequency ratio are presented in Table 4.4. From this table it can be seen that the calculated values by the GSM/ALE can match those from the references quite well. The slight differences among these values may be due to different parameter settings in the problem, e.g. different number of nodes, densities of the mesh and different time intervals used in the time integration.

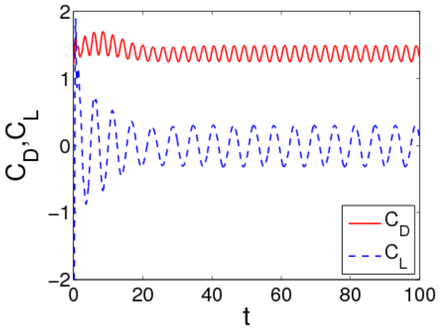

a) f_e/f_o=0.9

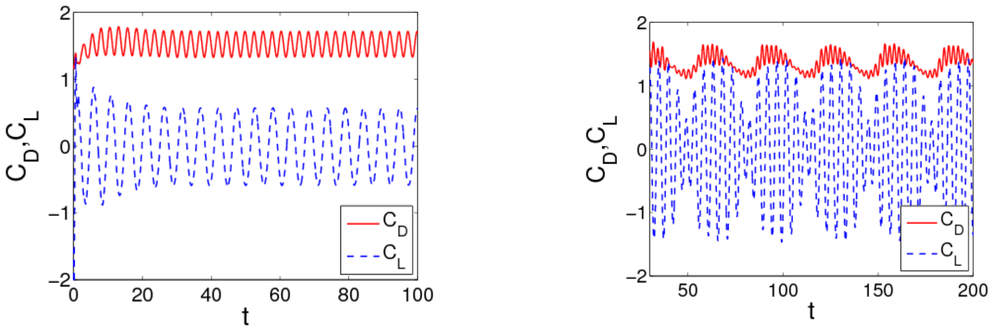

b) f_e/f_o=1.0 c) f_e/f_o=1.1

Fig. 4.23 Time history of the drag and lift coefficients (C_D and C_L) at different frequency ratios at Re=185 with A_m =0.2 in the case of the cross-line oscillation of the cylinder in a uniform flow

Table 4.4 Comparisons of the predicted C_D, C_L at Re=185 in the case of a cross-line oscillating cylinder in uniform flow

f_e/f_o	Coefficient of lift peak value			Coefficient of drag (mean/maximum/minimum)		
	Present	[18]	[25]	Present	[18]	[25]
0.9	0.278	0.242	0.247	1.33/1.45/1.21	1.34/1.44/1.25	1.31/1.47/1.20
1.0	0.592	0.590	0.585	1.49/1.72/1.26	1.51/1.68/1.30	1.51/1.70/1.29
1.1	1.438	1.449	1.450	1.36/1.65/1.12	1.45/1.71/1.104	-/1.71/1.10

Fig. 4.24 shows the instantaneous streamlines when the oscillating cylinder is at the topmost position of the oscillation cycle. From this figure it can be seen that for f_e/f_o =0.9 and 1.0, the general form of the streamline patterns are almost the same. However, for f_e/f_o =1.1 two saddle points are found in the form of closed streamlines which indicates a concentration of vorticity around the center of the closed

streamlines. These phenomenon is captured well by the present GSM/ALE which are similar with those described in [18, 25].

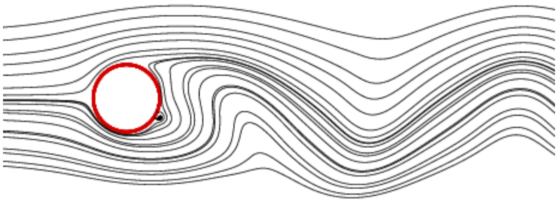

a) f_e/f_o=0.9

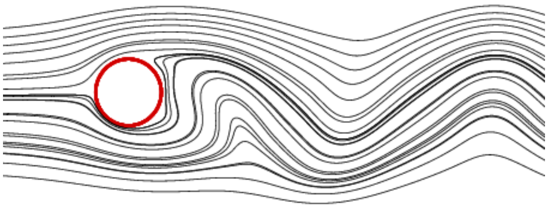

b) f_e/f_o=1.0

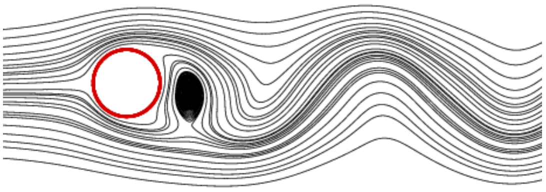

c) f_e/f_o=1.1

Fig. 4.24 Instantaneous streamline patterns at different frequency ratios at *Re*=185 with A_m =0.2 when the cylinder is at the topmost position in the case of the cross-line oscillation of the cylinder in a uniform flow

The instantaneous vorticity contours corresponding to the top position of the oscillation cycle are shown in Fig. 4.25. The vortices in the wake are also well captured by the present GSM/ALE. With the increase of f_e/f_o, it is found: i) the length of the elongated upper vortex decreases and diminishes in strength; ii) the lower vortex becomes the dominant vortex; iii) more vorticities are formed on the lower portion of the cylinder surface, and the base vorticity of opposite sense interacts with the vorticity in the upper shear layer to constraint the roll up in the wake [18].

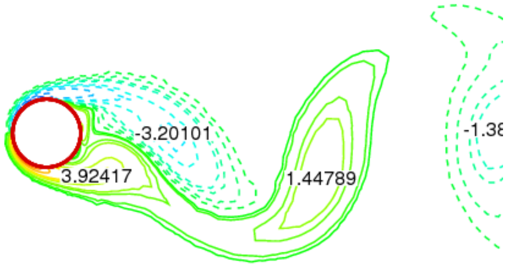

a) f_e/f_o=0.9

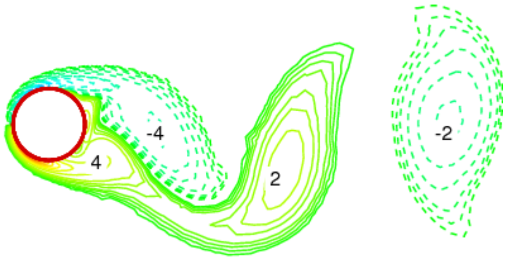

b) f_e/f_o=1.0

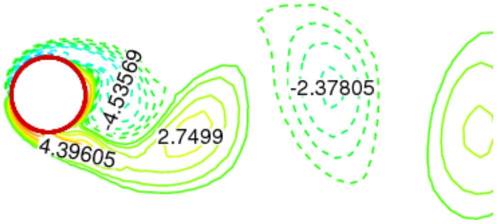

c) f_e/f_o=1.1

Fig. 4.25 Instantaneous vorticity contours at different frequency ratios at *Re*=185 with A_m =0.2 when the cylinder is at the topmost position in the case of the cross-line oscillation of the cylinder in a uniform flow: dotted and solid lines denote, respectively, the negative and positive contours

4.2.4.3 *In-line oscillating cylinder in a free stream*

In order to further explore the capability of the present GSM/ALE in computing moving boundary flows, a series of simulations are conducted for the case of in-line oscillating cylinder in a uniform stream at *Re*=100. The calculation domain and the boundary conditions are exactly the same as those for the cross-line oscillating cylinder problem, except that the cylinder is forced to oscillate parallel to the free stream by setting the horizontal velocity of the cylinder as

$$v_{in} = 2\pi f_e A_m \cos\left(2\pi f_e t\right). \qquad (4.43)$$

Here, A_m is the amplitude of the oscillation (A_m=0.14D as that in [24]); f_e is the oscillation frequency of the cylinder, and f_e =2f_o, i.e. two times of the natural vortex shedding frequency f_o of the fixed cylinder flow. The CFL number is about 10 in the present calculation.

Accordingly, the lock-in should occur at an oscillation frequency about twice the shedding frequency [24]. In this calculation, the natural vortex shedding frequency is f_o =0.165 which is comparable to the references as listed in Table 4.5.

Table 4.5 Comparisons of shedding frequency at Re=100 in the case of a in-line oscillating cylinder (f_e/f_o=0) in a uniform flow

	Present	Lai *et al.* [33]	Liu *et al.* [34]	Lima *et al.* [35]	Williamson (Exp) [36]
f_o	0.165	0.165	0.164	0.160	0.166

Fig. 4.26 plots the drag and lift coefficients during the lock-in. From this figure it can be seen that the drag and lift coefficients are characterized by periodic oscillations about a mean value and zero, respectively. The frequency of lift coefficient under f_e/f_o =2 is the same as that under f_e/f_o =0, which is half of that of the drag coefficient. Table 4.6 compares the computed drag and lift coefficients with those from references. From this table we can see that the values from the present GSM/ALE are compatible with those from the references. A slightly lower estimation of the mean drag coefficient is predicted by the present GSM/ALE, either for f_e/f_o=0 or for f_e/f_o=2. However, the maximum lift coefficient matches quite well with the references. From the table, we can also see that during the lock-in the computed lift amplitude is approximately three times than that obtained from a fixed cylinder at the same Re, and there is an obvious increase in mean drag over the rigid-cylinder value. This is consistent with the results from previous experiments and numerical studies, demonstrating that the present method can capture the important flow characteristics very well for this in-line oscillating problem.

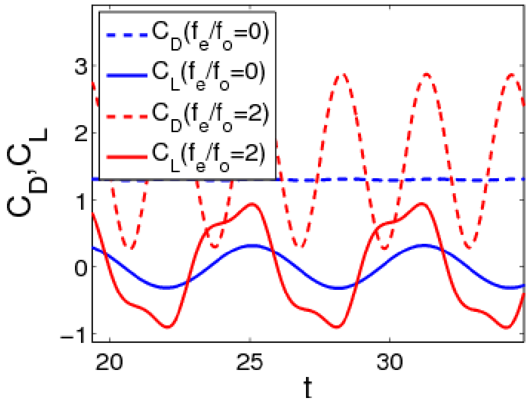

Fig. 4.26 Time history of drag and lift coefficients (C_D and C_L) at *Re*=100 with A_m =0.14*D* for stationary (f_e/f_o=0) and in-line oscillating (f_e/f_o=0) circular cylinder in a uniform flow

Table 4.6 Comparisons of the predicted C_D, C_L at *Re*=100 in the case of a in-line oscillating cylinder (f_e/f_o=0 and f_e/f_o=2) in a uniform flow

	Present		Liao *et al.* [26]		Hurlbut *et al.* [24]		Calhoun [37]	
f_e/f_o	0	2	0	2	0	2	0	2
$C_{D\text{-mean}}$	1.30	1.61	1.36	1.71	1.41	1.68	1.33	-
$C_{L\text{-max}}$	0.32	0.94	0.34	0.95	0.31	0.95	0.30	-

Examination of the vortex patterns is referred in the instantaneous vorticity contours over two oscillation periods of the cylinder as shown in Fig. 4.27. From this figure it can be seen that the wake is captured by the cylinder oscillation. The lock-in effect can be observed by the vortex patterns over two period of drag coefficient oscillation. Here “T” is the period of oscillation of the cylinder (the drag coefficient), and the period of the lift coefficient is 2T. Due to the lock-in effect, the contours indicate an essentially periodic behavior with a period equal to that of the enforced oscillations.

To further check that the ability of the present GSM/ALE to deal with the large movement of the solid, a series of the amplitude of the oscillation A_m, i.e. A_m=0.14*D*, 0.20*D*, 0.30*D*, 0.35*D*, 0.40*D* and 0.50*D*, is chosen. The oscillation frequency of the cylinder f_c is still kept at f_e=2f_o.

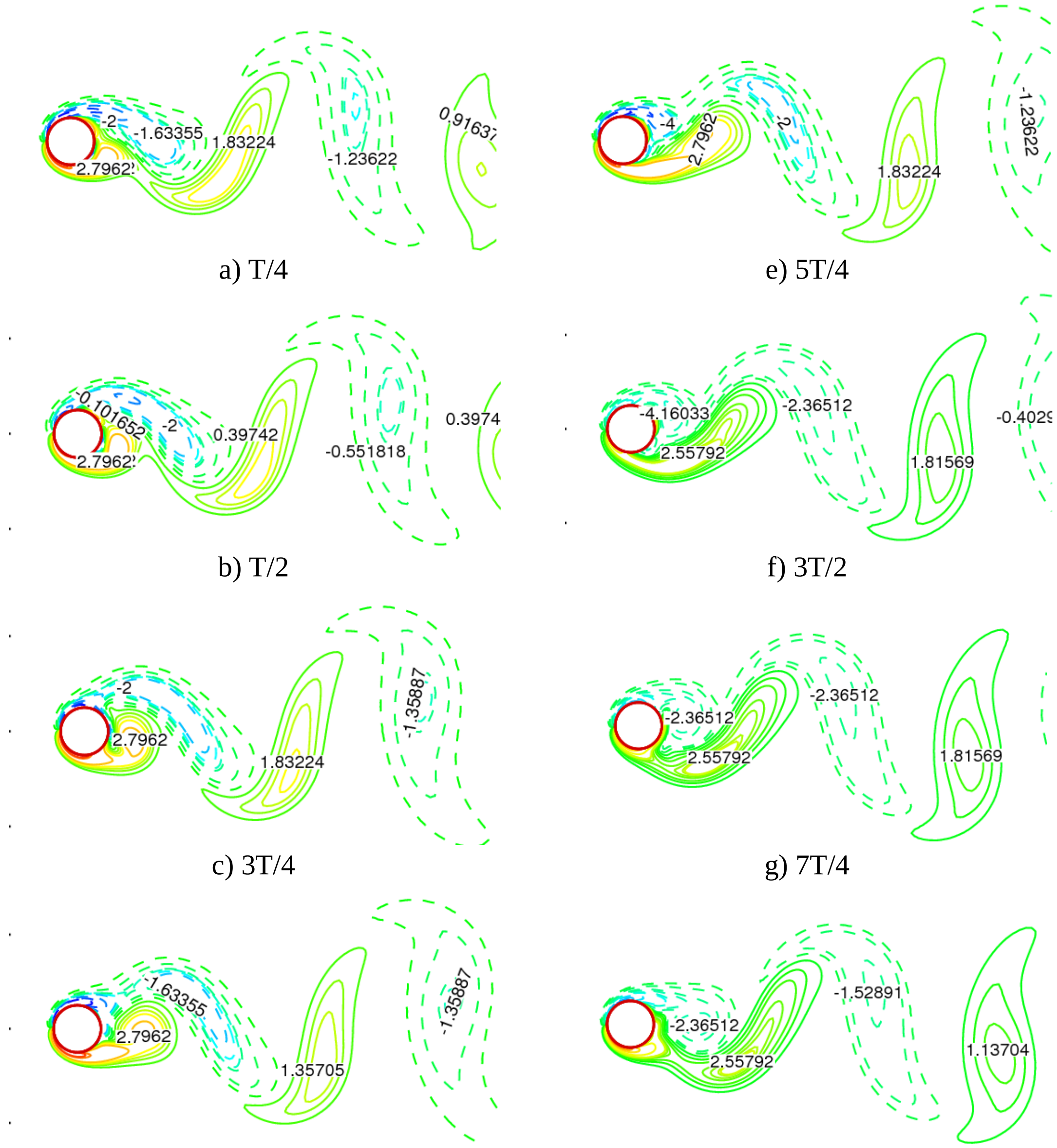

a) T/4 e) 5T/4

b) T/2 f) 3T/2

c) 3T/4 g) 7T/4

d) T h) 2T

Fig. 4.27 Instantaneous vorticity contours near oscillating cylinder at *Re*=100: dotted and solid lines denote, respectively, the negative and positive contours

Fig. 4.28 plots the time history of the drag and lift coefficients with different A_m. From this figure, we can see that: i) the time period of the drag/lift coefficients relates to the oscillation frequency of the cylinder f_e. ii) With the increase of the A_m, the maximum of drag coefficient becomes larger, which implies that a larger A_m will induce a larger drag force. iii) The maximum of lift coefficient, however, does not increase monotonically. It increases with the increase of A_m from 0.14*D* to 0.30*D*.

Then this value will become smaller with the increase of A_m. When the A_m =0.50*D*, the maximum of lift coefficient becomes extremely small, and it is comparable with that at A_m =0.40*D*. This trend may be illustrated by the shedding of the vortex with different A_m.

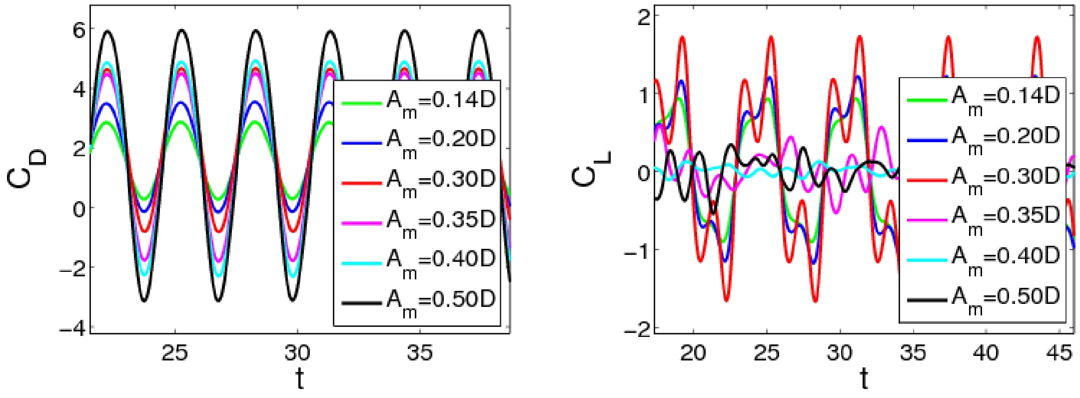

a) C_D b) C_L

Fig. 4.28 Time history of drag and lift coefficients (C_D and C_L) at *Re*=100 for a in-line oscillating (f_e/f_o=2) circular cylinder in a uniform flow at various A_m, A_m=0.14*D*, 0.20*D*, 0.30*D*, 0.35*D*, 0.40*D* and 0.50*D*

Vortex contours with different A_m are plotted in Fig. 4.29. These contours correspond to the time instant *t*=T/4 in one typical period cycle. From this figure, we can see that the ratio of positive and negative contours behind the cylinder becomes larger with the increase of A_m from 0.14*D* to 0.30*D*, which suggests that asymmetry of the positive and negative contours becomes larger. After that the positive and negative contours behind the cylinder become more and more symmetric, with A_m from 0.35*D* to 0.50*D*. As is known, the lift coefficient is direct proportion to the lift force. When the vortex contour becomes more symmetric, the difference of the positive and negative tractions becomes smaller. As the lift force comes from the integration of the surface traction, it and thus the lift coefficient will become smaller.

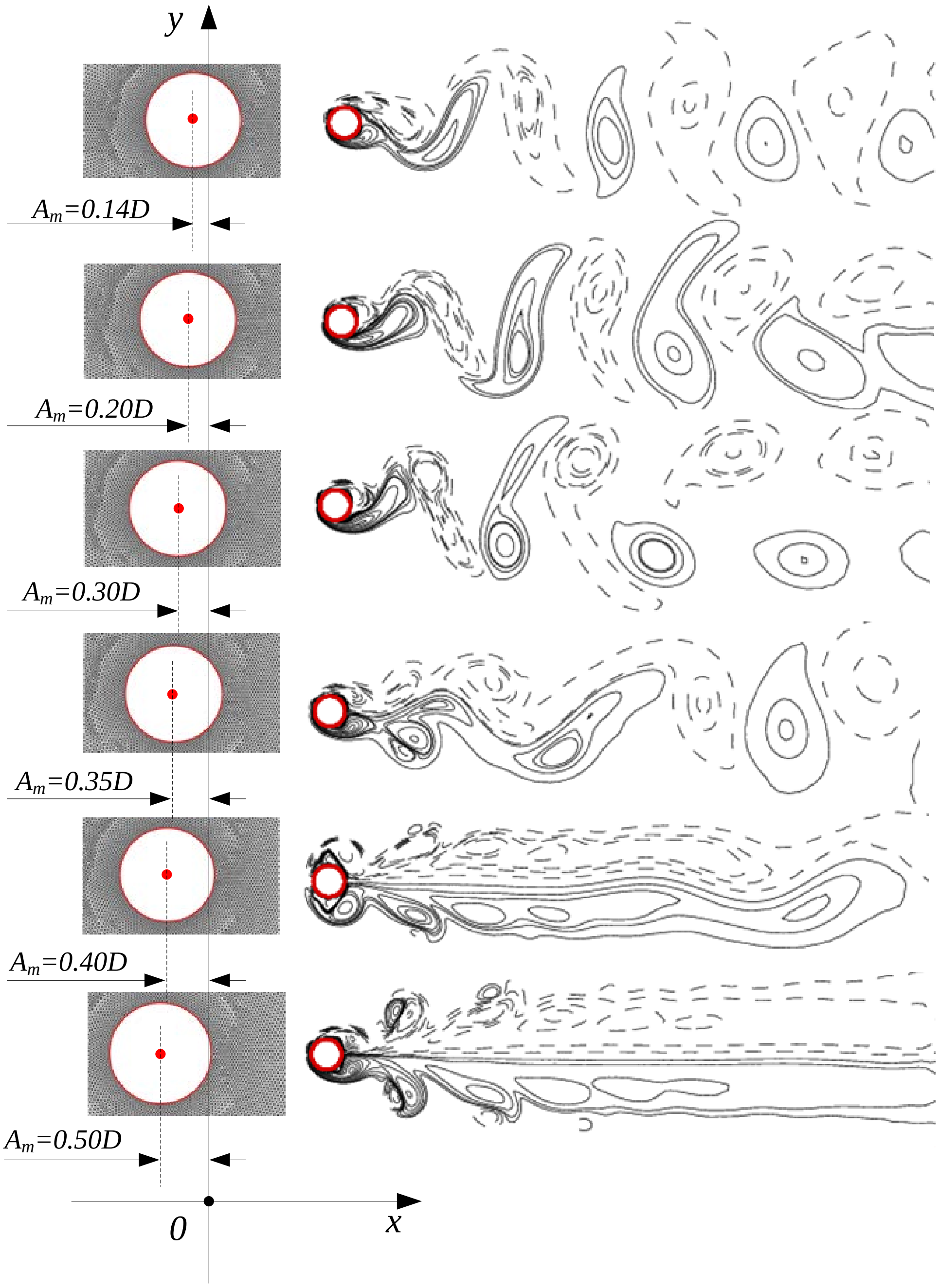

Fig. 4.29 Instantaneous vorticity contours near the oscillating cylinder at *Re*=100 with different A_m at *t*=T/4 in a period: dotted and solid lines denote, respectively, the negative and positive contours

4.3 Concluding remarks for Chapter 4

The GSM/ALE is successfully formulated for solving the fluid-rigid structure interaction problems. The uniform flow is automatically preserved irrespective of the mesh movement by adding an extra moving mesh source term derived from the GCL. The 2nd order accuracies are achieved in both spatial and temporal domains, which are the same as those in GSM on fixed mesh. Robustness of GSM/ALE to distorted meshes is discussed. Overall, our finding shows that the GSM/ALE can give accurate and stable results on extremely distorted meshes. However, a smaller time step should be chosen on those meshes to ensure the stability of the scheme. The corresponding numerical errors also become larger with the increase of the irregularity. So it is suggested that should irregularity become extreme, a re-meshing is still needed to ensure more accurate result. The proposed GSM/ALE has been applied to solve several benchmark problems and yields good agreement with referenced computational and experimental results, hence further indicating the viable use of the proposed method. During the calculation of the in-line oscillation of a cylinder in a free stream, an interesting phenomenon is found that the drag coefficient becomes larger with the increase of the maximum oscillation of the cylinder. However, the lift coefficient does not purely increase. When the maximum oscillation exceeds a critical value, the lift coefficient will decrease with the increase of the maximum oscillation, and the corresponding vortex behind the cylinder will then become more and more symmetric.

References for Chapter 4

1. Liu, G.R., Zhang, J., Lam, K.Y., Li, H., Xu, G., Zhong, Z.H., Li, G.Y. and Han, X., *A gradient smoothing method (GSM) with directional correction for solid mechanics problems.* Computational Mechanics, 2008. **41**(3): p. 457-472.
2. Xu., G.X., Liu, G.R. and Tani, A., *An adaptive gradient smoothing method (GSM) for fluid dynamics problems.* International Journal for Numerical Methods in Fluids, 2010. **62**(5): p. 499-529.
3. George, X.X. *Development of Gradient Smoothing method (GSM) for Fluid Flow Problems*. Department of Mechanical Engineering, 2009, Ph.D. thesis, National University of Singapore: Singapore.
4. Mavriplis, D.J. and Yang, Z., *Construction of the discrete geometric conservation law for high-order time-accurate simulations on dynamic meshes.* Journal of Computational Physics, 2006. **213**(2): p. 557-573.
5. Thomas, P.D. and Lombard, C.K., *Geometric conservation law and its application to flow computations on moving grids.* AIAA Paper, 1979. **17**(10): p. 1030-1037.
6. Visbal, M.R. and Gaitonde, D.V., *On the use of higher-order finite-difference schemes on curvilinear and deforming meshes.* Journal of Computational Physics, 2002. **181**(1): p. 155-185.
7. Koobus, B. and Farhat, C., *Second-order time-accurate and geometrically conservative implicit schemes for flow computations on unstructured dynamic meshes.* Computer Methods in Applied Mechanics and Engineering, 1999. **170**(1-2): p. 103-129.
8. Geuzaine, P., Grandmont, C. and Farhat, C., *Design and analysis of ALE schemes with provable second-order time-accuracy for inviscid and viscous flow simulations.* Journal of Computational Physics, 2003. **191**(1): p. 206-227.
9. Ahn, H.T. and Kallinderis, Y., *Strongly coupled flow/structure interactions with a geometrically conservative ALE scheme on general hybrid meshes.* Journal of Computational Physics, 2006. **219**(2): p. 671-696.
10. Gordnier, R.E. and Melville, R.B., *Transonic flutter simulations using an implicit aeroelastic solver.* Journal of Aircraft, 2000. **37**(5): p. 872-879.
11. Lesoinne, M. and Farhat, C., *Geometric conservation laws for flow problems with moving boundaries and deformable meshes, and their impact on aeroelastic computations.* Computer Methods in Applied Mechanics and Engineering, 1996. **134**(1-2): p. 71-90.
12. Roe, P.L., *Approximate Riemann solvers, parameter vectors, and difference schemes.* Journal of Computational Physics, 1981. **43**(2): p. 357-372.
13. Belytschko, T., Liu, W.K. and Moran, B., *Nonlinear finite elements for continua and structures*. 2000: John Wiley & Sons Ltd., Baffins Lane, Chichester, West Sussex, PO191 UD, England.
14. Donea, J., Huerta, A., Ponthot, J.P. and Rodríguez‐Ferran, A., *Arbitrary Lagrangian‐Eulerian methods.* Encyclopedia of Computational Mechanics, 2004.
15. Blazek, J., *Computational fluid dynamics: principles and applications*. 2005: Elsevier Science.

16. Viale, M. and Nigro, N., *Stabilized finite element method with an ALE strategy to solve moving boundaries problems.* Universidad Nacional de Rosario Pelegrini, 2000.
17. Kwak, D., Chang, J.L.C., Shanks, S.P. and Chakravarthy, S.R., *A three-dimensional incompressible Navier-Stokes flow solver using primitive variables.* AIAA Paper, 1986. **24**: p. 390-396.
18. Anwer, S.F., Hasan, N., Sanghi, S. and Mukherjee, S., *Computation of unsteady flows with moving boundaries using body fitted curvilinear moving grids.* Computers & Structures, 2009. **87**(11-12): p. 691-700.
19. Liu, G.R. and George, X.X., *A gradient smoothing method (GSM) for fluid dynamics problems.* International Journal for Numerical Methods in Fluids, 2008. **58**(10): p. 1101-1133.
20. Luo, H., Baum, J.D. and Lohner, R. *An improved finite volume scheme for compressible flows on unstructured grids*. *33rd Aerospace Sciences Meeting and Exhibit*. 1995. Reno, NV, UNITED STATES.
21. Ghia, U., Ghia, K.N. and Shin, C.T., *High-Re solutions for incompressible flow using the Navier-Stokes equations and a multigrid method.* Journal of Computational Physics, 1982. **48**(3): p. 387-411.
22. Su, S.W., Lai, M.C. and Lin, C.A., *An immersed boundary technique for simulating complex flows with rigid boundary.* Computers & Fluids, 2007. **36**(2): p. 313-324.
23. Bruneau, C.H. and Saad, M., *The 2D lid-driven cavity problem revisited.* Computers & Fluids, 2006. **35**(3): p. 326-348.
24. Hurlbut, S., Spaulding, M. and White, F., *Numerical solution for laminar two dimensional flow about a cylinder oscillating in a uniform stream.* Journal of Fluids Engineering, 1982. **104**: p. 214.
25. Guilmineau, E. and Queutey, P., *A numerical simulation of vortex shedding from an oscillating circular cylinder.* Journal of Fluids and Structures, 2002. **16**(6): p. 773-794.
26. Liao, C.C., Chang, Y.W., Lin, C.A. and McDonough, J.M., *Simulating flows with moving rigid boundary using immersed-boundary method.* Computers & Fluids, 2010. **39**(1): p. 152-167.
27. Taneda, A.S., *Experimental investigation of the wakes behind cylinders and plates at low Reynolds numbers.* Journal of the Physical Society of Japan, 1956. **11**(3): p. 302-307.
28. Huang, Y., Deng, J. and Ren, A., *Research on lift and drag in unsteady viscous flow around circular cylinders.* Zhejiang University Engineering Science, 2003. **37**(5): p. 596-601.
29. Lin, P., Martinelli, L., Baker, T.J. and Jameson, A. *Two-dimensional implicit time dependent calculations for incompressible flows on adaptive unstructured meshes*. *15th Computational Fluid Dynamics Conference*. 2001. Anaheim, CA.
30. Kallinderis, Y. and Ahn, H.T., *Incompressible Navier-Stokes method with general hybrid meshes.* Journal of Computational Physics, 2005. **210**(1): p. 75-108.
31. Belov, A., Martinelli, L. and Jameson, A., *A new implicit algorithm with multigrid for unsteady incompressible flow calculations*, in *33rd Aerospace Sciences Meeting and Exhibit*. 1995: Reno, NV.

32. Relf, E.F., *Discussion of the results of measurements of the resistance of wires, with some additional tests on the. resistance of wires of small diameter.* R. & M., 1914. **102**.
33. Lai, M.C. and Peskin, C.S., *An Immersed Boundary Method with Formal Second-Order Accuracy and Reduced Numerical Viscosity.* Journal of Computational Physics, 2000. **160**(2): p. 705-719.
34. Liu, C., Zheng, X. and Sung, C.H., *Preconditioned multigrid methods for unsteady incompressible flows.* Journal of Computational Physics, 1998. **139**(1): p. 35-57.
35. Lima, E.S., Silveira-Neto, A. and Damasceno, J., *Numerical simulation of two-dimensional flows over a circular cylinder using the immersed boundary method.* Journal of Computational Physics, 2003. **189**(2): p. 351-370.
36. Williamson, C.H.K., *Defining a universal and continuous Strouhal–Reynolds number relationship for the laminar vortex shedding of a circular cylinder.* Physics of Fluids, 1988. **31**: p. 2742-2744.
37. Calhoun, D., *A Cartesian grid method for solving the two-dimensional streamfunction-vorticity equations in irregular regions.* Journal of Computational Physics, 2002. **176**(2): p. 231-275.

Chapter 5

Coupling GSM/ALE with ES-FEM-T3 for fluid-deformable structure interactions

The fluid-rigid body interaction problems have been successfully solved via GSM/ALE in the previous chapter. In these cases the interaction between the fluid flow and rigid body is only one-way, i.e. the movement of the rigid body only affects the fluid flow but the dynamic force due to the viscous fluid flow does not affect the predefined movement of the rigid body. In this chapter, the solid body will be dealt as a deformable media, e.g. beam, shell/plate or structure, and thus the interactions between the fluid and solid become two-way, i.e. the deformation of the solid will affect the fluid flow and in return the dynamic force from the viscous fluid flow will also feed back to the deformation of the solid body. In order to successfully achieve the two-way interaction, the displacement/velocity compatibility and traction equilibrium need to be exactly satisfied at the FSI interface.

The weak coupling scheme is employed in the present study to enable the fluid and solid potions can be solved separately with different numerical methods. In the calculation, the conditions of displacement/velocity compatibility and traction equilibrium should be successively applied on the FSI interface to “link” these two portions. For the fluid portion, the GSM/ALE established in the previous chapter can be directly used with only minor modifications. For the solid portion, the explicit time integration ES-FEM-T3 will be used to describe its transient deformations. It should be noted that the formulation procedure of the transient deformation of the solid with ES-FEM-T3 in this FSI analysis is somewhat similar with that in Chapter 3 in the description of the dynamics of the nonlinear membrane structures except for the coordinates transformation part since no rigid body motion (rotation or translation) is considered in the deformation of the solid body in the present FSI analysis. Thus detailed procedures of constructing the kind of explicit time integration ES-FEM-T3 will be presented in this chapter. An illustration of the weak coupling scheme is shown in Fig. 5.1.

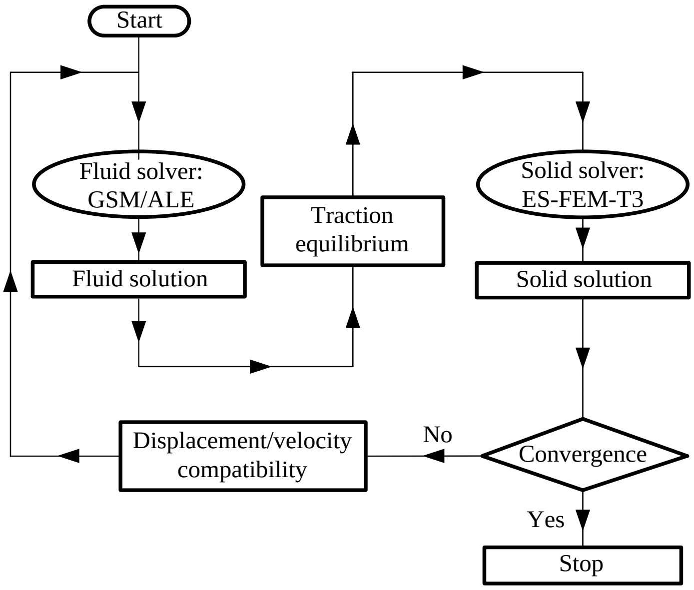

Fig. 5.1 Illustration of the weak coupling GSM/ALE with ES-FEM-T3 for solving FSI problems

The outline of this chapter is as follows. In order to give a clear description and easy illustration of the coupling scheme, the governing equations of both fluid and solid are firstly recalled and written as a system of equations together with the coupling conditions in Section 5.1. The formulation on solving the transient deformation of the solid portion with ES-FEM-T3 is presented in Section 5.2. A summary of implementing the GSM/ALE with ES-FEM-T3 for an FSI analysis is illustrated in Section 5.3. Three benchmarks are tested to verify the proposed coupling smoothed methods in Section 5.4. And some concluding remarks are drawn in Section 5.5.

5.1 Governing equations of fluid flows with structural interactions

Consider a FSI system with a deformable solid body fully immersed in a 2D incompressible viscous fluid flow, as illustrated in Fig. 5.2. The fluid and solid domains are denoted as Ω^{f} and Ω^{s} and bounded by Γ^{f} and Γ^{s}, respectively. The interaction interface between Ω^{f} and Ω^{s} is denoted by Γ^{fsi}. The fluid boundary Γ^{f} in this FSI system is composed by $\Gamma^{\mathrm{f}} = \Gamma^{\mathrm{fD}} \cup \Gamma^{\mathrm{fN}} \cup \Gamma^{\mathrm{fsi}}$ and the solid boundary is by $\Gamma^{\mathrm{s}} = \Gamma^{\mathrm{sD}} \cup \Gamma^{\mathrm{sN}} \cup \Gamma^{\mathrm{fsi}}$. Here the superscript "D" denotes Dirichlet boundary condition while superscript "N" denotes Neumann boundary condition applicable to both fluid and solid portions. Note that these boundaries should have no overlaps with each other. The other superscripts "f", "s" and "fsi" marked in these notations indicate the "fluid", "solid" and "fluid-structure interaction", respectively. These same superscripts will be further used to denote the variables below to indicate if a variable belongs to the fluid domain, solid domain or FSI interface. Because of the deformation of the solid, Ω^{f} and Ω^{s} are both time-dependent that leads to the transient movement of the FSI interface Γ^{fsi}.

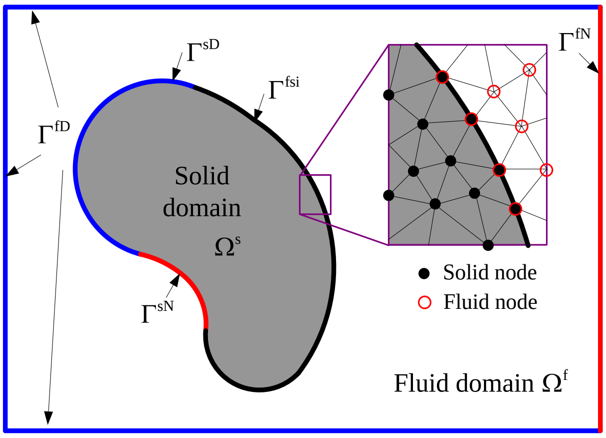

Fig. 5.2 Illustration of a FSI system

Theoretically in a FSI system: i) the fluid and solid domains can be discretized by two different sets of meshes with completely different element types and ii) the fluid and solid mesh nodes on the FSI interface Γ^{fsi} need not coincide with each other [1]. In the present study, we only use the simplest linear triangular element in both the fluid and solid domains, and the densities of the fluid and solid mesh nodes on the FSI interface are set to be the same, as illustrated in the enlarged part in Fig. 5.2. So that the fluid and solid nodes coincide with each other on the FSI interface, which greatly facilitate the applications of the coupling conditions of displacement compatibility and traction equilibrium. For the case where the fluid and solid mesh nodes do not coincide with each other on the FSI interface, interpolations of the displacements/velocities and tractions should be done with the help of shape functions of the solid element along the FSI interface [2-5], and even more some special techniques, e.g. constructing a reference FSI interface Γ_r^{fsi}, need to be introduced beyond the FSI interface to ensure the stability and accuracy of the interpolation in solving the FSI system [6-9].

In the present FSI analysis, the fluid flow is assumed to be incompressible or slight compressible and the solid is assumed to be fully-incompressible/nearly-incompressible or compressible and undergoing only a small volume change. As both the fluid and solid portions are continuums, equations governing these two mediums should have the same form. Although the governing equations of the individual fluid and solid portions have been independently presented in the previous chapters, they are rewritten here as one system with the coupling boundary conditions on the FSI interface, as shown in Eq. (5.1). For the sake of simplicity, the boundary conditions of velocities and tractions unrelated to the FSI interface are omitted in Eq. (5.1). Details of applying the relevant boundary conditions can be found in the corresponding parts in the previous two chapters. The combined governing equations are:

$$\begin{cases} \text{Fluid}: \\ \rho^{\mathrm{f}} \dfrac{\mathrm{D}v_i^{\mathrm{f}}}{\mathrm{D}t} = \mathrm{div}\sigma_{ij}^{\mathrm{f}} + \rho^{\mathrm{f}} g_i \\ \dfrac{\partial v_i^{\mathrm{f}}}{\partial x_j^{\mathrm{f}}} = 0 \\ \text{Solid}: \\ \rho^{\mathrm{s}} \dfrac{\mathrm{D}v_i^{\mathrm{s}}}{\mathrm{D}t} = \mathrm{div}\sigma_{ij}^{\mathrm{s}} + \rho^{\mathrm{s}} g_i \\ \text{FSI coupling conditions}: \\ u_i^{\mathrm{m,fsi}} = u_i^{\mathrm{s,fsi}},\ v_i^{\mathrm{f,fsi}} = v_i^{\mathrm{m,fsi}} = v_i^{\mathrm{s,fsi}} \\ n_j^{\mathrm{s,fsi}} \sigma_{ji}^{\mathrm{s,fsi}} = -n_j^{\mathrm{f,fsi}} \sigma_{ji}^{\mathrm{f,fsi}} \end{cases} , \quad i, j = x, y \tag{5.1}$$

where ρ, v_i, σ_{ij} and g_i, denote the density, components of velocity, Cauchy stress tensor and body force, respectively; t is the physical time; $n_j^{\mathrm{s,fsi}}$ and $n_j^{\mathrm{f,fsi}}$ are the outward normal of Γ^{fsi} as seen from the solid and fluid domains, respectively, which have the same amplitudes but opposite signs, as illustrated in Fig. 5.3; "*x*" and "*y*" denotes the two directions of a 2D Cartesian coordinate system; and the derivative $\mathrm{D}v_i/\mathrm{D}t$ denotes the material derivation of the velocity v_i.

The expansions of $\mathrm{D}v_i/\mathrm{D}t$ are different according to different descriptions, e.g. the Lagrangian, Eulerian or ALE descriptions, which requires particular numerical method for solving the expanded system equations. In practice the fluid is usually described with Eulerian description while the solid is described with Lagrangian description. In order to couple the fluid and solid in an FSI analysis, the ALE description is usually used.

5.1.1 For the fluid portion

As reviewed in Chapter 1, when the fluid flow is described with Eulerian description, the convection of momentum across the edge of the fluid mesh occurs and the velocity v_i^{f} is a function of both time-dependent Eulerian coordinates **x** and time *t*. In that case, the material derivative of the fluid velocities $\mathrm{D}v_i^{\mathrm{f}} / \mathrm{D}t$ should be fully expanded as

$$\frac{\mathrm{D}v_i^{\mathrm{f}}}{\mathrm{D}t} = \frac{\partial v_i^{\mathrm{f}}}{\partial t} + v_j^{\mathrm{f}} v_{i,j}^{\mathrm{f}} . \tag{5.2}$$

Especially, when the material derivative of the fluid velocity is fully expanded over the moving mesh instead of the Eulerian mesh, it becomes [3, 5]

$$\frac{\mathrm{D}v_i^{\mathrm{f}}}{\mathrm{D}t} = \frac{\partial v_i^{\mathrm{f}}}{\partial t} + \left(v_j^{\mathrm{f}} - v_j^{\mathrm{m}} \right) v_{i,j}^{\mathrm{f}} \tag{5.3}$$

where $\partial(\cdot)/\partial t$ is the transient term at the mesh position considered; v_j^{m} is the mesh velocity (the superscript “m” indicates the “mesh”) and v_j^{f} is the actual fluid particle velocity at that mesh point. In the solution process, v_j^{m} should be prescribed according to the mesh updating algorithm [5].

After substituting Eq. (5.3) back into the first equation of Eq. (5.1), the resultant equation can then be used to derive the ALE form of the governing equations as presented in Chapter 4, which will be finally solved with GSM/ALE in the fluid domain in an FSI analysis. Detailed formulation procedures of GSM/ALE have already been established in Chapter 4 and will not be repeated in this chapter.

5.1.2 For the solid portion

If the momentum conservation equation of the solid in Eq. (5.1) is described with Lagrangian description, the velocity v_i^{s} is thus a function of time-independent

Lagrangian coordinates **X** and time *t*. So the material derivative of the solid velocities $\mathrm{D}v_i^{\mathrm{s}}/\mathrm{D}t$ becomes a partial derivative of v_i^{s} [10], i.e.

$$\frac{\mathrm{D}v_i^{\mathrm{s}}}{\mathrm{D}t}=\frac{\partial v_i^{\mathrm{s}}}{\partial t}. \tag{5.4}$$

After substituting Eq. (5.4) into the third equation of Eq. (5.1), the resultant equation will be numerically solved with the explicit time integration ES-FEM-T3 to obtain the deformation of the solid portion. Detailed formulation procedures of the explicit ES-FEM-T3 will be presented below in Section 5.2.

5.1.3 For the FSI coupling conditions

In the weak coupling scheme, the fluid and solid domains are solved separately, and the information of displacement/velocity and traction on the FSI interface are successively transferred to these two domains during the time intervals according to the conditions of displacement/velocity compatibility and traction equilibrium on the FSI interface [2, 4, 5]. An illustration of the displacement/velocity and FSI force existing on the FSI interface is presented in Fig. 5.3. These conditions must be imposed carefully and efficiently in the numerical implementation.

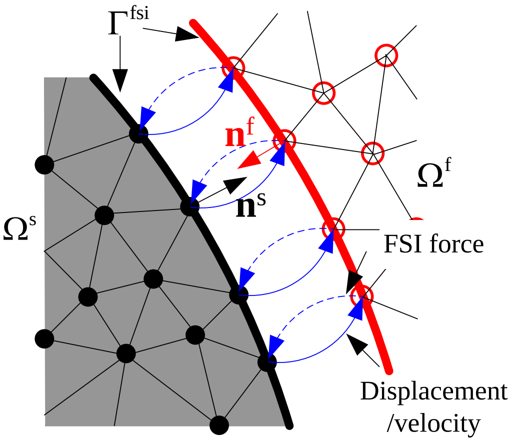

Fig. 5.3 Illustration of weak coupling: the dash arrows indicate FSI force mapping, the solid arrows indicate displacement/velocity mapping and **n** denotes the outward normal

5.1.3.1 Displacement/velocity compatibility

Displacement/velocity compatibility requires that: i) the FSI interface should exactly follow the deformation of the solid portion, i.e. $u_i^{\mathrm{m,fsi}} = u_i^{\mathrm{s,fsi}}$ on Γ^{fsi} at each time step, so that there is no gaps or overlaps between the solid and fluid domains near the FSI interface; and ii) the velocities of the fluid particle and fluid mesh node on Γ^{fsi} should be equal to the velocity of the solid node at the same point, i.e. $v_i^{\mathrm{f,fsi}} = v_i^{\mathrm{m,fsi}} = v_i^{\mathrm{s,fsi}}$ on Γ^{fsi} at each time step, so as to ensure the non-slip condition on the FSI interface. The accelerations of the mesh and solid nodes usually need not be the same at the same point on the FSI interface [1]. As a summary, the implementation orders of applying the displacement/velocity compatibility condition are i) solid→fluid mesh and ii) solid→fluid particle,

- Solve the solid problem to get the displacements and velocities of the nodes at the FSI interface
- Update the nodal coordinates/velocities of the fluid mesh on the FSI interface according to the nodal displacements/velocities of the solid at the same point on the FSI interface
- Update the nodal fluid velocities on the FSI interface according to the nodal velocities of the solid at the same point on the FSI interface

After determining the nodal coordinates and velocities of the fluid mesh on the FSI interface, these values inside the fluid domain should also be updated timely according to different mesh updating algorithms, e.g. simple velocity/displacement interpolation algorithm [11-14] and "pseudo-structure" algorithm [15-20], so as to ensure the accuracy of the fluid mesh inside the fluid domain.

5.1.3.2 Traction equilibrium

The condition of traction equilibrium is proposed to ensure the “consistency” in the stress transfer (or stress balance) between the fluid and solid portions, i.e. solid traction $t_i^{\mathrm{s,fsi}} = n_j^{\mathrm{s,fsi}} \sigma_{ji}^{\mathrm{s,fsi}}$ at an arbitrary node on the FSI interface Γ^{fsi} should be equal to the opposite of the fluid traction $t_i^{\mathrm{f,fsi}} = n_j^{\mathrm{f,fsi}} \sigma_{ji}^{\mathrm{f,fsi}}$ at the same point. This transferred traction will be further integrated along the solid interface in the current configuration to get the external nodal force on the solid portion, as follows

$$f_{Ii}^{\mathrm{s,fsi}}\left(\mathbf{v}^{\mathrm{f}}, p\right) = \int_{\Gamma_{IJ}^{\mathrm{fsi}}} N_I n_j^{\mathrm{s,fsi}} \sigma_{ji}^{\mathrm{s,fsi}} \mathrm{d}\Gamma \approx \sum_{n=1}^{N_{gau}} N_I\left(\mathbf{x}_n^{\mathrm{s}}\right) n_j^{\mathrm{s,fsi}}\left(\mathbf{x}_n^{\mathrm{s}}\right) \sigma_{ji}^{\mathrm{s,fsi}}\left(\mathbf{x}_n^{\mathrm{s}}\right) w_n \tag{5.5}$$

where the subscripts “*I*” and “*J*” denote the two connected nodal points *I* and *J* on the FSI interface, as shown in Fig. 5.4; N_I, $n_j^{\mathrm{s,fsi}}$, $\sigma_{ji}^{\mathrm{s,fsi}}$ and w_n are the shape function, components of the outward normal and Cauchy stress and the weight at the Gauss point $\mathbf{x}_n^{\mathrm{s}}$ on the segment $\Gamma_{IJ}^{\mathrm{fsi}}$, respectively.

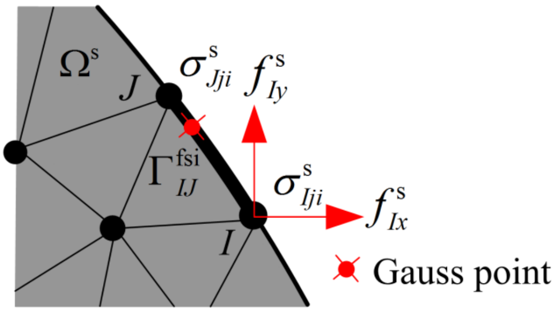

Fig. 5.4 Illustration of the FSI force

The Cauchy stress $\sigma_{ji}^{\mathrm{s,fsi}}$ at $\mathbf{x}_n^{\mathrm{s}}$ can be further interpolated with the Cauchy stresses at the two vertices *I* and *J* of $\Gamma_{IJ}^{\mathrm{fsi}}$ that are directly obtained from the viscous fluid portion as

$$\sigma_{ji}^{\mathrm{s,fsi}}\left(\mathbf{x}_n^{\mathrm{s}}\right) = N_I\left(\mathbf{x}_n^{\mathrm{s}}\right) \sigma_{Iji}^{\mathrm{s,fsi}} + N_J\left(\mathbf{x}_n^{\mathrm{s}}\right) \sigma_{Jji}^{\mathrm{s,fsi}} . \tag{5.6}$$

Substitute Eq. (5.6) into Eq. (5.5), we can finally get

$$\begin{bmatrix} f_{Ii}^{\mathrm{s,fsi}} \\ f_{Ji}^{\mathrm{s,fsi}} \end{bmatrix} = \sum_{n=1}^{N_{gau}} \begin{bmatrix} N_I^2 & N_I N_J \\ N_J N_I & N_J^2 \end{bmatrix} \begin{bmatrix} n_j^{\mathrm{s,fsi}} \sigma_{Iji}^{\mathrm{s,fsi}} \\ n_j^{\mathrm{s,fsi}} \sigma_{Jji}^{\mathrm{s,fsi}} \end{bmatrix} w_n$$

$$\text{or} \tag{5.7}$$

$$\mathbf{f}_{IJ}^{\mathrm{s}} = \sum_{n=1}^{N_{gau}} \mathbf{N}_{IJ} \mathbf{t}_{IJ}^{\mathrm{s,fsi}} w_n \ .$$

The nodal force in Eq. (5.7), which contains all the components and conditions of a fully coupled, steady-state or transient analysis of the FSI system, will be implemented as part of the external force on the solid portion during its explicit dynamic analysis.

As pointed out in [4], in contrast to the above description of applying the conditions, the solid stress boundary conditions can be imposed on the fluid element while the fluid velocity boundary conditions on the solid. However, this approach may be unstable for a general fluid-structure interaction analysis; any small error in the displacement imposed on the structure by the fluid velocities may result in a large error in the calculated traction imposed on the fluid. As such, this kind of coupling conditions is not recommended.

To fulfill the weak coupling scheme with the smoothed methods, the numerical procedures for solving the uncoupled fluid and solid should be firstly established. As the GSM/ALE derived in the previous chapter can be directly used for solving the fluid portion without any major modification, the description on the derivation of GSM/ALE is not repeated here. Only the numerical procedures for solving the individual solid portion with the explicit time integration ES-FEM-T3 are presented in some details in this chapter.

5.2 Explicit dynamics analysis for nonlinear solid using ES-FEM-T3

The central difference explicit time integration scheme using the total Lagrangian (TL) formulation is employed to describe the transient deformation of the solid, in which the ES-FEM-T3 is used to construct the smoothed strain field. As the TL formulation uses only the initial configuration as the reference configuration, the Cauchy stress σ_{ij}^{s} in the third equation of Eq. (5.1) should instead be given by the nominal stress P_{ij}^{s} expressed in terms of the area in the reference (non deformed) configuration.

If we let $v_i^{\mathrm{s}} = \dot{u}_i^{\mathrm{s}}$ where u_i^{s} denotes the displacement and the dot over u_i^{s} denotes the time derivation of u_i^{s}, the momentum balance of solid in the third equation of Eq. (5.1) can thus be rewritten as [10]

$$\rho^{\mathrm{s}} \ddot{u}_i^{\mathrm{s}} = \frac{\partial P_{ji}^{\mathrm{s}}}{\partial X_j^{\mathrm{s}}} + \rho^{\mathrm{s}} g_i \, . \tag{5.8}$$

It is subjected to the boundary conditions

$$\begin{cases} v_i^{\mathrm{s}} = \tilde{v}_i^{\mathrm{s}} & \text{on } \Gamma^{\mathrm{sD}} \\ n_j^{\mathrm{s}} \sigma_{ji}^{\mathrm{s}} = \tilde{t}_i^{\mathrm{s}} & \text{on } \Gamma^{\mathrm{sN}} \end{cases} \tag{5.9}$$

with the initial conditions

$$\begin{cases} v_i^{\mathrm{s}} = {}_0^0\tilde{v}_i^{\mathrm{s}}, a_i^{\mathrm{s}} = {}_0^0\tilde{a}_i^{\mathrm{s}} & \text{on } \Gamma^{\mathrm{sD}} \\ P_{ji}^{\mathrm{s}} = {}_0^0\tilde{P}_{ji}^{\mathrm{s}} & \text{on } \Gamma^{\mathrm{sN}} \\ t = 0 & \end{cases} \tag{5.10}$$

and FSI coupling conditions

$$n_j^{\mathrm{s,fsi}} \sigma_{ji}^{\mathrm{s,fsi}} = -n_j^{\mathrm{f,fsi}} \sigma_{ji}^{\mathrm{f,fsi}} \text{ on } \Gamma^{\mathrm{fsi}} \, . \tag{5.11}$$

Here, ${}_0^0\tilde{v}_i^{\mathrm{s}}$, ${}_0^0\tilde{a}_i^{\mathrm{s}}$ and ${}_0^0\tilde{P}_{ji}^{\mathrm{s}}$ are the initial velocity, acceleration and normal stress, where the marked wavy line indicates that these parameters are predefined and the additional left superscript and subscript introduced in these parameters indicates the time steps: the left superscript denotes the time for the current configuration, and the left subscript denotes the time for the reference configuration. In the TL formulation all the parameters are written referring to the reference configuration, hence the left subscript will be omitted in the following text. For example, ${}_{0}^{n}\mathbf{E}^{\mathrm{s}}$ is the Green strain tensor evaluated at time step "*n*" measured with respect to the reference configuration at time "0" (initial configuration) and it will be simplified as ${}^{n}\mathbf{E}^{\mathrm{s}}$.

5.2.1 Semi-discretization with ES-FEM-T3 in spatial domain

After implementing the smoothing operation with ES-FEM-T3 in the spatial domain, the semi-discretization of Eq. (5.8) can be finally written as

$$\tilde{M}_{IJij}^{\mathrm{s}}\ddot{u}_{Jj}^{\mathrm{s}} = \tilde{f}_{Ii}^{\mathrm{s,ext}} - \bar{f}_{Ii}^{\mathrm{s,int}} \tag{5.12}$$

where $\tilde{M}_{IJij}^{\mathrm{s}}$ is the entry of the lumped mass matrix; $\tilde{f}_{Ii}^{\mathrm{s,ext}}$ is the external force that contains the body force, initial traction and the FSI interaction force; and $\bar{f}_{Ii}^{\mathrm{s,int}}$ is the smoothed internal force vector, where the bar over it denotes that it has been implemented with a smoothing operation.

One may note that only the internal force $\bar{f}_{Ii}^{\mathrm{s,int}}$ in Eq. (5.12) is "affected" by the smoothing operation. The mass matrix and the external force have no "bars" over them and thus they are constructed exactly following the same way as in the standard FEM [10]. This process is similar to the illustrations in Chapter 2 for the implicit smoothed models that "*the S-FEM models change only the stiffness matrix*", although no stiffness matrix is needed to be constructed in the present explicit formulation. Thus only details of constructing this smoothed internal force vector with ES-FEM-

T3 will be specified in the text below. The way to construct the mass matrix and external force can be found in [10].

5.2.1.1 Expressions of smoothed strain and stress

Through the motion $\mathbf{x}^{\mathrm{s}} = f\left(\mathbf{X}^{\mathrm{s}}, t\right)$ the solid body moves from the initial configuration ${}^{0}\Omega^{\mathrm{s}}$ at the time *t*=0 to the current configuration ${}^{n}\Omega^{\mathrm{s}}$ at the time *t*, where $\mathbf{X}^{\mathrm{s}}$ and $\mathbf{x}^{\mathrm{s}}$ are the material and spatial coordinates of the solid particles, respectively. Assume that the initial configuration ${}^{0}\Omega^{\mathrm{s}}$ is discretized with N_{node}^{s} nodes and N_{ele}^{s} linear triangular elements. A set of N_{sd} non-overlapping edge-based smoothing domains is then constructed over these elements following the way described in Remark 2.1. The displacement ${}^{n}u_{i}^{\mathrm{s}}$ at an arbitrary point inside the solid domain can be interpolated with the corresponding nodal displacements using the shape functions, i.e.

$$ {}^{n}u_{i}^{\mathrm{s}} = \sum_{I \in S_{isd}^{\mathrm{s,sd}}} {}^{0}N_{I}^{\mathrm{s}}\, {}^{n}u_{Ii}^{\mathrm{s}}, \quad i = x, y \tag{5.13} $$

where ${}^{0}N_{I}^{\mathrm{s}}$ is the FEM shape function corresponding to the supporting node *I* (e.g. $I \in S_{isd}^{\mathrm{s,sd}} = \left\{A, B, C, D\right\}$ as in Fig. 2.2) evaluated at the initial configuration; and ${}^{n}u_{Ii}^{\mathrm{s}}$ is the nodal displacement at node *I* and is evaluated with the equation,

$$ {}^{n}u_{Ii}^{\mathrm{s}} = x_{Ii} - X_{Ii}. \tag{5.14} $$

From Eq. (5.13) we can see that the interpolations of the displacements in the ES-FEM-T3 and FEM-T3 are exactly the same. The difference between these two methods will appear in the following steps on how to estimate the gradient of the displacement field, the deformation gradient, the Green strain tensor, the PK2 stress and finally the internal nodal force.

As is known, in the standard FEM-T3 the gradient of the displacement field is constructed based on the background triangular mesh. Similarly, in the ES-FEM-T3 the smoothed gradient of the displacement field is constructed based on the newly constructed edge-based smoothing domains. Accordingly, one can get the smoothed gradient of the displacement field by referring Eq. 2.7 over the smoothing domain as

$$\begin{aligned} {}^{n}u^{\mathrm{s}}_{i,j} &= \sum_{I\in S^{\mathrm{s,sd}}_{isd}} \left(\frac{1}{{}^{0}A^{\mathrm{sd}}_{isd}} \int_{{}^{0}\Gamma^{\mathrm{sd}}_{isd}} {}^{0}N^{\mathrm{s}}_{I}\left(\mathbf{X}^{\mathrm{s}}\right) {}^{0}n^{\mathrm{sd}}_{j} \right) {}^{n}u^{\mathrm{s}}_{Ii} \\ &= \sum_{I\in S^{\mathrm{s,sd}}_{isd}} \left[\frac{1}{{}^{0}A^{\mathrm{sd}}_{isd}} \sum_{m=1}^{N_{seg}} \left(\sum_{n=1}^{N_{gau}} {}^{0}N^{\mathrm{s}}_{I}\left(\mathbf{X}^{\mathrm{s}}_{mn}\right) {}^{0}n^{\mathrm{sd}}_{j}\left(\mathbf{X}^{\mathrm{s}}_{mn}\right) w_{mn} \right) \right] {}^{n}u^{\mathrm{s}}_{Ii} \\ &= \sum_{I\in S^{\mathrm{s,sd}}_{isd}} {}^{0}\bar{N}^{\mathrm{s}}_{I,j}\left(\mathbf{X}^{\mathrm{s}}_{isd}\right) {}^{n}u^{\mathrm{s}}_{Ii} \end{aligned} \tag{5.15}$$

where ${}^{0}A^{\mathrm{sd}}_{isd}$ is the area of the isd^{th} (isd=1~N_{sd}) smoothing domain ${}^{0}\Omega^{\mathrm{sd}}_{isd}$ bounded by ${}^{0}\Gamma^{\mathrm{sd}}_{isd}$; ${}^{0}n^{\mathrm{sd}}_{j}$ is the outward surface normal of the boundary ${}^{0}\Gamma^{\mathrm{sd}}_{isd}$; N_{seg} is the total number of segments of ${}^{0}\Gamma^{\mathrm{sd}}_{isd}$: N_{seg}=3 for smoothing domains at the boundary of ${}^{0}\Omega^{\mathrm{s}}$ and N_{seg}=4 for the smoothing domains inside ${}^{0}\Omega^{\mathrm{s}}$; N_{gau} is the total number of Gauss points; and ${}^{0}\bar{N}^{\mathrm{s}}_{I,j}$ is the smoothed derivatives of the shape function corresponding to the supporting node I. Note that in the TL formulation the smoothed derivatives of shape function used in the ES-FEM-T3 only need to be calculated once at the initial stage.

By using ${}^{0}\bar{N}^{\mathrm{s}}_{I,j}$ the smoothed gradient of the displacement field ${}^{n}\bar{F}_{ij}$ can be evaluated as

$${}^{n}\bar{F}^{\mathrm{s}}_{ij}\left(\mathbf{X}^{\mathrm{s}}_{isd}\right) = {}^{n}u^{\mathrm{s}}_{i,j} + \delta_{ij} = \sum_{I\in S^{\mathrm{s,sd}}_{isd}} {}^{0}\bar{N}^{\mathrm{s}}_{I,j}\left(\mathbf{X}^{\mathrm{s}}_{isd}\right) {}^{n}u^{\mathrm{s}}_{Ii} + \delta_{ij}\,. \tag{5.16}$$

This smoothed deformation gradient ${}^{n}\bar{F}^{\mathrm{s}}_{ij}$ is then used as the primary strain measure to calculate the smoothed Green strain ${}^{n}\bar{E}^{\mathrm{s}}_{ij}$, i.e.

$$ {}^{n}E_{ij}^{\mathrm{s}}\left(\mathbf{X}_{isd}^{\mathrm{s}}\right)=\frac{1}{2}\left({}^{n}\bar{F}_{ki}^{\mathrm{s}}\,{}^{n}\bar{F}_{kj}^{\mathrm{s}}-\delta_{ij}\right). \tag{5.17} $$

For the St. Venant-Kirchhoff elastic material, the PK2 stress ${}^{n}\bar{S}_{ij}^{\mathrm{s}}$ can be expressed as a function of the smoothed Green strain ${}^{n}\bar{E}_{ij}^{\mathrm{s}}$ as

$$ {}^{n}\bar{S}_{ij}^{\mathrm{s}}\left(\mathbf{X}_{isd}^{\mathrm{s}}\right)=D_{ijkl}\,{}^{n}\bar{E}_{kl}^{\mathrm{s}},\quad i,j,k,l=x,y \tag{5.18} $$

where D_{ijkl} is the material response tensor under the plane strain condition.

5.2.1.2 Expression of smoothed internal force vector

Utilizing the smoothed strain and stress derived above, the total (smoothed) strain energy ${}^{n}\Pi^{\mathrm{int}}\left(\mathbf{u}^{\mathrm{s}}\right)$ of the solid at the time step n can be formulated as

$$ {}^{n}\Pi^{\mathrm{int}}\left(\mathbf{u}^{\mathrm{s}}\right)=\frac{1}{2}\int_{{}^{0}\Omega^{\mathrm{s}}}{}^{n}\bar{S}_{ij}\,{}^{n}\bar{E}_{ij}\mathrm{d}\Omega\approx\frac{1}{2}\sum_{isd=1}^{N_{sd}}\left\{{}^{n}\bar{\mathbf{S}}_{isd}^{\mathrm{s}}\left(\mathbf{X}_{isd}^{\mathrm{s}}\right)\right\}^{\mathrm{T}}\left\{{}^{n}\bar{\mathbf{E}}_{isd}^{\mathrm{s}}\left(\mathbf{X}_{isd}^{\mathrm{s}}\right)\right\}{}^{0}A_{isd}^{\mathrm{s}} \tag{5.19} $$

where $\left\{{}^{n}\bar{\mathbf{S}}_{isd}^{\mathrm{s}}\right\}$ and $\left\{{}^{n}\bar{\mathbf{E}}_{isd}^{\mathrm{s}}\right\}$ are the Voigt form of ${}^{n}\bar{\mathbf{S}}_{isd}^{\mathrm{s}}$ and ${}^{n}\bar{\mathbf{E}}_{isd}^{\mathrm{s}}$: $\left\{{}^{n}\bar{\mathbf{S}}_{isd}^{\mathrm{s}}\right\}=\left\{{}^{n}\bar{S}_{isd11}^{\mathrm{s}},{}^{n}\bar{S}_{isd22}^{\mathrm{s}},{}^{n}\bar{S}_{isd12}^{\mathrm{s}}\right\}^{\mathrm{T}}$, $\left\{{}^{n}\bar{\mathbf{E}}_{isd}^{\mathrm{s}}\right\}=\left\{{}^{n}\bar{\mathbf{E}}_{isd11}^{\mathrm{s}},{}^{n}\bar{\mathbf{E}}_{isd22}^{\mathrm{s}},{}^{n}\bar{\mathbf{E}}_{isd12}^{\mathrm{s}}\right\}^{\mathrm{T}}$; and ${}^{0}A_{isd}^{\mathrm{s}}$ is the area of the *isd*th smoothing domain at the initial configuration.

The smoothed internal force vector ${}^{n}\bar{\mathbf{f}}_{isd}^{\mathrm{s,int}}$ corresponding to the *isd*th smoothing domain ${}^{0}\Omega_{isd}^{\mathrm{s}}$ can thus be calculated as

$$ {}^{n}\bar{\mathbf{f}}_{isd}^{\mathrm{s,int}}=\int_{{}^{0}\Omega_{isd}^{\mathrm{s}}}\left[{}^{n}\bar{\mathbf{B}}_{isd}^{\mathrm{s}}\right]^{\mathrm{T}}\left\{{}^{n}\bar{\mathbf{S}}_{isd}^{\mathrm{s}}\right\}\mathrm{d}\Omega\approx\left[{}^{n}\bar{\mathbf{B}}_{isd}^{\mathrm{s}}\right]^{\mathrm{T}}\left\{{}^{n}\bar{\mathbf{S}}_{isd}^{\mathrm{s}}\right\}{}^{0}A_{isd}^{\mathrm{s}} \tag{5.20} $$

where $\left[{}^{n}\bar{\mathbf{B}}_{isd}^{\mathrm{s}}\right]$ is the smoothed strain-displacement matrix associated with the smoothing domain ${}^{0}\Omega_{isd}^{\mathrm{s}}$. Assuming the indices of the supporting nodes of the smoothing domain ${}^{0}\Omega_{isd}^{\mathrm{s}}$ are $I=A, B, C, D$, as illustrated in Fig. 2.2, the matrices and vectors in Eq. (5.20) can then be expressed as

$$ \left[{}^{n}\bar{\mathbf{B}}_{isd}^{\mathrm{s}}\right]=\left[{}^{n}\bar{\mathbf{B}}_{A}^{\mathrm{s}}\left(\mathbf{X}_{isd}^{\mathrm{s}}\right)\ \vdots\ {}^{n}\bar{\mathbf{B}}_{B}^{\mathrm{s}}\left(\mathbf{X}_{isd}^{\mathrm{s}}\right)\ \vdots\ {}^{n}\bar{\mathbf{B}}_{C}^{\mathrm{s}}\left(\mathbf{X}_{isd}^{\mathrm{s}}\right)\ \vdots\ {}^{n}\bar{\mathbf{B}}_{D}^{\mathrm{s}}\left(\mathbf{X}_{isd}^{\mathrm{s}}\right)\right] \tag{5.21} $$

$$\left[{}^{n}\overline{\mathbf{B}}_{I}^{\mathrm{s}}\left(\mathbf{X}_{isd}^{\mathrm{s}}\right)\right]=\begin{bmatrix} {}^{0}\overline{N}_{I,1}^{\mathrm{s}} & 0 \\ 0 & {}^{0}\overline{N}_{I,2}^{\mathrm{s}} \\ {}^{0}\overline{N}_{I,2}^{\mathrm{s}} & {}^{0}\overline{N}_{I,1}^{\mathrm{s}} \end{bmatrix}+\begin{bmatrix} {}^{n}\overline{u}_{1,1}^{\mathrm{s}}\,{}^{0}\overline{N}_{I,1}^{\mathrm{s}} & {}^{n}\overline{u}_{2,1}^{\mathrm{s}}\,{}^{0}\overline{N}_{I,1}^{\mathrm{s}} \\ {}^{n}\overline{u}_{1,2}^{\mathrm{s}}\,{}^{0}\overline{N}_{I,2}^{\mathrm{s}} & {}^{n}\overline{u}_{2,2}^{\mathrm{s}}\,{}^{0}\overline{N}_{I,2}^{\mathrm{s}} \\ {}^{n}A_{I1}^{\mathrm{s}} & {}^{n}A_{I2}^{\mathrm{s}} \end{bmatrix} \tag{5.22}$$

$${}^{n}A_{Ii}^{\mathrm{s}}={}^{n}\overline{u}_{i,1}^{\mathrm{s}}\,{}^{0}\overline{N}_{I,2}^{\mathrm{s}}+{}^{n}\overline{u}_{i,2}^{\mathrm{s}}\,{}^{0}\overline{N}_{I,1}^{\mathrm{s}},\quad i=1,2 \tag{5.23}$$

$${}^{n}\overline{\mathbf{f}}_{isd}^{\mathrm{s,int}}=\left[\begin{array}{cc|cc|cc|cc} {}^{n}\overline{f}_{A1}^{\mathrm{s,int}} & {}^{n}\overline{f}_{A2}^{\mathrm{s,int}} & {}^{n}\overline{f}_{B1}^{\mathrm{s,int}} & {}^{n}\overline{f}_{B2}^{\mathrm{s,int}} & {}^{n}\overline{f}_{C1}^{\mathrm{s,int}} & {}^{n}\overline{f}_{C2}^{\mathrm{s,int}} & {}^{n}\overline{f}_{D1}^{\mathrm{s,int}} & {}^{n}\overline{f}_{D2}^{\mathrm{s,int}} \end{array}\right]^{\mathrm{T}}. \tag{5.24}$$

The components of ${}^{n}\overline{\mathbf{f}}_{isd}^{\mathrm{s,int}}$ in Eq. (5.24) are the integrated internal nodal forces at the node *I* (*I*=*A*, *B*, *C*, *D*) in the *x*- or *y*-directions (1,2=*x*,*y*). It should be noted that the edge-based smoothing domains allocated proscribed at the boundaries of the solution domain ${}^{0}\Omega_{isd}^{\mathrm{s}}$ only have three supporting nodes. Hence, the size of the above equations will be correspondingly reduced.

Substituting Eq. (5.20) into Eq. (5.12), we can then get the semi-discretization governing equation with ES-FEM-T3. By integrating the semi-discretization governing equation in the time domain, the transient responses of the nonlinear solid can be finally achieved.

5.2.2 Explicit time integration with central difference scheme in temporal domain

The central difference explicit time integration scheme is used to integrate the semi-discretization governing equation. This scheme has already been well developed in [10]. It follows the standard procedures to integrate Eq. (5.12). Here we only summarize the general procedure for this explicit dynamics analysis in the following flowchart 5.1. On details about the central difference explicit time integration scheme, one can refer to [10].

Flowchart 5.1: Explicit dynamic analysis for nonlinear solid with ES-FEM-T3

(1) Construct the edge-based smoothing domains ${}^{0}\Omega_{isd}^{\mathrm{s}}$, $isd=1\sim N_{sd}$

(2) Initial conditions and initialization of parameters

```
        (2.1) Set initial conditions ${}^0\tilde{v}^{\mathrm{s}}_{Ii}$, ${}^0\tilde{a}^{\mathrm{s}}_{Ii}$, ${}^0\tilde{P}^{\mathrm{s}}_{ji}$, $t$=0 and the counter $n$=0; get ${}^0 f^{\mathrm{s,ext}}_{Ii}$
        (2.2) Loop over all smoothing domains ${}^0\Omega^{\mathrm{s}}_{isd}$ to compute the smoothed derivatives of the shape function ${}^0\bar{N}^{\mathrm{s}}_{I,j}$
        (2.3) Compute the lumped mass matrix $\tilde{M}^{\mathrm{s}}_{IJij}$
        (2.4) Call subroutine Cal_Internal_Force to compute the global nodal force vector ${}^0\bar{f}^{\mathrm{s,int}}_{Ii}$
        (2.5) Compute the accelerations ${}^0 a^{\mathrm{s}}_{Jj} = \left({}^0\tilde{f}^{\mathrm{s,ext}}_{Ii} - {}^0\bar{f}^{\mathrm{s,int}}_{Ii}\right) \Big/ \tilde{M}^{\mathrm{s}}_{IJij}$
    (3) Call the subroutine Solid_ExDyna ($n$, $\Delta t$, ${}^0 A^{\mathrm{sd}}_{isd}$, ${}^0\bar{N}^{\mathrm{s}}_{I,j}$, $\tilde{M}^{\mathrm{s}}_{IJij}$, ${}^0\tilde{v}^{\mathrm{s}}_{Ii}$, ${}^0\tilde{a}^{\mathrm{s}}_{Ii}$, ${}^0\tilde{P}^{\mathrm{s}}_{ji}$) to obtain ${}^{n+1}u^s_{Ii}$, ${}^{n+1}v^s_{Ii}$, ${}^{n+1}a^s_{Ii}$
    (4) Update the variables: ${}^n u^s_{Ii} = {}^{n+1}u^s_{Ii}$, ${}^n v^s_{Ii} = {}^{n+1}v^s_{Ii}$, ${}^n a^s_{Ii} = {}^{n+1}a^s_{Ii}$ and $n$=$n$+1; go to step (3)

Subroutine Solid_ExDyna
(S.1) Time update $t^{n+1}$=$t^n$+ $\Delta t$, $t^{n+1/2}$=($t^n$+ $t^{n+1}$)/2
(S.2) First partial update nodal velocities ${}^{n+1/2}v^{\mathrm{s}}_{Ii} = {}^{n+1/2}v^{\mathrm{s}}_{Ii} + \Delta t \cdot {}^n a^{\mathrm{s}}_{Ii} \big/ 2$
(S.3) Enforce velocity boundary conditions $g_{ibc}\left({}^{n+1/2}v^{\mathrm{s}}_{Ii}\right) = 0$, $ibc$=1~$n_{bc}$
(S.4) Enforce force boundary conditions to get the external force ${}^{n+1}\tilde{f}^{\mathrm{s,ext}}_{Ii}$
(S.5) Update the nodal displacements ${}^{n+1}u^{\mathrm{s}}_{Ii} = {}^n u^{\mathrm{s}}_{Ii} + \Delta t \cdot {}^{n+1/2}v^{\mathrm{s}}_{Ii}$
(S.6) Call subroutine Cal_Internal_Force to compute the internal force vector ${}^{n+1}\bar{f}^{\mathrm{s,int}}_{Ii}$ using the updated nodal displacements ${}^{n+1}u^{\mathrm{s}}_{Ii}$
(S.7) Compute nodal accelerations ${}^{n+1}a^{\mathrm{s}}_{Jj} = \left({}^{n+1}\tilde{f}^{\mathrm{s,ext}}_{Ii} - {}^{n+1}\bar{f}^{\mathrm{s,int}}_{Ii}\right) \Big/ \tilde{M}^{\mathrm{s}}_{IJij}$
(S.8) Second partial update nodal velocities ${}^{n+1}v^{\mathrm{s}}_{Ii} = {}^{n+1/2}v^{\mathrm{s}}_{Ii} + \Delta t \cdot {}^{n+1}a^{\mathrm{s}}_{Ii} \big/ 2$

Subroutine Cal_Internal_Force
(C.1) Initialization ${}^{n+1}\bar{f}^{\mathrm{s,int}}_{Ii} = 0$, $\Delta t_{crit} = \infty$
(C.2) Loop all smoothing domains ${}^n\Omega^{\mathrm{s}}_{isd}$, $isd$=1~$N_{sd}$
      i) Compute the smoothed PK2 stresses $\left\{{}^{n+1}\bar{\mathbf{S}}^{\mathrm{s}}_{isd}\right\}$
      ii) Compute ${}^{n+1}\bar{f}^{\mathrm{s,int}}_{Ii}$ according to Eq. (5.20)
      iii) Compute $\Delta t^{\mathrm{s}}_{crit}$, if $\Delta t^{\mathrm{s}}_{crit} < \Delta t_{crit}$ then $\Delta t_{crit} = \Delta t^{\mathrm{s}}_{crit}$
(C.3) End loop over smoothing domains
(C.4) Time step in next iteration $\Delta t = \alpha \Delta t_{crit}$
```

5.3 Solution procedures of FSI with GSM/ALE-ES-FEM-T3

By now the smoothed methods for solving the individual fluid and solid subsystems, i.e GSM/ALE for fluid and ES-FEM-T3 for solid, have been established.

To complete the FSI analysis, the unrelated solutions from these two smoothed methods should be "linked" with the coupling conditions on the FSI interface as discussed in Section 5.1.3. This section gives an illustration on how to implement the GSM/ALE and ES-FEM-T3 in the solution process in one typical time marching cycle, i.e. from time step *n* to its next time step *n*+1. The nodal values in both the fluid and solid domains at time step *n*, i.e. ${}^{n}v_{Ii}^{\rm f}$, ${}^{n}p_{I}^{\rm f}$, ${}^{n}u_{Ii}^{\rm s}$, ${}^{n}v_{Ii}^{\rm s}$, ${}^{n}a_{Ii}^{\rm s}$ and ${}^{n}f_{Ii}^{\rm s,fsi}$, are assumed to be known. The purpose is to find those nodal values at time step *n*+1. Note that at initial time step (*n*=1) all these variables are given by initial conditions.

Generally, one typical time marching cycle can be artificially divided into four successive steps, as illustrated in Fig. 5.5. The boundary conditions of the fluid and solid unrelated to the fluid-structure interaction are not marked in this figure and assumed to be satisfied by default.

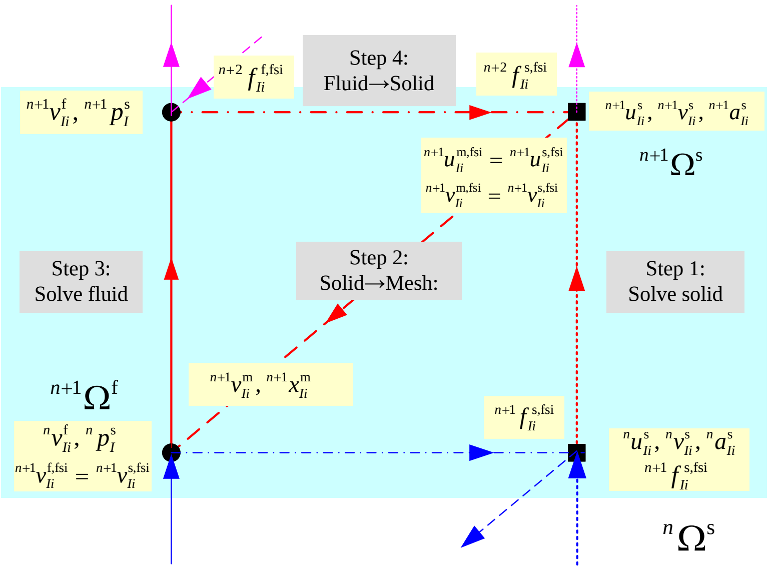

Fig. 5.5 Illustration of the time integration in one typical time marching cycle for the FSI analysis with GSM/ALE-ES-FEM-T3

Step 1: Solve for the solid portion by applying the updated FSI force

Firstly, we start the FSI analysis by solving the transient responses of the nonlinear solid with the algorithm proposed in Section 5.2. As the FSI traction equilibrium condition can be explicitly evaluated based on ${}^{n}v_{Ii,j}^{\mathrm{f,fsi}}$, ${}^{n}p_{I}^{\mathrm{f,fsi}}$ at time step *n*, the FSI force ${}^{n+1}f_{Ii}^{\mathrm{s,fsi}}$ evaluated according to Eq. (5.7) will be applied as a part entry of the external force ${}^{n+1}f_{Ii}^{\mathrm{s,ext}}$ on the solid during its dynamic analysis. If we omit the body force g_i, initial traction $\tilde{t}_i^{\mathrm{s}}$ but consider just the FSI force ${}^{n+1}f_{Ii}^{\mathrm{s,fsi}}$, the external force will be ${}^{n+1}f_{Ii}^{\mathrm{s,ext}} = {}^{n+1}f_{Ii}^{\mathrm{s,fsi}}$. After applying this updated external nodal force and the predefined Dirichlet (displacement/velocity) boundary conditions, the solid can be solved by calling the subroutine *Solid_ExDyna* in Flowchart 5.1. The outputs arising from solving the solid portion are the variables ${}^{n+1}u_{Ii}^{\mathrm{s}}$ and ${}^{n+1}v_{Ii}^{\mathrm{s}}$ in the solid domain ${}^{n+1}\Omega^{\mathrm{s}}$ at the time step *n*+1. ${}^{n+1}u_{Ii}^{\mathrm{s,fsi}}$ and ${}^{n+1}v_{Ii}^{\mathrm{s,fsi}}$ on the updated FSI interface ${}^{n+1}\Gamma^{\mathrm{fsi}}$ will be the separate output for the purpose of applying the displacement/velocity compatibility condition to the mesh and fluid portion in Steps 2 and 3.

Step 2: Update the fluid mesh by applying the FSI displacement/velocity condition

The nodal displacements/velocities of the fluid mesh on the FSI interface should be equal to those of the solid particles at the same point, i.e. ${}^{n+1}u_{Ii}^{\mathrm{m,fsi}} = {}^{n+1}u_{Ii}^{\mathrm{s,fsi}}$, ${}^{n+1}v_{Ii}^{\mathrm{m,fsi}} = {}^{n+1}v_{Ii}^{\mathrm{s,fsi}}$ as those in Eq. (5.1). At the same time, the mesh inside the fluid domain should also be updated accordingly so as to ensure the compatibility of mesh inside the fluid domain. As previously proposed, the fluid mesh can be updated with the simple velocity/displacement interpolation algorithm [11-14] or the “pseudo-structure” algorithm. In the present study, we chose the simpler velocity/displacement interpolation algorithm for the fluid mesh updating. The outcome of updating the fluid mesh is to get the new fluid mesh positions, ${}^{n+1}x^{\mathrm{m}}_{Ii}$, and the corresponding mesh velocities, ${}^{n+1}v^{\mathrm{m}}_{Ii}$.

Step 3: Solve the fluid portion by applying the FSI velocity condition

In order to ensure the non-slip boundary condition for the fluid at the FSI interface, the velocities of the fluid particles are set to be equal to the velocities of the solid particles at the same point, i.e. ${}^{n+1}v^{\mathrm{f,fsi}}_{Ii} = {}^{n+1}v^{\mathrm{s,fsi}}_{Ii}$ on ${}^{n+1}\Gamma^{\mathrm{fsi}}$. Then the fluid portion is solved via GSM/ALE. The output of the fluid portion are ${}^{n+1}v^{\mathrm{f}}_{Ii}$ and ${}^{n+1}p^{\mathrm{f}}_{I}$ in the time step *n*+1. ${}^{n+1}v^{\mathrm{f,fsi}}_{Ii,j}$ and ${}^{n+1}p^{\mathrm{f,fsi}}_{I}$ on ${}^{n+1}\Gamma^{\mathrm{fsi}}$ are output separately for the calculation of the FSI force in Step 4.

Step 4: Updating of the FSI force for next time step

According to the traction equilibrium condition, the FSI force at time step *n*+2 is evaluated according to Eq. (5.7) by using the parameters ${}^{n+1}v^{\mathrm{f,fsi}}_{Ii,j}$ and ${}^{n+1}p^{\mathrm{f,fsi}}_{I}$ on ${}^{n+1}\Gamma^{\mathrm{fsi}}$. This newly evaluated force will be applied to the solid portion in Step 1 for the next time cycle (i.e. from time step *n*+1 to *n*+2).

A flowchart of this weak coupling algorithm with smoothed method is summarized as follows.

Flowchart 5.2: Weak coupling of GSM/ALE with ES-FEM-T3 for FSI analysis

(1) Initialization for the fluid domain
  (1.1) Discretize the fluid domain ${}^{0}\Omega^{\mathrm{f}}$ and construct the nGSD and mGSD
  (1.2) Initialize the flow field, ${}^{-1}\mathbf{U}={}^{0}\mathbf{U}=\mathbf{0}$
(2) Initialization for the solid domain
  (2.1) Discretize the solid domain ${}^{0}\Omega^{\mathrm{s}}$ and constructed the edge-based smoothing domains ${}^{0}\Omega^{\mathrm{s}}_{isd}$, *isd*=1~$N_{sd}$
  (2.2) Loop over all smoothing domains ${}^{0}\Omega^{\mathrm{s}}_{isd}$ to compute the smoothed derivatives of the shape function ${}^{0}\bar{N}^{\mathrm{s}}_{I,j}$
  (2.3) Set the initial solid conditions ${}^{0}\tilde{v}^{\mathrm{s}}_{Ii}$, ${}^{0}\tilde{a}^{\mathrm{s}}_{Ii}$, ${}^{0}\tilde{P}^{\mathrm{s}}_{ji}$; get ${}^{0}\tilde{f}^{\mathrm{s,ext}}_{Ii}$

(2.4) Compute the lumped mass matrix $\tilde{M}^{\mathrm{s}}_{IJij}$
(3) Initialization for the coupling conditions
(3.1) Find the connection relationships "*node_FSI*" between the fluid nodes and solid nodes on the FSI interface
(3.2) Initialize the coupling equations, ${}^{0}f^{\mathrm{s,fsi}}_{Ii}=0$
(4) Initialize the step counter *n*=0 and the physical time $t^{n=0}$=0
(5) Call the subroutine *Solid_ExDyna* (*n*, Δt, ${}^{0}A^{\mathrm{sd}}_{isd}$, ${}^{0}\bar{N}^{\mathrm{s}}_{I,j}$, $\tilde{M}^{\mathrm{s}}_{IJij}$, ${}^{0}\tilde{v}^{\mathrm{s}}_{Ii}$, ${}^{0}\tilde{a}^{\mathrm{s}}_{Ii}$, ${}^{0}\tilde{P}^{\mathrm{s}}_{ji}$, ${}^{n}f^{\mathrm{s,fsi}}_{Ii}$) to obtain the ${}^{n+1}u^{s}_{Ii}$, ${}^{n+1}v^{s}_{Ii}$, ${}^{n+1}a^{s}_{Ii}$
(6) Update the mesh inner the fluid domain to obtain mesh velocities ${}^{n+1}v^{\mathrm{m}}_{Ii}$ and updated mesh position ${}^{n+1}x^{\mathrm{m}}_{Ii}$
(7) Update the quantities in Eqs. (2.42)-(2.44) and set the velocities of the fluid particles on the FSI interface be equal to those of the solid particles on the same point, ${}^{n+1}v^{\mathrm{f,fsi}}_{Ii}={}^{n+1}v^{\mathrm{s,fsi}}_{Ii}$
(8) Use GSM/ALE (*n*, Δt, variables in Step (7)) to get ${}^{n+1}v^{\mathrm{f}}_{Ii}$ and ${}^{n+1}p^{\mathrm{f}}_{I}$, and the ${}^{n+1}v^{\mathrm{f,fsi}}_{Ii,j}$ and ${}^{n+1}p^{\mathrm{f,fsi}}_{I}$ on FSI interface ${}^{n+1}\Gamma^{\mathrm{fsi}}$
(9) Calculate the FSI force ${}^{n+1}f^{\mathrm{s,fsi}}_{Ii}$ with Eq. (5.7)
(10) Update the variables: ${}^{n}v^{\mathrm{f}}_{Ii}={}^{n+1}v^{\mathrm{f}}_{Ii}$, ${}^{n}p^{\mathrm{f}}_{I}={}^{n+1}p^{\mathrm{f}}_{I}$, ${}^{n}u^{\mathrm{s}}_{Ii}={}^{n+1}u^{\mathrm{s}}_{Ii}$, ${}^{n}v^{\mathrm{s}}_{Ii}={}^{n+1}v^{\mathrm{s}}_{Ii}$, ${}^{n}a^{\mathrm{s}}_{Ii}={}^{n+1}a^{\mathrm{s}}_{Ii}$, ${}^{n}f^{\mathrm{s,fsi}}_{Ii}={}^{n+1}f^{\mathrm{s,fsi}}_{Ii}$, *n*=*n*+1 and $t^{n+1}=t^{n}+\Delta t$;
(11) Stop criteria of the calculation
(11.1) For transient analysis, go to step (5) until get the total simulation time t_{total};
(11.2) For steady analysis, if the steady error is little or equal to the critical error, i.e. *error_steady<tol*, stop the looping; otherwise, go to step (5)

The *error_steady* above is defined as

$$error\_steady=\sqrt{\sum_{I}\left({}^{n+1}v^{\mathrm{f}}_{Ii}-{}^{n}v^{\mathrm{f}}_{Ii}\right)\Big/\sum_{I}\left({}^{n+1}v^{\mathrm{f}}_{Ii}-{}^{0}v^{\mathrm{f}}_{Ii}\right)}\,. \tag{5.25}$$

In the calculation, explicit time integrations are employed in both the fluid and solid domains, which indicate that the calculations for both fluid and solid portions are only conditionally stable. As such, the time step Δt used in the whole weak coupling process should be chosen carefully. How to determine the suitable or critical time steps $\Delta t^{\mathrm{s}}_{crit}$ ($\Delta t^{\mathrm{s}}\le\Delta t^{\mathrm{s}}_{crit}$) and $\Delta t^{\mathrm{f}}_{crit}$ ($\Delta t^{\mathrm{f}}\le\Delta t^{\mathrm{f}}_{crit}$) for the solid and fluid domains has already been discussed in the previous chapters. The critical time step Δt_{crit} in this weak coupling process is thus determined by $\Delta t_{crit}=\min\left(\Delta t^{\mathrm{s}}_{crit},\Delta t^{\mathrm{f}}_{crit}\right)$. In this work, a constant time step Δt is used and it is constrained by $\Delta t \leq \Delta t_{crit}$. In practice, $\Delta t_{crit}^{\mathrm{s}}$ is usually smaller than $\Delta t_{crit}^{\mathrm{f}}$. So the constant time step Δt only needs to satisfy $\Delta t \leq \Delta t_{crit}^{\mathrm{s}}$.

5.4 Verification of the coupled GSM/ALE-ES-FEM-T3

Three benchmarks are tested in the present section to demonstrate the validity and performance of the weak coupling GSM/ALE with ES-FEM-T3 for solving FSI problems. The application of displacement/velocity compatibility has already been verified in the previous chapter during using the GSM/ALE to solve for fluid-rigid solid interaction problems. In this section, the application of the other coupling condition, i.e. the traction equilibrium, will be further verified firstly in this section through a benchmark of the vibration of a circular cylinder in a quiescent flow. The consideration of implementing this verification is that accurately applying the FSI force on the FSI interface is the basis of correctly and accurately predicting the deformation of the solid and thus the solution of the fluid-deformable solid interaction system. Next, a flexible flag flapping in a fluid tunnel is tested to verify that the coupled smoothed method in solving the transient FSI problems. Finally a beam deforming in a fluid tunnel is used to confirm that the proposed coupled smoothed method can give accurate and stable steady solutions in the FSI analysis. Numerical results from published literature are chosen as the benchmark for the comparisons.

5.4.1 Vibration of a circular cylinder in a quiescent fluid

5.4.1.1 Problem description

The vibration of a circular cylinder in a viscous fluid is illustrated in Fig. 5.6. When the cylinder vibrates in the viscous fluid, the presence of the fluid gives rise to a FSI interaction force that will influence the vibration of the cylinder. This example was originally studied by Chen *et al*. in [21] in the form of a cylindrical rod vibrating in a viscous fluid enclosed by a rigid, concentric cylindrical shell. A closed form solutions for the added mass and damping coefficients were obtained and verified by comparing with the experimental data in their study. Subsequently, Nomura and Hughes [12] simplified this model into a cylinder-spring system where the stiffness of the elastic spring was specially designed to make the natural frequency of this cylinder-spring system coincide with that of the cantilever rod. The displacement history of the cylinder, the added mass and damping coefficients were compared with the analytical solutions in [21] to verify their ALE finite element solution procedure.

We reprise this example here to verify the implementation of our FSI coupling conditions in the form of proposed weak coupling smoothed method via comparison of the calculated displacement damping history of the cylinder and the added mass coefficient with the reference in [12, 21]. It should be noted that in this FSI problem the cylinder is still assumed as a rigid body. However, this fluid-rigid cylinder interaction is totally different from those discussed in the previous chapter: the vibration history of the rigid cylinder here is not prescribed but decays with time due to the effect of the FSI force existed via in Eq. (5.7).

The parameters of the cylinder are r=0.635cm and m=3.408g. It is attached to the outer boundary of the fluid domain with a horizontal elastic spring of stiffness k=34611.3g/s^2. The radius of the fluid domain is set to be 5 times larger than that of the cylinder, i.e. R=5r. Two types of fluid are put into the fluid domain, i.e.

Case 1: the fluid is air, ρ^{air} =1.18×10^{-3}g/cm^3 and μ^{f} =1.82×10^{-4}g/(cm $\cdot$ s)

Case 2: the fluid is mineral oil, ρ^{mineral} =0.935g/cm^3 and μ^{f} =0.41g/(cm $\cdot$ s).

Initially, the fluid is at rest and the cylinder is released with an initial displacement a=0.02r and zero initial velocity ${}^{0}\tilde{v}^{\mathrm{s}}$ =0. Because no gravity is considered and the fluid domain is symmetric, the cylinder will only vibrate in the horizontal direction after the release. Accordingly, the mesh in the fluid domain is updated by using the displacement/velocity interpolation procedures [11-14]. The pressure condition, i.e., p=0, is applied at point A as a referential pressure.

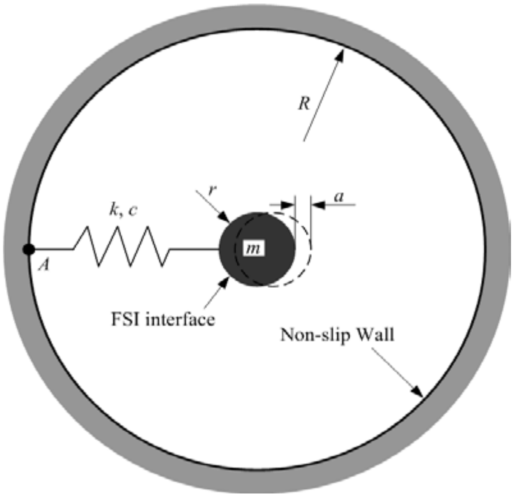

Fig. 5.6 Illustration of the vibration of a single circular cylinder immersed in a quiescent fluid

The fluid flow is solved with the developed GSM/ALE, and the vibration of the cylinder governed by Eq. (5.26) is solved with the Newmark method [22].

$$ma^{\mathrm{s}} + cv^{\mathrm{s}} + ku^{\mathrm{s}} = f^{\,\mathrm{s,ext}} \tag{5.26}$$

where a^{s}, v^{s} and u^{s} are the acceleration, velocity and displacement of the cylinder in the horizontal direction; and $f^{\,\mathrm{s,ext}}$ is the external force that is assumed to be zero in the present study; the drag force (or say the FSI force in Eq. (5.7)) which acts opposing the cylinder motion is used as the damping force during the vibration of the cylinder. The interaction conditions proposed in Section 5.1.3 are applied on the FSI interface during the time marching process.

5.4.1.2 Quantitative comparison

The convergence property of the fluid-cylinder interaction is firstly studied based on four sets of unstructured fluid mesh (770, 1529, 3162 and 5961 nodes, respectively) as shown in Fig. 5.7a; here each mesh has approximately 2 times nodes than the previous one. Because the fluid domain is symmetric, only the upper part of the fluid mesh is plotted here. Fig. 5.7b plots the displacement history of the cylinder immersed in the mineral oil with different meshes. From the zoom-in part of this figure, it can be seen that with the increase of the mesh nodes, the difference between the two neighboring curves becomes smaller, which means that the calculation becomes increasingly less dependent on the mesh. By considering the computational efficiency and accuracy, the set of mesh with 3162 nodes is thus chosen in the following analysis. Based on this set of mesh, the velocity and pressure contours at a time instant *t*=0.6s is plotted in Fig. 5.8.

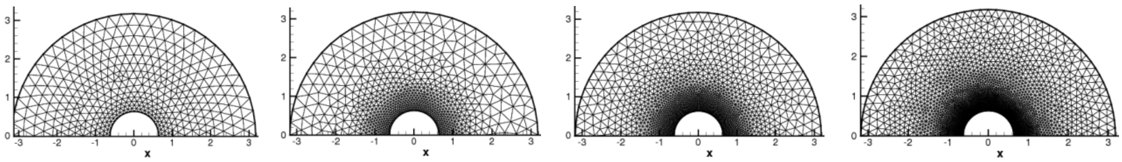

a. 770 nodes b. 1529 nodes c. 3162 nodes d. 5961 nodes

a) fluid mesh with different nodes

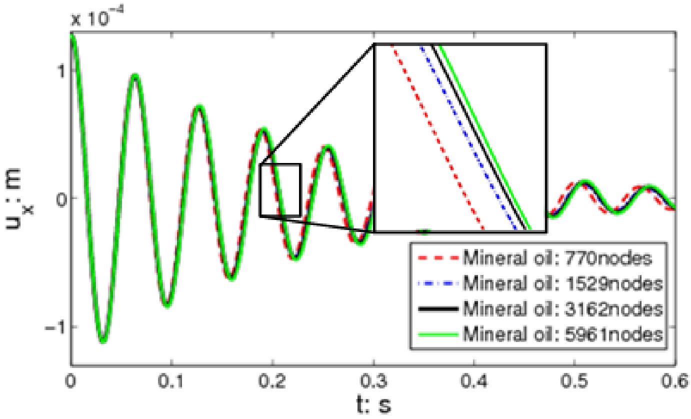

b) mesh convergence analysis

Fig. 5.7 Convergence study of the displacement field of the cylinder with different mesh densities

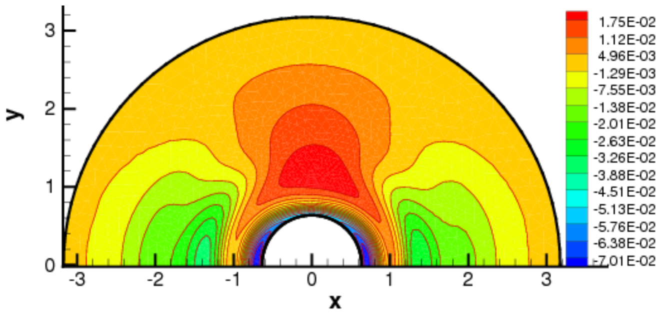

a) v_x

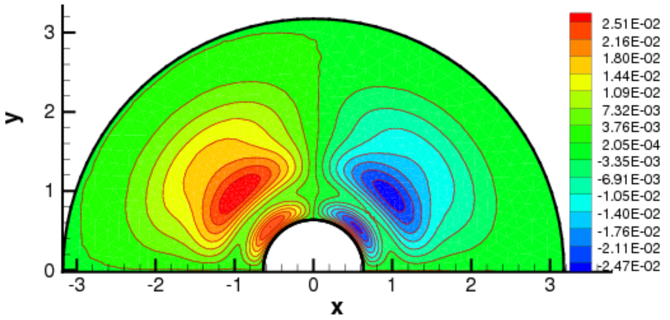

b) v_y

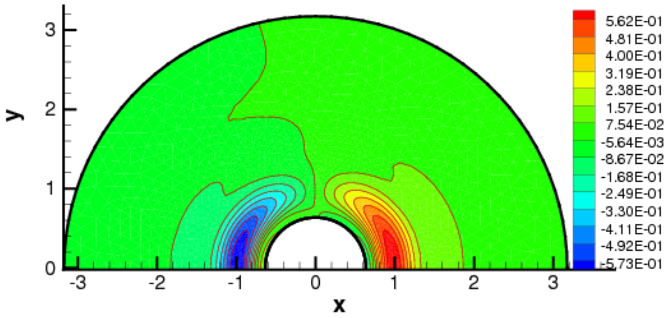

c) p

Fig. 5.8 Contour plots of the flow field of mineral oil at time t=0.6s

From Fig. 5.7b we can further observed that the vibration of the cylinder will decay with the increase of time, which is mainly due to the drag of the viscous fluid. Comparisons of the displacement history of the cylinder with the reference data from [12] are shown in Fig. 5.9. From this figure it can be seen that i) good agreement of predicted displacement by the our coupled smoothed method is achieved indicating the viable application of the FSI force condition in the assembled codes; ii) the vibration of the cylinder decays much faster in the mineral oil, which is in agreement with the higher dynamic viscosity of the mineral oil than air; and iii) there is almost no decay of the vibration when the cylinder is immersed in the air, which may be attributed to the extremely low dynamic viscosity of the air. Further comparisons of the displacement history of the cylinder vibrating in the air and vibrating without any damping are presented in Fig. 5.10. From this figure we can see that the two displacement curves match quite well with each other, which indicates that the fluid with extremely low dynamic viscosity has quite small effect on the vibration of the cylinder.

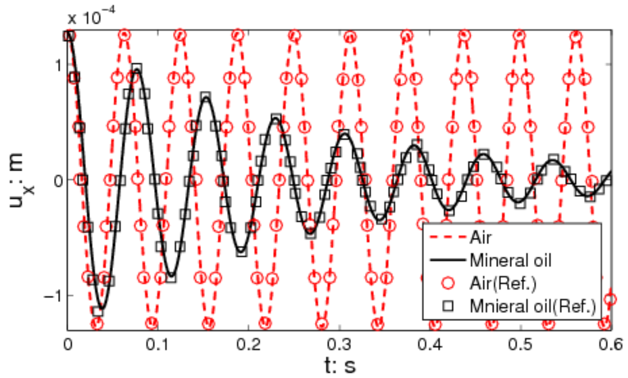

Fig. 5.9 Displacement field of the vibration of a circular cylinder in a quiescent fluid

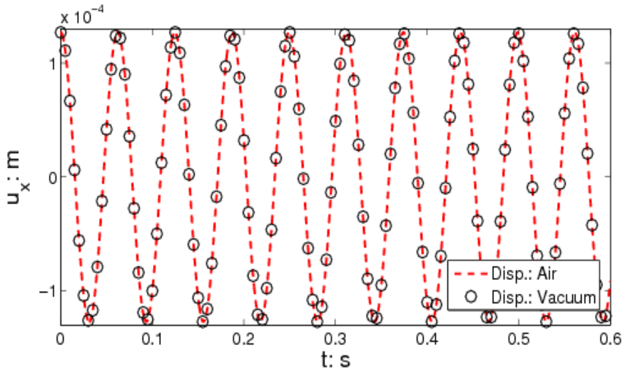

Fig. 5.10 Displacement field of the vibration of a circular cylinder in the air and without any damping (or say in vacuum)

The added mass coefficient was analytically derived by Chen *et al.* in [21]

$$C_m = \frac{m}{M}\left[\left(\frac{\mathrm{T}^{\mathrm{fsi}}}{\mathrm{T}^{\mathrm{natural}}}\right)^2 - 1\right] \tag{5.27}$$

where m and M are the mass of cylinder and the fluid filled in the equivalent volume of the cylinder, respectively; $\mathrm{T}^{\mathrm{fsi}}$ and $\mathrm{T}^{\mathrm{natural}}$ are the cycle of the coupled system and the cylinder free vibration in space, respectively.

In the present study, we have m=3.408g,

$$\mathrm{M}^{\mathrm{air}}=\rho^{\mathrm{air}}\pi r^2=0.0015\mathrm{g} \tag{5.28}$$

$$\mathrm{M}^{\mathrm{mineral}}=\rho^{\mathrm{mineral}}\pi r^2=1.184\mathrm{g} \tag{5.29}$$

$$\mathrm{T}^{\mathrm{natural}}=2\pi\Big/\sqrt{k/m}=0.06235\mathrm{s} \tag{5.30}$$

, and $\mathrm{T}^{\mathrm{fsi}}$ can be drawn from the displacement history in Fig. 5.9, i.e. $\mathrm{T}^{\mathrm{fsi,\ air}}$= 0.06238s and $\mathrm{T}^{\mathrm{fsi,\ mineral}}$=0.0763s.

By using these data, the added mass coefficient corresponding to the mineral oil is $C_m^{\mathrm{mineral}}=1.432$. The reference value of the added mass coefficient is $C_m^{\mathrm{ref,mineral}}=1.590$ in [12, 21]. Comparing the calculated value with the reference, we can see that our calculated results are quite close to these referential ones, which once more indicates the correction of applying the FSI force condition in the FSI code and the accuracy of our proposed coupled smoothed method.

Furthermore, the calculated and reference values of the added mass coefficient corresponding to the air are $C_m^{\mathrm{air}}=2.186$ and $C_m^{\mathrm{ref,air}}=1.647$, respectively. It can be found that there are some differences between these two values, and the differences was also observed by Nomura and Hughes in [12]. It is may because the displaced mass of air is very small due to its small density, and so even a small numerical error may significantly affect the evaluation of the coefficients [12].

5.4.2 Flow past a cylinder with a flexible flag

5.4.2.1 Problem description

In this section, the FSI force will be applied on a deformable solid. The benchmark FSI problem is that of a flexible flag at the downstream side of an upstream cylindrical pole which serves to verify of the proposed coupling smoothed method can give an accurate transient solution of a “real” FSI problem.

As illustrated in Fig. 5.11 [23, 24], the fluid domain is assumed to be a 2D channel with the parameters given as: L=2.5m and H=0.41m. The geometry parameters of the rigid cylinder and the flexible flag are given as: r=0.05m, l=0.35m, a=0.1 and h=0.02m. If we set the origin of the coordinate system at the lower left corner of the fluid domain, the center of the rigid cylinder is located at (0.2m, 0.2m). At the top and bottom edge of the fluid domain, the non-slip wall boundary condition is assumed.

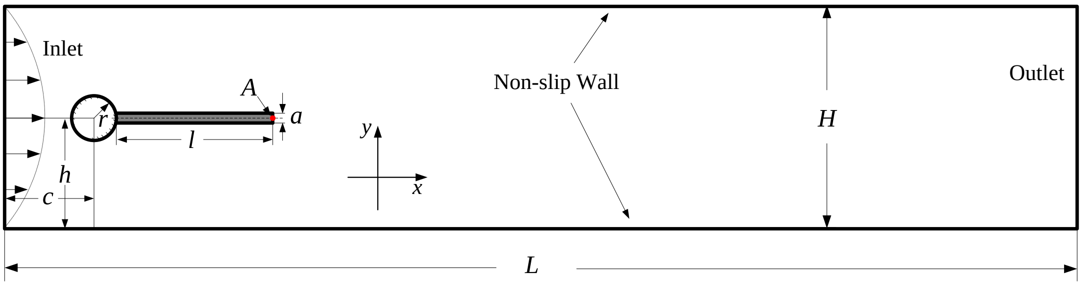

Fig. 5.11 Illustration of fluid flow past a cylinder with a flexible flag

The inflow velocity $\tilde{v}^{\mathrm{f}}(t)$ is prescribed at the left edge of the fluid domain with the following parabolic streamwise velocity profile

$$\tilde{v}^{\mathrm{f}}(t)=\begin{cases}\tilde{v}\dfrac{1-\cos(\pi t/2)}{2} & t<2.0\mathrm{s}\\ \tilde{v} & t\geq 2.0\mathrm{s}\end{cases} \tag{5.31}$$

where $\tilde{v}=6v_{\mathrm{mean}}\,y(H-y)/H^{2}$ in which v_{mean} is the mean inflow velocity when the inflow is steady after about t=2.0s.

The calculation starts at the rest state of the fluid and solid. The boundary conditions for fluid and solid are prescribed as follows:

V.B.C. for fluid: ${}^{n}v_{1}^{\mathrm{f}}=\tilde{v}^{\mathrm{f}}(t)$, ${}^{n}v_{2}^{\mathrm{f}}=0$ at $x=0$; ${}^{n}v_{i}^{\mathrm{f}}=0$ (i=1,2) at y=0 and y=H

P.B.C. for fluid: ${}^{n}p^{\mathrm{f}}=0$ at $x=L$

V.B.C. for solid: ${}^{n}v_i^{\mathrm{s}}=0$ (i=1,2) if $\left(x_1-c\right)^2+\left(x_2-c\right)^2=r^2$.

Parameters of the fluid and solid materials are listed in Table 5.1[23].

Table 5.1 Physical parameters utilized in FSI problem of fluid flow passing a cylinder with a flexible flag

Fluid				Solid		
ρ^{f} 10^3kg/m^3	μ^{f} kg/(ms)	v_{mean} m/s	Re	ρ^{s} 10^3kg/m^3	μ^{s} 10^6kg/(ms^2)	υ^{s}
1	1	3	200	1	2.0	0.4

where μ^{s} is the shear modulus of solid, $\mu^{\mathrm{s}}=0.5E^{\mathrm{s}}\big/\left(1+\upsilon^{\mathrm{s}}\right)$.

5.4.2.2 Quantitative comparison

With the parameters given above, the flag oscillates with time leading to a periodically oscillating fluid flow with regular vortex pattern. The displacement of point *A*(0.6m,0.2m) on the right tip of the flag and the cycle of the oscillation of the flag are the two main quantities used for comparison with the reference. Three sets of meshes are employed, i.e. mesh set 1 (or in short MS(1)), 3476 nodes for the fluid and 427 nodes for the solid; MS(2), 5113 nodes for the fluid and 1111 nodes for the solid; and MS(3) 7371 nodes for the fluid and 2057 nodes for the solid. As will be noted below, the solution of the FSI system is stable using the finer mesh MS(3) and thus used for comparison.

In the FSI analysis with *Re*=200, the system settles into a large-amplitude self-excited oscillation following the initial transient quiescent period. The oscillating flag produces a regular vortex pattern that is advected along the channel, as shown in Fig. 5.12, where four typical snapshots of the pressure contour together with the streamlines are plotted. The vertical tip displacement history of u_y^{s} at point *A* is plotted in Fig. 5.13. This displacement range of tip *A* is $u_y^{\mathrm{s}}\approx0.001\pm0.0344$m, which is fairly comparable with the reference solution $u_y^s \approx 0.00148 \pm 0.03438$m [23-25]. Furthermore, the cycle of the oscillation of the flag is T=0.198s, which also agrees well with the value T=0.19s calculated in [25]. Both of the comparisons demonstrate that our coupling smoothed method can give accurate and stable transient solution in an FSI analysis.

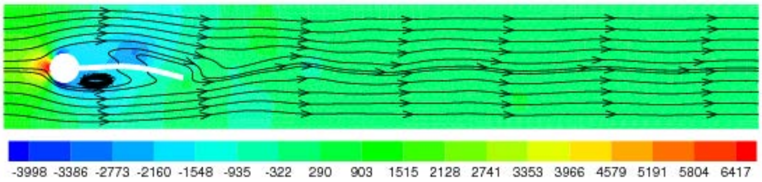

a) T/4

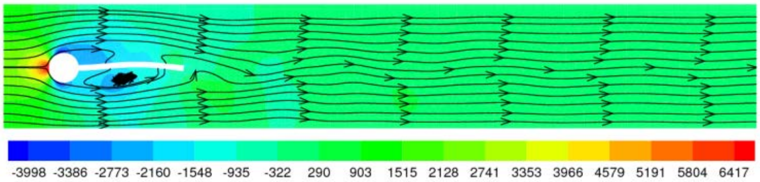

b) T/2

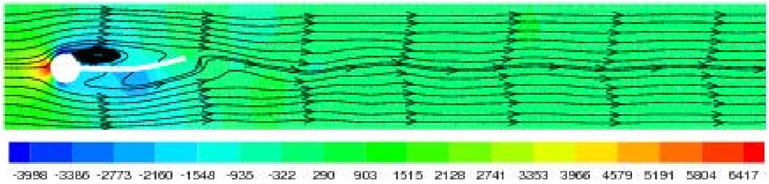

c) 3T/4

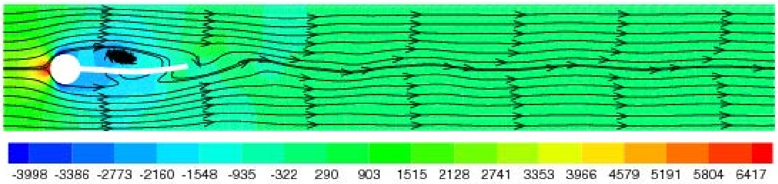

d) T

Fig. 5.12 Snapshots of the fluid pressure contours and streamlines for the problem of fluid flow past a cylinder with a flexible flag

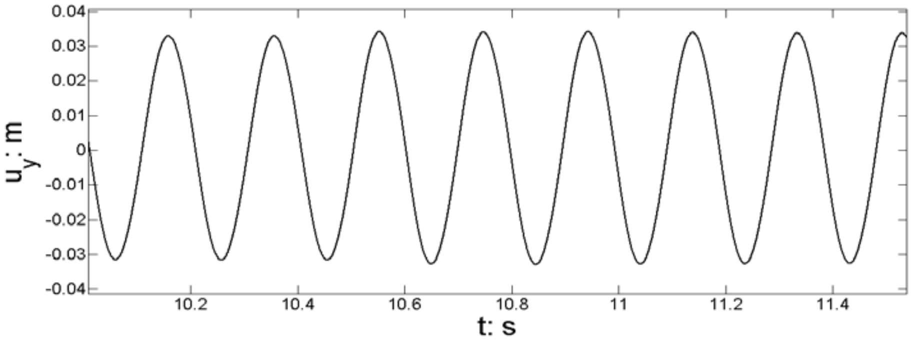

Fig. 5.13 History of displacement component of the point *A* for the problem of fluid flow past a cylinder with a flexible flag

5.4.3 Beam in a fluid tunnel

5.4.3.1 Problem description

In this example, a beam immersed in a fluid tunnel is analyzed, as illustrated in Fig. 5.14. The beam will undergo a large deformation driven by viscous fluid flow and become steady only after a certain period of oscillations. This kind of problem can be usually found in biomechanics, e.g. the opening and closing behavior of aortic heart valves involving intricate delicate interaction between the blood flow and heart-valve leaflet [26].

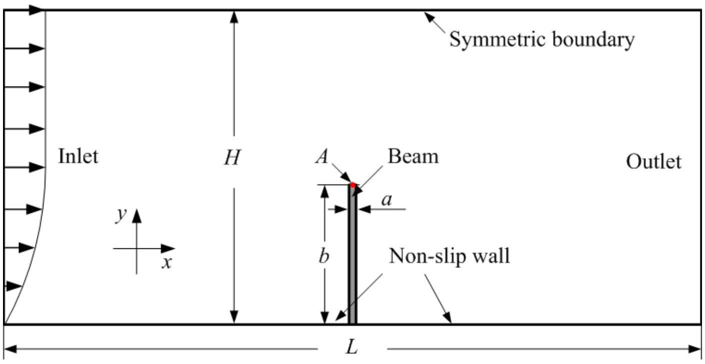

a) Geometry of the FSI system

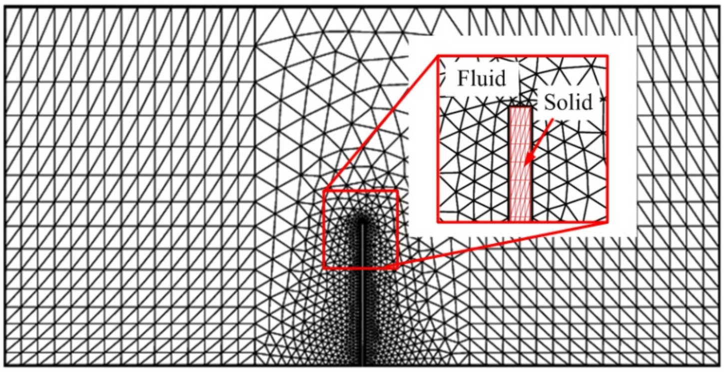

b) Mesh of the FSI system: MS(1)

Fig. 5.14 Problem setting and mesh of a beam in a fluid tunnel

Geometric parameters of the fluid tunnel are: L=4cm and H=2cm. The beam is fixed in the middle of the tunnel with its geometric parameters: a=0.025cm and b=0.8cm. Gravity is not considered in the present calculation. Non-slip wall boundary condition is assigned at the bottom edge of the fluid domain and symmetric boundary condition is assumed at the top edge of the fluid domain. The FSI coupling conditions are applied at the fluid-beam interface. The inlet boundary condition at the left edge of the fluid domain is defined as

$$\begin{cases} \tilde{v}_1^{\mathrm{f}}\left(t\right)=1.5\left(-y^2+2y\right) & 0\le y<1.0\mathrm{cm} \\ \tilde{v}_1^{\mathrm{f}}\left(t\right)=1.5 & 1.0\mathrm{cm}\le y\le 2.0\mathrm{cm} \\ \tilde{v}_2^{\mathrm{f}}\left(t\right)=0 & \end{cases} \tag{5.32}$$

and at the right edge of the tunnel the reference pressure at the corner point is set to be zero. The fluid properties are chosen as: ρ^{f} =1g/cm^3 and μ^{f} =0.1g/(cm$\cdot$s). The solid material is chosen as Saint Venant-Kirchhoff material and two types of material properties are chosen, i.e.

Case 1: ρ^{s} =7.8g/cm^3, E^{s}=10^{6}g/(cm$\cdot$s^2) and v^{s}=0.3

Case 2: ρ^{s} =7.8g/cm^3, E^{s}=10^{11}g/(cm$\cdot$s^2) and v^{s}=0.3

In both cases, the fluid and solid are at rest at t=0 and the FSI system will arrive at the steady state, which is determined by the criterion

$$\sqrt{\sum_I\left({}^{n+1}v_{Ii}^{\mathrm{f}}-{}^{n}v_{Ii}^{\mathrm{f}}\right)\Big/\sum_I\left({}^{n+1}v_{Ii}^{\mathrm{f}}-{}^{0}v_{Ii}^{\mathrm{f}}\right)}\le 10^{-6}\,. \tag{5.33}$$

After getting the steady state the FSI force applied on the deformed beam are in balance with the internal force.

Three sets of irregular meshes are created as follows: MS(1), 1152 nodes for the fluid and 155 nodes for the solid; MS(2), 1945 nodes for the fluid and 205 nodes for the solid; and MS(3), 3856 nodes for the fluid and 305 nodes for the solid. Different meshes are established to verify the convergence properties and thus the stability of the proposed smoothed methods. A typical mesh set of MS(1) is plotted in Fig. 5.14b.

5.4.3.2 Quantitative comparison: Case 1

In Case 1, the beam undergoes large deformation due to the relative "softness" (low Young's modulus) of the solid material. Fig. 5.15 plots the time histories of *x*-component of the velocity and deflection measured at the tip *A* based on different meshes. From this figure it can be seen that i) after a certain period of time the velocity approaches to zero and the deflection stabilizes at a constant value, which indicates that the final steady state of the beam has been successfully captured in the present calculation; ii) the solutions of either velocity or deflection using different meshes agree very well with each other although there are minor differences among these curves which are attributed to the deployed meshes.

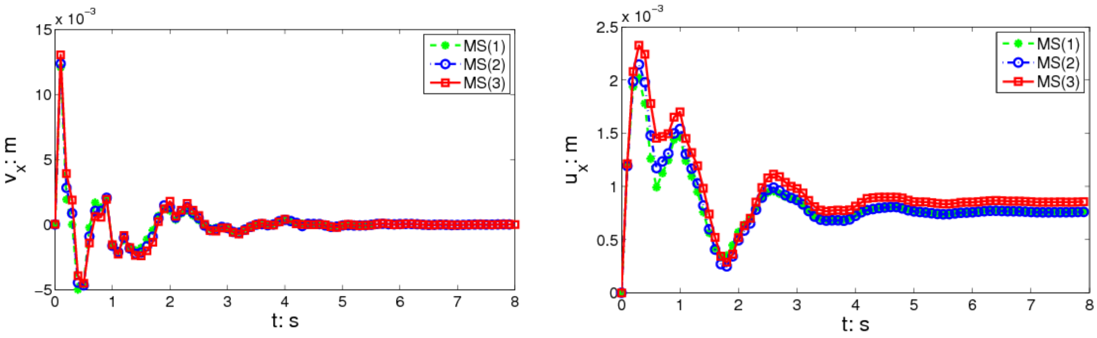

a) the tip velocity v_x^s b) the tip displacement u_x^s

Fig. 5.15 Solutions of a beam in a fluid tunnel (Case 1 solved with MS(3))

Fig. 5.16 plots the contours of the velocity component in the *x*-direction and the pressure *p* at some typical time instants during the time marching process. From the zoom-in parts of these figures, it can be seen that there are oscillations in the pressure field near the tip zone of the beam. This observed phenomenon is mainly due to the singularity of the velocity gradient resulting from the sharp corner of the beam end. In the farfield zone of the fluid domain the singularity of the velocity gradient vanishes and thus the oscillation of pressure disappears in these distance zones. No oscillations are observed in the velocity field in the whole fluid domain, as shown in the zoom-in parts in Fig. 5.16a.

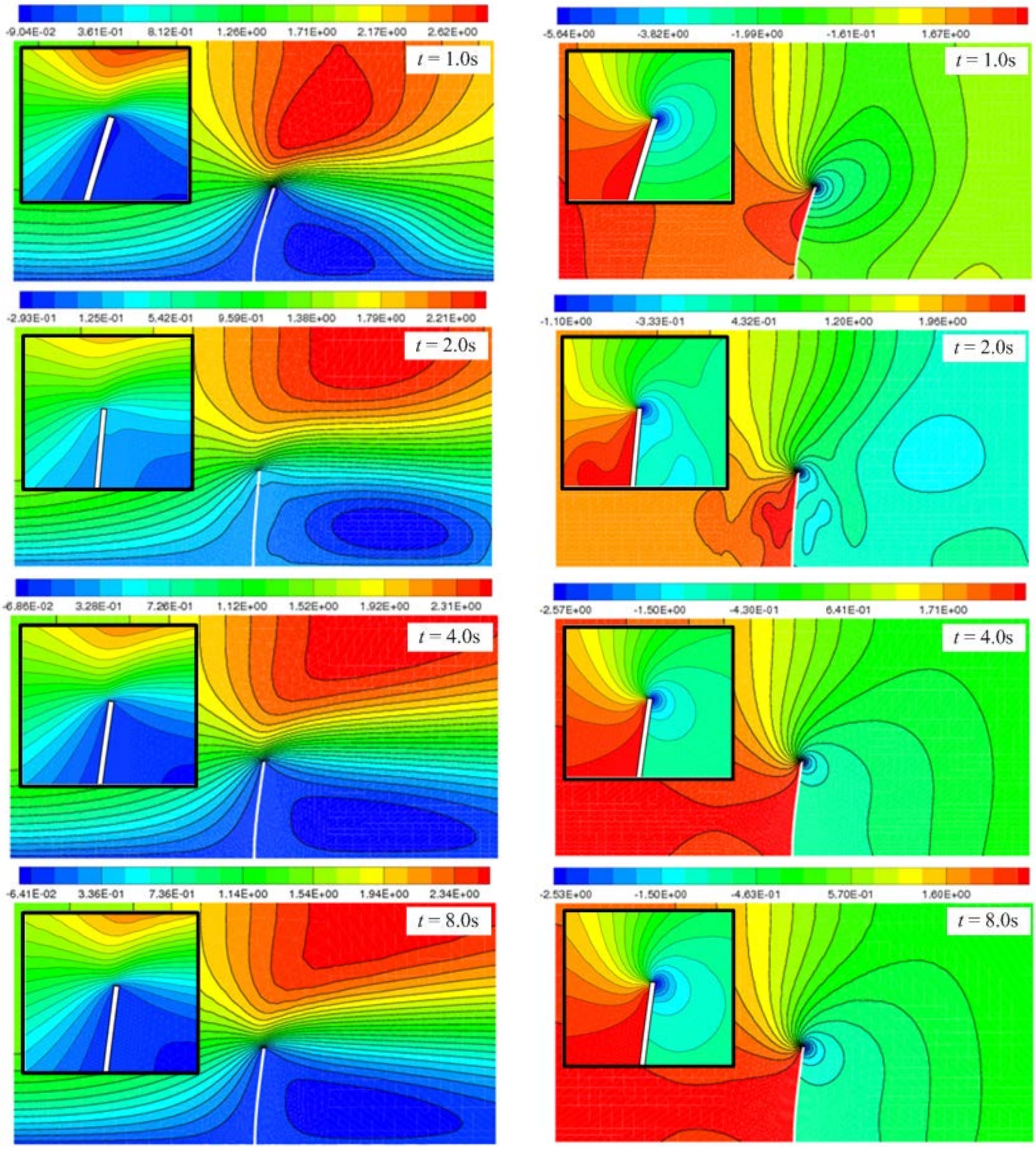

a) velocity v_x^{f} b) pressure p^{f}

Fig. 5.16 Snapshots of the contours: a) velocity v_x^{f}, and b) p^{f} (Case 1 solved with MS(3)) for the problem of a beam in a fluid tunnel

The solutions of the velocity and deflection are mesh-dependent. With the refinement of the meshes in both the fluid and solid domains, the solutions convergence to the "exact" ones. However, the meshes in different domains may have different "contributions" to the rate of convergence. An examination of the individual effect of the fluid and solid meshes to the final solutions is presented here. To aid in the examination, one extra mesh set, i.e. EMS with 1285 nodes in the fluid domain and 205 nodes in the solid domain, is created by referring to as MS(1) and MS(2): we define the fluid mesh of EMS are (almost) the same as that in MS(1) but with a change of the solid mesh on comparing with MS(1), while the solid mesh of EMS are the same as that in MS(2) while has a change of the fluid mesh on comparing with MS(2). The intent for this arrangement is to ascertain the effect of the solid mesh on the final solutions while keeping the fluid mesh unchanged when using MS(1) and EMS, and separating to check the effect of the fluid mesh on the final solutions while keeping the solid mesh unchanged when using EMS and MS(2).

The time histories of *x*-component of the velocity and deflection measured at the tip *A* based on MS(1), MS(2) and EMS are plotted in Fig. 5.17a and Fig. 5.17b, respectively. From these two figures it can be easily found that the distributions based on EMS and MS(2) are much closer to one another as compared to those based on MS(1) and EMS. The finding suggests that by changing only the solid mesh while keeping the fluid mesh unchanged has much more obvious effect on the final solutions than that only changing the fluid mesh but keeping the solid mesh unchanged. This implication is that in the FSI analysis it is better or perhaps imperative the solid mesh be more refined at least in comparison to the fluid mesh in the event that the total number of mesh nodes in the whole domain remains the same. However, as pointed out previously, with the increase of the DOFs in the solid domain, the critical length of mesh edge, l_e, will become shorter. This would in turn affect the critical time step in the solid domain ($\Delta t_{crit}^{s} \propto l_e$) and thus the whole FSI analysis with the explicit time integration process. Thus there must be a balance regarding the effect of the solid mesh on the converged solution and the critical time step for time marching.

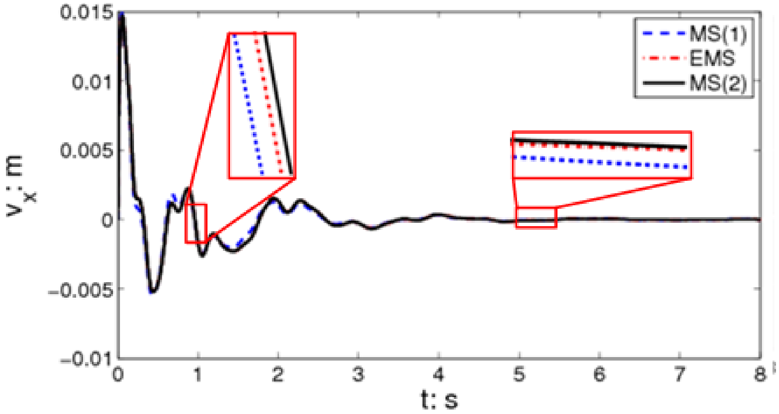

a) v_x^s

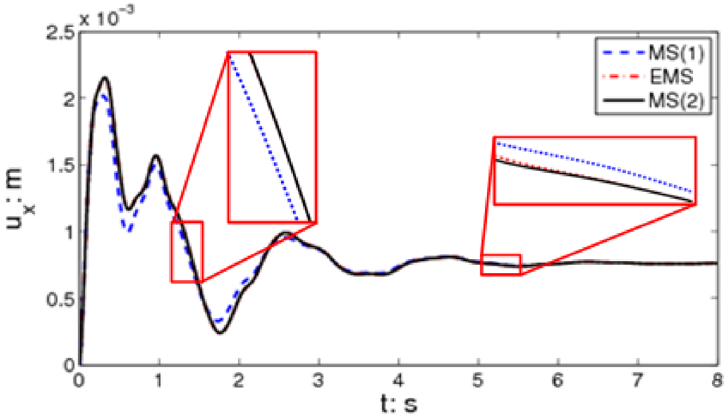

b) u_x^s

Fig. 5.17 Illustration of the mesh effects on the convergence of the solutions for the problem of a beam in a fluid tunnel

Furthermore, if the solid material is chosen even "softer", the solid beam will deform extremely large, which may distort the solid mesh especially near the beam region, as shown in Fig. 5.18, where the Young's modulus of the beam is set to be $E^s = 10^5 \ \mathrm{g} \big/ \left(\mathrm{cm} \cdot \mathrm{s}^2\right)$. Although it can still work because we have already checked the robust of our GSM/ALE on extremely distorted mesh, the accuracy of the calculation should be at least affected by the distorted mesh. Thus for the problem with large mesh distortion, extra technique such as adaptive analysis should be used in the mesh updating process in order to ensure the quantity of the fluid mesh. In my research group, some studies on the adaptive analysis have already been done in both solid and fluid mechanics [27, 28]. Further study of implementing these techniques to FSI analysis will be done in the next step.

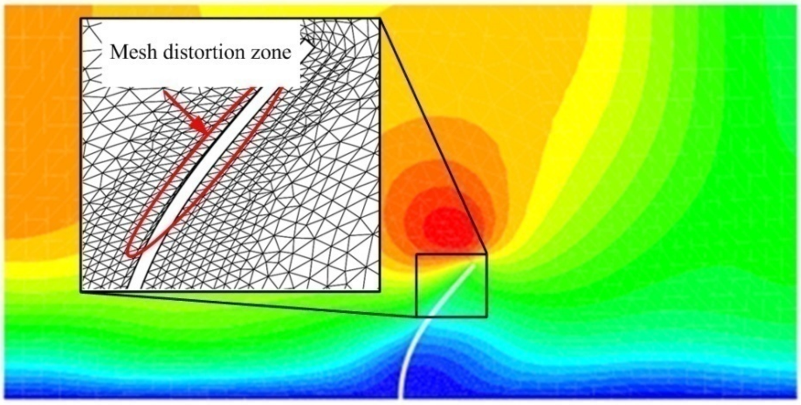

Fig. 5.18 Mesh distortions at extremely large deflections with the $E^s=10^5$g/(cm·s^2) for the beam

5.4.3.3 Quantitative comparison: Case 2

In Case 2, the Young's modulus of the beam is 10^6 order's lower than that in Case 1, which enforces the critical time step of the FSI analysis (that is mainly determined by the critical time step of the solid, $\Delta t^{s}_{crit} \propto \sqrt{1/E^{s}}$) to be 1/10^3 of that in Case 1 on using the same fluid and solid meshes. As such, the appropriate time step needs to be chosen for Case 2. In the present calculation, the time step used is in the order of 10^{-8}s. Because of the high stiffness of the beam, it will deform extremely small in the viscous fluid which is fairly similar in behavior to that of a rigid body. The contour plot of the *x*-component of velocity and the pressure in fluid domain are, respectively, shown in Fig. 5.19a and 5.19b based on MS(3). From these two figures we can again observe the oscillation of the pressure near the tip region of the beam as a result of the sharp corner. However, no pressure oscillation is observed in the farfield region. Moreover, there is an absence of oscillation observed for the velocity field since there is no singularity encountered in the calculation of the velocity field.

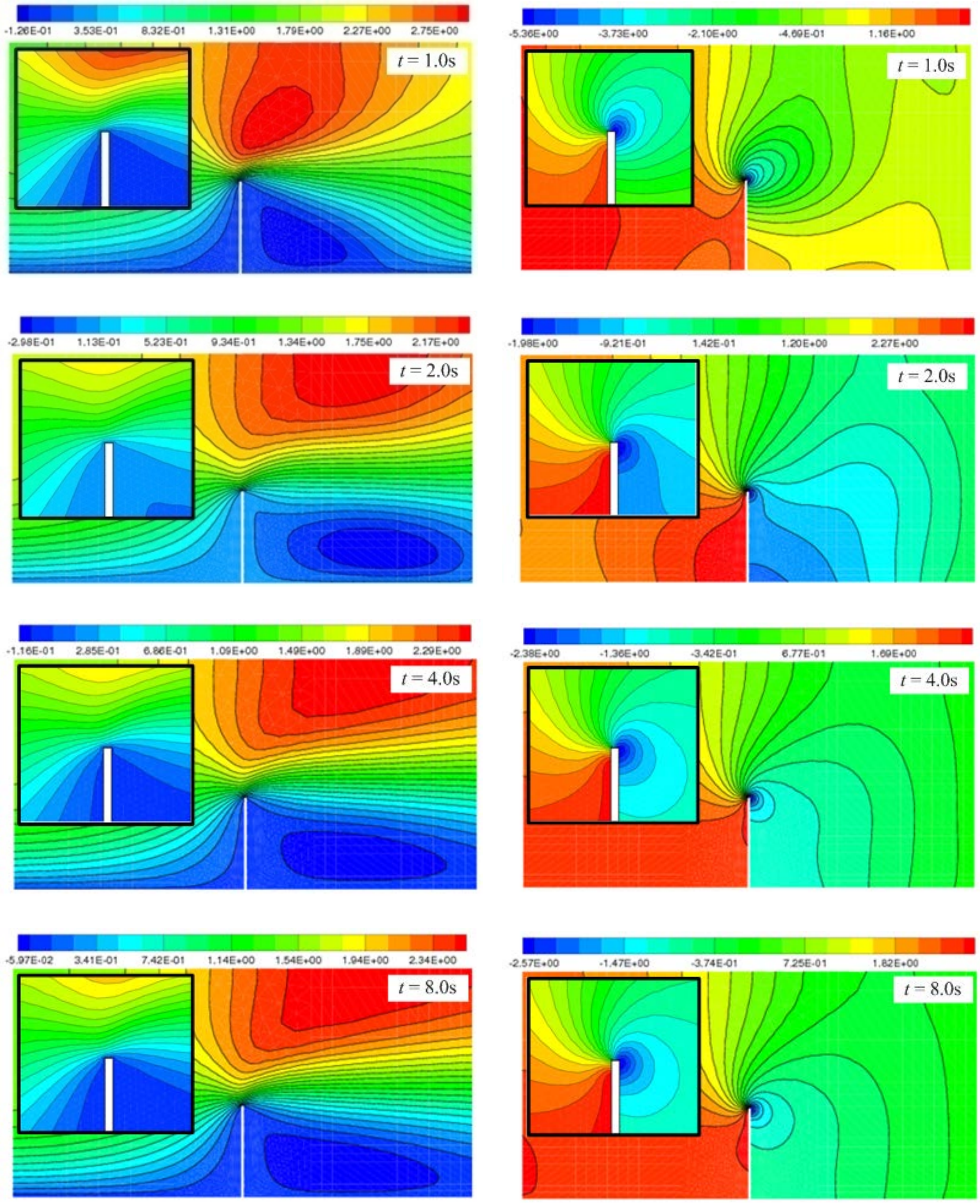

a) the tip velocity v_x^{f} b) pressure p^{f}

Fig. 5.19 Snapshots of the contours (Case 2 solved with MS(3)) for the problem of a beam in a fluid tunnel

In the present FSI analysis, only one constant Δt is employed for both the fluid and solid domains. This procedure on the one hand make it easy to couple the physical solution of the fluid and solid at every time step, on the other hand it is quite restrictive in terms of the critical time step in the solid domain; the critical time step Δt^{s}_{crit} for the solid portion becomes extremely small when the Young's modulus of the solid is very high, leading to a very small time step for the whole FSI analysis. As pointed out in [25], one possible way to reduce the total computation time is to set $\Delta t^{s}_{crit} < \Delta t < \Delta t^{f}_{crit}$ and $\Delta t = \Delta t^{f} = m\Delta t^{s}$. That is, in one real time step from n to n+1, the coupling smoothed method solves the fluid portion for one physical time step from t to $t + \Delta t^{f}$, and takes m (pseudo) solid time steps in the solid domain. This kind of time integration process will avoid the solving for the fluid portion when the solid undergoes deformation in the mth internal solid time steps. However, this dual time stepping scheme may also bring about some other issues, e.g. the accuracy of the fluid solutions near the FSI interface region. This is because the solid may undergo quite large deformation after the mth time integration process leading possibly to (relatively) large volume change of the fluid mesh near the FSI interface. Detailed examination of this kind of time integration process will be addressed in a future study.

Both cases produce stable vortex in the downwind side of the beam in the steady state as shown by the streamline plots in Fig. 5.20.

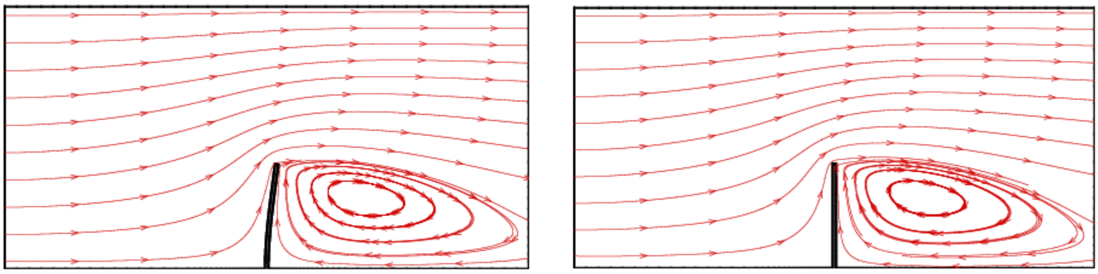
a) Case 1 b) Case 2

Fig. 5.20 Streamlines at the steady state of a) Case 1 and b) Case 2 for the problem of a beam in a fluid tunnel

5.5 Concluding remarks for Chapter 5

In this chapter, a weak coupling scheme of the smoothed methods, i.e. coupling of the GSM/ALE with ES-FEM-T3, has been successfully established for solving fluid-deformable solid interaction problems. GSM/ALE is implemented in the fluid domain and the newly developed explicit time integration ES-FEM-T3 is implemented in the solid domain. In order to link the GSM/ALE and ES-FEM-T3, the FSI coupling conditions are carefully formulated and successively applied on the FSI interface in the time marching process.

The accuracy of the formulation and application of these coupling conditions are verified through the benchmark of the free vibration of a cylinder in a quiescent fluid. Reasonable agreement of the displacement and added mass coefficient of the cylinder with the references are obtained. From the benchmark of the flow past a cylinder with a flexible flag, it is observed our coupled smoothed method can give accurate solution in the transient FSI problems. From the benchmark of a beam in a fluid tunnel where the solid beam is assume to be either extremely flexible or near-rigid, it is clear that our coupled smoothed method can give accurate and stable steady solutions in the steady FSI problems.

Through the mesh sensitivity analysis discussed in this benchmark, we may also draw the conclusion that the whole FSI system is more sensitive to the changing in the solid mesh as compared to the fluid mesh. Thus it is suggested that for the solid portion a more refined mesh may be considered. In the calculation for the case where the beam is extremely soft, the fluid mesh becomes highly distorted, especially near the FSI interface region. Although our GSM/ALE can still work reasonably in the fluid domain using this extremely distorted mesh, the overall accuracy of the FSI solution may still be affected. Thus in order to ensure the required accuracy, adaptive meshing of the fluid meshes is suggested for extreme cases; this is the subject of our future work.

References for Chapter 5

1. Rugonyi, S. and Bathe, K.J., *On finite element analysis of fluid flows fully coupled with structural interactions.* Computer Modeling in Engineering and Sciences, 2001. **2**(2): p. 195-212.
2. Bathe, K., Zhang, H. and Wang, M., *Finite element analysis of incompressible and compressible fluid flows with free surfaces and structural interactions.* Computers & Structures, 1995. **56**(2): p. 193-213.
3. Bathe, K., Zhang, H. and Zhang, X., *Some advances in the analysis of fluid flows.* Computers & Structures, 1997. **64**(5): p. 909-930.
4. Bathe, K.J. and Zhang, H., *Finite element developments for general fluid flows with structural interactions.* International Journal for Numerical Methods in Engineering, 2004. **60**(1): p. 213-232.
5. Bathe, K.J., Zhang, H. and Ji, S., *Finite element analysis of fluid flows fully coupled with structural interactions.* Computers & Structures, 1999. **72**(1): p. 1-16.
6. Jaiman, R., Geubelle, P., Loth, E. and Jiao, X., *Combined interface boundary condition method for unsteady fluid-structure interaction.* Computer Methods in Applied Mechanics and Engineering, 2011. **200**(1-4): p. 27-39.
7. Jaiman, R., Geubelle, P., Loth, E. and Jiao, X., *Stable and accurate loosely-coupled scheme for unsteady fluid-structure interaction.* AIAA Paper, 2007. **334**.
8. Jaiman, R., Jiao, X., Geubelle, P. and Loth, E., *Conservative load transfer along curved fluid–solid interface with non-matching meshes.* Journal of Computational Physics, 2006. **218**(1): p. 372-397.
9. Jaiman, R., Jiao, X., Geubelle, P. and Loth, E., *Assessment of conservative load transfer for fluid‐solid interface with non‐matching meshes.* International Journal for Numerical Methods in Engineering, 2005. **64**(15): p. 2014-2038.
10. Belytschko, T., Liu, W.K. and Moran, B., *Nonlinear finite elements for continua and structures*. 2000: John Wiley & Sons Ltd., Baffins Lane, Chichester, West Sussex, PO191 UD, England.
11. Anwer, S.F., Hasan, N., Sanghi, S. and Mukherjee, S., *Computation of unsteady flows with moving boundaries using body fitted curvilinear moving grids.* Computers & Structures, 2009. **87**(11-12): p. 691-700.
12. Nomura, T. and Hughes, T.J.R., *An arbitrary Lagrangian-Eulerian finite rigid element method for interaction of fluid and a rigid body.* Computer Methods in Applied Mechanics and Engineering, 1992. **95**(1): p. 115-138.
13. Kjellgren, P. and Hyvärinen, J., *An arbitrary Lagrangian-Eulerian finite element method.* Computational Mechanics, 1998. **21**(1): p. 81-90.
14. Sarrate, J., Huerta, A. and Donea, J., *Arbitrary Lagrangian–Eulerian formulation for fluid–rigid body interaction.* Computer Methods in Applied Mechanics and Engineering, 2001. **190**(24): p. 3171-3188.
15. Chiandussi, G., Bugeda, G. and Oñate, E., *A simple method for automatic update of finite element meshes.* Communications in Numerical Methods in Engineering, 2000. **16**(1): p. 1-19.
16. Xu, Z. and Accorsi, M., *Finite element mesh update methods for fluid–structure interaction simulations.* Finite Elements in Analysis and Design, 2004. **40**(9): p. 1259-1269.

17. Farhat, C., Degand, C., Koobus, B. and Lesoinne, M., *Torsional springs for two-dimensional dynamic unstructured fluid meshes.* Computer Methods in Applied Mechanics and Engineering, 1998. **163**(1): p. 231-245.
18. Blom, F.J., *Considerations on the spring analogy.* International Journal for Numerical Methods in Fluids, 2000. **32**(6): p. 647-668.
19. Degand, C. and Farhat, C., *A three-dimensional torsional spring analogy method for unstructured dynamic meshes.* Computers & Structures, 2002. **80**(3): p. 305-316.
20. Markou, G.A., Mouroutis, Z.S., Charmpis, D.C. and Papadrakakis, M., *The ortho-semi-torsional (OST) spring analogy method for 3D mesh moving boundary problems.* Computer Methods in Applied Mechanics and Engineering, 2007. **196**(4): p. 747-765.
21. Chen, S., Wambsganss, M. and Jendrzejczyk, J., *Added mass and damping of a vibrating rod in confined viscous fluids.* Journal of Applied Mechanics, 1976. **43**: p. 325.
22. Newmark, N.M., *A method of computation for structural dynamics.* Journal of the Engineering Mechanics Division, 1959. **85**(7): p. 67-94.
23. Turek, S. and Hron, J., *Proposal for numerical benchmarking of fluid-structure interaction between an elastic object and laminar incompressible flow.* Fluid-Structure Interaction, 2006: p. 371-385.
24. Heil, M., Hazel, A.L. and Boyle, J., *Solvers for large-displacement fluid–structure interaction problems: segregated versus monolithic approaches.* Computational Mechanics, 2008. **43**(1): p. 91-101.
25. Zhang, Z.Q., Liu, G.R. and Khoo, B.C., *Immersed smoothed finite element method for two dimensional fluid–structure interaction problems.* International Journal for Numerical Methods in Engineering, 2012. **90**(10): p. 1292-1320.
26. Zhang, L.T. and Gay, M., *Immersed finite element method for fluid-structure interactions.* Journal of Fluids and Structures, 2007. **23**(6): p. 839-857.
27. Xu., G.X., Liu, G.R. and Tani, A., *An adaptive gradient smoothing method (GSM) for fluid dynamics problems.* International Journal for Numerical Methods in Fluids, 2010. **62**(5): p. 499-529.
28. Zhang, G.Y., Liu, G.R. and Li, Y., *An efficient adaptive analysis procedure for certified solutions with exact bounds of strain energy for elasticity problems.* Finite Elements in Analysis and Design, 2008. **44**(14): p. 831-841.

Chapter 6

Conclusions and recommendations

As a continuation of the smoothed theory, this thesis explores the coupling of two typical smoothed methods, i.e. coupling the GSM with ES-FEM-T3, for solving the challenging FSI problems. Novel numerical schemes, i.e. the implicit/explicit ES-FEM-T3 and GSM/ALE, are firstly formulated for solving the uncoupled linear/nonlinear solid deformation and fluid flow with moving mesh, respectively. Properties of these two schemes, e.g. accuracy, convergence and stability, are quantitatively checked through numerous benchmark tests to demonstrate their validities. Due to the viable performance of these two schemes in solving particular solid and fluid flow problems, a coupling of GSM/ALE with ES-FEM-T3 is next constructed to solve the FSI problems. Numerical innovations ensued and distinct features are observed during the formulation and verification processes of these schemes, both of which are combined to enable further understanding of the characteristics of smoothed models and fundamentals of the smoothed theory. In this chapter, specific contributions and findings during the development of these schemes are summarized and potential further work associated with the present study is also suggested.

6.1 Conclusions

(1) The implicit ES-FEM-T3 for 2D linear bending stress analysis

The implicit ES-FEM-T3 method is possibly the first time to be implemented into a practical engineering problem, i.e. analyze the stress distributions in the gear tooth during the gear transmissions. A numerical operation of converting the concentrated transferred load to the distributed load is taken to avoid the stress singularity at the loading point. A more accurate stress field is obtained by the implicit ES-FEM-T3 than the standard FEM-T3. Thus it is further used in the optimizations of the gear tooth profiles. The governing equations of the gear tooth profiles are derived and five typical gear tooth models with pressure angles α_d / α_c = $20^\circ/20^\circ$, $25^\circ/20^\circ$, $30^\circ/20^\circ$, $35^\circ/20^\circ$, $40^\circ/20^\circ$ are tested. Finally the optimized asymmetric gear tooth profile with pressure angle $\alpha_d / \alpha_c = 35^\circ/20^\circ$ is found considering both the stress distributions in the drive side of the gear tooth and the transmission ability of the gear pair.

(2) The explicit ES-FEM-T3 membrane model for 3D nonlinear membrane structure deformation analysis

The necessity and difficulty of introducing the nonlinear strain term into the analytical expressions of the membrane deflections are firstly demonstrated. This is followed by formulating the explicit ES-FEM-T3 membrane model, which can easily incorporate the crucial nonlinear strain term, in which the edge-based strain smoothing is performed in the global Cartesian coordinate system and then transformed to the local co-rotational coordinate system for further calculation. Explicit time integration scheme is used to compute the transient response of the 3D spatial membrane structure. The dynamic relaxation method is employed to obtain the steady-state solutions of the membrane structure. Numerical results show that accuracy of the estimated membrane deflections is greatly improved by the explicit ES-FEM-T3 membrane model compared with the mechanical, FEM-T3 membrane and FEM-T3 shell models. Further examination of the explicit ES-FEM-T3 membrane model reveals that two main factors, i.e. the pressure fluctuations in the experiment and boundary constraints in numerical models, are found to attribute to the slight differences observed between the numerical and experimental results.

(3) The novel GSM/ALE method for the fluid flows over moving mesh.

The ALE form of Navior-Stokes equations are discretized with GSM in the spatial domain. The recovery of uniform flow is ensured through the introduction of the moving mesh source term derived directly from the geometric conservation law. The spatial stability is ensured through the implementation of the second order Roe flux differencing splitting unwinding scheme in the convective flux. The artificial compressibility formulation is utilized with a dual time stepping approach for the accurate time integration. Through the benchmark tests it can be seen that the proposed GSM/ALE method is accurate, stable and fairly robust to extremely distorted mesh for solving fluid-rigid body interaction problems. It can also achieve the 2nd order accuracies in both spatial and temporal domains.

(4) Coupling GSM/ALE with ES-FEM-T3 for FSI analysis

In consideration of the effective performance of the GSM/ALE and ES-FEM-T3 in solving for the pure fluid and solid problems, respectively, the novel weak coupling smoothed method, i.e. coupling of GSM/ALE with ES-FEM-T3, is proposed to solve the fluid-deformable solid interaction problem. The GSM/ALE is implemented in the fluid domain and a newly developed explicit time integration ES-FEM-T3 is implemented in the solid domain. The FSI coupling conditions are implemented on the FSI interface to “link” these two smoothed methods so as to conform to the dynamics of FSI. Through the tests of three benchmarks, it is found that the proposed FSI coupling conditions are accurately formulated and correctly implemented in the FSI code. And the proposed coupling smoothed method can give accurate, convergent, stable and robust solution for both transient and steady-state FSI problems. The proposed coupling smoothed methods are also robust to extremely distorted mesh. Furthermore, the FSI system is more sensitive to the changing in the solid mesh as compared to the fluid mesh. Thus it is suggested that for the solid portion a more refined mesh may be considered.

6.2 Recommendations for further work

Based on the work presented in the thesis, the following topics may be considered worthwhile for further exploration in future:

(1) As pointed out in the present research, the mesh condition can become indeed very distorted when the solid part undergoes extremely large deformations. Adaptive analysis of the dynamic mesh is a straightforward way to reassure the good quantities of the fluid mesh. The adaptive GSM with isotropic grids has already been developed for solving compressible flow problems previously. A formulation of the adaptive GSM/ALE should be effective and practical for solving FSI problems in the further work.

(2) The fluid-thin structure interaction exists in several engineering applications, e.g. the fluid-cell interaction in biomechanics and the wind-membrane interaction in the large-span structures. However, they are not so easy to be simulated due to the absence of bending momentum in the thin structure. The present ES-FEM-T3 has been found to work very well for solving the membrane deformation. Thus an extension of coupling GSM/ALE with ES-FEM-T3 for solving the fluid-thin structure interactions can be further studied in the future work.

(3) It is needed to extend the present coupling code into 3D space so that the code can be extensively applied for the real-life problems, which will in turn definitely generalize and promote the gradient smoothing methods.

(4) Develop the coupling scheme of GSM/ALE with ES-FEM-T3 for compressible fluid-deformable solid interaction analysis. The initial work of developing the compressible GSM solver and GSM/ALE solver has

already been done and more verification would be done to confirm the validity of the proposed solver in the future.

Appendix A

Governing equations of the asymmetric gear tooth profile

A kind of asymmetric gear tooth is novelly designed. An optimization process is presented in Chapter 3 to find the optimized set of gear tooth pressure angles to ensure that the optimized asymmetric gear can perform the best in consideration of both the stress distributions in the drive side of the gear tooth and the transformation ability of the gear pair. The governing equations of the five portions of the asymmetric tooth, i.e. the trochoidal and involute potions in the drive side, the trochoid and involute potions in the coast side and the addendum connecting the two involutes, as illustrated in Fig. 3.10, are driven as follows.

- ❖ Governing equations of the involutes: portions ① and ③

Set the center of the gear as the origin of the coordinate system, and the connection of origin and mid-point of tooth thickness in pinch circle as the *y* axis, as shown in Fig. A.1a, the involute coordinate (x_M, y_M) of an arbitrary point *M* in the drive side of the tooth (portion ①) can be expressed as

$$\begin{cases} x_M = r_M \sin\left(\mathrm{inv}\alpha_{Md} - \mathrm{inv}\alpha_d - \alpha_q\right) \\ y_M = r_M \cos\left(\mathrm{inv}\alpha_{Md} - \mathrm{inv}\alpha_d - \alpha_q\right) \end{cases} \tag{A.1}$$

where r_M is the radius of the circle passing through point *M*; $r_M = mz\cos\alpha_d \big/ \left(2\cos\alpha_{Md}\right)$, *z* is the total number of the gear teeth, α_{Md} is the pressure angle at point *M*, $\alpha_{Md} \in \left[\alpha_{ld}, \alpha_{ad}\right]$, α_{ad} is the pressure angle of the addendum circle in the drive side, $\alpha_{ad} = z\cos\alpha_d \Big/ \left(z + 2h_c^*\right)$, α_{ld} is the lower bound of

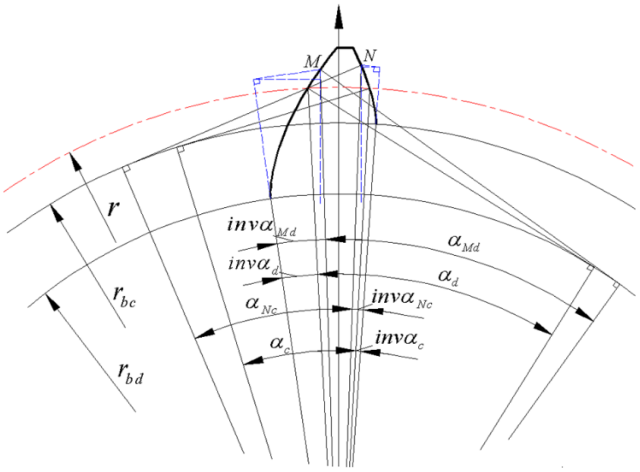

a) Involute portions of the gear tooth profile

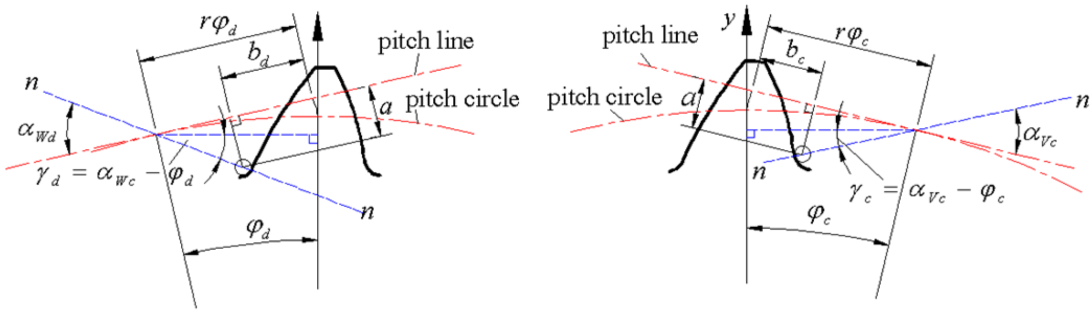

b) Trochoidal fillets of the gear tooth profile: the left one illustrates the drive side and the right one illustrates the coast side

Fig. A.1 Illustrations of the asymmetric gear tooth profile

the pressure angle in the drive side, $\alpha_{ld} = \arctan\left(\tan\alpha_d - 2h_c^* / \left(z\sin\alpha_d\cos\alpha_d\right)\right)$; $\mathrm{inv}\alpha_{Md} = \tan\alpha_{Md} - \alpha_{Md}$, so as the $\mathrm{inv}\alpha_d$; and $\alpha_q = \pi/(2z)$.

The involute coordinate (x_N, y_N) of an arbitrary point N in the coast side of the tooth (portion ③) can be expressed as

$$\begin{cases} x_N = -r_N\sin\left(\mathrm{inv}\alpha_{Nc} - \mathrm{inv}\alpha_c - \alpha_q\right) \\ y_N = \quad r_N\cos\left(\mathrm{inv}\alpha_{Nc} - \mathrm{inv}\alpha_c - \alpha_q\right) \end{cases} \tag{A.2}$$

where r_N is the radius of the circle passing through point N; $r_N = mz\cos\alpha_c / \left(2\cos\alpha_{Nc}\right)$, α_{Nc} is the pressure angle at point N, $\alpha_{Nc} \in \left[\alpha_{lc}, \alpha_{ac}\right]$, α_{ac} is the pressure angle of the addendum circle in the coast side, $\alpha_{ac} = z\cos\alpha_c / \left(z + 2h_c^*\right)$,

α_{lc} is the lower bound of the pressure angle in the coast side, $\alpha_{lc} = \arctan\left[\tan\alpha_c - 2h_c^* / \left(z\sin\alpha_c \cos\alpha_c\right)\right]$; $\mathrm{inv}\left(\alpha_{Nc}\right) = \tan\alpha_{Nc} - \alpha_{Nc}$, so as the $\mathrm{inv}\alpha_c$; $\alpha_q = \pi/(2z)$.

- Governing equations of the trochoid: portions ② and ④

Based on Fig. A.1b, the fillet coordinate (x_W, y_W) of an arbitrary point W in the drive side of the tooth (portion ②) can be expressed as

$$\begin{cases} x_W = -r\sin\varphi_d + \left(a/\sin\alpha_{Wd} + \rho\right)\cos\left(\alpha_{Wd} - \varphi_d\right) \\ y_W = \quad r\cos\varphi_d - \left(a/\sin\alpha_{Wd} + \rho\right)\sin\left(\alpha_{Wd} - \varphi_d\right) \end{cases} \tag{A.3}$$

where r is the radius of pinch circle, $r=mz/2$; α_{Wd} is the pressure angle at point W, $\alpha_{Wd} \in \left[\alpha_d, \pi/2\right]$; φ_d is the angle between the y axis and the vertical line of the pinch line in the drive side, $\varphi_d = \left(a\cot\alpha_{Wd} - b_d\right)/r$ with $b_d = \pi m/4 + mh_d^* \tan\alpha_d + \rho\cos\alpha_d$ and $a = h_c^* m + c_c^* m - \rho$.

The coordinates (x_V, y_V) of an arbitrary point V in the coast side of the tooth (portion ④) can be expressed as follows:

$$\begin{cases} x_V = r\sin\varphi_c - \left(a/\sin\alpha_{Vc} + \rho\right)\cos\left(\alpha_{Vc} - \varphi_c\right) \\ y_V = r\cos\varphi_c - \left(a/\sin\alpha_{Vc} + \rho\right)\sin\left(\alpha_{Vc} - \varphi_c\right) \end{cases} \tag{A.4}$$

where α_{Vc} is the pressure angle at point V, $\alpha_{Vc} \in \left[\alpha_c, \pi/2\right]$; φ_c is the angle between the y axis and the norm of the pinch line in the coast side, $\varphi_c = \left(a\cot\alpha_{Vc} - b_c\right)/r$ with $b_c = \pi m/4 + mh_c^* \tan\alpha_c + \rho\cos\alpha_c$ and $a = h_c^* m + c_c^* m - \rho$.

- Governing equations of the addendum: portion ⑤

The addendum is an arc with its center as the center of the gear. It is used to connect the two involutes of portions ① and ③.

Different portions of the asymmetric gear tooth profile are mechanically cut out by different portions of a specially designed asymmetric rack cuter, as illustrated in Fig. A.2a. In this rack cutter, a standard pressure angle α_c is applied in the coast side, a modified pressure angle α_d is applied in the drive side and one tip with radius ρ is designed to connect the curves in the drive and coast side. The parameters which are not clarified in Eqs. (A.1)-(A.4) could be totally found in the illustrations of the rack cutter here. It should be noted that the profile of the specially designed rack cutter here is somewhat similar with that in [1] but adopts a set of totally different parameters comparing with that in [1].

Parameters of the specially designed rack cutter labeled in Fig. A.2 are: module *m*, coast side pressure angle α_c, drive side pressure angle α_d, coast side addendum coefficient h_c^*, drive side addendum coefficient h_d^*, coast side bottom clearance coefficient c_c^*, drive side bottom clearance coefficient c_d^*, and the radius of the tip ρ. Among these parameters, *m*, α_c, α_d and h_c^* are the four design constants for a rack cutter design. The other parameters can be directly or indirectly derived from these four constants based on some mechanical relationships. In details, the radius of the tip ρ can be derived as

$$\rho = \left[\pi m/2 - h_c^* \times m \times (\tan\alpha_c + \tan\alpha_d)\right] \Big/ \left(\cos\alpha_c - \sec\alpha_d - \sin\alpha_c \times \tan\alpha_d\right). \tag{B.5}$$

The coast and drive side bottom clearance coefficient c_c^* and c_d^* can be, respectively, expressed as

$$c_c^* = \rho \times (1 - \sin\alpha_c)/m,\ c_d^* = \rho \times (1 - \sin\alpha_d)/m. \tag{B.6}$$

And the drive side addendum coefficient h_d^* is

$$h_d^* = h_c^* + c_c^* - c_d^* \ . \tag{B.7}$$

A much clear mechanical relationship among these parameters is labeled in Fig. A.2b.

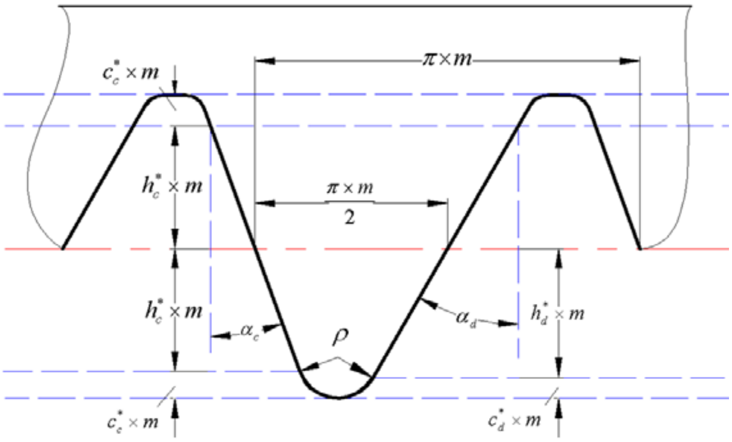

a) General profile of the asymmetric rack cutter

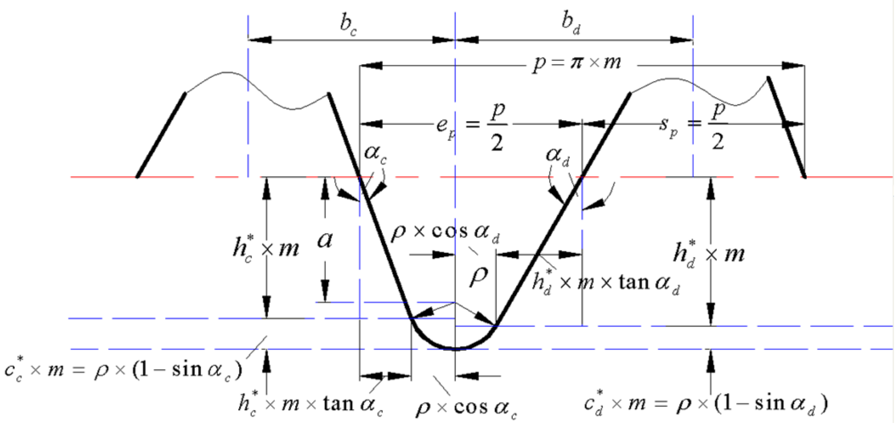

b) Detailed relationship among the parameters

Fig. A.2 Profile of the specially designed rack cutter with one fillet in the tip

The straight-line parts of the rack cutter are used to generate the involute profiles (portions ① and ③ in Fig. A.1a) and the fillet parts of the rack cutter are used to generate the trochoidal fillet profiles (portions ② and ④ in Fig. A.1a) during the gear generation process. Accordingly, a simulation of generating one typical asymmetric gear through a gear generation process are presented in Fig. A.3a and a gear pair cut out according to this cutting process is plotted in Fig. A.3b. For gears with different radiuses (different tooth numbers), the same rack cutter can still be used. As long as changing the relative movement speeds between the rack cutter and the blank gear in a cutting process, asymmetric gear with any tooth numbers can be cut out.

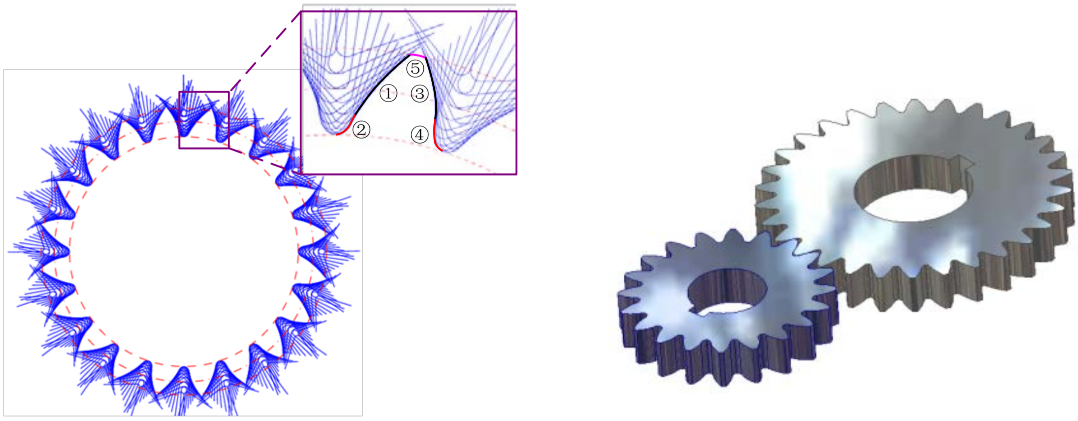

a) Simulation of the gear generation process for one typical gear tooth

b) Virtual model of an asymmetric gear pair

Fig. A.3 Gear generation process for the virtual asymmetric gear model by using the specially designed ractter cutter

References for Appendix A

1. Senthil Kumar, V., Muni, D.V. and Muthuveerappan, G., *Optimization of asymmetric spur gear drives to improve the bending load capacity*. Mechanism and Machine Theory, 2008. **43**(7): p. 829-858.